

UC Berkeley

UC Berkeley Electronic Theses and Dissertations

Title

Liquefaction Ejecta-Induced Damage

Permalink

<https://escholarship.org/uc/item/7gp6n23p>

Author

Mijic, Zorana

Publication Date

2022

Supplemental Material

<https://escholarship.org/uc/item/7gp6n23p#supplemental>

Peer reviewed|Thesis/dissertation

Liquefaction Ejecta-Induced Damage

By

Zorana Mijic

A dissertation submitted in partial satisfaction of the

requirements for the degree of

Doctor of Philosophy

in

Engineering – Civil and Environmental Engineering

in the

Graduate Division

of the

University of California, Berkeley

Committee in charge:

Professor Jonathan D. Bray, Chair

Professor Michael F. Riemer

Professor Misko Cubrinovski

Professor Douglas S. Dreger

Spring 2022

© Copyright 2022
Zorana Mijic
All rights reserved

Abstract

Liquefaction Ejecta-Induced Damage

by

Zorana Mijic

Doctor of Philosophy in Engineering – Civil and Environmental Engineering

University of California, Berkeley

Professor Jonathan D. Bray, Chair

The 2010-2011 Canterbury earthquake sequence (CES) devastated Christchurch, New Zealand. Liquefied soil were ejected onto the ground surface, damaging more than 15,000 houses beyond economic repair. Thick, clean sand deposits were largely responsible for the observed ejecta-induced damage. However, strongly shaken silty sites did not exhibit evidence of liquefaction despite the expectation that they would, based on the existing empirical liquefaction triggering methods. At silty soil sites, liquefaction triggering methods indicate expensive ground improvements and robust foundations are necessary, but field evidence during the CES indicate they are not required. This research addresses ejecta-induced settlement at all sites and the potential for liquefaction manifestation at silty soil sites.

Comprehensive assessment and documentation of liquefaction-induced land damage resulted in an unparalleled opportunity to study the effects of liquefaction. In this study, 235 case histories that document the occurrence and quantity of ejecta and its effects on infrastructure are compiled. Fifty-eight sites in the database are each analyzed for the four main earthquakes of the CES, and three additional sites are analyzed for the first event of the CES only because it did not induce lateral spreading. Direct measurements of ejecta were not conducted for the CES; hence, the ejecta-induced settlement values are estimated using LiDAR-based and photographic-based approaches. The information related to ground conditions and seismic demand leading to differing quantities of ejecta-induced settlement during the CES are also described. This unique database of detailed ejecta case histories was then examined for general trends associated with the severity of liquefaction ejecta-induced settlement and to evaluate the efficacy of some of the liquefaction-induced damage indices. Most sites in the database can be characterized by thick, clean sand deposits, which frequently underwent severe-to-extreme ejecta-induced settlement, especially as the equivalent $M_w = 6.1$ PGA exceeded 0.40 g. The severe-to-extreme ejecta-induced settlement tends to be systematically underestimated by current state-of-practice liquefaction-induced damage indices, especially if they do not incorporate the post-shaking hydraulic mechanisms in their formulation. The systematic underestimation of liquefaction ejecta at thick, clean sand sites, and, similarly, the systematic overestimation of liquefaction ejecta at stratified silty soil sites suggests the importance of the seismic soil system response, which is not considered in the simplified liquefaction triggering methods. Additionally, the severely damaged land by the Feb 2011 liquefaction ejecta formed cracks and defects in the non-liquefiable crust which liquefied soil at depth could exploit to form ejecta at the ground surface during the Jun 2011 earthquake. Therefore, the liquefaction ejecta case histories provide a sound basis for the investigation of the occurrence

and effects of ejecta and the development of a procedure to estimate the quantity of ejecta in an earthquake.

The first cyclic simple shear tests on high-quality retrieved specimens of Christchurch silty and sandy soil were performed to evaluate their liquefaction potential. The soil's undrained cyclic stress-strain responses indicate cyclic mobility. The differences in the cyclic responses of the soil with different amounts of non-plastic silt (2%-99% fines) are subtle. The soil stiffness was significantly lower in post-cyclic tests than in monotonic tests due to the large differences in the initial effective stresses between the two types of tests, loss of strength, age, and fabric effects. The field-adjusted laboratory-based cyclic resistances agree with CPT-based cyclic resistances from simplified liquefaction triggering procedures. Both assessments indicate the silty soil deposits generated high excess pore water pressures and liquefied during the Christchurch earthquake even though surface manifestations of liquefaction were not observed at the considered sites. The absence of liquefaction manifestation at the stratified silty soil sites highlights the importance of their system response.

An alternative method to the Japanese Standard JIS A 1224:2009 Test Method for evaluating the dry minimum and maximum densities of soil is proposed for those cases when a test specimen does not provide enough material to use the standard-size mold. The alternative test method was applied to soil from 42 small simple shear test specimens of retrieved high-quality soil samples. Soil from test specimens of the same material were subsequently mixed to produce eight soil composites for which their minimum and maximum densities could be determined using both the standard and alternative methods. The minimum and maximum void ratios determined by both methods for the composite soil are in good agreement. Moreover, trends in the dataset are consistent with those from previous studies on sand and non-plastic fine-grained soil. The alternative and standard test methods can be used to estimate the maximum and minimum void ratios of non-plastic silty soil with up to 70% fines so that relative density can be used to describe the state of the soil.

To my parents, Radmila and Marijan, my sister, Dejana, and my fiancé, Farzin

TABLE OF CONTENTS

Abstract	1
TABLE OF CONTENTS	ii
LIST OF FIGURES.....	vii
LIST OF TABLES	xx
ACKNOWLEDGMENTS	xxii
1 INTRODUCTION.....	1
1.1 OVERVIEW.....	1
1.2 ORGANIZATION	2
2 LIQUEFACTION EJECTA CASE HISTORIES FOR 2010-11 CANTERBURY EARTHQUAKES	4
2.1 INTRODUCTION	4
2.2 DATA AND MATERIALS AVAILABLE.....	5
2.2.1 Airborne LiDAR Surveys.....	6
2.2.2 Aerial Photography	7
2.2.3 Detailed LDAT Property Inspection Mapping.....	7
2.2.4 Conditional PGA.....	7
2.2.5 Event-Specific Groundwater Depths.....	8
2.3 SITES USED FOR THE DEVELOPMENT OF CASE HISTORIES	8
2.4 METHODOLOGY	9
2.4.1 Photographic-Based Ejecta-Induced Settlement.....	9
2.4.2 LiDAR-Based Ejecta-Induced Settlement.....	11
2.4.3 Best Estimate of Ejecta-Induced Settlement.....	12
2.5 DETAILED EVALUATION OF THE SHIRLEY INTERMEDIATE SCHOOL CASE HISTORIES	12
2.6 CONCLUSION	15
3 DETAILED ANALYSIS OF LIQUEFACTION EJECTA CASE HISTORIES FOR THE 2010-11 CANTERBURY EARTHQUAKES.....	30
3.1 INTRODUCTION	30
3.2 OVERVIEW OF THE LIQUEFACTION EJECTA DATABASE FOR THE 2010-2011 CANTERBURY EARTHQUAKES	32
3.2.1 Site Geology	32
3.2.2 Liquefaction Ejecta-Induced Settlement Estimates.....	33

3.3	EXAMINATION OF TRENDS FOR EJECTA-INDUCED SETTLEMENT AND AVAILABLE VARIABLES	35
3.3.1	The Effect of PGA on Ejecta-Induced Settlement	35
3.3.2	The Effect of Groundwater Depth on Ejecta-Induced Settlement	36
3.3.3	The Effect of Soil Profile on Ejecta-Induced Settlement	37
3.3.4	The Effect of Crust Thickness on Liquefaction Ejecta-Induced Settlement.....	38
3.3.5	The Effect of First Liquefiable Layer Thickness on Ejecta-Induced Settlement ...	39
3.4	EVALUATING THE EFFICACY OF LIQUEFACTION-INDUCED DAMAGE INDICES	40
3.4.1	Ishihara (1985) Boundary Curves	40
3.4.2	Liquefaction Potential Index, LPI.....	41
3.4.3	Liquefaction Severity Number, LSN.....	42
3.4.4	Liquefaction Ejecta Demand, L_D , and Crust Resistance, C_R , parameters.....	42
3.5	SITE PERFORMANCE DIFFERENCES AMONG THE FOUR MAIN CANTERBURY EARTHQUAKES	44
3.6	ADDITIONAL OBSERVATIONS REQUIRING FURTHER INVESTIGATION.....	45
3.7	CONCLUSION	46
4	TEST METHOD FOR MINIMUM AND MAXIMUM DENSITIES OF SMALL QUANTITIES OF SOIL	75
4.1	INTRODUCTION	75
4.2	TEST MATERIALS AND METHOD.....	75
4.2.1	Test Materials	75
4.2.2	Development of the Alternative Test Method.....	76
4.2.3	Alternative Test Method.....	77
4.2.4	Previous Studies Investigating the Effects of Fines Content	78
4.3	TEST RESULTS AND DISCUSSION.....	79
4.4	CONCLUSIONS	81
5	CYCLIC AND MONOTONIC SIMPLE SHEAR TESTING OF NATIVE CHRISTCHURCH SILTY SOIL.....	88
5.1	INTRODUCTION	88
5.2	SITES AND RETRIEVAL OF HIGH-QUALITY SAMPLES.....	89
5.2.1	Geological Setting of Christchurch	89
5.2.2	Sites and Soil Profiles.....	90
5.2.3	Selection of Sampling Depths.....	91
5.2.4	Dames and Moore Sampling Procedure	92
5.3	CHRISTCHURCH SOIL	94

5.3.1	SEM Imaging.....	94
5.3.2	Index Soil Properties	95
5.4	ADVANCED LABORATORY TESTING.....	96
5.5	RESULTS AND DISCUSSION.....	98
5.5.1	Relative Density.....	98
5.5.2	Monotonic Simple Shear Testing.....	99
5.5.3	Cyclic Simple Shear Testing.....	100
5.5.4	Post-Cyclic Monotonic Simple Shear Testing	104
5.5.5	Comparison of Field-Corrected Laboratory-Based CRR with CPT-Based CRR	105
5.6	CONCLUSIONS	106
6	CONCLUSIONS.....	123
6.1	SUMMARY	123
6.2	FINDINGS	123
6.2.1	Liquefaction Ejecta Case Histories Database	123
6.2.2	Liquefaction Potential of Stratified Silty Soil Deposits	125
6.3	FUTURE RESEARCH RECOMMENDATIONS.....	126
	REFERENCES	128
	Appendix A	135
A.1	Shirley Intermediate School – VsVp 57203.....	136
A.2	Rydal Reserve – VsVp 57190	136
A.3	Rawhiti Domain – VsVp 57188	136
A.4	Caulfield Ave – VsVp 38175	136
A.5	70 Langdons Rd – VsVp 57142.....	136
A.6	Vivian St – CPT 5586	136
A.7	50 Eureka St – VsVp 57195	136
A.8	Parnwell St & Bassett St – CPT 27709.....	136
A.9	Vangelis Ln & Fernbrook Pl – CPT 49582.....	136
A.10	Pinewood Ave – CPT 61991	136
A.11	Carisbrooke Playground – VsVp 57193.....	136
A.12	Avondale Playground – VsVp 57062	136
A.13	Bower Ave – CPT 3937	136
A.14	Wattle Dr – CPT 90678.....	136
A.15	Warrington St – CPT 44959	136
A.16	Hunt Ln – CPT 4674.....	136
A.17	Sandown Cres – CPT 15498.....	137

A.18	Travis Country Dr – CPT 29778.....	137
A.19	Aldershot St – CPT 5261	137
A.20	1/19 Chardale St – VsVp 57320.....	137
A.21	15b Royds Pl – VsVp 57326	137
A.22	31 Landy St – CPT 44439	137
A.23	Normans Rd/Papanui Rd – VsVp 57200.....	137
A.24	St. Teresa's School – VsVp 57191.....	137
A.25	Kaiwara Reserve – VsVp 57182.....	137
A.26	Ti Rakau Reserve – VsVp 57186	137
A.27	Avondale Park – VsVp 57187.....	137
A.28	Sabina Playground – VsVp 57192.....	137
A.29	Barrington Park – VsVp 38172	137
A.30	Shortland St – CPT 6551.....	137
A.31	Mark Treffers Dr – CPT 62594	137
A.32	Shirley Primary School – CPT 54376.....	137
A.33	Cashmere High School – CPT 33732	138
A.34	Dunarnan St – CPT 17908.....	138
A.35	Baker St – CPT 14070	138
A.36	Randolph St – CPT 44440.....	138
A.37	Woodham Rd – CPT 25514	138
A.38	Rudds Rd – CPT 5687	138
A.39	Palmers Rd – CPT 27040.....	138
A.40	Willryan Ave – CPT 2168.....	138
A.41	Bideford Pl – CPT 17200.....	138
A.42	Wharenui School – VsVp 57165	138
A.43	Heaton Normal Intermediate School – VsVp 57181	138
A.44	Hillmorton High School – VsVp 57201.....	138
A.45	St. Albans Catholic School – VsVp 57180	138
A.46	113A Palmers Rd – CPT 29740.....	138
A.47	Hurst Pl – CPT 25981	138
A.48	Shirley Boys High School – CPT 56468.....	138
A.49	Bracken St – CPT 59661	139
A.50	Palinurus Rd 1 – VsVp 57185	139
A.51	Palinurus Rd 2 – CPT 62761	139
A.52	Nursery Rd – CPT 17262.....	139

A.53	Gainsborough Reserve – VsVp 38176.....	139
A.54	55 Papanui Rd – VsVp 57189	139
A.55	Keers Rd – CPT 28986	139
A.56	200 Cashmere Rd – VsVp 38171	139
A.57	Armagh St – CPT 45795	139
A.58	Lakewood Dr – CPT 54736.....	139
A.59	Kensington Ave – CPT 88252.....	139
A.60	Tonks St – CPT 128494	139
A.61	Marblewood Reserve – VsVp 57155	139
Appendix B.....		140
B.1	Subsurface Investigation Overview	141
B.1.1	Site 2 – Gainsborough Reserve.....	141
B.1.2	Site 14 – Barrington Park	143
B.1.3	Site 23 – 85 Riccarton Road	145
B.1.4	Site 33 – 200 Cashmere Road.....	147
B.2	Boring Logs for Dames and Moore Sampling.....	149
B.2.1	Site 2 – Gainsborough Reserve.....	149
B.2.2	Site 14 – Barrington Park	150
B.2.3	Site 23 – 85 Riccarton Road	151
B.2.4	Site 33 – 200 Cashmere Road.....	152
B.3	Dames and Moore Sampling and Soil Sample Extrusion	153
Appendix C.....		154
C.1	Particle Size Distribution	155
C.2	Plasticity Index per ASTM D4318 and NGI Fall Cone Test.....	162
C.3	Scanning Electron Microscope Images	168
Appendix D.....		172
D.1	Cyclic and Monotonic Simple Shear Test Specimen Photographs	173
D.2	Processed Monotonic, Cyclic, and Post-Cyclic Monotonic Simple Shear Data.....	187
D.2.1	Monotonic Simple Shear Test Results	187
D.2.2	Cyclic Simple Shear Test Results	189
D.2.3	Post-cyclic Monotonic Simple Shear Test Results.....	208
Appendix E.....		226

LIST OF FIGURES

Figure 2.1. Location of 4 Sep 2010 Darfield main shock and subsequent aftershocks up to 11 Apr 2014 (GNS Science 2021).	18
Figure 2.2. Liquefaction observations at the ground surface for the (a) 4 Sep 2010, (b) 22 Feb 2011, (c) 13 Jun 2011, and (d) 23 Dec 2011 earthquakes (T+T 2015). (CBD = Christchurch Business District)	19
Figure 2.3. The maximum liquefaction ejecta-induced damage map (T+T 2015) with site locations. (CBD = Christchurch Business District)	20
Figure 2.4. (a) Ejecta shaped as a prism with irregular curvilinear bases, (b) Ejecta on the road shaped as a prism with triangular bases, and (c) Ejecta occurring naturally as a cone.	20
Figure 2.5. The Shirley Intermediate School site plan with the area analyzed for ejecta-induced settlement.....	23
Figure 2.6. Aerial photographs acquired for Shirley Intermediate School in Sep 2010, Feb 2011, Jun 2011, and Dec 2011 (CGD 2012a) with ejecta outlines for the 10-, 20-, and 50-m buffers.....	24
Figure 2.7. LiDAR survey points used to compute the average ground surface elevation in Global Mapper within the assessment area (outlined in red) for Mar 2011 (T+T 2015).	25
Figure 2.8. Vertical Ground Movements (adjusted for the tectonic component) for the Sep 2010 and Feb 2011 earthquakes (CGD 2012b) – the site is in the zone of overestimated ground surface subsidence for the Sep 2010 earthquake and the zone of underestimated ground surface subsidence for the Feb 2011 earthquake.....	26
Figure 2.9. Comparison between the ground surface subsidence determined using the individual LiDAR elevation points and the ground surface subsidence estimated using the LiDAR DEMs.	26
Figure 2.10. CPT traces and simplified soil profile for Shirley Intermediate School. (The soil layer colors are arbitrary.).....	27
Figure 2.11. The Boulanger and Idriss (2016) estimated cyclic resistance (CRR_{BI16}) and the cyclic stress ratio (CSR_{BI16}) adjusted for $M_w = 7.5$ and $\sigma'_{vo} = 1$ atm for the Sep 2010, Feb 2011, Jun 2011, and Dec 2011 earthquakes for CPTs 56473 and 57366 at Shirley Intermediate School. Layers with $FS_L < 1$ for the Feb 2011 event are shaded.	29

Figure 3.1. Box and whiskers showing distribution of liquefaction ejecta-induced settlement for each of the four main Canterbury earthquakes (magenta = median and cyan = mean)..... 49

Figure 3.2. The number of sites per liquefaction ejecta-induced settlement category for each of the four main Canterbury earthquakes. 50

Figure 3.3. Localized versus areal ejecta-induced settlement at each site for each of the four main Canterbury earthquakes. 50

Figure 3.4. Distribution of sites for the (a) Sep 2011, (b) Feb 2011, (c) Jun 2011, and (d) Dec 2011 earthquakes across Christchurch and relative to the Bradley and Hughes (2012) median PGA contours. The ejecta-induced settlement experienced at each site is shown as none (0 mm), minor (1-25 mm), moderate (26-50 mm), severe (51-100 mm), and extreme (> 100 mm). 51

Figure 3.5. The number of sites within each settlement category for each earthquake event and a range of $PGA_{6.1}$ 52

Figure 3.6. The relationship between $PGA_{6.1}$ and liquefaction ejecta-induced settlement for all 235 case histories (Spearman’s correlation coefficient = 0.45). Symbols differ for $PGA_{6.1} \leq 0.20$, 0.21-0.30, 0.31-0.40, and > 0.40g..... 53

Figure 3.7. Liquefaction ejecta-induced settlement versus $PGA_{6.1}$ for the (a) Sep 2010, (b) Feb 2011, (c) Jun 2011, and (d) Dec 2011 earthquakes. Spearman’s correlation coefficients for the Feb 2011, Jun 2011, and Dec 2011 earthquakes are 0.18, 0.47, and 0.50, respectively. 54

Figure 3.8. Distribution of sites with none (0 mm), minor (1-25 mm), moderate (26-50 mm), severe (51-100 mm), and extreme (>100 mm) ejecta-induced settlement across the regional groundwater depth models for the four main Canterbury earthquakes (T+T 2015)..... 55

Figure 3.9. Liquefaction ejecta-induced settlement versus groundwater depth for the Jun 2011 earthquake for different $PGA_{6.1}$ ranges: (a) ≤ 0.20 , (b) 0.21-0.30, (c) 0.31-0.40, and (d) > 0.40 g. Spearman’s correlation coefficients when $PGA_{6.1} = 0.21-0.30$, 0.31-0.40, and > 0.40 g are -0.32, -0.67, and -1.00, respectively. 56

Figure 3.10. CPT tip resistance, q_c , and soil behavior type index, I_c , for case histories with (a) zero, minor (1-25 mm), and moderate (26-50 mm) and (b) zero-to-minor (0-25 mm), moderate (26-50 mm), and severe-to-extreme (> 50 mm) liquefaction ejecta-induced settlement for $PGA_{6.1} \leq 0.20$, 0.21-0.30, 0.31-0.40, and > 0.40 g. 57

Figure 3.11. The relationship between the ejecta-induced settlement and the I_c -based crust thickness for different $PGA_{6.1}$ ranges: (a) ≤ 0.20 , (b) 0.21-0.30, (c) 0.31-0.40, and (d) > 0.40 g. Spearman’s correlation coefficients for $PGA_{6.1} = 0.21-0.30$, 0.31-0.40, and > 0.40 g are -0.17, 0.03, and -0.20, respectively..... 59

- Figure 3.12. The relationship between the ejecta-induced settlement and the I_c -based crust thickness for the (a) Feb 2011 ($PGA_{6.1} = 0.31-0.40$ and > 0.40 g), (b) Jun 2011 ($PGA_{6.1} = 0.21-0.30$ and $0.31-0.40$ g), and (c) Dec 2011 ($PGA_{6.1} = 0.21-0.30$ and $0.31-0.40$ g) earthquakes. Spearman's correlation coefficients are 0.31 and -0.20 for $PGA_{6.1} = 0.31-0.40$ and > 0.40 g, respectively, for the Feb 2011 earthquake, -0.31 and -0.50 for $PGA_{6.1} = 0.21-0.30$ and $0.31-0.40$ g, respectively, for the Jun 2011 earthquake, and -0.42 and -0.35 for $PGA_{6.1} = 0.21-0.30$ and $0.31-0.40$ g, respectively, for the Dec 2011 earthquake..... 60
- Figure 3.13. The relationship between the ejecta-induced settlement and the first significant liquefiable layer thickness, Z_{ab} , for different $PGA_{6.1}$ ranges: (a) ≤ 0.20 , (b) $0.21-0.30$, (c) $0.31-0.40$, and (d) > 0.40 g. Spearman's correlation coefficients for $PGA_{6.1} = 0.21-0.30$, $0.31-0.40$, and > 0.40 g are 0.37, 0.26, and 0.36, respectively. 61
- Figure 3.14. The relationship between the ejecta-induced settlement and the first significant liquefiable layer thickness, Z_{ab} , for the Feb 2011 earthquake for (a) $PGA_{6.1} = 0.31-0.40$ g and (b) $PGA_{6.1} > 0.40$ g. Spearman's correlation coefficients for $PGA_{6.1} = 0.31-0.40$ g and $PGA_{6.1} > 0.40$ g are 0.62 and 0.37, respectively. 62
- Figure 3.15. Zero, minor (1-25 mm), moderate (26-50 mm), severe (51-100 mm), and extreme (> 100 mm) liquefaction ejecta-induced settlement relative to the Ishihara (1985) boundary curves for (a) all four main Canterbury earthquakes, (b) Sep 2010, (c) Feb 2011, (d) Jun 2011, and (e) Dec 2011 earthquakes. The Ishihara (1985) boundary curves correspond to $PGA_{7.5} = 0.20, 0.30,$ and 0.45 g, while the case histories superimposed on the respective curves correspond to $PGA_{7.5} \leq 0.20, 0.30,$ and 0.45 g. 63
- Figure 3.16. Liquefaction potential index, LPI, and thickness of the first liquefiable layer, Z_{ab} , for all case histories relative to the severity of ejecta-induced settlement shown for (a) all ejecta-induced settlement categories, (b) none, (c) minor, (d) moderate, (e) severe, and (f) extreme ejecta-induced settlement categories represented by different symbols..... 64
- Figure 3.17. Liquefaction potential index, LPI, and thickness of the first liquefiable layer, Z_{ab} , for the (a) Sep 2010, (b) Feb 2011, (c) Jun 2011, and (d) Dec 2011 earthquakes relative to the ejecta-induced settlement categories represented by different symbols. 65
- Figure 3.18. Liquefaction severity number, LSN, and thickness of the first liquefiable layer, Z_{ab} , for all case histories relative to the severity of ejecta-induced settlement shown for (a) all ejecta-induced settlement categories, (b) none, (c) minor, (d) moderate, (e) severe, and (f) extreme ejecta-induced settlement categories represented by different symbols..... 66
- Figure 3.19. Liquefaction severity number, LSN, and thickness of the first liquefiable layer, Z_{ab} , for the (a) Sep 2010, (b) Feb 2011, (c) Jun 2011, and (d) Dec 2011 earthquakes

relative to the ejecta-induced settlement categories represented by different symbols.	67
Figure 3.20. Ejecta-induced settlement versus crust resistance, C_R , for all 235 case histories grouped based on their $PGA_{6.1}$. Spearman's correlation coefficient for $PGA_{6.1} = 0.21-0.30, 0.31-0.40, \text{ and } > 0.40$ g are $-0.13, 0.10, \text{ and } -0.36$, respectively.	68
Figure 3.21. The relationship between the ejecta-induced settlement and crust resistance, C_R , for the (a) Sep 2010, (b) Feb 2011, (c) Jun 2011, and (d) Dec 2011 earthquakes.	69
Figure 3.22. The correlation between the ejecta-induced settlement and liquefaction ejecta demand, L_D , for the (a) Sep 2010, (b) Feb 2011, (c) Jun 2011, and (d) Dec 2011 earthquakes. Spearman's correlation coefficients are $0.52, 0.60, \text{ and } 0.55$ for the Feb 2011, Jun 2011, and Dec 2011 earthquakes, respectively.	70
Figure 3.23. Liquefaction ejecta demand, L_D , and crust resistance, C_R , for all case histories relative to the severity of ejecta-induced settlement, shown for (a) all ejecta-induced settlement categories, (b) none, (c) minor, (d) moderate, (e) severe, and (f) extreme ejecta-induced settlement categories represented by different symbols.	71
Figure 3.24. Liquefaction ejecta demand, L_D , and crust resistance, C_R , for the (a) Sep 2010, (b) Feb 2011, (c) Jun 2011, and (d) Dec 2011 earthquakes relative to the ejecta-induced settlement categories represented by different symbols.	72
Figure 3.25. Comparison of (a) $PGA_{6.1}$, (b) groundwater depth, (c) first liquefiable soil layer thickness, and (d) crust thickness between the Sep 2010 and Jun 2011 earthquakes at sites that did not have ejecta for the Sep 2010 earthquake but had it for the Jun 2011 earthquake.	73
Figure 3.26. The relationship between the ejecta-induced settlement for the Feb 2011 earthquake and the ejecta-induced settlement for the Jun 2011 earthquake. Spearman's correlation coefficient is 0.73	74
Figure 4.1. Particle size distribution curves for 42 individual soil samples (curves in black) and eight soil composites (curves in green, yellow, and magenta).	82
Figure 4.2. (a) Dimensions of the alternative mold and (b) additional tools used to perform the alternative maximum dry density test.	84
Figure 4.3. Dimensions of the alternative funnel.	84
Figure 4.4. Minimum and maximum void ratios as a function of fines content for 42 individual soils and eight soil composites.	85
Figure 4.5. Void ratio range as a function of fines content for 42 individual soils and eight soil composites.	85

Figure 4.6. Comparison of void ratios between the alternative method and the Japanese Standard method. 87

Figure 4.7. Percent difference between the Japanese Standard method and the alternative method as a function of fines content for eight soil composites. 87

Figure 5.1. Site locations and liquefaction observations following the 2011 Christchurch earthquake; aerial photographs show absence of liquefaction ejecta at Sites 2, 23, and 33 and presence of moderate liquefaction ejecta at Site 14. 109

Figure 5.2. CPT tip resistance corrected for thin-layer effects and soil behavior type index profiles for sites 2, 14, 23, and 33. The q_{t1ncs} and I_c range for each set of specimens is based on q_{t1ncs} and I_c values that correspond to CPT measurements 10 cm above and below the specimen’s mid-depth as well as agreement between I_c and the retrieved soil; q_{t1ncs} was computed using the I_c -FC correlation with $C_{FC} = 0.13$ and laboratory-based FC; q_{t1ncs} for S33-DM3-3U is with the application of $I_{c,cutoff} = 2.9$ 110

Figure 5.3. Test specimen appearance: (a) S14-DM3-4U-M (ML) before testing, (b) S23-DM2-6U-T3 (SM) after testing, and (c) S33-DM3-3U-T5 (ML) after testing. 111

Figure 5.4. SEM images of soil [enlarged 200x except (e) which is enlarged 1000x]: (a) S14-DM3-3U-T5 (FC=44%): (i) “as-is” (coarse plus fines fraction), (ii) coarse fraction (particles $\geq 75\mu m$), and (iii) fines fraction (particles $\leq 75\mu m$); (b) S14-DM3-3U-T1 (FC=54%): (i) “as-is”; (ii) coarse fraction, and (iii) fines fraction; (c) S33-DM3-1U-T3 (FC=2%): “as-is”; (d) S33-DM3-4U-T1 (FC=99%): “as-is”; and (e) S14-DM3-3U-T1(FC=54%): “as-is”. 111

Figure 5.5. Particle size distribution curves for the test specimens. 114

Figure 5.6. (a) UC Berkeley unidirectional simple shear device and arrangement of vertical LVDTs (modified after Cappellaro et al. (2021), not drawn to scale), and (b) simple shear test specimen encased in plain latex membrane and subjected to vacuum pressure. 114

Figure 5.7. Comparison between laboratory-based D_R and in-situ D_R estimated using the Cubrinovski and Ishihara (1999) and Robertson and Cabal (2015) correlations. The horizontal bars correspond to the upper and lower q_{t1n} values measured over a depth range typically 10 cm above and below the specimen’s mid-depth. 116

Figure 5.8. Monotonic simple shear response of four test specimens with the dashed lines representing phase transformation lines for the test specimens. 116

Figure 5.9. Cyclic simple shear response of test specimens: (a) SP-2-88, (b) SM-43-76, (c) SM-43-56, (d) ML-64-82, and (e) ML-74-100. 117

Figure 5.10. Shear stress-strain response in the second, liquefaction-triggering, and third post-liquefaction-triggering cycle: (a) SP-2-88, (b) SM-43-76, (c) SM-43-56, (d) ML-64-82, and (e) ML-74-100.	118
Figure 5.11. Excess pore water pressure generation during the first ten loading cycles for test specimens: SP-2-88, SM-43-76, SM-43-56, ML-64-82, and ML-74-100; values in parentheses correspond to CSR and σ'_{vo} , respectively.	119
Figure 5.12. Cyclic resistance ratio curves for the simple shear test specimens; the provided D_R and σ'_{vo} represent an average for a set of test specimens.	120
Figure 5.13. Comparison of cyclic simple shear responses of soil with 44% fines (SM-44-80) and 54% fines (ML-54-74).	121
Figure 5.14. Post-cyclic monotonic simple shear response of the test specimens.	121
Figure 5.15. Comparison of the field-adjusted laboratory-based cyclic resistance ratio (CRR_{CSS}) and the Boulanger and Idriss (2016) estimated cyclic resistance (CRR_{BI16}) based on the I_c -FC correlation and laboratory-based FC at the test specimen origin depths with the cyclic stress ratio (CSR_{BI16}) adjusted for $M_w = 7.5$ and $\sigma'_{vo} = 1$ atm for the 2010 Darfield, 2011 Christchurch, and June 2011 earthquakes. Layers with $FS_L < 1$ for the Christchurch event are shaded.	122
Figure B.3.1. Tri-cone roller bit and thin-walled brass tube attached to the Dames and Moore sampler.	153
Figure B.3.2. Brass tube cutting prior to soil extrusion.	153
Figure B.1.1.1. Plan view of the Gainsborough Reserve site with the Dames and Moore sampling location (S2-BH_DM2) relative to the locations of previous investigations.	141
Figure B.1.1.2. Photograph of the Gainsborough Reserve site (date: 18 July 2019).	141
Figure B.1.1.3. I_c and q_{t1ncs} profiles at the Gainsborough Reserve site with Dames and Moore sampling depths for the simple shear testing program and depths of cyclic triaxial test specimens from previous research studies.	142
Figure B.1.2.1. Plan view of the Barrington Park site with the Dames and Moore sampling location (S14-BH3_DM) relative to the locations of previous investigations.	143
Figure B.1.2.2. Photographs of the Barrington Park site (date: 23 May 2019; the 2 nd day of sampling).	143

Figure B.1.2.3. I_c and q_{t1ncs} profiles at the Barrington Park site with Dames and Moore sampling depths for the simple shear testing program and depths of cyclic triaxial test specimens from previous research studies..... 144

Figure B.1.3.1. Plan view of the 85 Riccarton Road site with the Dames and Moore sampling location (S23-BH_DM2) relative to the locations of previous investigations. 145

Figure B.1.3.2. Photograph of the 85 Riccarton Road site (date: 20 July 2019). 145

Figure B.1.3.3. I_c and q_{t1ncs} profiles at the 85 Riccarton Road site with Dames and Moore sampling depths for the simple shear testing program and depths of cyclic triaxial test specimens from previous research studies..... 146

Figure B.1.4.1. Plan view of the 200 Cashmere Road site with the Dames and Moore sampling location (S23-BH_DM2) relative to the locations of previous investigations. 147

Figure B.1.4.2. Photographs of the 200 Cashmere Road site (date: 21 May 2019)..... 147

Figure B.1.4.3. I_c and q_{t1ncs} profiles at the 200 Cashmere Road site with Dames and Moore sampling depths for the simple shear testing program and depths of cyclic triaxial test specimens from previous research studies..... 148

Figure B.3.1. Tri-cone roller bit and thin-walled brass tube attached to the Dames and Moore sampler. 153

Figure B.3.2. Brass tube cutting prior to soil extrusion..... 153

Figure C.1.1. Particle size distribution curves for S33-DM3-1U-T2, -T3, and -T4. 155

Figure C.1.2. Particle size distribution curves for S33-DM3-1U-T1 and S33-DM3-2U-T1. 155

Figure C.1.3. Particle size distribution curves for S23-DM2-6U-T1, -T2, -T3, and -M. 156

Figure C.1.4. Particle size distribution curves for S2-DM2-3U-T1, -T2, -T3, and -M... 156

Figure C.1.5. Particle size distribution curves for S14-DM3-3U-T1, -T5, -T6, and -T7. 157

Figure C.1.6. Particle size distribution curves for S14-DM3-4U-T1, -T2, -T3, and -M. 157

Figure C.1.7. Particle size distribution curves for S2-DM2-6U-T1 and -T2..... 158

Figure C.1.8. Particle size distribution curves for S14-DM3-6U-T1, -T2, -T3, and -M.	158
Figure C.1.9. Particle size distribution curves for S33-DM3-3U-T4, -T5, and -T6.	159
Figure C.1.10. Particle size distribution curves for S33-DM3-4U-T1, -T2, and -T3.	159
Figure C.1.11. Particle size distribution curves for S2-DM2-1U-T1, -T2, and -T3.	160
Figure C.1.12. Particle size distribution curves for S23-DM2-3U-T1, -T2, -T3, and -T5.	160
Figure C.1.13. Particle size distribution curves for soil composites: S2-DM2-3U, S14-DM3-3U, S14-DM3-4U, S14-DM3-6U, S23-DM2-3U, S23-DM2-6U, S33-DM3-1U, and S33-DM3-4U.....	161
Figure C.1.14. Particle size distribution curves for D-1 and K-4 (Table 4.1). D-1 is an equivalent of S14-DM3-3U-T2 not presented in Chapter 5.....	161
Figure C.2.1. Soil is too dry so its liquid limit cannot be determined using the Casagrande's method.	165
Figure C.2.2. Soil is at its plastic limit yet above its liquid limit according to the Casagrande's method.	165
Figure C.3.1. SEM images of S33-DM3-1U-T3 (FC = 2%) enlarged 100 and 250 times. The one enlarged 100 times was used to assess the particle shape (Table 5.1).....	168
Figure C.3.2. SEM images of S14-DM3-3U-T5 (FC = 44%) fines + coarse fractions ("as-is") enlarged 100 and 600 times.....	168
Figure C.3.3. SEM images of S14-DM3-3U-T5 coarse fraction enlarged 100 and 300 times. The one enlarged 100 times was used to assess the particle shape (Table 5.1).....	168
Figure C.3.4. SEM images of S14-DM3-3U-T5 fines fraction enlarged 150 and 800 times. The one enlarged 150 times was used to assess the particle shape (Table 5.1).....	169
Figure C.3.5. SEM images of S14-DM3-3U-T1 (FC = 54%) coarse + fines fractions ("as-is") enlarged 100 and 600 times.....	169
Figure C.3.6. SEM images of S14-DM3-3U-T1 coarse fraction enlarged 100 and 300 times. The one enlarged 100 times was used to assess the particle shape (Table 5.1).....	169
Figure C.3.7. SEM images of S14-DM3-3U-T1 fines fraction enlarged 150 and 800 times. The one enlarged 150 times was used to assess the particle shape (Table 5.1).....	170
Figure C.3.8. SEM images of S14-DM3-6U-T3 (FC = 74%) coarse + fines fractions ("as-is") enlarged 100 and 1000 times.....	170

Figure C.3.9. SEM images of S14-DM3-6U-T3 coarse fraction enlarged 100 and 300 times. The one enlarged 100 times was used to assess the particle shape (Table 5.1).....	170
Figure C.3.10. SEM images of S14-DM3-6U-T3 fines fraction enlarged 200 and 1500 times. The one enlarged 200 times was used to assess the particle shape (Table 5.1).	171
Figure C.3.11. SEM images of S33-DM3-4U-T1 (FC = 99%) enlarged 300 and 1500 times. The one enlarged 300 times was used to assess the particle shape (Table 5.1).....	171
Figure D.1.1. S33-DM3-1U-T2 before and after CSS testing.....	173
Figure D.1.2. S33-DM3-1U-T3 before and after CSS testing.....	173
Figure D.1.3. S33-DM3-1U-T4 before and after CSS testing.....	173
Figure D.1.4. S33-DM3-1U-T1 before and after CSS testing.....	174
Figure D.1.5. S33-DM3-2U-T1 before and after CSS testing.....	174
Figure D.1.6. S23-DM2-6U-T1 before and after CSS testing.....	174
Figure D.1.7. S23-DM2-6U-T2 before and after CSS testing.....	175
Figure D.1.8. S23-DM2-6U-T3 before and after CSS testing.....	175
Figure D.1.9. S23-DM2-6U-M before and after MSS testing.....	175
Figure D.1.10. S2-DM2-3U-T1 before and after CSS testing.....	176
Figure D.1.11. S2-DM2-3U-T2 before and after CSS testing.....	176
Figure D.1.12. S2-DM2-3U-T3 before and after CSS testing.....	176
Figure D.1.13. S2-DM2-3U-M before and after MSS testing.....	177
Figure D.1.14. S14-DM3-3U-T1 before and after CSS testing.....	177
Figure D.1.15. S14-DM3-3U-T5 before and after CSS testing.....	177
Figure D.1.16. S14-DM3-3U-T6 before and after CSS testing.....	178
Figure D.1.17. S14-DM3-3U-T7 before and after CSS testing.....	178
Figure D.1.18. S14-DM3-4U-T1 before and after CSS testing.....	178
Figure D.1.19. S14-DM3-4U-T2 before and after CSS testing.....	179
Figure D.1.20. S14-DM3-4U-T3 before and after CSS testing.....	179
Figure D.1.21. S14-DM3-4U-M before and after MSS testing.....	179
Figure D.1.22. S2-DM2-6U-T1 before and after CSS testing.....	180

Figure D.1.23. S2-DM2-6U-T2 before and after CSS testing.....	180
Figure D.1.24. S14-DM3-6U-T1 before and after CSS testing.....	180
Figure D.1.25. S14-DM3-6U-T2 before and after CSS testing.....	181
Figure D.1.26. S14-DM3-6U-T3 before and after CSS testing.....	181
Figure D.1.27. S14-DM3-6U-M before and after MSS testing.....	181
Figure D.1.28. S33-DM3-3U-T4 before and after CSS testing.....	182
Figure D.1.29. S33-DM3-3U-T5 before and after CSS testing.....	182
Figure D.1.30. S33-DM3-3U-T6 before and after CSS testing.....	182
Figure D.1.31. S33-DM3-4U-T1 before and after CSS testing.....	183
Figure D.1.32. S33-DM3-4U-T2 before and after CSS testing.....	183
Figure D.1.33. S33-DM3-4U-T3 before and after CSS testing.....	183
Figure D.1.34. S2-DM2-1U-T1 before and after CSS testing.....	184
Figure D.1.35. S2-DM2-1U-T2 before and after CSS testing.....	184
Figure D.1.36. S2-DM2-1U-T3 before and after CSS testing.....	184
Figure D.1.37. S23-DM2-3U-T1 before and after CSS testing.....	185
Figure D.1.38. S23-DM2-3U-T2 before and after CSS testing.....	185
Figure D.1.39. S23-DM2-3U-T3 before and after CSS testing.....	185
Figure D.1.40. S23-DM2-3U-T5 before and after CSS testing.....	186
Figure D.1.41. S14-DM3-3U-T2 before and after CSS testing. This test specimen is not presented in Chapter 5.....	186
Figure D.2.1.1. MSS test results for SM-15-72 (S23-DM2-6U-M).....	187
Figure D.2.1.2. MSS test results for SM-40-66 (S2-DM2-3U-M).....	187
Figure D.2.1.3. MSS test results for ML-85-89 (S14-DM3-4U-M).	187
Figure D.2.1.4. MSS test results for ML-76-98 (S14-DM3-6U-M).	188
Figure D.2.2.1. CSS test results for SP-3-84 (S33-DM3-1U-T2).....	189
Figure D.2.2.2. CSS test results for SP-2-88 (S33-DM3-1U-T3).....	190
Figure D.2.2.3. CSS test results for SP-3-78 (S33-DM3-1U-T4).....	190

Figure D.2.2.4. CSS test results for SM-28-85 (S33-DM3-1U-T1).....	191
Figure D.2.2.5. CSS test results for SM-15-75 (S33-DM3-2U-T1).....	191
Figure D.2.2.6. CSS test results for SM-43-76 (S23-DM2-6U-T1).....	192
Figure D.2.2.7. CSS test results for SM-39-79 (S23-DM2-6U-T2).....	192
Figure D.2.2.8. CSS test results for SM-29-71 (S23-DM2-6U-T3).....	193
Figure D.2.2.9. CSS test results for SM-43-56 (S2-DM2-3U-T1).	193
Figure D.2.2.10. CSS test results for SM-44-58 (S2-DM2-3U-T2).....	194
Figure D.2.2.11. CSS test results for SM-47-65 (S2-DM2-3U-T3).....	194
Figure D.2.2.12. CSS test results for ML-54-74 (S14-DM3-3U-T1).	195
Figure D.2.2.13. CSS test results for SM-44-80 (S14-DM3-3U-T5).....	195
Figure D.2.2.14. CSS test results for ML-54-82 (S14-DM3-3U-T6).	196
Figure D.2.2.15. CSS test results for ML-62-83 (S14-DM3-3U-T7).	196
Figure D.2.2.16. CSS test results for SM-46-76 (S14-DM3-4U-T1).....	197
Figure D.2.2.17. CSS test results for ML-64-82 (S14-DM3-4U-T2).	197
Figure D.2.2.18. CSS test results for ML-59-81 (S14-DM3-4U-T3).	198
Figure D.2.2.19. CSS test results for ML-72-89 (S2-DM2-6U-T1).	198
Figure D.2.2.20. CSS test results for ML-87-84 (S2-DM2-6U-T2).	199
Figure D.2.2.21. CSS test results for ML-57-87 (S14-DM3-6U-T1).	199
Figure D.2.2.22. CSS test results for ML-71-99 (S14-DM3-6U-T2).	200
Figure D.2.2.23. CSS test results for ML-74-100 (S14-DM3-6U-T3).....	200
Figure D.2.2.24. CSS test results for ML-99-86 (S33-DM3-3U-T4).	201
Figure D.2.2.25. CSS test results for ML-99-92 (S33-DM3-3U-T5).	201
Figure D.2.2.26. CSS test results for ML-98-82 (S33-DM3-3U-T6).	202
Figure D.2.2.27. CSS test results for ML-99-94 (S33-DM3-4U-T1).	202
Figure D.2.2.28. CSS test results for ML-97-85 (S33-DM3-4U-T2).	203
Figure D.2.2.29. CSS test results for ML-98-89 (S33-DM3-4U-T3).	203
Figure D.2.2.30. CSS test results for ML-92-82 (S2-DM2-1U-T1).	204
Figure D.2.2.31. CSS test results for ML-89-77 (S2-DM2-1U-T2).	204

Figure D.2.2.32. CSS test results for ML-96-93 (S2-DM2-1U-T3).	205
Figure D.2.2.33. CSS test results for ML-92-97 (S23-DM2-3U-T1).	205
Figure D.2.2.34. CSS test results for ML-98-99 (S23-DM2-3U-T2).	206
Figure D.2.2.35. CSS test results for ML-99-91 (S23-DM2-3U-T3).	206
Figure D.2.2.36. CSS test results for ML-99-91 (S23-DM2-3U-T5).	207
Figure D.2.2.37. CSS test results for SM-25-73 (S14-DM3-3U-T2), not in Chapter 5..	207
Figure D.2.3.1. Post-cyclic MSS test results for SP-3-84 (S33-DM3-1U-T2).....	208
Figure D.2.3.2. Post-cyclic MSS test results for SP-2-88 (S33-DM3-1U-T3).....	208
Figure D.2.3.3. Post-cyclic MSS test results for SP-3-78 (S33-DM3-1U-T4).....	209
Figure D.2.3.4. Post-cyclic MSS test results for SM-28-85 (S33-DM3-1U-T1).....	209
Figure D.2.3.5. Post-cyclic MSS test results for SM-15-75 (S33-DM3-2U-T1).....	210
Figure D.2.3.6. Post-cyclic MSS test results for SM-43-76 (S23-DM2-6U-T1).....	210
Figure D.2.3.7. Post-cyclic MSS test results for SM-39-79 (S23-DM2-6U-T2).....	211
Figure D.2.3.8. Post-cyclic MSS test results for SM-29-71 (S23-DM2-6U-T3).....	211
Figure D.2.3.9. Post-cyclic MSS test results for SM-43-56 (S2-DM2-3U-T1).....	212
Figure D.2.3.10. Post-cyclic MSS test results for SM-44-58 (S2-DM2-3U-T2).....	212
Figure D.2.3.11. Post-cyclic MSS test results for SM-47-65 (S2-DM2-3U-T3).....	213
Figure D.2.3.12. Post-cyclic MSS test results for ML-54-74 (S14-DM3-3U-T1).....	213
Figure D.2.3.13. Post-cyclic MSS test results for SM-44-80 (S14-DM3-3U-T5).....	214
Figure D.2.3.14. Post-cyclic MSS test results for ML-54-82 (S14-DM3-3U-T6).....	214
Figure D.2.3.15. Post-cyclic MSS test results for SM-46-76 (S14-DM3-4U-T1).....	215
Figure D.2.3.16. Post-cyclic MSS test results for ML-64-82 (S14-DM3-4U-T2).....	215
Figure D.2.3.17. Post-cyclic MSS test results for ML-59-81 (S14-DM3-4U-T3).....	216
Figure D.2.3.18. Post-cyclic MSS test results for ML-72-89 (S2-DM2-6U-T1).	216
Figure D.2.3.19. Post-cyclic MSS test results for ML-87-84 (S2-DM2-6U-T2).	217
Figure D.2.3.20. Post-cyclic MSS test results for ML-57-87 (S14-DM3-6U-T1).....	217
Figure D.2.3.21. Post-cyclic MSS test results for ML-71-99 (S14-DM3-6U-T2).....	218

Figure D.2.3.22. Post-cyclic MSS test results for ML-74-100 (S14-DM3-6U-T3).....	218
Figure D.2.3.23. Post-cyclic MSS test results for ML-99-86 (S33-DM3-3U-T4).....	219
Figure D.2.3.24. Post-cyclic MSS test results for ML-99-92 (S33-DM3-3U-T5).....	219
Figure D.2.3.25. Post-cyclic MSS test results for ML-98-82 (S33-DM3-3U-T6).....	220
Figure D.2.3.26. Post-cyclic MSS test results for ML-99-94 (S33-DM3-4U-T1).....	220
Figure D.2.3.27. Post-cyclic MSS test results for ML-97-85 (S33-DM3-4U-T2).....	221
Figure D.2.3.28. Post-cyclic MSS test results for ML-98-89 (S33-DM3-4U-T3).....	221
Figure D.2.3.29. Post-cyclic MSS test results for ML-92-82 (S2-DM2-1U-T1).	222
Figure D.2.3.30. Post-cyclic MSS test results for ML-89-77 (S2-DM2-1U-T2).	222
Figure D.2.3.31. Post-cyclic MSS test results for ML-96-93 (S2-DM2-1U-T3).	223
Figure D.2.3.32. Post-cyclic MSS test results for ML-92-97 (S23-DM2-3U-T1).....	223
Figure D.2.3.33. Post-cyclic MSS test results for ML-98-99 (S23-DM2-3U-T2).....	224
Figure D.2.3.34. Post-cyclic MSS test results for ML-99-91 (S23-DM2-3U-T3).....	224
Figure D.2.3.35. Post-cyclic MSS test results for ML-99-91 (S23-DM2-3U-T5).....	225
Figure D.2.3.36. Post-cyclic MSS test results for SM-25-73 (S14-DM3-3U-T2) retrieved from a 4.740-m depth. This test specimen is not presented in Chapter 5.....	225
Figure E.1. Steady-state test data for S23-DM2-6U. (D_R = relative density at the end of consolidation, prior to shearing.)	228
Figure E.2. Steady-state test data for S14-DM3-4U. (D_R = relative density at the end of consolidation, prior to shearing.)	229
Figure E.3. Steady-state test data for S33-DM3-4U. (D_R = relative density at the end of consolidation, prior to shearing.)	230

LIST OF TABLES

Table 2.1. Best estimates of areal ejecta-induced free-field settlement for each site.	20
Table 2.2. Coverage area and height of ejecta estimates for 10-m buffer using photographs.	24
Table 2.3. Photographic-based areal and localized ejecta-induced settlement.....	24
Table 2.4. Raw liquefaction-induced ground surface subsidence using original LiDAR points.	25
Table 2.5. LiDAR flight error adjustments, global adjustments for the difference between average LiDAR point elevations and benchmark survey elevations, and vertical tectonic movement adjustments.	25
Table 2.6. Corrected liquefaction-induced ground subsidence using Table 2.4 values and Table 2.5 adjustments.....	26
Table 2.7. Ejecta-induced settlement for the top 20 m of the soil profile within the 10-m buffer for the 50 th %ile PGA, $P_L=50\%$, and $C_{FC}=0.13$ using BI-2016, ZRB-2002, and I_c cutoff of 2.6.....	27
Table 2.8. CPT-based results for Shirley Intermediate School.....	28
Table 2.9. Best estimates of ejecta-induced settlement for Shirley Intermediate School.	29
Table 3.1. Distribution of soil deposit types across the geologic quadrants.....	49
Table 4.1. Void ratios of 42 Christchurch soil samples.	83
Table 4.2. Soil composites and their minimum and maximum void ratios determined by the alternative method and the Japanese Standard method.	86
Table 5.1. Particle shape characteristics of eight soil specimens.....	112
Table 5.2. Test specimen characteristics.	113
Table 5.3. CSS, MSS, and post-cyclic MSS test results.....	115
Table B.1.1.1. Dames and Moore sampling depths at Site 2 – Gainsborough Reserve..	142

Table B.1.2.1. Dames and Moore sampling depths at Site 14 – Barrington Park. 144

Table B.1.3.1. Dames and Moore sampling depths at Site 23 – 85 Riccarton Road. 146

Table B.1.4.1. Dames and Moore sampling depths at Site 33 – 200 Cashmere Road.... 148

Table C.2.1. Liquid limit, plastic limit, and plasticity index using ASTM D4318 and fall cone test method..... 166

Table E.1. Index properties of soil composites and individual soil samples used to build them. 228

ACKNOWLEDGMENTS

First and foremost, I would like to thank my advisor, Professor Jonathan Bray, for his continuous support, guidance, encouragement, and for blessing me with exceptional research opportunities. I thank him for challenging me to think beyond what I thought could be possible. I am honored to have worked with and learned from such an outstanding researcher, engineer, mentor, and, above all, a great person. His motivation and passion for geotechnical earthquake engineering have been truly inspiring. Professor Bray is the kind of a scholar I aspire to be.

The research presented in this dissertation was supported by many organizations, including the U.S. Geological Survey (USGS) [grant number G20AP00079], U.S. National Science Foundation (NSF) [grant numbers CMMI-1561932 and CMMI-1956248], Pacific Earthquake Engineering Research (PEER) Center [grant number NC3KT101114], the Faculty Chair in Earthquake Engineering Excellence at UC Berkeley; Earthquake Commission (EQC), Natural Hazards Research Platform (NHRP), Tonkin and Taylor, Ltd., University of Canterbury, and University of California, Berkeley. Additional support was provided by The Deep Foundations Institute Charles J. Berkel Memorial Scholarship. The financial support of these organizations is gratefully acknowledged. The findings, opinions, and conclusions presented in this dissertation do not necessarily reflect the views of the sponsoring bodies.

Laboratory work would not have been possible without Professor Michael Riemer. Countless thanks go to him for sharing his insights and for always being available to provide advice and help with troubleshooting. Dr. Sean Rees was also instrumental in my accomplishing the field and laboratory work. I have no words to describe how thankful I am for everything he has done to help me succeed. I consider him a truly valuable colleague and friend. Working with Professor Misko Cubrinovski has been a tremendous honor. I am very grateful to have learned from him about liquefaction and geotechnical earthquake engineering. He was a wonderful host during my stay in Christchurch. Liquefaction ejecta research would not have been possible without Dr. Sjoerd van Ballegooy. I thank him for selflessly sharing his knowledge and expertise with me; it is very much appreciated. I am grateful to have collaborated with the best researchers and engineers.

Many thanks go to the Tonkin and Taylor team: James Russell, Oliver Hay, and Nathan McDougall for their help on the liquefaction ejecta project, Mike Jacka for providing site information and helping secure access to 200 Cashmere Rd, Branco Barnes for always quickly and patiently resolving every technical issue I had, and everyone in the Geotechnical Engineering Group for their kindness and hospitality during my stay in Auckland. I would like to thank Christchurch City Council for access to Gainsborough Reserve and Barrington Park, McMillan Drilling, especially Iain Haycock and Kortni Morris, for the drilling and sampling work, and Matthew Cataleta, Irik Larson, and Jeffrey Higginbotham of UC Berkeley for their help in manufacturing the laboratory testing equipment. I am especially grateful for the immense help Dr. Christine Beyzaei and Dr. Claudio Cappellaro provided toward the field and laboratory work. Dr. Cappellaro's kindness and hospitality during my stay in Christchurch are very much appreciated. I would like to extend my gratitude to Dr. Daniel Hutabarat for providing the code to compute the ejecta potential and crust resistance parameters.

I would like to thank Professor Nicholas Sitar for his guidance and warm welcome at UC Berkeley, Professor Douglas Dreger for serving on both my dissertation and qualifying exam committees, and Professors Kenichi Soga and Khalid Mosalam for serving on my qualifying exam committee. I enjoyed taking their classes and learning from them, as well as from other UC Berkeley professors. My best ‘earthquake’ friends, Franklin Olaya and Grigorios Lavrentiadis, made Davis Hall my second home. I truly enjoyed sharing office space and having long, insightful discussions with them. My PhD experience would not have been complete without my dearest UC Berkeley friends: Evania Kristanti, Shuyi Yang, Lilian Lorincz, Vangelis Petas, Franco de Paola, Guanzhi Deng, Zhenxiang Su, Estéfan Garcia, Zhen Yang, and Camilo Pinilla. I am especially thankful for Camilo’s and Fernanda Corvillón’s hospitality during my last PhD days at Berkeley.

During my PhD, I have befriended many great people. I cannot properly thank Dianne Campton for her hospitality during my research work in Auckland. I am extremely grateful for everything Dianne Campton, Monique Williamson, Jean and Danny Paton, Beverly and Philip have done for me. My New Zealand experience would not have been as wonderful had it not been for them and other people: Shaurya Sood, Ali Tasalloti, Siale Faitotonu, Elizabeth Ackermann, Mark Stringer, Aneta Cubrinovska, Ilina Cubrinovska, Hayley McIntyre, Pippa and Georgia Rees, Angela, and many others. I hold all memories from Auckland and Christchurch close to my heart.

Special thanks go to Kim and Chheng Sear for their kindness and for making my stay in Berkeley all these years a very pleasant one. Grazie mille a Claudia Corcione, Judy Kleppe, Teresa Coleman, Tom Edwards, John Montopoli, and Nancy Karp for always cheering me up. Many thanks go to Shelley Okimoto, Maribel Castillo, and Jean Lin-Wong of UC Berkeley for always patiently answering my questions and helping resolve any administrative issues.

Dr. Ahmet Aydilek, Dr. Asli Yalcin Dayioglu, Dr. Sherif Aggour, and Dr. Nicholas Schmerr introduced me to geotechnical engineering and seismology, which essentially shaped my research interests. Dr. Aydilek’s invaluable advice, continuous support, encouragement, and guidance toward my PhD are greatly appreciated. I would also like to acknowledge my late teacher, Miladin Mijatovic, my math professor, Mira Gredo, and my physics professor, Jovan Prodanov, who have influenced my career choices and have contributed to who I am today.

I want to thank my mom, Radmila, and my dad, Marijan, for their unconditional support and love, for nurturing my curiosity, and always encouraging me to pursue my goals and dreams. Having my baby sister, Dejana, give me so much love and laughter and having her always by my side means the world to me. Many thanks to my fiancé, Farzin, for loving me and supporting me every step of the way. My dearest grandmother, Dobrila, and her wisdom have got me through stressful times. I also greatly appreciate my mom-in-law, Rakhshandeh, and her support. I am grateful to have each of them in my life.

1 INTRODUCTION

1.1 OVERVIEW

Soil liquefaction is one of the most catastrophic effects of earthquakes (e.g., Seed and Idriss 1967, Seed et al. 1991, Soga 1998, Bray et al. 2004, Arduino et al. 2010, Cubrinovski et al. 2011, Cubrinovski et al. 2017a). The ground damage it induces occurs primarily through three mechanisms: volumetric, shear, and ejecta (Bray and Dashti 2014). Volumetric-induced ground deformation results from partial drainage, sedimentation, and post-liquefaction reconsolidation. Shear-induced ground deformation is a consequence of soil-structure-interaction ratcheting and punching failure. Ejecta-induced ground deformation is caused by the loss of soil ejected onto the ground surface. The settlement due to both the volumetric and shear mechanisms can be estimated using several methods (e.g., Zhang et al. 2002 and Bray and Macedo 2017 for volumetric- and shear-induced settlement, respectively). However, a procedure to estimate the ejecta-induced settlement is currently lacking.

The 2010-2011 Canterbury, New Zealand (NZ), earthquake sequence (CES) triggered extensive repeated liquefaction within Christchurch and its suburbs, virtually unprecedented in a modern urban setting. Liquefaction affected 51,000 of 140,000 residential properties, damaging approximately 15,000 properties beyond economic repair (Rogers et al. 2015). Liquefaction ejecta were a key mechanism of liquefaction-induced land damage and light-weight residential house damage during the CES (Rogers et al. 2015). The scale and extent of land damage and having land insured for natural disaster damage in NZ under the 1993 Earthquake Commission (EQC) Act resulted in a comprehensive geotechnical land damage assessment across Christchurch. Therefore, the 2010-2011 CES represents an unparalleled opportunity for developing a liquefaction ejecta database with detailed case histories, which can be used to develop a procedure to evaluate the occurrence and amount of ejecta and gain insights into the complex mechanism of ejecta, ground conditions, and seismic demand leading to the occurrence or non-occurrence of ejecta and differing degrees of ejecta-induced settlement.

Moreover, the post-CES field observations (e.g., Green and Cubrinovski 2010, Cubrinovski et al. 2011) and subsequent research studies (e.g., van Ballegooy et al. 2014, Maurer et al. 2015) provided important findings related to the efficacy of current state-of-practice liquefaction assessment methodologies. They lead to overestimation of ground failure at sites in southwest Christchurch, which are characterized by silty soil deposits. The discrepancy between observations of liquefaction manifestation at ground surface and overestimations by existing empirical methods prompted the undertaking of the comprehensive “silty soils project” by researchers at the Univ. of Canterbury, Univ. of California, Berkeley, Univ. of Texas at Austin, and Tonkin and Taylor, Ltd., to investigate the liquefaction resistance of the silty soil deposits.

The overestimation of liquefaction manifestation at silty soil sites as evidence of liquefaction triggering by the simplified methods may in part be due to the predominance of case histories from clean sand sites in the existing empirical database used in their development. Additionally, our understanding of the cyclic response of soil is founded on the cyclic response of reconstituted clean sand test specimens due to the difficulties associated with obtaining “undisturbed” sand specimens and the predominance of case

histories from sites with clean sand deposits (e.g., Tatsouka et al. 1986, Vaid and Sivathayalan 1996, Wu 2002).

Following the CES, the liquefaction response of Christchurch silty soil was investigated through cyclic triaxial (CTX) testing of “undisturbed” specimens by Taylor (2015), Stringer et al. (2016), Markham et al. (2018), and Beyzaei et al. (2018b), and cyclic simple shear (CSS) testing of reconstituted specimens by Cappellaro et al. (2021). A major advantage of the CSS test configuration over the CTX test configuration is its ability to test a soil element in a K_o -consolidated state experiencing a smooth, continuous rotation of the principal stress directions and a close representation of the earthquake loading conditions in the field. A key advantage of high-quality “undisturbed” retrieved specimens over reconstituted specimens is their ability to capture the fabric formed under different depositional conditions, age since deposition, and previous seismic strain history; thus, their cyclic strength is generally considered to reflect the actual response of in-situ soil deposits during earthquakes (Seed 1979, Ishihara 1996). Therefore, the CSS testing of high-quality “undisturbed” silty soil specimens is warranted to investigate their liquefaction response during the Canterbury earthquakes.

The research presented in this dissertation addresses both issues presented above. One of its goals is to better understand the occurrence and mechanism of ejecta and provide a sound basis for the development of the first liquefaction ejecta-induced settlement procedure through the development of the first liquefaction ejecta database with case histories from sites throughout Christchurch. Its other goal is to evaluate the liquefaction potential of stratified silty soil deposits in southwest Christchurch and explore mitigating factors of surficial liquefaction manifestation at these sites through monotonic and cyclic simple shear testing of high-quality “undisturbed” silt, sandy silt, and silty sand specimens retrieved from the silty soil deposits.

1.2 ORGANIZATION

The main research topic addressed in this dissertation is liquefaction ejecta-induced damage observed throughout Christchurch, New Zealand, as a result of the 2010-2011 Canterbury earthquakes. The following chapters explore the liquefaction ejecta potential at both clean sand sites and silty soils sites:

- Chapter 2 describes the development of the first liquefaction ejecta case histories database, which is essential for the development of the first procedure to estimate the amount of liquefaction ejecta-induced settlement in future earthquakes. Liquefaction ejecta-induced settlement is estimated at 61 sites for the four main events of the 2010-2011 Canterbury earthquake sequence using the photographic evidence- and LiDAR-based methods because direct measurements of ejecta were not taken after the earthquakes. The database contains various sites throughout Christchurch including, but not limited to, sites comprised of thick, clean sand deposits and stratified silty soil deposits. The detailed case histories files are provided as an electronic supplement, as described in Appendix A.
- Chapter 3 analyzes the liquefaction ejecta database described in the previous chapter. It identifies trends between the liquefaction ejecta-induced settlement and the available earthquake characteristics and site parameters. The ejecta-

induced settlement is also evaluated against several of the existing liquefaction-induced damage indices. The presented analyses exemplify what can be done with the newly developed liquefaction ejecta case histories database to help advance our understanding of the liquefaction phenomenon.

- Chapter 4 discusses the test method for minimum and maximum densities of small quantities of soil and its application to soil with high non-plastic fines content, which was developed to evaluate the relative density of soil for liquefaction assessment and the state of soil in the field. The minimum and maximum void ratios are evaluated for soils with 2%-99% non-plastic fines.
- Chapter 5 presents the liquefaction response of native Christchurch silts, sandy silts, and silty sands evaluated through monotonic and cyclic simple shear testing. The high-quality “undisturbed” test specimens were retrieved from stratified silty soil deposits in southwest Christchurch, which did not manifest liquefaction at the ground surface despite the estimations of severe ground failure by the existing liquefaction assessment methods. The post-cyclic monotonic simple shear response is also discussed. Additional test data are provided in Appendix D and as an electronic supplement. Appendix E presents a subsequent steady-state testing of reconstituted specimens using the soil from simple shear test specimens.
- Chapter 6 summarizes the presented research and provides conclusions with a focus on key insights and recommendations for future research.

2 LIQUEFACTION EJECTA CASE HISTORIES FOR 2010-11 CANTERBURY EARTHQUAKES

The contents of this chapter are primarily from a journal article submitted to the ISSMGE International Journal of Geoengineering Case Histories by Mijic, Z., Bray, J. D., and van Ballegooy, S., entitled “Liquefaction Ejecta Case Histories for 2010-11 Canterbury Earthquakes,” which was under review when this dissertation was submitted.

2.1 INTRODUCTION

This article summarizes the development of detailed liquefaction ejecta case histories for the four main events of the 2010-2011 Canterbury earthquake sequence (CES): the 4 Sep 2010 M_w 7.1, 22 Feb 2011 M_w 6.2, 13 Jun 2011 M_w 6.2, and 26 Dec 2011 M_w 6.1 events (Figure 2.1). The 13 Jun 2011 earthquake was modeled as a M_w 6.2 earthquake to account for the excess pore water pressure that resulted from the first M_w 5.3 earthquake and did not dissipate fully at the time of the second M_w 6.0 earthquake that occurred 80 min later (van Ballegooy et al. 2014). Based on piezometer measurements reported in T+T (2013), 25% of the excess pore water pressure generated by the first event was estimated to be present when the second earthquake occurred, which increased its effective magnitude by 0.2 based on magnitude-dependent liquefaction triggering curves. By the same reasoning, the Dec 2011 earthquake was modeled as a M_w 6.1 earthquake.

The extensive, repeated occurrence of liquefaction ejecta in the greater Christchurch area is virtually unprecedented in a modern urban setting. Liquefaction ejecta were a key mechanism of liquefaction-induced land damage and light-weight residential house damage during the CES (Rogers et al. 2015). Liquefaction affected 51,000 of 140,000 residential properties, damaging approximately 15,000 properties beyond economic repair. The level of infrastructure damage and the occurrence of liquefaction ejecta were strongly correlated. Areas without liquefaction ejecta or lateral spreading, although some areas likely had liquefaction at depth, typically had negligible liquefaction-induced land or building damage. Conversely, areas with liquefaction ejecta or lateral spreading had moderate-to-severe land or building damage (Rogers et al. 2015).

No procedures for estimating the occurrence and the amount of ejecta-induced settlement are currently available. There is no database with detailed case histories that could be used to develop the procedure or gain insights into the complex mechanism of ejecta, ground conditions, and seismic demand leading to the occurrence or non-occurrence of ejecta and the differing degrees of ejecta-induced settlement. The 2010-2011 CES represents an unprecedented opportunity for developing a liquefaction ejecta database that can be used as a basis for the development of procedures to evaluate the occurrence and amount of ejecta.

Liquefaction-induced ground deformation has three primary components: (1) shear-induced ground deformation resulting from soil-structure-interaction ratcheting and punching failure, (2) volumetric-induced deformation due to sedimentation and post-liquefaction reconsolidation, and (3) ejecta-induced ground deformation due to the loss of

soil ejected onto the ground surface (Bray and Dashti 2014). The shear-induced building settlement can be estimated using several methods (e.g., Bray and Macedo 2017). The volumetric-induced settlement can be estimated using several methods (e.g., Zhang et al. 2002). However, there is not a procedure for estimating the ejecta-induced ground settlement. The Liquefaction Severity Number, LSN, (van Ballegooy et al. 2014) and Liquefaction Potential Index, LPI, (Iwasaki et al. 1978) indices were not specifically developed to estimate the amount of liquefaction ejecta. Rough estimates of liquefaction ejecta occurrence and amounts can be made by the liquefaction ejecta demand, L_D , and crust resistance, C_R , parameters, a new procedure by Hutabarat and Bray (2022), but it requires additional validation with case history data.

Liquefaction ejecta tend to form in the presence of the low-permeability crust above the liquefied soil (Obermeier 1996). A mixture of water and sediments is typically ejected onto the ground surface through preexisting gaps in the crust or dikes produced by hydraulic fracturing of the crust. The severity of liquefaction manifestation at the ground surface is influenced by the thickness and properties of the cap, characteristics of the underlying liquefying soil strata, and depositional environment (e.g., Beyzaei et al. 2018). A non-liquefying crust that is thicker than underlying liquefying soil strata tends to reduce the effects of liquefaction at the ground surface (van Ballegooy et al. 2014). Formation of ejecta is also affected by the built environment due to the load applied by infrastructure, disruption of an upward drainage path by an impervious constructed layer which may force the liquefied material to migrate sideways around it, and defects created in the crust, such as from light poles.

This chapter summarizes the data that were used to conduct the research and explains the methodology used to estimate the ejecta-induced settlement to develop detailed ejecta case histories. The methodology is described for one illustrative site in Christchurch. Closing remarks regarding the research outcomes as well as guidance for future work are also provided.

2.2 DATA AND MATERIALS AVAILABLE

The scale and extent of land damage caused by the Canterbury earthquakes and having land insured for natural disaster damage in NZ under the 1993 Earthquake Commission (EQC) Act resulted in a comprehensive geotechnical land damage assessment across Christchurch. The initial assessment of the extent and severity of land damage through regional-scale mapping and rapid property-by-property mapping identified the areas that needed detailed EQC Land Damage Assessment Team (LDAT) inspection of individual properties (T+T 2013). Following the detailed inspection of liquefaction-induced land damage at approximately 65,000 properties by assessment teams, over 25,000 cone penetration tests (CPTs), over 5,000 boreholes, many with piezometers installed, and several kilometers of geophysical surveys were conducted in Christchurch.

Sites throughout Christchurch were shaken multiple times and experienced no-to-extreme quantities of liquefaction ejecta (Figure 2.2). The degree of liquefaction ejecta-induced damage varied from site to site and from earthquake to earthquake. Although direct measurements of ejecta after the Canterbury earthquakes are not available, liquefaction ejecta coverage and amounts for each of the four major Canterbury earthquakes can be characterized with access to the comprehensive T+T (2015) and LDAT (2021) databases. The T+T (2015) database contains aerial photographs for each earthquake, pre- and post-

earthquake airborne Light Detection And Ranging (LiDAR) surveys, thousands of CPTs and boreholes with installed instruments, earthquake-specific groundwater depth models, and robust estimates of PGA with uncertainties. The LDAT (2021) database is comprised of ground photographs and detailed land damage inspection notes.

2.2.1 Airborne LiDAR Surveys

Airborne LiDAR surveys of Christchurch were conducted before and after each of the four main CES events to estimate the ground surface subsidence caused by each earthquake. The surveys were acquired by AAM Brisbane Pty. Ltd. and New Zealand Aerial Mapping (NZAM) Ltd. on (1) 6-9 Jul 2003, (2) 5 Sep 2010, (3) 8-10 Mar 2011, (4) 20-30 May 2011, (5) 18 and 20 Jul, 11 Aug, 25-27 Aug, and 2-3 Sep 2011 (Russell and van Ballegooy 2015), and (6) 25 Oct 2015. Thus, each LiDAR survey, apart from the Sep 2010 LiDAR survey, was flown at least a month after each main earthquake when much of liquefaction ejecta were removed from most properties and roads. The position data points were acquired as a LiDAR survey point cloud and were classified as ground points or points that reflected off vegetation and structures (non-ground points). The accuracy of the acquired LiDAR points was verified against elevations of the Land Information New Zealand (LINZ) benchmarks that were surveyed before and after the main Canterbury earthquakes using GPS-based equipment and precise levelling (Russell and van Ballegooy 2015, CERA 2014). “The [vertical] accuracy of the LiDAR points relative to the LINZ benchmarks were estimated by subtracting the mean elevations of the LiDAR points around each LINZ benchmark from the surveyed elevation of the LINZ benchmark,” which is referred to as the approximate error due to a typical vertical accuracy of ± 30 mm of LINZ benchmark elevations (Russell and van Ballegooy 2015). Low mean and median approximate errors suggest reasonable overall accuracy. Approximately 80% of the LiDAR point elevations for all post-Sep 2010 LiDAR surveys have a vertical accuracy of ± 70 mm, while approximately 80% of the LiDAR point elevations for the Jul 2003 LiDAR survey are within ± 150 mm of the LINZ benchmark elevations. The standard deviation of the approximate error for the Jul 2003 LiDAR survey is larger than for the post-Sep 2010 LiDAR surveys likely due to the lower density of LiDAR points and the lower precision in the LiDAR equipment in 2003 (Russell and van Ballegooy 2015).

The ground classified points were also used to develop the bare earth digital elevation models (DEMs) that consist typically of 5 m by 5 m cells (Russell and van Ballegooy 2015). Each cell represents an average ground surface elevation obtained by averaging the ground classified points within the DEM cell (Russell and van Ballegooy 2015). The difference between a pre-earthquake DEM and a post-earthquake DEM can be used to estimate the change in vertical ground surface elevation due to an earthquake. However, there are limitations to estimating the ground surface subsidence from a difference DEM. The limitations include a localized error due to the interpolation of adjacent DEM cell elevations in areas with vegetation and buildings thus fewer ground classified points and the difference between the actual ground surface elevation and the average DEM elevation in areas with step changes in the ground surface (Russell and van Ballegooy 2015). The difference DEMs can also be used to identify areas of greater uplift or subsidence due to anthropogenic changes (e.g., construction and vegetation removal) and error bands of apparent greater subsidence that are centered on and are parallel to individual LiDAR flight paths. These error bands are the artefacts of the LiDAR point

acquisition as well as the post-acquisition processing that involves a combination of automated and manual classification of non-ground classified points. Detailed explanation of the accuracy and limitations of the DEMs and the LiDAR points is provided in Russell and van Ballegooy (2015).

2.2.2 Aerial Photography

High-resolution aerial photographs of Christchurch and its suburbs were acquired by NZAM after each main CES event – 5 Sep 2010, 24 Feb 2011, 14-15 Jun 2011, 16 Jun 2011, and 24 Dec 2011 – to identify areas with liquefaction ejecta to which inspection teams were dispatched to map damage. They were supplied as orthorectified, color-balanced, geolocated, tiled images and were transformed into image pyramids for efficient use (CGD 2012a). The image locations may have some inaccuracy because the locations of the reference datums used during acquisition were not verified at the time of supply, in addition to an approximate, average 1-m residual error that stems from the orthorectification process (CGD 2012a).

2.2.3 Detailed LDAT Property Inspection Mapping

About 65,000 properties in Christchurch and its suburbs were visually inspected in detail for liquefaction-related land damage to resolve the EQC land damage insurance claims (T+T 2013). The inspection of individual properties was performed by the EQC LDAT comprised of approximately 400 geotechnical engineers and engineering geologists (T+T 2013). The LDAT used a land damage template to collect land damage information: lateral spreading, cracks, undulating land, local ponding, localized settlement causing drainage issues, new groundwater springs, and inundation of land with ejected soil. They also identified damage to any sloping land, retaining wall, foundation, and dwelling. Additionally, the LDAT used a property map with a recent aerial photograph to sketch locations of observed damage for each individual property. Liquefaction ejecta were often removed or eroded at the time of inspection, which makes the high-resolution aerial photographs an important supplement in assessing the extent of ejecta. The LDAT took photographs of ejecta remnants, sketched their approximate locations on individual property maps, and often reported the maximum height of ejecta remnants. Claimants sometimes provided useful information regarding ejecta and its volume and height.

2.2.4 Conditional PGA

Robust estimates of conditional peak ground accelerations (PGAs) were developed for each main Canterbury earthquake as a combination of an empirical ground motion model and recordings at 19 strong motion stations within the Canterbury region (Bradley and Hughes 2012). The estimated PGAs were conditioned on the recorded PGAs at the strong motion stations to improve the fit of the generalized ground motion model for each earthquake. The conditional PGA at each location was estimated in terms of its median value and uncertainty (lognormal standard deviation). The accuracy of the estimated PGA increases with the increasing proximity to the strong motion stations. For site locations that are far from the strong motion stations, the conditional distribution of PGA is similar to the unconditional distribution of PGA. For sites close to the strong motion stations, the

conditional distribution approaches the PGA value recorded at the station (Bradley and Hughes 2012). The PGAs are available in the form of contour maps (CGD 2015).

2.2.5 Event-Specific Groundwater Depths

The event-specific groundwater depths are based on water level measurements from wells installed prior to and after the 4 Sep 2010 earthquake and the most appropriate LiDAR-derived DEM (CGD 2014). Groundwater levels in the wells were converted to free surface elevations based on surveyed well-head levels. The elevations at the wells and the adjacent rivers prior to each main Canterbury earthquake were used to develop surface models that were subtracted from the corresponding LiDAR DEM. The obtained groundwater depths are based on the mean free surface elevations at the time of each earthquake. In case of geographical sparsity of wells for earlier earthquakes, water level measurements at the newly installed wells were used to extrapolate the free surface elevations back in time. The fitted surface models for each earthquake are color-banded and available as an image pyramid (CGD 2014).

2.3 SITES USED FOR THE DEVELOPMENT OF CASE HISTORIES

The NZ-US researchers developed a comprehensive dataset of 55 Christchurch sites to investigate liquefaction triggering aspects in detail. The dataset includes field investigation data (e.g., CPT measurements and sonic borehole logs), liquefaction observations using aerial photographs, coarse estimates of liquefaction-related ground surface subsidence based on the LiDAR-derived difference digital elevation models (discussed subsequently), liquefaction-induced damage indices, etc. However, as is the case for all of Christchurch, direct measurements of liquefaction ejecta were not conducted at these sites. The dataset consists predominantly of sites that had the severity of surficial manifestation of liquefaction misestimated by simplified liquefaction triggering methods and liquefaction-induced damage indices. The “55 sites” data are discussed in Russell and van Ballegooy (2015) and are used in several research papers (e.g., Cubrinovski et al. 2017a). In this study, 27 sites from the “55 sites” dataset were investigated in detail and an additional 8 sites had coarse analyses performed because they had no to minor ejecta, no LiDAR surveys, or only one CPT. The remaining 20 sites of the “55 sites” were not used due to lateral spreading, topographical features, and ejecta that were not recognizable in the aerial photographs but the property inspection reports suggested their occurrence.

An additional 34 sites, primarily from the NE quadrant of Christchurch, were selected to form a database with no-to-extreme liquefaction ejecta. The NE quadrant had the most predominant liquefaction ejecta-induced damage and was without significant discrepancies between observations and estimations of liquefaction-induced damage according to the preliminary regional-scale assessment of the LSN and LPI accuracy in the site selection process (e.g., using the LPI accuracy map for Christchurch developed by Maurer et al. 2014). These were high-quality sites with good observations (i.e., aerial and ground photographs and EQC LDAT property inspection reports), reliable settlement estimates based on the LiDAR survey data, at least two closely spaced CPTs with investigation depths of 15-20 m, a nearby borehole, and without significant discrepancies between liquefaction observations and liquefaction manifestation estimations as per state-of-the-practice liquefaction triggering procedures and corresponding liquefaction damage

indices. These 34 sites and the 27 detailed sites from the “55 sites” dataset were used to build 235 detailed case histories (i.e., 58 sites times four earthquakes plus 3 sites times one earthquake due to lateral spreading). Figure 2.3 illustrates the site locations. All details related to the case histories are provided as an electronic supplement as Appendix A.1 through Appendix A.61 (hereinafter referred to as Appendix A). The important information related to each site and each earthquake is provided in the *EjectaCaseHistories_FlatFile.xlsx* spreadsheet as an electronic supplement to this dissertation.

2.4 METHODOLOGY

Each site was centered on a CPT or cross-hole shear wave velocity (V_s) survey location and encompassed an area within a 50-m radius of its center (termed a 50-m buffer) due to the spatial variation in ejecta distribution and presence of buildings. However, the 10-m and 20-m radii (10-m and 20-m buffers, respectively) were used primarily in the analyses. A site was first inspected for the presence of free-face features, sloping land, retaining walls, buildings, vegetation, pavement, and anthropogenic changes, as they could affect liquefaction manifestation at the ground surface and LiDAR survey measurements. This information for each site can be found in each site description in Appendix A. Supporting figures for each site are also included in Appendix A. An area free of vegetation, buildings, anthropogenic changes, and with representative distribution of ejecta for the site was selected for detailed settlement assessment. Other important information, including the soil profile category, PGA, groundwater depth, crust thickness, LPI, LSN, L_D , C_R , ejecta pattern, ejecta distribution, and ejecta quantum for each case history, are provided in the *EjectaCaseHistories_FlatFile.xlsx* spreadsheet. The discrepancy between the liquefaction severity indices and the ejecta coverage is also provided.

As mentioned previously, direct measurements of ejecta amounts were not made. Two alternative methods for estimating the free-field ejecta-induced settlement were employed. The photographic-based method involved the use of aerial and ground photographs, EQC LDAT property inspection reports and maps, and geometrical approximations of the ejected soil shapes. The second method was based on LiDAR point elevations and one-dimensional, free-field volumetric-induced settlement for level ground as per Zhang et al. (2002). The best final estimate of the ejecta-induced settlement was determined as the weighted average of the two estimates.

2.4.1 Photographic-Based Ejecta-Induced Settlement

To obtain the photographic-based settlement due to ejecta, $S_{E,P}$, the shape of ejecta manifestations was estimated. Ejecta were typically shaped as a prism with irregular curvilinear bases, prism with triangular bases, isolated and naturally occurring cone, and artificially formed pile as a result of cleaning. The portion of the assessment area covered by ejecta was quantified using Google Earth™ by outlining the coverage area on the high-resolution aerial photograph for each earthquake. The available photographs, reports, and geometrical approximations were used to estimate the height of ejecta.

For ejecta shaped as a prism with irregular curvilinear bases (Figure 2.4a), the differing thicknesses of ejecta were identified on a high-resolution aerial photograph as having different colors (i.e., darker colors were assumed to correspond to thicker ejecta

layers because of the longer time required to dry the soil) and the corresponding areas were measured using a polygon tool. The height of each ejecta layer was estimated based on the available ground photographs, LDAT property inspection maps, reports that occasionally included the height of ejecta remnants, visibility of the ejecta layer in the aerial photograph, and measurements of the ejecta height in neighboring, similarly affected areas. The volume of ejecta shaped as a prism with irregular curvilinear bases, $V_{E,thick+thin}$, was then estimated as

$$V_{E,thick+thin} = \sum_{i=1}^m A_{E,thick,i} * H_{E,thick,i} + \sum_{j=1}^n A_{E,thin,j} * H_{E,thin,j} \quad (1)$$

where $A_{E,thick,i}$ and $H_{E,thick,i}$ are the area and the height, respectively, of an i^{th} thick ejecta layer, $A_{E,thin,j}$ and $H_{E,thin,j}$ are the area and the height, respectively, of a j^{th} thin ejecta layer.

Ejecta on the road were typically shaped as a series of triangular-base prisms with different dimensions (Figure 2.4b). The rectangular shapes of ejecta on the road were outlined on the high-resolution aerial photograph for each earthquake and their dimensions were measured using the Google Earth tools. The width of a rectangle, $W_{E,prism,k}$, is perpendicular to the curb, while the length of a rectangle, $L_{E,prism,k}$, aligns with the curb. The lower and upper estimates of the height of ejecta at the curb, $H_{E,prism,k}$, were based on the typical cross-slopes of normal crown of 2% and 4%, respectively. The height of ejecta was capped at a typical curb height of 150 mm unless ejecta extended above the curb and onto the ground surface toward properties. The volume of ejecta shaped as a triangular-base prism, $V_{E,prism}$, was estimated as

$$V_{E,prism} = \frac{1}{2} \sum_{k=1}^p W_{E,prism,k} * H_{E,prism,k} * L_{E,prism,k} \quad (2)$$

Ejecta that occurred naturally in a form of an isolated cone (Figure 2.4c) had its area $A_{E,cone,l}$ measured on a high-resolution aerial photograph in Google Earth and its height $H_{E,cone,l}$ estimated based on the best available physical evidence to obtain the volume, $V_{E,cone}$, as

$$V_{E,cone} = \frac{1}{3} \sum_{l=1}^r A_{E,cone,l} * H_{E,cone,l} \quad (3)$$

When ejecta were cleaned from properties and roads into a pile, the pile consisted usually of an isolated cone or partially overlapping cones of ejecta with an assumed angle of repose of 30° (similar shape as Figure 2.4c). The radius and the area of a cone's circular base, $R_{E,cc,s}$ and $A_{E,cc,s}$, respectively, were measured in Google Earth and the height of a conically shaped pile component, $H_{E,cc,s}$, was approximated as $R_{E,cc,s} * \tan(30^\circ)$. The volume of piled ejecta was estimated using Eq. 3.

The volumes of all differently shaped ejecta present within a settlement assessment area were summed and divided by the total settlement assessment area, A_T , to obtain the areal ejecta-induced settlement, S_{E,P_areal} (also denoted as $S_{E,P}$). In addition, the photographic-based localized ejecta-induced settlement, $S_{E,P_localized}$, was calculated as the total volume of ejecta, V_E , divided by only the area covered by ejecta, A_E . If ejecta did not completely cover A_T , S_{E,P_areal} was lower than $S_{E,P_localized}$ due to its areal averaging of ejecta-induced settlement. The S_{E,P_areal} and $S_{E,P_localized}$ values for each case history and all supporting estimates are provided in Appendix A.

2.4.2 LiDAR-Based Ejecta-Induced Settlement

The first step in estimating the free-field ejecta-induced settlement using the LiDAR-based approach was to identify the location of a site relative to the LiDAR flight error bands and the zones of overestimated (and underestimated) ground surface subsidence to account for errors (CGD 2012b), and to estimate the vertical tectonic movement of a site for each earthquake (CGD 2012b). The adjustments for each earthquake event at each site due to the global offset, i.e., due to subtracting the post-earthquake ground surface elevations from the pre-earthquake ground surface elevations wherein both the pre-earthquake and post-earthquake LiDAR survey point elevations have an approximate median error (the accuracy of the measured elevations relative to the corresponding LINZ benchmarks), are summarized in Appendix A.

LAS files containing LiDAR point cloud data were imported into Global Mapper to estimate the ground surface elevation within each site's settlement assessment area. After removing visible vegetation, buildings, and similar features, the remaining points were selected to compute the average ground surface (a centroid of the selected points). This was performed for each LiDAR survey to evaluate the change in the ground surface elevation due to each earthquake. For instance, the change in the ground surface elevation within the settlement assessment area due to the 4 Sep 2010 earthquake was calculated by subtracting the average ground surface elevation of the 5 Sep 2010 LiDAR survey points from the average ground surface elevation of the Jul 2003 LiDAR survey points. The earthquake-induced change in ground surface elevation is provided for each site in the Electronic Appendix A (termed as raw liquefaction-related ground surface subsidence using original LiDAR points). These values were then adjusted for the LiDAR flight error, vertical tectonic movement, global offset, and presence of ejecta at a site at the time of a LiDAR survey. The obtained liquefaction-induced ground surface subsidence, S_T , for each earthquake is then provided in Table 6 of each site description in Appendix A.

Considering that liquefaction effects in Christchurch were not significant for earthquakes other than the main four events, the LiDAR surveys repeated after the Feb 2011 and Dec 2011 earthquakes provided an estimate of the repeat measurement error as the absolute difference between the Mar 2011 and May 2011 ground surface elevations and the Feb 2012 and Oct 2015 ground surface elevations averaged over the assessment area. The standard deviations available for each set of pre-earthquake and post-earthquake LiDAR surveys were combined to account for the effect of areal averaging of the surveyed elevations on the standard deviation of the LiDAR measurement error for individual points (the accuracy of the supplied LiDAR points relative to the LINZ benchmarks) for each LiDAR survey provided by Russell and van Ballegooy (2015). The standard deviation obtained for each main Canterbury earthquake was then multiplied by the maximum percent change in standard deviation (i.e., the maximum ratio of the repeat measurement error and the standard deviation for individual points). The adjusted standard deviation values are provided in Table 4 of each site description in Appendix A.

As rough check, the estimated liquefaction-induced ground surface subsidence for each earthquake was compared with the coarse estimate of liquefaction-induced ground surface subsidence based on the difference between the corresponding pre- and post-earthquake LiDAR DEMs (the difference DEM). The latter values had to be corrected for the appropriate LiDAR flight errors and the presence of ejecta at a site at the time of a

LiDAR survey. The LiDAR DEM-based values of liquefaction-induced settlement were not used in calculations of the ejecta-induced settlement.

The volumetric settlement due to sedimentation and post-liquefaction reconsolidation, S_{V1D} , was subtracted from the total liquefaction-induced settlement, S_T , to obtain the free-field liquefaction ejecta-induced settlement, $S_{E,L}$ (Table 8 of each site description in Appendix A). The shear-induced ground settlement was neglected because the selected case histories originated from the free-field sites. The S_{V1D} was computed in *CLiq v.3.0.3.2* with the CPTs presented in Appendix A using the Zhang et al. (2002) procedure, which used the factor of safety against liquefaction, FS_L , from the Boulanger and Idriss (2016) procedure. The input parameters were the median PGA by Bradley and Hughes (2012), probability of liquefaction, P_L , of 50%, I_c cutoff value of 2.6 as a threshold between liquefiable and non-liquefiable soil (Lees et al. 2015), C_{FC} of 0.13 developed for Christchurch soil by Maurer et al. (2019), and the groundwater depth at the time of each earthquake (CGD 2014). The average S_{V1D} for each settlement assessment area was estimated for each earthquake and was reported in Table 8 of each site description in Appendix A. The sensitivity of volumetric settlement to PGA, C_{FC} , and P_L for each earthquake event was derived for two sites (V_sV_p 57203 – Shirley Intermediate School and CPT 5586 – Vivian St). The arithmetic mean of the range of the minimum and maximum difference was evaluated for each assessment area of the two sites. The maximum arithmetic mean for each earthquake event was rounded to the nearest five millimeters and was used as the uncertainty value. Accordingly, the volumetric settlement uncertainties of ± 20 , ± 50 , ± 25 , and ± 50 mm for the Sep 2010, Feb 2011, Jun 2011, and Dec 2011 earthquakes, respectively, were used for all sites in this study.

2.4.3 Best Estimate of Ejecta-Induced Settlement

The best estimate of the ejecta-induced settlement, $S_{E,final}$, was calculated as the weighted average of the two estimates per the photographic evidence-based method, $S_{E,P}$, and the LiDAR-based method, $S_{E,L}$ (Table 11 of each site description in Appendix A). The weighting coefficients were based on the LiDAR measurement errors, misestimates of liquefaction severity using the liquefaction triggering procedures as per Maurer et al. (2014), and completeness of visual evidence. Table 2.1 summarizes the best estimates of the ejecta-induced free-field settlement for the 61 sites.

2.5 DETAILED EVALUATION OF THE SHIRLEY INTERMEDIATE SCHOOL CASE HISTORIES

The detailed evaluation of one site is presented to illustrate the methods employed to develop the ejecta-induced ground settlement case histories. The Shirley Intermediate School site (Table 2.1) is a level, open-field site covered largely in grass and did not undergo lateral spreading during the Canterbury earthquakes. The nearest free-face feature is a creek that is approximately 55 m from the center of the site. Ten percent of the site's 50-m buffer is occupied by school buildings, which were constructed between Apr 2011 and Jun 2011, and 15% of the site is covered by a road. Some minor earthwork was performed in the building area between Oct 2009 and Feb 2011. Trees, bushes, and plants other than grass (all termed vegetation) cover 10% of the 20-m buffer and 20% of the 50-

m buffer. All these features and anthropogenic changes were considered when selecting the settlement assessment area as they could affect the LiDAR survey measurements. The area selected for the ejecta-induced settlement analysis excludes vegetation, buildings, and significant anthropogenic changes (Figure 2.5). This area also has good spatial distribution of ejecta (Figure 2.6).

The aerial photographs in Figure 2.6 were used to estimate the occurrence of ejecta and to measure the area of ejecta coverage within the assessment area (the red outline). The absence of ejecta is evident for the Sep 2010 earthquake. For the Feb 2011 earthquake, ejecta occurred across the site in a pattern of interconnected soil deposits originating from different fissures and forming irregularly shaped ejecta blankets rather than in a pattern of individual conically shaped soil boils. Different shades of gray of the ejecta were interpreted as different ejecta thicknesses. The light gray ejecta outlined in yellow were classified as thin ejecta, while the dark gray ejecta outlined in pink were classified as thick ejecta. The total areas of the outlined thick ejecta layers and the outlined thin ejecta layers ($A_{E,thick}$ and $A_{E,thin}$, respectively) were measured in Google Earth™. The $A_{E,thick}$ and $A_{E,thin}$ values for the 10-m buffer are summarized in Table 2.2. In the absence of ground photographs, the height range for the thick and thin ejecta layers ($H_{E,thick}$ and $H_{E,thin}$, respectively) was estimated based on the typical height of similar-looking ejecta for the neighboring area and observations made by people. Finally, the volume of ejecta was estimated using Eq. 1 and was divided by the total assessment area, A_T , to obtain the areal ejecta-induced free-field settlement, $S_{E,P_{areal}}$ (Table 2.3), while the localized ejecta-induced settlement, $S_{E,P_{localized}}$ (Table 2.3) was obtained by dividing the total volume of ejecta within A_T by the coverage area of ejecta, A_E . Figure 2.6 also shows the presence of ejecta for the Jun 2011 earthquake. However, ejecta appeared to be partially cleaned from the site. To account for this uncertainty, the height of ejecta was provided as a wider range, while assuming that ejecta covered the portion of the site in light brown color. The area for the Jun 2011 earthquake reported in Table 2.2 corresponds to the area outlined in orange and within the 10-m buffer. Also, cars, shadows, and construction equipment obscured a portion of the assessment area in the Jun 2011 aerial photograph, resulting in that portion of the site being excluded from the analysis. For the Dec 2011 earthquake, only minor ejecta (outlined in yellow in Figure 2.6) were present.

To estimate the LiDAR-based ejecta-induced settlement, the change in ground surface elevation within the assessment area was determined for individual LiDAR points, such as those shown in Figure 2.7, for each earthquake (Table 2.4). These values were then adjusted for the LiDAR flight error, global offset, and tectonic movement (Table 2.5). The site is in the apparent zone of higher ground surface subsidence for the Sep 2011 earthquake and the apparent zone of lower ground surface subsidence for the Feb 2011 earthquake (Figure 2.8). To account for this LiDAR flight error, 100 mm were subtracted from the ground surface elevation change in Table 2.4 for the Sep 2011 earthquake and 100 mm were added to the ground surface elevation change in Table 2.4 for the Feb 2011. The final estimates of liquefaction-induced ground surface subsidence provided in Table 2.6 were compared with the coarse estimates of the ground surface subsidence using the LiDAR DEMs (Figure 2.9). No major discrepancies between the two sets of estimates were observed. The average S_{V1D} was then calculated and subtracted from the values in Table 2.6 to obtain $S_{E,L}$ (Table 2.7). The PGA ranged from 0.19 g for the Sep 2011 earthquake to 0.38 g for the Feb 2011 earthquake. The depth to groundwater was in the range from 2.0

m below ground surface (BGS) for the Dec 2011 earthquake to 2.5 m BGS for the Sep and Feb 2011 earthquakes. All CPTs shown in Figure 2.10 were used to calculate the average S_{V1D} for the 50-m buffer (four of them were outside the 50-m buffer, CPT 55672 was 90 m away from the center of the site), whereas only CPTs 56473 and 57366 were used to calculate the average S_{V1D} for the 10-m and 20-m buffers. The S_{V1D} values for individual CPTs for each earthquake event are provided in Table 2.8. Figure 2.11 illustrates the cyclic resistance ratio (CRR) and the cyclic stress ratio (CSR) for each main earthquake event, which were computed in *CLiq v.3.0.3.2* for CPTs 56473 and 57366 using the Boulanger and Idriss (2016) procedure.

The $S_{E,L}$ values in Table 2.7 were used in combination with the areal $S_{E,P}$ values in Table 2.3 to provide the best final estimate of ejecta-induced free-field settlement, $S_{E,final}$ (Table 2.9). The mean and the estimated uncertainty for $S_{E,final}$ are rounded to the nearest 5 mm to indicate an inclusive range of possible $S_{E,final}$ values for comparison among the sites in this study. Due to the inherent uncertainty in estimating ejecta-induced settlement, these values should be rounded off to the nearest 10 mm for practical engineering purposes. The $S_{E,final}$ represents the weighted average of $S_{E,L}$ and $S_{E,P}$ with respective weight coefficients of 1/3 and 2/3 for the Feb 2011 and Jun 2011 earthquakes and the respective weight coefficients of 0 and 1 for the Sep 2010 and Dec 2011 earthquakes. The lower weight coefficient for the Feb 2011 and Jun 2011 earthquakes was assigned to $S_{E,L}$ because the Shirley Intermediate School site was in the zone of overestimated/underestimated ground surface movements for the Sep 2010/Feb 2011 earthquake due to the LiDAR flight error and had slight to moderate underestimation of liquefaction manifestation at the ground surface than was observed (Maurer et al. 2014). $S_{E,L}$ was assigned 0 weight for the Sep 2010 and Dec 2011 earthquakes due to the absence of ejecta for the Sep 2010 earthquake and due to negligible ejecta and negative $S_{E,L}$ values for the Dec 2011 earthquake. The best estimates of the ejecta-induced free-field ground settlement at the Shirley Intermediate School site for the Sep 2010, Feb 2011, Jun 2011, and Dec 2011 earthquakes are 0 mm, 125 ± 25 mm, 50 ± 15 mm, and <5 mm, respectively, considering that the 10-m buffer is the most representative buffer in terms of spatial distribution of ejecta across the site.

The soil profile at the Shirley Intermediate School site indicates a thick, clean sand site. A borehole log at the center of the site and the CPTs indicate a 5.5-m thick layer of fine to medium sand, SP, in the upper 10 m (from the 3.5- to 9-m depth) and below the average groundwater depth of approximately 2.3 m BGS (Figure 2.10). This marine/estuarine SP layer of the Christchurch formation has an average q_t of 9 MPa. The top 3.5 m of the soil profile consist of the 0.4-m thick organic silty, OL, topsoil ($q_{t,avg} = 4$ MPa) and underlying interchangeable layers of alluvial non-plastic to low plasticity silt, ML, and alluvial silty sand, SM, of the Springston formation ($q_{t,avg} = 4$ MPa). Below the 9-m depth, sandy subrounded marine/estuarine gravel, GW, with $q_{t,avg} = 18$ MPa extends to a depth of 12 m and overlies fine to coarse marine/estuarine sand, SP, which extends to a depth of 20 m. The provided q_t values corrected for thin-layer effects using the de Greef and Lengkeek (2018) procedure are based on CPTs 56473 and 57366. Two additional CPTs from outside the 50-m buffer show the presence of gravelly layers at depths shallower than 8 m close to the rim of the 50-m buffer.

CPTs 56473 and 57366, as the CPTs within the most representative buffer at the Shirley Intermediate School site, i.e., the 10-m buffer, were used to estimate the average

crust thickness. The depth to the first $FS_L < 1$ layer that is at least 200-mm thick was 3.2 m and 4.3 m for the Feb 2011 and Dec 2011, respectively. For the Sep 2010 and Jun 2011 earthquakes, the 200-mm thick layer with $FS_L < 1$ did not exist (Table 2.8). The average crust thickness was also defined as the depth to the first $I_c < 2.6$ layer that is at least 200-mm thick and below the groundwater level; these values are not provided in Appendix A, but the electronic supplement only. They were estimated as 2.8, 2.8, 2.7, and 2.6 m BGS for the Sep 2010, Feb 2011, Jun 2011, and Dec 2011 earthquakes, respectively. For the most representative buffer, i.e., the 10-m buffer, the average LPI = 0, 5, 0, and 1 and LSN = 1, 13, 2, and 5 for the Sep 2010, Feb 2011, Jun 2011, and Dec 2011 earthquake, respectively, based on CPTs 56473 and 57366. Considering the percent coverage of the unobstructed area of the 10-m buffer by liquefaction ejecta (Figure 2.6), the severity of liquefaction manifestation at the ground surface was none (i.e., 0 %), extreme (i.e., 50%-100%), severe (i.e., 20%-50%), and minor (i.e., < 5 %) for the Sep 2010, Feb 2011, Jun 2011, and Dec 2011 earthquake, respectively. Thus, the severity of surficial manifestation of liquefaction was higher than estimated by LPI or LSN for the Feb 2011 and Jun 2011 earthquakes and was correctly estimated for the Sep 2010 and Dec 2011 earthquakes. Similarly, the average L_D of 0, 77, 1, and 8 kN/m and C_R of 46, 46, 44, and 43 kN/m for the Sep 2010, Feb 2011, Jun 2011, and Dec 2011 earthquake, respectively, capture well the severity of liquefaction manifestation at the site for the Sep 2010 and Dec 2011 earthquakes and underestimate it for the Feb 2011 and Jun 2011 earthquakes, according to the L_D - C_R chart developed by Hutabarat and Bray (2022).

2.6 CONCLUSION

The liquefaction ejecta-induced free-field settlement at 61 sites in Christchurch was estimated for each of the four major Canterbury earthquakes using photographic evidence and airborne LiDAR survey elevation points because direct measurements of ejected soil and the associated settlement were not available. The best estimate of ejecta-induced settlement was calculated as the weighted average of the two estimates. The *EjectaCaseHistories_FlatFile.xlsx* spreadsheet summarizes key characteristics of the 61 sites and the ejecta-induced settlement at each of these sites for each of the four main earthquakes. The flat file also lists the sites from the “55 sites” dataset that were not considered for the ejecta-induced settlement analysis (e.g., due to lateral spreading) as well as the sites for which the best-final estimates of ejecta-induced settlement were provided without detailed analyses.

The photographic evidence-based approach for estimating the ejecta-induced settlement relies on high-resolution aerial photographs, ground photographs, and the detailed inspection notes for individual properties by the EQC LDAT comprised of engineers, engineering geologists, and engineering technicians. The area of a site covered with ejecta was measured approximately by utilizing the Google Earth™ tools on the high-resolution aerial photograph supplied for each earthquake event. The height of ejecta was estimated based on ground photographs and detailed LDAT property inspection notes that had measurements of ejecta remnants. The uncertainty in estimating the height of ejecta was accounted for by providing a range of potential heights rather than a single value.

The LiDAR-based approach for estimating the ejecta-induced settlement made use of elevation points surveyed by airborne LiDAR prior to and after each major earthquake event. The pre-earthquake and post-earthquake ground surface elevations were averaged

in Global Mapper over the assessment area of a site and the difference between the two elevations was the earthquake-induced ground surface subsidence. The earthquake-induced ground surface subsidence was then adjusted for the vertical tectonic movement, artefacts of LiDAR (flight error bands), and global offset due to the median approximate error of each pre- and post-earthquake LiDAR survey relative to the GPS-surveyed benchmark points to obtain the liquefaction-induced ground settlement. The accuracy of the surveyed LiDAR elevation points was ± 70 mm for all surveys except for the Jul 2003 survey that had the vertical accuracy of ± 150 mm. The errors related to LiDAR measurements supported the range of liquefaction-induced settlement estimates. The ejecta-induced settlement was obtained by subtracting the volumetric-induced settlement, which was calculated using the Zhang et al. (2002) procedure.

The best estimate of ejecta-induced settlement was calculated by assigning weights to each of the two estimated values described previously. This was done on a site-by-site basis, and it depended on site conditions, including the site's location relative to the LiDAR flight error bands, liquefaction performance of soil at the site relative to the estimations made by liquefaction triggering procedures, and reasonableness of values estimated by the LiDAR. There were cases of negligible ejecta observed at the site as evidenced by the photographs, yet LiDAR-based values indicated significant ejecta-induced settlement. Additionally, the LiDAR approach in a few cases estimated ground uplift (i.e., negative ejecta-induced settlement), although accounting for the uncertainty of the estimate typically led to a reasonable settlement value being within a range of values estimated using photographic evidence.

The aerial LiDAR was found to be a good means of estimating ground surface subsidence on a regional scale. However, errors associated with the LiDAR flights can become significant for individual sites that typically have the ground surface subsidence within the LiDAR margin of error. The LiDAR measurements are also affected by vegetation and topographic features such as undulations that appeared at many sites in Christchurch following the earthquakes. The uncertainty in the LiDAR-based approach can also be attributed to the vertical tectonic movements that resulted from each earthquake. Subtracting the volumetric-induced settlement from the LiDAR-based liquefaction-induced settlement further added to the uncertainty associated with the estimates of ejecta-induced settlement.

The photographic evidence generally provided more consistent results of ejecta-induced settlement, mainly due to the method's dependence on the area covered by ejecta, which could be obtained with reasonable confidence. Geometrically approximating the complex shapes of ejecta introduced some uncertainty; however, the greatest uncertainty in the method could be ascribed to estimating the height of ejecta, especially in the absence of ground photographs and detailed property inspection notes. Additionally, grass could obscure ejecta.

Nevertheless, the analyzed geotechnical database for the 2010-2011 Canterbury earthquakes provides a good set of data for developing detailed ejecta case histories. Rarely is there the wealth of data related to liquefaction-induced land damage like those for the 2010-2011 CES as few countries in earthquake-prone regions have residential land insured for damage from natural disasters. Also, rarely does a single site experience significant, repeated liquefaction and formation of ejecta under varying levels of ground motion in a short span of time, like the sites in Christchurch. Therefore, the detailed 235 case histories

developed in this study constitute a unique database that can be used to examine the occurrence and effects of ejecta. The data provide a reasonable basis for the development of a procedure to evaluate when liquefaction ejecta will or will not occur and to estimate the quantity of ejecta in earthquakes.

Post-earthquake reconnaissance teams should take direct measurements of ejecta immediately after future earthquakes while all related evidence remains intact. This can be performed by utilizing terrestrial LiDAR, structure-from-motion, or conventional land surveys, photographs, and hand measurements. The volume of ejecta can also be measured by placing the ejected soil into standard-size buckets. For regional assessment of liquefaction-induced damage, high control of ground points is recommended. The inspection teams can use individual property maps to add locations of ejecta and sketch their approximate shapes. Many high-quality ground photographs with measurement placards should be taken. Subsurface investigations such as CPT soundings, soil sampling, groundwater measurements, shear wave and compressional wave velocity measurements can be performed later at sites. With reliable PGA estimates, these data would provide an excellent set of data that can be interrogated and appended to the database developed in this study with an aim of developing a robust procedure for estimating the ejecta-induced settlement.

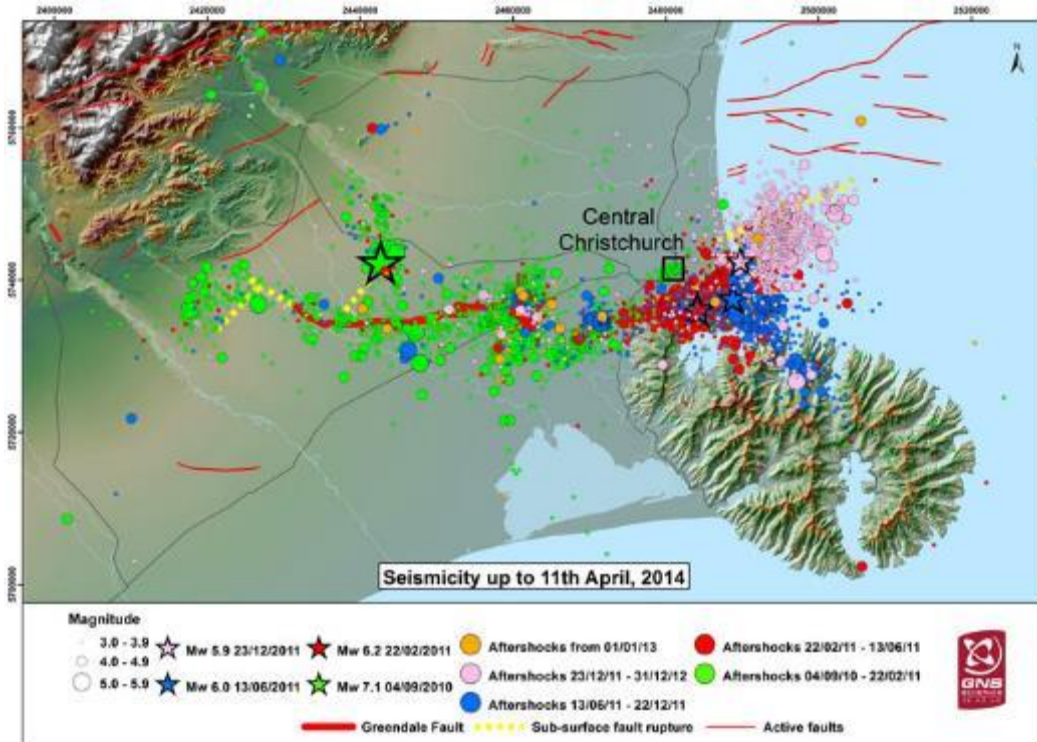


Figure 2.1. Location of 4 Sep 2010 Darfield main shock and subsequent aftershocks up to 11 Apr 2014 (GNS Science 2021).

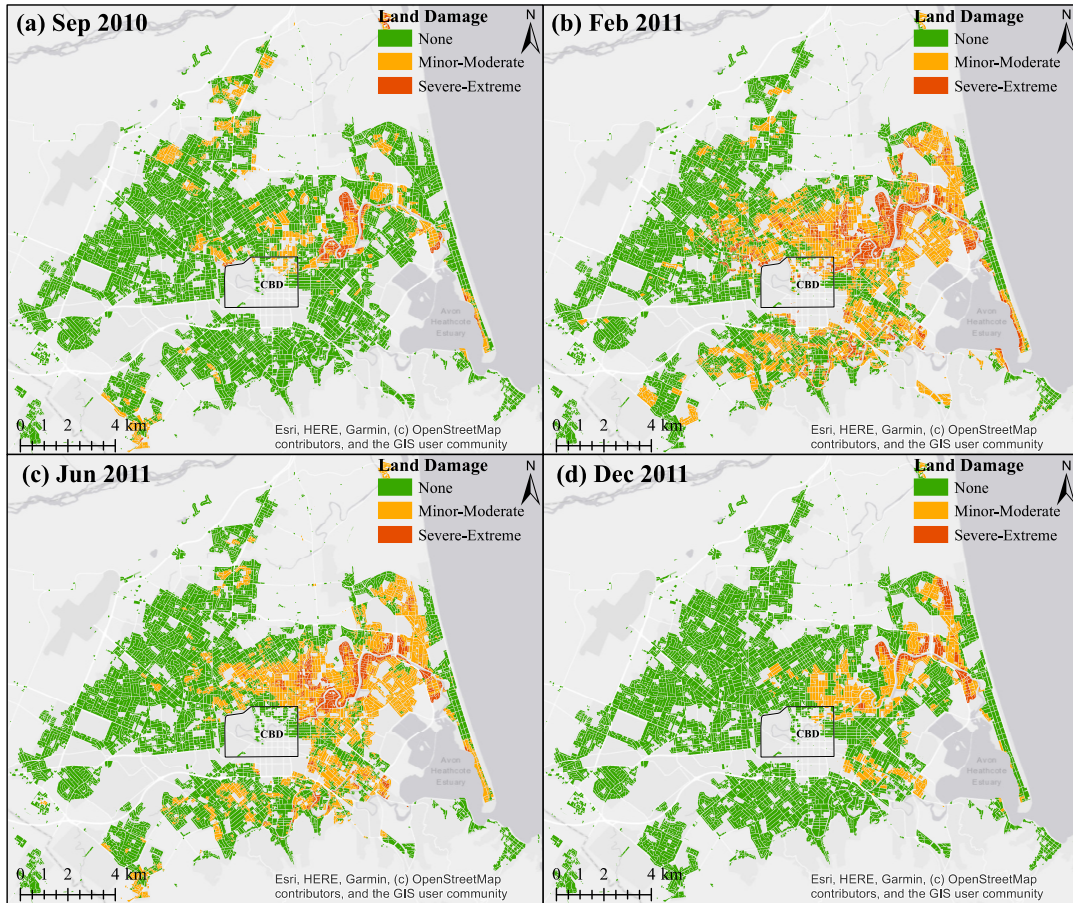


Figure 2.2. Liquefaction observations at the ground surface for the (a) 4 Sep 2010, (b) 22 Feb 2011, (c) 13 Jun 2011, and (d) 23 Dec 2011 earthquakes (T+T 2015). (CBD = Christchurch Business District)

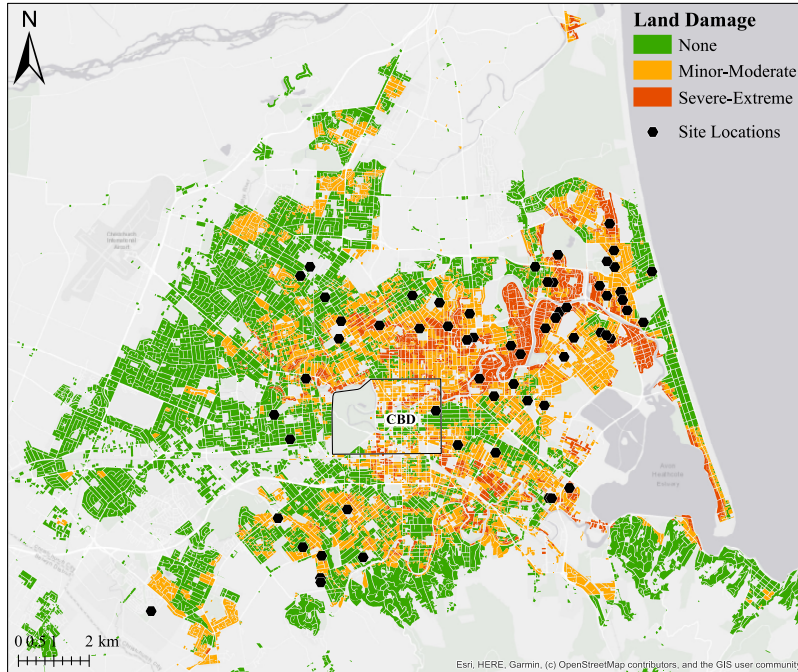


Figure 2.3. The maximum liquefaction ejecta-induced damage map (T+T 2015) with site locations. (CBD = Christchurch Business District)

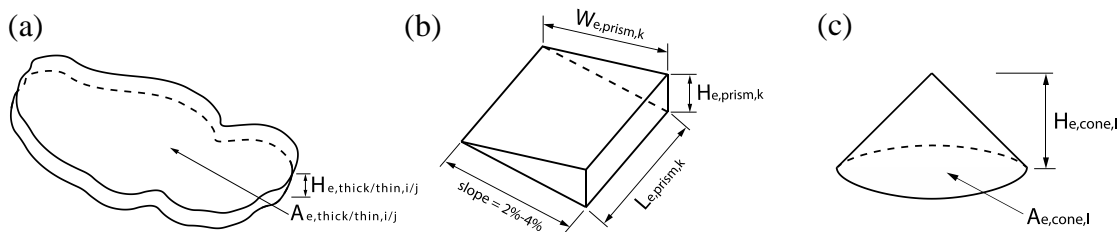


Figure 2.4. (a) Ejecta shaped as a prism with irregular curvilinear bases, (b) Ejecta on the road shaped as a prism with triangular bases, and (c) Ejecta occurring naturally as a cone.

Table 2.1. Best estimates of areal ejecta-induced free-field settlement for each site.

Site Name	Site ID	Long. (deg)	Lat. (deg)	SPC	Ejecta-Induced Free-Field Settlement (mm)			
					Sep 2010	Feb 2011	Jun 2011	Dec 2011
Shirley Intermediate School	VsVp 57203	172.661995	-43.510408	1	0	125 ±25	50 ±15	<5
Rydal Reserve	VsVp 57190	172.608493	-43.565806	4	<5	30 ±10	0	0
Rawhiti Domain	VsVp 57188	172.721404	-43.506685	1	0	0	0	0
Caulfield Ave	VsVp 38175	172.548658	-43.579706	4	<5	0	0	0
70 Langdons Rd	VsVp 57142	172.604872	-43.492195	3	0	0	0	0

Site Name	Site ID	Long. (deg)	Lat. (deg)	SPC	Ejecta-Induced Free-Field Settlement (mm)			
					Sep 2010	Feb 2011	Jun 2011	Dec 2011
Vivian St	CPT 5586	172.689983	-43.496445	1	0	80 ±30	50 ±30	<5
50 Eureka St	VsVp 57195	172.706500	-43.509273	1	0	70 ±70	<5	0
Parnwell St & Bassett St	CPT 27709	172.687992	-43.496341	1	0	90 ±25	20 ±10	5 ±5
Vangelis Ln & Fernbrook Pl	CPT 49582	172.650158	-43.501489	1	0	10 ±5	0	<5
Pinewood Ave	CPT 61991	172.711272	-43.488333	1	0	25 ±5	10 ±5	5 ±5
Carisbrooke Playground	VsVp 57193	172.709944	-43.510815	1	0	<5	0	0
Avondale Playground	VsVp 57062	172.687194	-43.508109	1	0	60 ±45	35 ±65	0
Bower Ave	CPT 3937	172.711488	-43.492600	1	0	95 ±35	20 ±5	10 ±5
Wattle Dr	CPT 90678	172.706167	-43.497325	1	0	120 ±30	85 ±25	65 ±15
Warrington St	CPT 44959	172.643107	-43.508034	1	5 ±5	40 ±10	15 ±20	<5
Hunt Ln	CPT 4674	172.692150	-43.503948	1	0	90 ±30	20 ±20	5 ±5
Sandown Cres	CPT 15498	172.708479	-43.509917	1	0	50 ±10	10 ±5	0
Travis Country Dr	CPT 29778	172.691683	-43.489401	1	0	15 ±20	<5	<5
Aldershot St	CPT 5261	172.697064	-43.510579	1	0	130 ±35	50 ±15	25 ±5
1/19 Chardale St	VsVp 57320	172.694632	-43.502797	1	5 ±5	--	--	--
15b Royds Pl	VsVp 57326	172.603276	-43.520686	4	0	--	--	--
31 Landy St*	CPT 44439	172.678436	-43.514681	1	25 ±5	50 ±10	40 ±10	10 ±5
Normans Rd/Papanui Rd	VsVp 57200	172.615699	-43.506100	4	0	--	--	--
St. Teresa's School	VsVp 57191	172.592135	-43.529873	2	0	0	0	0
Kaiwara Reserve	VsVp 57182	172.608046	-43.571492	3	0	10 ±5	0	0
Ti Rakau Reserve	VsVp 57186	172.695373	-43.548825	1	0	100 ±15	85 ±10	5 ±5
Avondale Park	VsVp 57187	172.690763	-43.505496	2	0	20 ±10	10 ±5	5 ±5
Sabina Playground	VsVp 57192	172.660660	-43.504340	1	0	50 ±10	30 ±10	5 ±5
Barrington Park	VsVp 38172	172.617541	-43.554035	2	0	15 ±5	<5	0
Shortland St	CPT 6551	172.693665	-43.515402	1	0	25 ±25	25 ±20	0

Site Name	Site ID	Long. (deg)	Lat. (deg)	SPC	Ejecta-Induced Free-Field Settlement (mm)			
					Sep 2010	Feb 2011	Jun 2011	Dec 2011
Mark Treffers Dr	CPT 62594	172.708784	-43.491115	1	0	35 ±10	10 ±5	5 ±5
Shirley Primary School	CPT 54376	172.653071	-43.507478	1	0	75 ±25	25 ±5	0
Cashmere High School	CPT 33732	172.623013	-43.566259	1	0	65 ±20	0	0
Dunarnan St	CPT 17908	172.675985	-43.522271	1	0	40 ±25	20 ±20	10 ±5
Baker St	CPT 14070	172.715770	-43.503609	1	0	155 ±40	105 ±10	120 ±20
Randolph St	CPT 44440	172.669546	-43.539782	1	0	90 ±20	30 ±5	0
Woodham Rd	CPT 25514	172.669086	-43.525337	1	0	5 ±5	5 ±5	0
Rudds Rd	CPT 5687	172.686716	-43.527755	1	0	35 ±10	15 ±5	0
Palmers Rd	CPT 27040	172.713519	-43.498906	1	0	95 ±30	75 ±55	15 ±5
Willryan Ave	CPT 2168	172.708731	-43.499905	1	0	55 ±30	35 ±35	5 ±5
Bideford Pl	CPT 17200	172.675071	-43.512497	1	<5	90 ±30	25 ±20	0
Wharenui School	VsVp 57165	172.597625	-43.536096	2	0	0	0	0
Heaton Normal Intermediate School	VsVp 57181	172.614886	-43.510572	2	40 ±10	25 ±10	15 ±5	<5
Hillmorton High School	VsVp 57201	172.593252	-43.556187	3	0	10 ±5	0	0
St. Albans Catholic School	VsVp 57180	172.629117	-43.507198	2	0	5 ±5	<5	0
113A Palmers Rd	CPT 29740	172.714230	-43.500972	1	0	80 ±45	70 ±40	65 ±20
Hurst Pl	CPT 25981	172.709763	-43.481524	1	0	60 ±15	25 ±10	30 ±5
Shirley Boys High School	CPT 56468	172.659684	-43.511008	1	0	25 ±10	25 ±20	10 ±5
Bracken St	CPT 59661	172.663966	-43.520893	1	40 ±10	75 ±10	25 ±5	15 ±5
Palinurus Rd 1	VsVp 57185	172.688215	-43.551331	1	0	0	0	0
Palinurus Rd 2	CPT 62761	172.689145	-43.551414	1	0	35 ±10	30 ±5	0
Nursery Rd	CPT 17262	172.656360	-43.537748	2	0	60 ±15	10 ±5	0
Gainsborough Reserve	VsVp 38176	172.601913	-43.563623	3	0	0	0	0
455 Papanui Rd	VsVp 57189	172.610136	-43.499954	3	0	0	0	0

Site Name	Site ID	Long. (deg)	Lat. (deg)	SPC	Ejecta-Induced Free-Field Settlement (mm)			
					Sep 2010	Feb 2011	Jun 2011	Dec 2011
Keers Rd	CPT 28986	172.680817	-43.526519	1	0	0	0	0
200 Cashmere Rd	VsVp 38171	172.608100	-43.572615	2	0	0	0	0
Armagh St	CPT 45795	172.648678	-43.529008	1	0	0	0	0
Lakewood Dr	CPT 54736	172.683682	-43.492444	1	0	0	0	0
Kensington Ave	CPT 88252	172.640665	-43.499634	2	0	0	0	0
Tonks St	CPT 128494	172.724500	-43.493746	1	0	0	0	0
Marblewood Reserve	VsVp 57155	172.601543	-43.494509	3	0	0	0	0

Note: SPC = Soil Profile Categories, which can be defined as (1) thick, clean sand, (2) partially stratified, (3) highly stratified silty soil, and (4) gravel-dominated soil profile; * VsVp site moved to CPT.

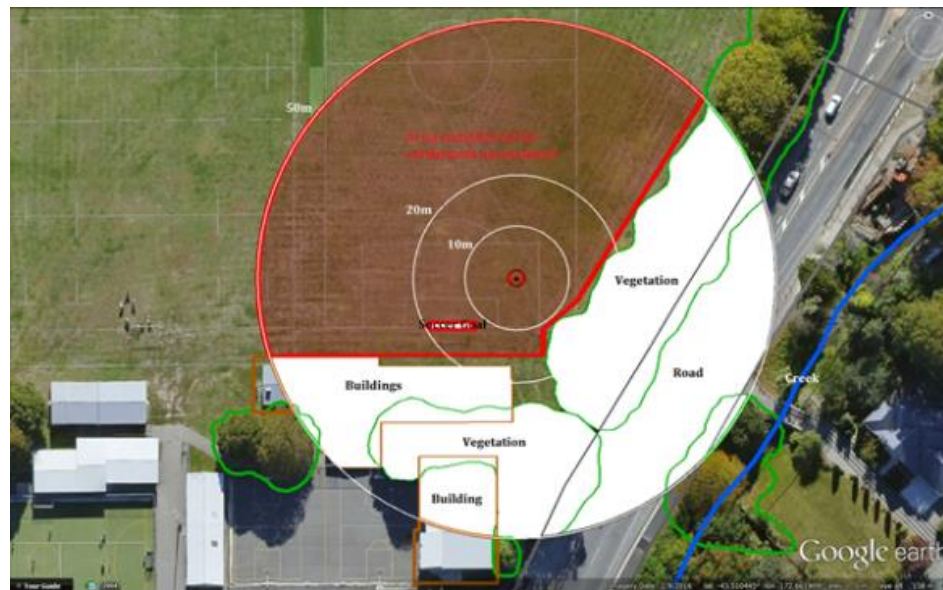


Figure 2.5. The Shirley Intermediate School site plan with the area analyzed for ejecta-induced settlement.



Figure 2.6. Aerial photographs acquired for Shirley Intermediate School in Sep 2010, Feb 2011, Jun 2011, and Dec 2011 (CGD 2012a) with ejecta outlines for the 10-, 20-, and 50-m buffers.

Table 2.2. Coverage area and height of ejecta estimates for 10-m buffer using photographs.

Earthquake Event	$A_{E,thick}$ (m ²)	$H_{E,thick}$ (mm)	$A_{E,thin}$ (m ²)	$H_{E,thin}$ (mm)	A_T (m ²)
Sep 2010	0	0	0	0	314
Feb 2011	143	150-250	39	50-100	314
Jun 2011	94	30-100	0	0	269*
Dec 2011	0	0	3	10-20	314

Notes: A_T = Total assessment area of a buffer being considered; * indicates that A_T is lower due to the presence of vehicles and their shadows at portions of the site when the aerial photograph was acquired.

Table 2.3. Photographic-based areal and localized ejecta-induced settlement.

Earthquake Event	10-m buffer		20-m buffer		50-m buffer	
	S_{E,P_areal} (mm)	$S_{E,P_localized}$ (mm)	S_{E,P_areal} (mm)	$S_{E,P_localized}$ (mm)	S_{E,P_areal} (mm)	$S_{E,P_localized}$ (mm)
Sep 2010	0	0	0	0	0	0
Feb 2011	100±25	175±45	130±35	175±45	75±20	175±45
Jun 2011	25±10	65±35	30±15	65±35	20±10	65±35
Dec 2011	<5	15±5	<5	15±5	<5	15±5

Note: The estimates are rounded to the nearest 5 mm.

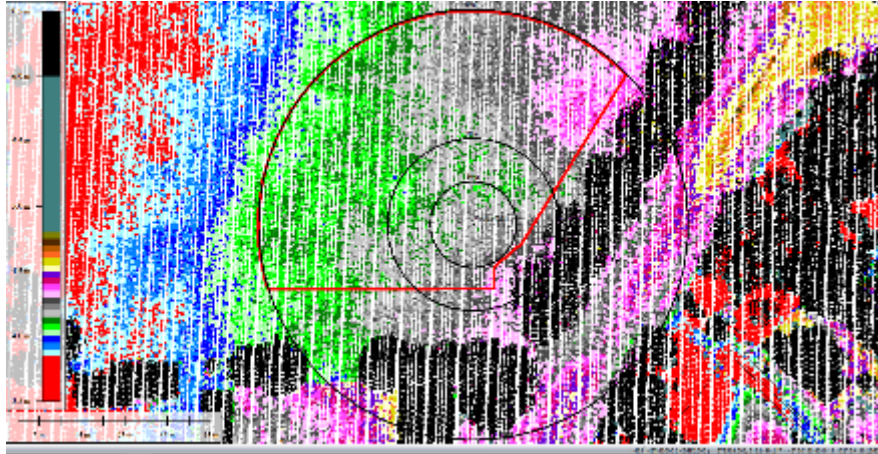


Figure 2.7. LiDAR survey points used to compute the average ground surface elevation in Global Mapper within the assessment area (outlined in red) for Mar 2011 (T+T 2015).

Table 2.4. Raw liquefaction-induced ground surface subsidence using original LiDAR points.

Earthquake Event(s)	Average Ground Surface Subsidence (mm)		
	10-m Buffer	20-m Buffer	50-m Buffer
Sep 2010	134	138	124
Feb 2011	214	213	148
Jun 2011	114	98	75
Dec 2011	7	12	15
CES	469	461	362

Table 2.5. LiDAR flight error adjustments, global adjustments for the difference between average LiDAR point elevations and benchmark survey elevations, and vertical tectonic movement adjustments.

Earthquake Event(s)	LiDAR Flight Error	Adjustments (mm)	
		Global Offset	Tectonic Vertical Movement
Sep 2010	-100	-3	0
Feb 2011	100	16	-85
Jun 2011	0	38	-40
Dec 2011	0	-65	0
CES	0	-14	-125
Any LiDAR survey affected by ejecta?			No

Note: The negative sign indicates the subtraction from the ground surface subsidence, while the positive sign indicates the addition to the ground surface subsidence.



Figure 2.8. Vertical Ground Movements (adjusted for the tectonic component) for the Sep 2010 and Feb 2011 earthquakes (CGD 2012b) – the site is in the zone of overestimated ground surface subsidence for the Sep 2010 earthquake and the zone of underestimated ground surface subsidence for the Feb 2011 earthquake.

Table 2.6. Corrected liquefaction-induced ground subsidence using Table 2.4 values and Table 2.5 adjustments.

Earthquake Event(s)	Average Calculated Ground Surface Subsidence (mm)		
	10-m Buffer	20-m Buffer	50-m Buffer
Sep 2010	31±75	35±75	21±75
Feb 2011	245±25	244±25	179±25
Jun 2011	112±25	96±25	73±25
Dec 2011	-58±50	-53±50	-50±50
CES	330±75	322±75	223±75

Notes: Positive values indicate ground surface subsidence; negative values indicate ground surface uplift.

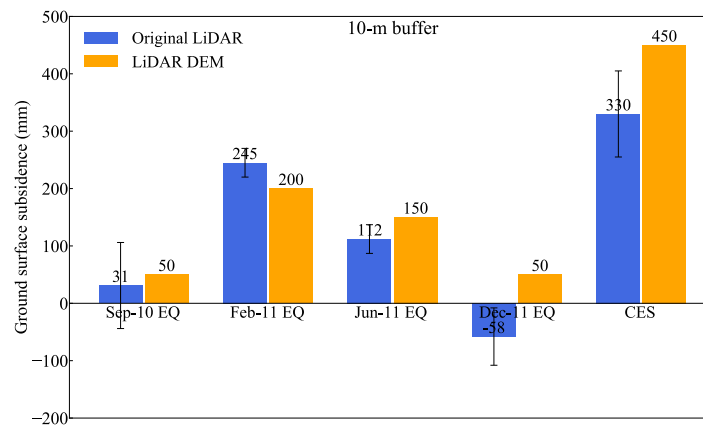


Figure 2.9. Comparison between the ground surface subsidence determined using the individual LiDAR elevation points and the ground surface subsidence estimated using the LiDAR DEMs.

Table 2.7. Ejecta-induced settlement for the top 20 m of the soil profile within the 10-m buffer for the 50th %ile PGA, $P_L=50\%$, and $C_{FC}=0.13$ using BI-2016, ZRB-2002, and I_C cutoff of 2.6.

Earthquake Event	M_w	PGA (g)	Depth to Groundwater (m)	S_T (mm)	S_{VID} (mm)	$S_{E,L}$ (mm)
Sep 2010	7.1	0.19	2.5	31±75	7±20	24±78
Feb 2011	6.2	0.38	2.5	245±25	71±50	174±56
Jun 2011	6.2	0.22	2.2	112±25	10±25	102±35
Dec 2011	6.1	0.26	2.0	-58±50	25±50	-83±71

Notes: S_T = Total settlement (Table 2.6); S_{VID} = Average vertical settlement due to volumetric compression using the Boulanger and Idriss (2016) (BI-2016) and Zhang et al. (2002) (ZRB-2002) procedures and the de Greef and Lengkeek (2018) thin-layer correction procedure; $S_{E,L}$ = Ejecta-induced settlement as the difference between the LiDAR-based S_T and S_{VID} .

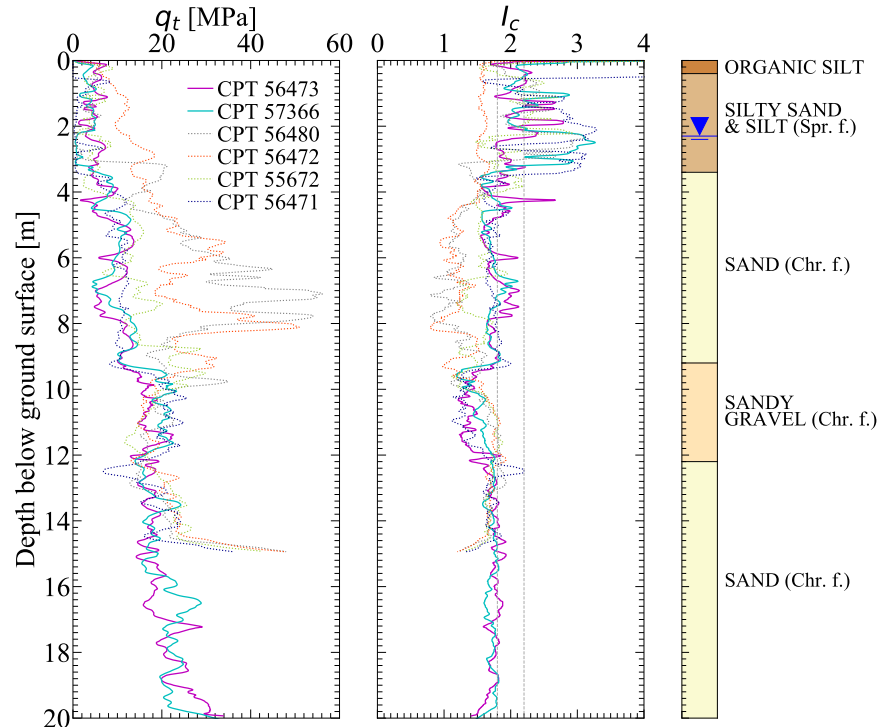


Figure 2.10. CPT traces and simplified soil profile for Shirley Intermediate School. (The soil layer colors are arbitrary.)

Table 2.8. CPT-based results for Shirley Intermediate School.

Earthquake Event	Parameter	CPT ID					
		56473	57366	56480	56472	55672	56471
Sep 2010	S _{VID} (mm)	7	7	1	0	4	1
	LSN	1	1	0	0	1	0
	LPI	0	0	0	0	0	0
	LPI _{ish}	0	0	0	0	0	0
	D _{FS<1} (m)	undet.	undet.	undet.	undet.	undet.	undet.
Feb 2011	S _{VID} (mm)	71	70	7	0	43	36
	LSN	13	13	2	0	11	7
	LPI	5	5	1	0	4	1
	LPI _{ish}	3	4	1	0	3	1
	D _{FS<1} (m)	3.20	3.18	undet.	undet.	2.72	3.45
Jun 2011	S _{VID} (mm)	9	10	1	0	7	1
	LSN	2	2	1	0	2	0
	LPI	0	0	0	0	0	0
	LPI _{ish}	0	0	0	0	0	0
	D _{FS<1} (m)	undet.	undet.	undet.	undet.	undet.	undet.
Dec 2011	S _{VID} (mm)	22	28	4	0	20	6
	LSN	4	6	1	0	6	1
	LPI	0	1	0	0	1	0
	LPI _{ish}	0	1	0	0	1	0
	D _{FS<1} (m)	4.27	6.70	undet.	undet.	3.45	undet.

Notes: D_{FS<1} = Depth to the first liquefiable layer (FS_L<1) that is at least 200-mm thick, as determined by the Boulanger and Idriss (2016) liquefaction-triggering procedure (P_L=50%, C_{FC}=0.13, and I_{c,cutoff} =2.6), and exported from *CLiq v.3.0.3.2*; undet. = the specified soil layer was not detected.

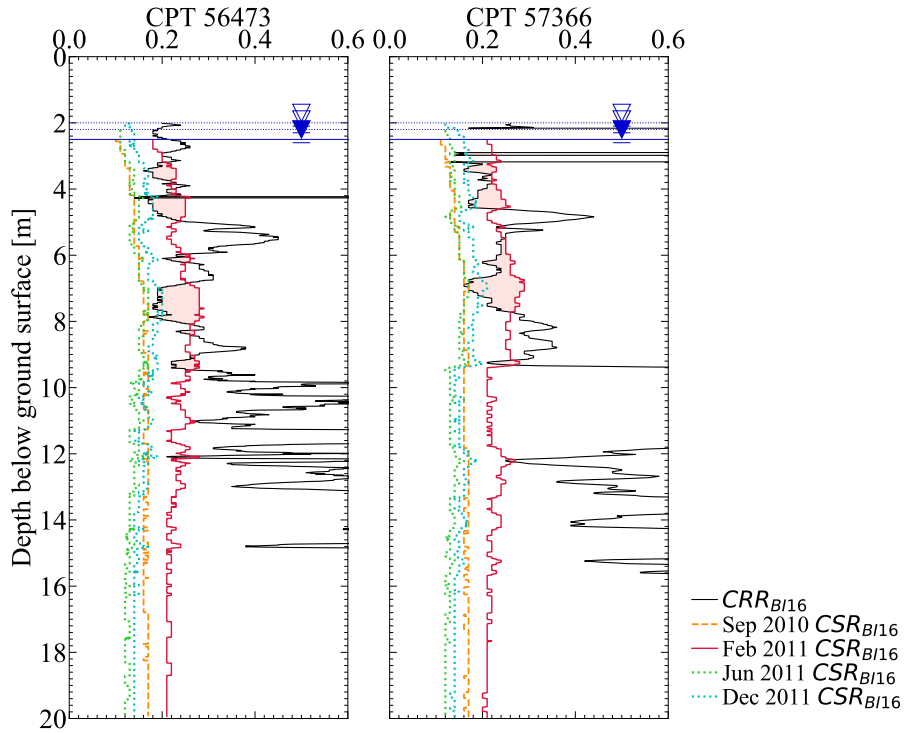


Figure 2.11. The Boulanger and Idriss (2016) estimated cyclic resistance (CRR_{BI16}) and the cyclic stress ratio (CSR_{BI16}) adjusted for $M_w = 7.5$ and $\sigma'_{vo} = 1$ atm for the Sep 2010, Feb 2011, Jun 2011, and Dec 2011 earthquakes for CPTs 56473 and 57366 at Shirley Intermediate School. Layers with $FS_L < 1$ for the Feb 2011 event are shaded.

Table 2.9. Best estimates of ejecta-induced settlement for Shirley Intermediate School.

Eq. Event	10-m radius			20-m radius			50-m radius		
	$S_{E,L}$ (mm)	$S_{E,P}$ (mm)	$S_{E,final}$ (mm)	$S_{E,L}$ (mm)	$S_{E,P}$ (mm)	$S_{E,final}$ (mm)	$S_{E,L}$ (mm)	$S_{E,P}$ (mm)	$S_{E,final}$ (mm)
Sep 2010	24±78	0	0	28±78	0	0	18±78	0	0
Feb 2011	174±56	101±25	125±25	173±56	131±34	145±30	141±56	76±19	100±25
Jun 2011	102±35	23±12	50±15	86±35	31±16	50±15	68±35	20±10	35±15
Dec 2011	-83±71	≈0	<5	-78±71	≈0	<5	-63±71	≈0	<5

Notes: $S_{E,L}$ = Ejecta-induced settlement based on LiDAR data and reported in Table 2.7; $S_{E,P}$ = Median ejecta-induced settlement for the range of values in Table 2.3; $S_{E,final}$ = Best final estimate of ejecta-induced settlement rounded to the nearest 5 mm; Final plus/minus values are also rounded to the nearest 5 mm.

3 DETAILED ANALYSIS OF LIQUEFACTION EJECTA CASE HISTORIES FOR THE 2010-11 CANTERBURY EARTHQUAKES

3.1 INTRODUCTION

Earthquake-induced liquefaction ejecta have the potential to cause substantial damage to the land and infrastructure. The 2010-2011 Canterbury, New Zealand, earthquakes, primarily the 4 Sep 2010 M_w 7.1, 22 Feb 2011 M_w 6.2, 13 Jun 2011 M_w 6.2, and 26 Dec 2011 M_w 6.1 events, triggered widespread, damaging liquefaction throughout Christchurch and its suburbs (e.g., Cubrinovski et al. 2011, Green et al. 2012). Approximately 51,000 residential properties were affected by liquefaction (Rogers et al. 2015). The amount of liquefaction ejecta-induced settlement varied from site to site and from earthquake to earthquake. The Feb 2011 earthquake caused the most severe and widespread liquefaction ejecta (Cubrinovski et al. 2011). Compared to the rest of Christchurch, residential areas to the east of the Christchurch Business District (CBD) experienced the most severe effects of liquefaction due to the stronger ground shaking and closer proximity to the causative fault, shallower groundwater table, and soil deposits that are more susceptible to liquefaction (Cubrinovski et al. 2011).

In the current state of practice, the occurrence and severity of surficial liquefaction manifestation are commonly estimated via index models in conjunction with simplified stress-based liquefaction triggering procedures, which are then used as a proxy for liquefaction-induced damage. One of the earliest index models is the liquefaction potential index, LPI, which was proposed by Iwasaki et al. (1978). It considers the influence of the liquefiable layer thicknesses and their proximities to the ground surface, as well as the relative densities through the factors of safety against liquefaction triggering, FS_L , on the severity of liquefaction manifestation at the ground surface. However, LPI does not explicitly account for the influence of contractive/dilative tendencies of soils and the thickness of a non-liquefiable layer immediately below the ground surface, i.e., crust, on the severity of liquefaction manifestation. Due to the limited performance of LPI as a proxy for liquefaction-induced damage in Christchurch for the 2010-2011 Canterbury earthquakes and the importance of crust thickness for liquefaction manifestation, van Ballegooy et al. (2014) developed the liquefaction severity number, LSN. They used the Ishihara and Yoshimine (1992) relationships among the FS_L , relative density, and post-liquefaction volumetric strain and thus accounted explicitly for the soils' contractive/dilative tendencies and incorporated the hyperbolic depth-weighting function to emphasize the importance of crust thickness on the severity of liquefaction manifestation. Although not a numerical index, the Ishihara (1985) boundary curves for different peak ground accelerations (PGAs) separate sites with and without surficial manifestation of liquefaction based on the relative thickness between the crust and an underlying liquefiable soil layer on liquefaction-induced damage, the work based on observations from two earthquakes. Maurer et al. (2015) developed LPI_{ish} wherein the Ishihara boundary curves and the power-law depth-weighting function were utilized to account for the crust thickness effect on the severity of surficial liquefaction manifestation. Upadhyaya et al. (2022)

merged the positive attributes of LSN (the post-liquefaction volumetric strain) and LPI_{ish} (the crust thickness effect) into LSN_{ish} and concluded that the efficacies of LSN_{ish} and LSN in estimating the surficial manifestation of liquefaction were lower than those of LPI and LPI_{ish} . This is contrary to the expectations based on the liquefaction manifestation mechanics “likely due to the double-counting of the dilative tendencies of medium-dense to dense soils ... because the liquefaction triggering model, to some extent, inherently accounts for such effects” (Upadhyaya et al. 2022). Hutabarat and Bray (2022) incorporated the depth of liquefaction triggering, soil stratification, and vertical hydraulic conductivity, as governing factors in the occurrence and severity of surficial liquefaction manifestation at strongly shaken sites, into the liquefaction ejecta demand, L_D , and crust layer resistance, C_R , parameters. These two parameters account for the post-shaking hydraulic mechanisms ignored by the previously mentioned liquefaction-induced damage indices. However, the L_D - C_R chart proposed by Hutabarat and Bray (2022) would benefit from additional validation from field case histories.

None of the liquefaction-induced damage indices can quantitatively estimate the settlement due to ejecta. Some of these methods rely on a correlation between the index and settlement to roughly estimate settlement. Additionally, existing procedures used to estimate the liquefaction-induced settlement do not capture the settlement due to ejecta. They are primarily used to estimate the settlement caused by the volumetric- and shear-induced displacement mechanisms. The volumetric-induced mechanism encompasses partial drainage, sedimentation, and consolidation, while the shear-induced mechanism involves punching failure and soil-structure-interaction ratcheting (Bray and Dashti 2014). Zhang et al. (2002) is one of the empirical procedures commonly used to estimate the free-field, one-dimensional volumetric settlement. The Bray and Macedo (2017) procedure can estimate the amount of settlement due to shear-induced liquefaction mechanism.

To address the issue of not having a procedure for estimating quantitatively the liquefaction ejecta-induced settlement and to advance understanding and knowledge of the formation and effects of ejecta, Mijic et al. (2022) developed the first liquefaction ejecta database comprised of detailed case histories for 58 sites shaken by the four main Canterbury earthquakes. Additional three sites were analyzed for the Sep 2010 earthquake only because they underwent lateral spreading for the Feb 2011 earthquake. Because direct measurements of ejecta and associated free-field damage had not been conducted after the Canterbury earthquakes, Mijic et al. (2022) estimated the ejecta-induced settlement with access to the comprehensive T+T (2015) and LDAT (2021) databases. They employed the photographic- and LiDAR-based methods to evaluate the free-field ejecta-induced settlement. The photographic-based method involved the use of aerial and ground photographs, detailed property inspection reports and maps, and geometrical approximations of the ejected soil shapes, while the second method was based on LiDAR point elevations and one-dimensional, free-field volumetric-induced settlement for level ground as per Zhang et al. (2002). The weighted average of the two estimates provided the best estimate of the ejecta-induced settlement. The details of the data, materials, and methodology used to develop the database are described in Chapter 2.

In this chapter, the detailed liquefaction ejecta case histories database developed by Mijic et al. (2022) is interrogated to better understand the formation and effects of ejecta. In the subsequent sections, factors that could have contributed to the manifestation of ejecta and differing amounts of ejecta-induced settlement from site to site and from earthquake

to earthquake are examined. The free-field ejecta-induced settlement is also evaluated against several of the existing liquefaction-induced damage indices.

3.2 OVERVIEW OF THE LIQUEFACTION EJECTA DATABASE FOR THE 2010-2011 CANTERBURY EARTHQUAKES

3.2.1 Site Geology

Christchurch is situated in the northern Canterbury Plains, just north of the Port Hills of Banks Peninsula, an extinct volcanic complex on the eastern shore of the South Island, New Zealand. Due to the complexity of depositional environment, four geologic quadrants centered on the Christchurch Business District (CBD) –southwest (SW), northwest (NW), northeast (NE), and southeast (SE) – can be identified (Beyzaei et al. 2018a). The main characteristics of the SW quadrant are thick successions of thinly interbedded fine sand and silt swamp deposits and the influence of the Port Hills on the depositional setting. The NW quadrant, too, is comprised of silty soil swamp deposits; however, it lacks depositional effects from the Port Hills and likely contains younger sediments than the SW quadrant as well as thicker sand strata and thinner silt strata than the SW quadrant. The NE and SE quadrants are characterized by interchanging layers of coastal and fluvial sediments and thicker layers of clean sand (Beyzaei et al. 2018a).

The Mijic et al. (2022) liquefaction ejecta database contains nine, eight, four, and forty sites with detailed case histories in the SW, NW, SE, and NE quadrants, respectively. Most sites are in the NE quadrant due to the predominance of ejecta-induced land and lightweight house damage in this quadrant. Considering the complexity of liquefaction phenomenon and the depositional Christchurch environment, localized geology, as well as the simplified conventional liquefaction assessment methodologies, four soil deposit categories were introduced for all of Christchurch (Mijic et al. 2022). The first and third soil deposit categories are with the greatest contrast. Thick, clean sand deposits (Category 1) are characterized by at least 3-m thick sand layer below the groundwater table in the top 10 m of the soil profile, while highly stratified silty soil deposits (Category 3) do not have a sand layer thicker than 1 m below the groundwater table in the top 10 m of the soil profile. Partially stratified silty soil deposits belong to Category 2 and have a sand stratum between 1 m and 3 m in thickness below the groundwater table in the top 10 m of the soil profile. Lastly, gravel-dominated soil deposits (Category 4) are characterized by at least 3-m thick gravel layer below the groundwater table in the upper 10 m of the soil profile. The available CPT profiles in combination with borehole logs were used to classify a soil deposit at each of 61 sites (Mijic et al. 2022). The CPT soil behavior type index, I_c , thresholds of 1.3 and 1.8 were used to distinguish between gravelly soil and clean sand and between clean sand and fines-containing sand, respectively, as adopted by Cubrinovski et al. (2019). A layer was considered continuous if it was not interrupted by a layer of different soil type which was more than 200-mm thick. There are forty-two thick, clean sand sites, nine partially stratified silty soil sites, six highly stratified silty soil sites, and four gravel-dominated sites. Their distribution among the four geologic quadrants is summarized in Table 3.1.

3.2.2 Liquefaction Ejecta-Induced Settlement Estimates

The liquefaction ejecta-induced free-field settlement was estimated at 61 sites for 10-, 20-, and 50-m radial areas (herein called buffers). The settlement assessment area within each buffer typically contained at least one CPT and depended on the presence of dwellings, vegetation, human-made alterations of the natural and built environment, and similar factors that could have obscured ejecta or affected the LiDAR surveys (Mijic et al. 2022). Sites in an open field (e.g., parks and playgrounds) typically had a large portion of each buffer assessed for ejecta-induced settlement, while sites at residential properties typically had one to three open patches of their properties and adjacent roads considered for the evaluation of ground settlement due to ejecta. The ejecta-induced settlement was evaluated using the photographic-based approach only or the photographic-based approach in combination with the LiDAR-based approach. For the photographic-based approach, both areal and localized ejecta-induced settlements were estimated to account for spatial distribution and localized effects of ejecta. For a settlement assessment area, the areal ejecta-induced settlement was evaluated as the ratio of the total volume of ejecta to the total area, whereas the localized ejecta-induced settlement was evaluated by dividing the total volume of ejecta with only the area covered by ejecta (Mijic et al. 2022).

Fifty-eight sites were analyzed for all four main Canterbury earthquakes, while three sites were analyzed for the Sep 2010 earthquake only due to lateral spreading caused by the Feb 2011 earthquake. Typically, three areal buffers and more than one assessment area were assessed for each site to develop one representative value (best estimate) of the ejecta-induced settlement at a site for each earthquake, which produced 235 case histories in total.

Figure 3.1 illustrates the distribution of areal ejecta-induced settlement values for each of the four main earthquake events. The Sep 2010 dataset contains the representative settlement values at 61 sites, while each of the Feb 2011, Jun 2011, and Dec 2011 datasets consists of representative settlement values at 58 sites. Having three extra case histories for the Sep 2010 dataset had a negligible impact on its range, mean, or median; thus, their ejecta-induced settlement values were included in the following discussion. The ranges of the Sep 2010, Feb 2011, Jun 2011, and Dec 2011 ejecta-induced settlement values are 0-40 mm, 0-155 mm, 0-105 mm, and 0-120 mm, respectively. The arithmetic mean values (referred to as mean values) of the Sep 2010, Feb 2011, Jun 2011, and Dec 2011 ejecta-induced settlements are < 5 mm, 40 mm, 20 mm, and 10 mm, respectively. These values as well as the following ones are rounded to the nearest 5 mm to enable comparisons. Due to the inherent uncertainty in estimating ejecta-induced settlement, these values should be rounded off to the nearest 10 mm for practical engineering purposes. The median ejecta-induced settlements for the Sep 2010, Feb 2011, Jun 2011, and Dec 2011 earthquakes are 0 mm, 35 mm, 10 mm, and 0 mm, respectively. Therefore, the greatest ejecta-induced settlement was due to the Feb 2011 earthquake, while the lowest ejecta-induced settlement was due to the Sep 2010 earthquake. The Jun 2011 ejecta-induced settlement was generally lower than the Feb 2011 ejecta-induced settlement and generally higher than the ejecta-induced settlement generated by the Dec 2011 earthquake or the Sep 2010 earthquake. The ejecta-induced settlement due to the Dec 2011 earthquake was generally higher than the Sep 2010 ejecta-induced settlement and generally lower than the ejecta-induced settlement for the Jun 2011 earthquake or the Feb 2011 earthquake.

The areal ejecta-induced settlement, defined previously, can be grouped in five categories – none (0 mm), minor (1-25 mm), moderate (26-50 mm), severe (51-100 mm), and extreme (> 100 mm). Figure 3.2 summarizes the number of sites within each settlement category for each of the four main Canterbury earthquakes. Among the four earthquakes, the number of sites that did not undergo ejecta-induced settlement is the greatest for the Sep 2010 earthquake (51 sites analyzed for all four earthquakes plus 2 sites analyzed for the Sep 2010 earthquake only) and the lowest for the Feb 2011 earthquake (15 sites). By contrast, the greatest number of sites with severe-to-extreme ejecta-induced settlement corresponds to the Feb 2011 earthquake (21 sites), while no sites with severe-to-extreme ejecta-induced settlement are identified for the Sep 2010 earthquake. The number of sites that underwent zero-to-minor ejecta-induced settlement increases for the Jun 2011 earthquake (44 sites) and then increases further for the Dec 2011 earthquake (54 sites), while the number of sites with severe-to-extreme ejecta decreases for the Jun 2011 and Dec 2011 earthquakes (5 sites and 3 sites, respectively).

The Mijic et al. (2022) database also contains estimates of localized ejecta-induced settlement (defined previously), which can be of great interest to engineers. Figure 3.3 illustrates the relationship between the localized ejecta-induced settlement and the areal ejecta-induced settlement at a site for each of the four main Canterbury earthquakes. The localized ejecta-induced settlement values are generally higher than the areal ejecta-induced settlement values because they do not incorporate areal averaging. There are a few cases where the localized ejecta-induced settlement is lower than the areal ejecta-induced settlement, which stems from the estimation method. The areal ejecta-induced settlement is higher due to the weighted average of the photographic- and LiDAR-based estimates, unlike the localized settlement which is based solely on the photographic evidence. The Mijic et al. (2022) database also provides areal ejecta-induced settlement estimates for each settlement assessment area based on the photographic evidence only; however, those values are not discussed herein for brevity. The mean localized ejecta-induced settlement values (rounded to the nearest 5 mm) for the Sep 2010, Feb 2011, Jun 2011, and Dec 2011 earthquakes are 5 mm, 55 mm, 25 mm, and 15 mm, respectively, while the respective median values are 0 mm, 50 mm, 20 mm, and 0 mm. The localized ejecta-induced settlement ranges are 0-70 mm, 0-200 mm, 0-105 mm, and 0-120 mm for the Sep 2010, Feb 2011, Jun 2011, and Dec 2011 earthquakes, respectively. In summary, the localized non-zero ejecta-induced settlement values are on average 5.6, 1.8, 2.7, and 4.6 times higher than the areal non-zero ejecta-induced settlement values for the Sep 2010, Feb 2011, Jun 2011, and Dec 2011 earthquakes, respectively, while the respective ranges of the localized-to-areal non-zero ejecta-induced settlement ratio are 1.2-18, 0.6-11, 0.5-14, and 1.0-12. The median and geometric mean values of the localized-to-areal ejecta-induced settlement ratios are 3.0 and 3.6, 1.2 and 1.4, 1.6 and 1.7, and 3.0 and 3.5 for the Sep 2010, Feb 2011, Jun 2011, and Dec 2011 earthquakes, respectively. The subsequent sections will discuss only the representative areal ejecta-induced settlement (hereinafter called the ejecta-induced settlement).

3.3 EXAMINATION OF TRENDS FOR EJECTA-INDUCED SETTLEMENT AND AVAILABLE VARIABLES

The relationships between the liquefaction ejecta-induced settlement and parameters available in the Mijic et al. (2022) database are examined. Specifically, the effects of key parameters, such as PGA, groundwater depth, soil profile, crust thickness, and liquefiable layer thickness, on the amount of settlement due to ejecta are investigated. The relationship between the ejecta-induced settlement and other variables is explored using Spearman's correlation coefficient, R , which is mathematically equivalent to Pearson's correlation coefficient for the ranked data. The choice stems primarily from the distribution of the data which was not always normal and the possibility of having variables that are associated nonlinearly. In theory, the correlation coefficient definition applies only to the bivariate normal distribution of two variables (Ang and Tang 2007). Spearman's correlation coefficient does not require the jointly normally distributed data and can measure a monotonic association between two variables (Schober et al. 2018, Forthofer et al. 2007). The strength of the correlation in this study is described as very weak, weak, moderate, strong, and very strong for the absolute value of $R_s = 0.00-0.19, 0.20-0.39, 0.40-0.59, 0.60-0.79,$ and $0.80-1.0,$ respectively.

3.3.1 The Effect of PGA on Ejecta-Induced Settlement

PGA is an earthquake intensity measure commonly used in simplified liquefaction triggering procedures to evaluate the earthquake demand on soil (cyclic stress ratio) and thus the factor of safety against liquefaction triggering. The median PGA with the associated uncertainty for each of the four main Canterbury earthquakes was estimated by Bradley and Hughes (2012). These values are provided in Mijic et al. (2022) for each liquefaction ejecta case history. The range of the median PGA (hereinafter referred to as PGA) at the analyzed sites is 0.17-0.31, 0.23-0.68, 0.13-0.43, and 0.12-0.41 g for the M_w 7.1 Sep 2010, M_w 6.2 Feb 2011, M_w 6.2 Jun 2011, and M_w 6.1 Dec 2011 earthquakes, respectively. The geometric mean (arithmetic mean is given in the parentheses) and median Sep 2010, Feb 2011, Jun 2011, and Dec 2011 PGA values are 0.20 (0.20) and 0.20, 0.42 (0.43) and 0.43, 0.23 (0.24) and 0.22, and 0.25 (0.26) and 0.28 g, respectively. It is important to note that local site conditions can affect the actual PGA experienced at each site.

The distribution of sites with none, minor, moderate, severe, and extreme liquefaction ejecta-induced settlement relative to the PGA contours is illustrated in Figure 3.4 for each of the four main Canterbury earthquakes. The PGA contours are presented in four groups: $PGA \leq 0.20$ g, 0.21-0.40 g, 0.31-0.40 g, and > 0.40 g. In general, there appears to be the tendency of the ejecta-induced settlement severity to decrease with the decrease in PGA and thus the increase in source-to-site distance for individual earthquake events.

To compare the settlement among the four earthquakes with different M_w , the raw Bradley and Hughes (2012) PGA values are scaled to an equivalent M_w 6.1 earthquake (the lowest M_w of the four earthquakes, which is the Dec 2011 event) using the Idriss and Boulanger (2008) magnitude scaling factor, MSF, which is related to the ground motion duration (i.e., $MSF = 6.9 \exp(-M_w/4) - 0.058 \leq 1.8$). The raw PGA for the Sep 2011, Feb 2011, and Jun 2011 earthquakes are, therefore, multiplied by 1.30, 1.03, and 1.03,

respectively (i.e., $MSF(M_w=6.1) / MSF(M_w=7.1) = 1.30$ and $MSF(M_w=6.1) / MSF(M_w=6.2) = 1.03$), to obtain the magnitude-weighted PGA, hereinafter referred to as $PGA_{6.1}$. The Feb 2011 earthquake is generally characterized by the most intense $PGA_{6.1}$ (min = 0.24 g, max = 0.70 g, geometric mean = 0.43 g, arithmetic mean = median = 0.44 g) compared to the Sep 2010, Jun 2011, and Dec 2011 earthquake-generated $PGA_{6.1}$ (Sep 2010: min = 0.22 g, max = 0.40 g, and geometric mean = arithmetic mean = median = 0.26 g; Jun 2011: min = 0.13 g, max = 0.44 g, geometric mean = arithmetic mean = 0.24 g, and median = 0.23 g; and Dec 2011: min = 0.12 g, max = 0.41 g, geometric mean = 0.25 g, arithmetic mean = 0.26 g, and median = 0.28 g). This is consistent with the observations of the greatest number of sites with severe-to-extreme liquefaction ejecta-induced settlement for the Feb 2011 earthquake (21 sites), all triggered by $PGA_{6.1} > 0.30$ g (Figure 3.5). There are no sites with severe-to-extreme ejecta-induced settlement for the Sep 2010 earthquake for any $PGA_{6.1}$ range.

The relationship between the ejecta-induced settlement and the estimated $PGA_{6.1}$ at each site for each Canterbury earthquake is shown in Figure 3.6. The ejecta-induced settlement generally tends to increase with an increase in $PGA_{6.1}$. Sites shaken with $PGA_{6.1} \leq 0.20$ g typically had no ejecta-induced settlement. Sites shaken with $PGA_{6.1} = 0.21$ - 0.30 g mostly experienced ejecta-induced settlement of up to 50 mm. Sites subjected to $PGA_{6.1} > 0.30$ g typically experienced < 100 mm of ejecta-induced settlement. Zero ejecta-induced settlement case histories are present for all $PGA_{6.1}$ ranges. Spearman's correlation coefficient, R_s , of 0.45 also indicates a positive moderate correlation between the ejecta-induced settlement and $PGA_{6.1}$ for all 235 case histories together. The magnitude of positive correlation between the ejecta-induced settlement and $PGA_{6.1}$ for individual earthquake events ranges from very weak for the Feb 2011 earthquake ($R_s = 0.18$) to moderate for the Jun 2011 and Dec 2011 earthquakes ($R_s = 0.47$ and $R_s = 0.50$, respectively). The relationship between the ejecta-induced settlement and $PGA_{6.1}$ for individual earthquakes is shown in Figure 3.7.

3.3.2 The Effect of Groundwater Depth on Ejecta-Induced Settlement

The distribution of sites with none, minor, moderate, severe, and extreme liquefaction ejecta-induced settlement across the groundwater depth models for Christchurch for the Sep 2010, Feb 2011, Jun 2011, and Dec 2011 earthquakes is illustrated in Figure 3.8. No effect of the groundwater depth on the ejecta-induced settlement can be deduced from these regional maps. The groundwater depth at the studied sites ranges from 0.5 m to 3.5 m for all earthquake events. The arithmetic and geometric mean groundwater depths are 1.8 m and 1.6, respectively, for both the Sep 2010 and Feb 2011 case histories, 1.7 m and 1.5 m, respectively, for the Jun 2011 case histories, and 1.6 m and 1.4 m, respectively, for the Dec 2011 case histories. The median groundwater depth for each of the Sep 2010, Jun 2011, and Dec 2011 case histories datasets is 1.5 m, while the median groundwater depth for the Feb 2011 case histories is 1.6 m. The estimated groundwater depth at a site often varied from earthquake to earthquake. The maximum change in the groundwater depth at a site from earthquake to earthquake ranged from 0 m to 2.2 m with an average of 0.5 m (median = 0.5 m) for 58 sites. Spearman's correlation coefficients, R_s , for the groundwater depth and the ejecta-induced settlement are very weak for the Sep 2010, Feb 2011, and Jun 2011 earthquakes ($R_s = -0.13$, 0.10, and -0.11, respectively) and weak

for the Dec 2011 earthquake ($R_S = -0.23$). Negative correlation indicating an increase in the ejecta-induced settlement with a decrease in the groundwater depth is expected.

The effect of groundwater depth on the ejecta-induced settlement for 235 case histories is further investigated for different $PGA_{6.1}$ ranges. When all case histories with a specified $PGA_{6.1}$ range are grouped regardless of the earthquake event, the correlation between the ejecta-induced settlement and the groundwater depth is very weak ($R_S = 0.00, -0.18, 0.04,$ and -0.11 for $PGA_{6.1} \leq 0.20, 0.21-0.30, 0.31-0.40,$ and > 0.40 g, respectively). When case histories with a specified $PGA_{6.1}$ range are grouped for each individual earthquake, the correlation becomes more significant for the Jun 2011 earthquake (Figure 3.9) with $R_S = -0.32, -0.67,$ and -1.00 for $PGA_{6.1} = 0.21-0.30, 0.31-0.40,$ and > 0.40 g, respectively, indicating a decrease in the ejecta-induced settlement with the increasing groundwater depth. For the Feb 2011 earthquake and $PGA_{6.1} > 0.30$ g, there is a very weak positive correlation between the groundwater depth and the ejecta-induced settlement ($R_S = 0.04$), while the strength of positive correlation somewhat increases for $PGA_{6.1} = 0.31-0.40$ g ($R_S = 0.29$). If only sites shaken by $PGA_{6.1} > 0.40$ g for the Feb 2011 earthquake are considered, the correlation between the groundwater depth and the ejecta-induced settlement becomes negative although very weak ($R_S = -0.09$).

3.3.3 The Effect of Soil Profile on Ejecta-Induced Settlement

The effect of clean sand deposits and stratified silty soil deposits on the amount of settlement due to ejecta is investigated by combining a total of 136 CPT traces into four groups based on $PGA_{6.1}$ for the Canterbury earthquakes (Figure 3.10). The CPT traces colored in green, orange, and red indicate that the settlement assessment areas they belong to underwent (a) zero, minor (1-25 mm), and moderate (26-50 mm) ejecta-induced settlement, respectively (Figure 3.10a), and (b) none-to-minor (0-25 mm), moderate (26-50 mm), and severe-to-extreme (> 50 mm) ejecta-induced settlement, respectively (Figure 3.10b), for a given $PGA_{6.1}$ range, $\leq 0.20, 0.21-0.30, 0.31-0.40,$ and > 0.40 g. When a site experienced the $PGA_{6.1}$ within the same range more than once yet had different ejecta-induced settlements, the highest settlement value was used in the analysis.

Only zero-to-minor ejecta-induced settlement is present for $PGA_{6.1} \leq 0.20$ g regardless of the cone penetration tip resistance, q_c , and the soil behavior type index, I_c . The severe-to-extreme ejecta-induced settlement is pronounced at sites where $q_c \approx 10-25$ MPa and $I_c \approx 1.3-1.8$ dominate the soil profiles, which are typically sand deposits. This trend becomes more dominant as $PGA_{6.1}$ increases, especially when $PGA_{6.1}$ exceeds 0.40 g. Sites whose soil profiles can be described with $q_c \lesssim 10-15$ MPa and $I_c \approx 2-3$, i.e., typically silty soil deposits, tend to be more resistant to the formation of ejecta at the ground surface, at least for $PGA_{6.1} < 0.40$ g. Moreover, sites with silty material in the upper 4-5 m of the soil profile typically experienced severe-to-extreme amounts of ejecta-induced settlement, whereas sites with silty material in at least the top 10 m of the soil profile had no-to-minor ejecta-induced settlement, a trend more pronounced for $PGA_{6.1} < 0.40$ g. $PGA_{6.1} = 0.21-0.30$ g typically triggered more than 25 mm of ejecta-induced settlement only at soil deposits where sand is predominant in both the top 5 and top 10 m. It is important to acknowledge that the number of CPT traces belonging to a different site category is not even within a single $PGA_{6.1}$ bin or evenly distributed among the four $PGA_{6.1}$ bins; there are more CPTs corresponding to thick, clean sand deposits than highly stratified silty soil deposits. Also, each preceding event within the Canterbury earthquake sequence

(CES) could have compromised the quality of the crust in the subsequent event(s) within the CES.

3.3.4 The Effect of Crust Thickness on Liquefaction Ejecta-Induced Settlement

Crust thickness can be defined based on I_c and FS_L (Mijic et al. 2022). It is the thickness of soil between the ground surface level and the depth at or below the groundwater table where soil has $I_c < 2.6$ or $FS_L < 1$ for at least 200 mm. Hutabarat and Bray (2022) used the same I_c crust thickness definition in their study with the difference of the first significant liquefiable layer thickness (i.e., the thickness of a layer at or below the ground water table with $I_c < 2.6$) being at least 250-mm thick instead of 200-mm thick. This difference has negligible impact on the observed trends. Thus, the focus of the discussion in this section is on a 200-mm thickness for more consistent assessment relative to the FS_L crust definition. $FS_L \leq 1$ was computed in *CLiq 3.0* using the Boulanger and Idriss (2016) CPT-based liquefaction triggering procedure and the de Greef and Lengkeek (2018) thin-layer correction procedure (Mijic et al. 2022). The thickness is estimated based on the average I_c or FS_L value for the CPTs corresponding to the most representative settlement assessment area (Mijic et al. 2022).

The crust thickness effect is first analyzed for the four main Canterbury earthquakes altogether. The crust thickness values based on the I_c definition and the corresponding ejecta-induced settlement values are separated into four $PGA_{6.1}$ groups, ≤ 0.20 , 0.21-0.30, 0.31-0.40, and > 0.40 g (Figure 3.11). The $PGA_{6.1} \leq 0.20$ g group has 30 case histories with the crust thickness ranging from 0.5 m to 3.5 m. All 30 case histories correspond to the Jun 2011 and Dec 2011 earthquakes. Twenty-seven case histories had no ejecta-induced settlement regardless of the crust thickness, while only three case histories had minor ejecta-induced settlement, specifically < 5 mm, < 5 mm, and 15 mm for the respective crust thicknesses of 0.7 m, 2.1 m, and 2.1 m. The $PGA_{6.1} = 0.21-0.30$ g group is comprised of 115 case histories with the crust thickness ranging from 0.5 m to 4.3 m and the ejecta-induced settlement ranging from 0 mm to 105 mm. These case histories belong primarily to the Sep 2010, Jun 2011, and Dec 2011 earthquakes and have a very weak tendency to the higher ejecta-induced settlement with the crust thinning ($R_S = -0.17$). The $PGA_{6.1} = 0.31-0.40$ g group has 50 case histories with the crust thickness ranging from 0.5 m to 3.6 m and the ejecta-induced settlement ranging from 0 mm to 125 mm. These case histories correspond to all four earthquake events and are with insignificant correlation between the crust thickness and the ejecta-induced settlement ($R_S = 0.03$). The $PGA_{6.1} > 0.40$ g group contains 40 case histories with the crust thickness ranging from 0.6 m to 4.3 m and the ejecta-induced settlement ranging from 0 mm to 155 mm. These case histories belong primarily to the Feb 2011 earthquake and result in a negative weak correlation between the crust thickness and the ejecta-induced settlement ($R_S = -0.20$).

Additionally, the effect of crust thickness is analyzed for the Feb 2011, Jun 2011, and Dec 2011 earthquakes individually for $PGA_{6.1} = 0.21-0.30$, 0.31-0.40, and > 0.40 g groups because they encompass most non-zero ejecta case histories (Figure 3.12). The Jun 2011 and Dec 2011 case histories resulted in a negative correlation between the crust thickness and the ejecta-induced settlement for both $PGA_{6.1} = 0.21-0.30$ g ($R_S = -0.31$ and $R_S = -0.42$, respectively) and $PGA_{6.1} = 0.31-0.40$ g ($R_S = -0.50$ and $R_S = -0.35$, respectively), whereas the Feb 2011 case histories resulted in a positive correlation for $PGA_{6.1} = 0.31-0.40$ g ($R_S = 0.31$) and a negative correlation for $PGA_{6.1} > 0.40$ g ($R_S = -0.20$). (For the

Feb 2011 case histories with $PGA_{6.1} > 0.30$ g, $R_S = -0.04$.) The positive correlation is contrary to the common expectation of the ejecta-induced settlement increasing as the crust thickness decreases. However, there are case histories and methods that support the observed trends (e.g., Hutabarat and Bray 2022). For the meizoseismal region of the 1811-1812 New Madrid earthquakes, Obermeier (1989) observed the “greatly enhanced” amount of subaerial venting where the crust was very thin. The formation of ejecta through a low-permeability crust on the level ground is driven by hydraulic fracturing and surface ground oscillations occurring independently or in combination with one another (Obermeier 1996). Additionally, venting of liquefied material can be affected by holes in the crust such as those left by decayed roots (Audemard and de Santis 1991, Obermeier 1996).

The relationship between the $FS_L > 1$ crust thickness and the ejecta-induced settlement is then analyzed. In case of the first liquefiable layer with $FS_L \leq 1$ and thickness of at least 200 mm not being detected within the upper 20 m of the soil profile, the ejecta-induced settlement was typically zero. For the Sep 2010, Jun 2011, and Dec 2011 earthquakes altogether, 58 of 70 case histories without the first liquefiable layer being detected had no ejecta-induced settlement. Thus, the probability of having zero settlement due to ejecta when a 200-mm or thicker liquefiable layer with $FS_L \leq 1$ did not exist in the top 20 m of the soil profile was 83%. The specified liquefiable layer could be detected at a depth ranging from 1.0 m to 18.0 m for all Feb 2011 earthquake case histories. The crust thicknesses of 18.0 m, 9.0 m, and 8.1 m resulted in zero ejecta-induced settlement, while the crust thicknesses in the range from 1.0 m to 6.3 m resulted in the ejecta-induced settlement ranging from 0 mm to 155 mm. The extreme ejecta-induced settlements of 120 mm, 125 mm, 130 mm, and 155 mm correspond to the crust thicknesses of 2.1 m, 3.2 m, 2.9 m, and 2.9 m, respectively.

3.3.5 The Effect of First Liquefiable Layer Thickness on Ejecta-Induced Settlement

The liquefaction ejecta database also contains the thickness of the first significant liquefiable soil layer that may contribute to ejecta production, Z_{ab} , for each case history. The definition originates from the Hutabarat and Bray (2022) study wherein a liquefiable soil layer has these properties: $I_c < 2.6$, is at least 250-mm thick, and extends from the bottom of the crust (previously defined) to the top of a soil layer with $I_c \geq 2.6$ and a minimum thickness of 250 mm. The Z_{ab} ranges from 0.4 m for all four main earthquakes to 13.7 m for the Sep 2010 and Feb 2011 earthquakes, 14.2 m for the Jun 2011 earthquake, and 14.3 m for the Dec 2011 earthquake. The geometric mean (the arithmetic mean is provided in the parentheses) and median Z_{ab} values for the Sep 2010, Feb 2011, Jun 2011, and Dec 2011 earthquakes are 4.8 m (8.1 m) and 11.4 m, 4.9 m (8.1 m) and 11.2 m, 4.6 m (7.9 m) and 11.2 m, and 5.1 m (8.3 m) and 11.6 m, respectively. The effect of Z_{ab} on the ejecta-induced settlement is examined for the available ejecta case histories subjected to $PGA_{6.1} \leq 0.20$, 0.21-0.30, 0.31-0.40, and > 0.40 g for all four earthquakes together and for each individual earthquake.

The ejecta-induced settlement generally tends to increase as the liquefiable layer thickness increases (Figure 3.13). This trend is apparent for $PGA_{6.1} = 0.21$ -0.30 g ($R_S = 0.37$), $PGA_{6.1} = 0.31$ -0.40 g ($R_S = 0.26$), and $PGA_{6.1} > 0.40$ g ($R_S = 0.36$). The zero ejecta-induced settlement is present for all $PGA_{6.1}$ ranges regardless of the liquefiable layer thickness. The same trend of the increasing ejecta-induced settlement as Z_{ab} increases can be observed for the Feb 2011 earthquake. Figure 3.14 shows that the scatter in the data

points generally increases as Z_{ab} increases for both $PGA_{6.1} = 0.31-0.40$ g ($R_S = 0.62$) and $PGA_{6.1} > 0.40$ g ($R_S = 0.37$). For $PGA_{6.1} = 0.21-0.30$ and $0.31-0.40$ g, $R_S = 0.31$ and $R_S = -0.70$, respectively, for the Jun 2011 earthquake and $R_S = 0.56$ and $R_S = 0.09$, respectively for the Dec 2011 earthquake. Having all other parameters equal, the increase in the ejecta-induced settlement with the increasing thickness of the first liquefiable soil layer is expected.

3.4 EVALUATING THE EFFICACY OF LIQUEFACTION-INDUCED DAMAGE INDICES

3.4.1 Ishihara (1985) Boundary Curves

The Ishihara (1985) boundary curves provide an opportunity to examine the joint effect of the crust thickness and the liquefiable soil layer thickness on the ejecta-induced settlement for different levels of PGA. The Bradley and Hughes (2012) PGA estimate for each earthquake event is now scaled using MSF for an equivalent M_w 7.5 earthquake ($PGA_{7.5}$) for which the curves were developed. Figure 3.15 shows the crust thickness versus the liquefiable layer thickness data points, as defined by Hutabarat and Bray (2022), superimposed over the Ishihara (1985) boundary curves for $PGA_{7.5} \leq 0.20, 0.30, \text{ and } 0.45$ g for the four main earthquakes together (Figure 3.15a) and each of them individually (Figure 3.15b,c,d,e). Each data point is colored differently to show the ejecta-induced settlement as none (0 mm), minor (1-25 mm), moderate (26-50 mm), severe (51-100 mm), and extreme (> 100 mm).

The crust thickness for 235 case histories does not exceed 5 m, while the thickness of the first liquefiable layer underlying the crust is less than 15 m. Consequently, the data points are clustered in the left third of the plots. Most data points located to the right of the 0.20, 0.30, and 0.45 g Ishihara (1985) boundary curves thus corresponding to the combination of the crust thickness in the approximate range from 1 m to 5 m and the liquefiable layer thickness of up to approximately 1 m had zero ejecta-induced settlement, which is consistent with the interpretation of the Ishihara (1985) plot – no liquefaction effects at the ground surface if data points plot to the right of the $PGA_{7.5}$ boundary curves. Except for several data points corresponding to the minor ejecta-induced settlement, the non-zero ejecta-induced settlement points are located to the left of the boundary curves, which is again consistent with the interpretation of the Ishihara (1985) plot – liquefaction effects are expected at the ground surface if data points plot to the left of the $PGA_{7.5}$ boundary curves. These trends are observed for all four earthquakes together and for each individual earthquake. However, there is a large scatter of the zero ejecta-induced settlement data points with many being on the left side of the boundary curves. This trend is most prominent for the Sep 2010 earthquake and is least prominent for the Feb 2011 earthquake, which has most overestimations of zero ejecta-induced settlement for the liquefiable layer thickness less than 2 m. The increase in the thickness of the liquefiable soil layer from 1 m to 15 m relative to the typical 1-4 m range of the overlying crust thickness appears to not have a notable effect on the ejecta-induced settlement for the Sep 2010 earthquake regardless of $PGA_{7.5}$. By contrast, most non-zero ejecta-induced settlement points for the Feb 2011 earthquake appear for the liquefiable layer thickness greater than 3 m in combination with the crust thickness of less than 4 m, while most zero ejecta case histories correspond to the liquefiable layer thickness of less than 2 m.

3.4.2 Liquefaction Potential Index, LPI

The ejecta-induced settlement is compared with the liquefaction potential index, LPI. LPI was proposed by Iwasaki et al. (1978) as:

$$LPI = \int_{0\text{ m}}^{20\text{ m}} Fw(z)dz$$

where $F = 1 - FS_L$ for $FS_L \leq 1$ and $F = 0$ for $FS_L > 1$, $w(z) = 10 - 0.5z$, and z is depth in meters below the ground surface. LPI, therefore, assumes the severity of liquefaction manifestation is proportional to the liquefiable layer thickness and its proximity to the ground surface and the amount by which FS_L is less than 1. It is important to note the sensitivity of LPI to groundwater depth estimates because of the liquefiable soil layers' proximity to the ground surface (Maurer et al. 2014). The criteria for LPI and the observed liquefaction ejecta-induced settlement used in this study is based on the studies by Maurer et al. (2014) and Hutabarat and Bray (2022). The liquefaction ejecta-induced settlement is estimated as none, minor, moderate, and severe-to-extreme if $LPI = 0-4$, $4-8$, $8-15$, and ≥ 15 , respectively.

Figure 3.16 illustrates the distribution of case histories with zero-to-extreme ejecta-induced settlement relative to LPI and Z_{ab} , the thickness of the first significant liquefiable layer immediately below the crust, for all four main Canterbury earthquakes. Non-zero settlement due to ejecta is mostly concentrated in the Z_{ab} range from 11 m to 14 m. There is a cluster of data points corresponding to zero ejecta-induced settlement in the $Z_{ab} \lesssim 1$ m range wherein LPI is more dispersed compared to the zero ejecta data points with $Z_{ab} > 5$ m. Of 122 case histories with zero ejecta-induced settlement, there are 99 correct estimates and 23 overestimates of settlement with LPI. Most of the 23 overestimates are for the sites with the thin ($\lesssim 1$ -m thick) first liquefiable layer, which are often stratified silty soil deposits. The number of overestimates for case histories with minor and moderate ejecta-induced settlement is 13 out of 84 in total. Ten of these instances correspond to the case histories with minor ejecta-induced settlement and three correspond to the case histories with moderate ejecta-induced settlement. It appears that the overestimation of minor ejecta-induced settlement tends to decrease with the increase in Z_{ab} . LPI underestimates the ejecta-induced settlement for 83% of case histories with severe-to-extreme ejecta-induced settlement. There are 24, 13, and 38 LPI underestimates of 29 severe-to-extreme, 21 moderate, and 63 minor ejecta-induced settlement case histories, respectively. Additionally, as shown in Figure 3.17, the underestimation of the non-zero ejecta-induced settlement is present for each of the four main earthquakes, whereas the overestimation of zero ejecta-induced settlement is nearly absent for the Jun 2011 and Dec 2011 earthquakes (the overestimation occurred for 5% and 6% zero ejecta case histories, respectively) compared to the Sep 2011 and Feb 2011 earthquakes (the overestimation occurred for 21% and 60% zero ejecta case histories, respectively). The systematic underestimation or overestimation of ejecta occurrence by liquefaction-induced damage indices, such as LPI, is primarily due to the absence of incorporation of system-response effects in simplified liquefaction assessment methods (Cubrinovski et al. 2019).

3.4.3 Liquefaction Severity Number, LSN

The liquefaction ejecta-induced settlement can also be compared with liquefaction severity number, LSN. LSN was proposed by van Ballegooy et al. (2014) as:

$$LSN = 1,000 \int \frac{\varepsilon_v}{z} dz$$

where ε_v is the post-liquefaction volumetric strain provided as a decimal and z is the depth below ground surface in meters. The ejecta-induced settlement is estimated as none, minor, moderate, severe, and extreme if $LSN = 0-10, 10-20, 20-30, 30-40,$ and ≥ 40 , respectively, the criterion used by Hutabarat and Bray (2022). For comparison with LPI, the severe and extreme categories are discussed subsequently as a single severe-to-extreme category (i.e., severe-to-extreme ejecta-induced settlement is correctly estimated with $LSN \geq 30$).

Figures 3.18 and 3.19 do not show much difference in the overall performance of LSN compared to the performance of LPI in terms of estimating the ejecta-induced settlement correctly. The dispersion of the zero ejecta-induced settlement points is again greater for $Z_{ab} \lesssim 1$ m than $Z_{ab} > 5$ m, which often indicates the overestimation of settlement due to ejecta at stratified silty soil sites. The number of correct estimates of zero-ejecta induced settlement with LSN is slightly lower than with LPI (88 versus 99, respectively), meaning the number of overestimates of zero ejecta-induced settlement with LSN is 34 compared to 23 with LPI. Of 84 case histories with minor and moderate ejecta-induced settlement, there are 13 overestimates of ejecta-induced settlement with LSN, which is the same number of minor and moderate cases overestimated with LPI. Ten of these instances correspond to the case histories with minor ejecta-induced settlement and the other three correspond to the case histories with moderate ejecta-induced settlement. The overestimation of minor ejecta-induced settlement again shows a slight tendency to decrease with the increasing Z_{ab} . LSN underestimates the ejecta-induced settlement in 83% of case histories with severe-to-extreme ejecta-induced settlement, which is equal to the percentage of severe-to-extreme ejecta cases underestimated with LPI. Of 29 severe-to-extreme, 21 moderate, and 63 minor ejecta-induced settlement case histories, there are 24, 15, and 32 LSN underestimates, respectively. LSN correctly estimates the severity of ejecta-induced settlement in 50% cases (117 cases of 235 cases) compared to 53% cases (124 cases of 235 cases) with LPI. Additionally, LSN underestimated the non-zero ejecta-induced settlement for each of the four main earthquakes (Figure 3.19). The overestimation of zero ejecta-induced settlement with LSN was greater for the Sep 2011 and Feb 2011 earthquakes than for the Jun 2011 and Dec 2011 earthquakes. LSN overestimated the zero ejecta-induced settlement in 32% and 60% of the zero ejecta case histories for the Sep 2010 and Feb 2011 earthquakes, respectively, compared to 14% and 15% of the zero ejecta case histories for the Jun 2011 and Dec 2011 earthquakes, respectively.

3.4.4 Liquefaction Ejecta Demand, L_D , and Crust Resistance, C_R , parameters

The liquefaction ejecta-induced settlement can also be compared with liquefaction ejecta demand, L_D , and crust resistance, C_R , parameters. The two parameters were proposed by Hutabarat and Bray (2022) are:

$$L_D \left(\frac{kN}{m} \right) = \gamma_w \int_{z_a}^{z_b} \frac{k_v}{k_{cs}} (h_{exc} - h_a) dz \quad \begin{cases} \text{when } h_{exc} \geq h_a \\ 0, \quad \text{otherwise} \end{cases}$$

$$C_R \left(\frac{kN}{m} \right) = \int_0^{z_a} S_u dz \quad \begin{cases} S_u = K_o \sigma'_{vo} \tan(\varphi_{cs}), & \text{if } I_B > 22 \text{ (sand-like soil)} \\ S_u = \frac{q_t - \sigma_{vo}}{N_{kt}}, & \text{if } I_B \leq 22 \text{ (clay-like soil)} \end{cases}$$

where Z_a is the depth from the ground surface to the top of the first liquefiable soil layer (i.e., the first soil layer below the groundwater table with $I_c < 2.6$ and at least 250-mm thick), Z_b is the depth from the ground surface to the top of the first non-liquefiable soil layer underlying the previously defined liquefiable layer (i.e., it is depth to the first soil layer located between Z_a and 15-m depth with $I_c \geq 2.6$ and thickness ≥ 250 mm), k_v is the vertical hydraulic conductivity, k_{cs} is the hydraulic conductivity of clean sand, h_{exc} is the excess hydraulic head, h_a is the required h_{exc} at a depth Z to generate the artesian flow, S_u is the CPT-based shear strength of the crust layer, $K_o = 0.5$, $\varphi_{cs} = 33^\circ$, and $N_{kt} = 15$. Further explanation of the variables is provided in Hutabarat and Bray (2022). The severity of liquefaction ejecta chart has none-to-minor, minor-to-moderate, moderate-to-severe, and severe-to-extreme zones separated by bilinear boundary lines defined by three $[C_R, L_D]$ data points: $[0, 2.5]$, $[100, 2.5]$, and $[250, 25]$; $[0, 6]$, $[90, 6]$, and $[250, 70]$; $[0, 15]$, $[85, 15]$, and $[250, 150]$; and $[0, 85]$, $[75, 85]$, and $[200, 250]$, respectively (Hutabarat and Bray 2022). For comparison with LPI, the severe and extreme categories are discussed subsequently as a single severe-to-extreme category (i.e., severe-to-extreme ejecta-induced settlement is correctly estimated with $[C_R, L_D] > [0, 15]$, $[85, 15]$, and $[250, 150]$).

The relationship between the ejecta-induced settlement as a function of C_R is first examined. Figure 3.20 shows a general tendency of the ejecta-induced settlement to decrease with the increasing C_R , which validates the expectation. For example, there are no cases with $PGA_{6.1} \leq 0.30$ g with more than 30 mm of liquefaction ejecta-induced settlement when C_R is greater than 45 kN/m. Spearman's correlation coefficient, R_s , of -0.36 for the case histories with $PGA_{6.1} > 0.40$ g is in agreement with the observed/expected trend. R_s for $PGA_{6.1} = 0.21-0.30$ g and $PGA_{6.1} = 0.31-0.40$ g groups are very weak (-0.13 and 0.10, respectively). Although the data points are scattered, the same general trend of the decreasing ejecta-induced settlement with the increasing crust resistance can be observed for individual earthquakes (Figure 3.21).

The relationship between the ejecta-induced settlement and L_D is then examined for individual earthquake events (Figure 3.22). The L_D values for the Sep 2010, Jun 2011, and Dec 2011 earthquakes do not exceed 41, 38, and 62 kN/m, respectively, while the maximum L_D for the Feb 2011 earthquake corresponds to 164 kN/m at the studied sites. The relationship between the ejecta-induced settlement and L_D in Figure 3.22 is most visually apparent for the Feb 2011 earthquake. There is a general increase in the ejecta-induced settlement with an increase in L_D , as expected. This trend is validated by Spearman's correlation coefficient of 0.52 for the Feb 2011 earthquake as well as Spearman's correlation coefficients of 0.60 and 0.55 for the Jun 2011 and Dec 2011 earthquakes, respectively. When the correlation is analyzed for all 235 data points (i.e., for the four main Canterbury earthquakes together), $R_s = 0.60$, which indicates a strong positive correlation of ejecta-induced settlement as a function of L_D .

The 235 case histories are used to evaluate the overall performance of the Hutabarat and Bray (2022) L_D-C_R chart in Figures 3.23 and 3.24. For 122 zero ejecta-induced settlement case histories, the number of correct estimates is 101 compared to 88 with LSN and 99 with LPI. Thus, the number of overestimates of zero ejecta-induced settlement with L_D-C_R is 21 compared to 34 with LSN and 23 with LPI. The overestimation of zero ejecta-induced settlement occurred for 11 %, 40 %, 5 %, and 24 % of the zero ejecta case histories for the Sep 2010, Feb 2011, Jun 2011, and Dec 2011 earthquakes, respectively. For minor and moderate ejecta-induced settlement, there are 36 overestimates of the ejecta-induced settlement compared to 13 with both LPI and LSN. Thirty of these instances correspond to the case histories with minor ejecta-induced settlement and the remaining six correspond to the case histories with moderate ejecta-induced settlement. L_D-C_R underestimates severe-to-extreme ejecta-induced settlement in 35% cases, which is more than two times less than the percentage of underestimations with LSN and LPI (83%). Of 29 severe-to-extreme, 21 moderate, and 63 minor ejecta-induced settlement case histories, there are 10, 10, and 24 L_D-C_R underestimates, respectively. Figure 3.24 illustrates that the underestimation as well as the overestimation of ejecta-induced settlement by the L_D-C_R chart occurred for all earthquake events. In summary, the L_D-C_R chart correctly estimated the severity of ejecta-induced settlement in 57% cases (considering none, minor, moderate, and severe-to-extreme categories and four earthquake events altogether) compared to 50% and 53% with LSN and LPI, respectively.

3.5 SITE PERFORMANCE DIFFERENCES AMONG THE FOUR MAIN CANTERBURY EARTHQUAKES

The examination of 232 case histories in the liquefaction ejecta database (excluding 3 sites analyzed for the Sep 2010 earthquake only) reveals that ejecta did not induce settlement for the following combinations of earthquake events: Jun 2011 only, Dec 2011 only, Jun 2011 & Dec 2011, Sep 2010 & Jun 2011, Sep 2010 & Dec 2011, Sep 2010 & Jun 2011 & Dec 2011, and Sep 2010 & Feb 2011 & Dec 2011. Thus, ejecta were not generated by the Jun 2011 earthquake or Dec 2011 earthquake or both if the Feb 2011 earthquake did not result in the formation of ejecta at the ground surface. The two most common earthquake combinations in the database that generated the ejecta-induced settlement are Feb 2011 & Jun 2011 & Dec 2011 (20 sites) and Feb 2011 & Jun 2011 (12 sites). The ejecta-induced settlement was also generated by the following combinations of earthquakes: Sep 2010 only (1 site), Feb 2011 only (4 sites), Sep 2010 & Feb 2011 (1 site), Feb 2011 & Dec 2011 (1 site), Sep 2010 & Feb 2011 & Jun 2011 (1 site), and Sep 2010 & Feb 2011 & Jun 2011 & Dec 2011 (4 sites). The Sep 2010 & Feb 2011 & Jun 2011 & Dec 2011 earthquake combination also resulted in zero ejecta-induced settlement at 14 sites.

Thirty-two sites which experienced the ejecta-induced settlement for the Feb 2011, Jun 2011, and/or Dec 2011 earthquakes but did not have any ejecta generated by the Sep 2011 earthquake are further examined. This type of site performance was predominant for the thick, clean sand sites (28 of 32 sites), which is not surprising considering ~70% of the sites in the database are also clean sand sites. In general, the sites were not shaken by much different $PGA_{6.1}$ and did not have much different groundwater depths, crust thicknesses, or first liquefiable layer thicknesses. The sites typically experienced $PGA_{6.1}$ levels that were only slightly higher for the Jun 2011 earthquake compared to the Sep 2010 earthquake

(Figure 3.25a). The geometric mean and median $PGA_{6.1}$ for 32 sites are 0.25 g and 0.23 g, respectively, for the Sep 2010 earthquake, and 0.26 g and 0.25 g, respectively, for the Jun 2011 earthquake. The $PGA_{6.1}$ range for 32 sites is 0.22-0.31 g for the Sep 2010 earthquake and 0.18-0.44 g for the Jun 2011 earthquake. The groundwater depth was generally slightly lower during the Jun 2011 earthquake than the Sep 2010 earthquake (Figure 3.25b). The geometric mean and median groundwater depths for 32 sites are 1.7 m and 1.8 m, respectively, for the Sep 2010 earthquake, and 1.5 m and 1.5 m, respectively, for the Jun 2011 earthquake. The groundwater depth range for 32 sites is 0.5-3.3 m for the Sep 2010 earthquake and 0.5-3.0 m for the Jun 2011 earthquake. The geometric mean and median values of the 32 first liquefiable layer thicknesses, Z_{ab} , are 8.5 m and 12.2 m, respectively, for the Sep 2010 earthquake and 7.6 m and 12.5 m, respectively, for the Jun 2011 earthquake (Figure 3.25c). The Z_{ab} for 32 sites ranges from 0.8 m to 13.5 m for the Sep 2010 earthquake and from 0.5 m to 13.7 m for the Jun 2011 earthquake. The crust thickness (based on the I_c definition in Section 3.3.4) was slightly higher for the Sep 2010 earthquake than the Jun 2011 earthquake (Figure 3.25d). The scatter in the data is similar to that in Figure 3.20b, which is not unusual considering the utilization of the groundwater depth in the crust thickness definition. The geometric mean and median crust thickness values are 1.9 m and 2.0 m, respectively, for the Sep 2010 earthquake, and 1.7 m and 1.5 m, respectively, for the Jun 2011 earthquake. For 32 sites, the crust thickness ranged from 0.5 m to 3.6 m for the Sep 2010 earthquake and from 0.6 m to 3.6 m for the Jun 2011 earthquake.

All 32 sites with no ejecta for the Sep 2010 earthquake but with ejecta for the Jun 2011 earthquake were strongly shaken during the Feb 2011 earthquake ($PGA_{6.1} \geq 0.35$ g) and experienced at least 5 mm of the ejecta-induced settlement. Figure 3.26 shows that the ejecta-induced settlement for the Jun 2011 earthquake tends to increase as the ejecta-induced settlement for the Feb 2011 earthquake increases. Spearman's correlation coefficient of 0.73 confirms this trend is strong. Additionally, lower $PGA_{6.1}$ levels ($PGA_{6.1} = 0.21$ -0.30 g) resulted in most non-zero ejecta case histories for the Jun 2011 earthquake compared to most non-zero ejecta case histories for the Feb 2011 earthquake resulting from more intense $PGA_{6.1}$ ($PGA_{6.1} > 0.30$ g), as shown in Figure 3.5. Thus, the Feb 2011 earthquake triggered widespread and extensive liquefaction ejecta, severely damaging the ground and forming new holes and cracks through which the liquefied soil migrated more easily onto the ground surface during the Jun 2011 earthquake. Recurrence of liquefaction ejecta at the same site and via the same path through the crust is not uncommon (Obermeier 1996).

3.6 ADDITIONAL OBSERVATIONS REQUIRING FURTHER INVESTIGATION

During the examination of the liquefaction ejecta database, additional patterns were observed and require further assessment. The additional patterns and proposed work are:

- Some sites that had ejecta for the Jun 2011 earthquake did not have it for the Dec 2011 earthquake. The site parameters and $PGA_{6.1}$ could be compared between the two events at these sites. If none of the available parameters can explain the differing response, it may be beneficial to examine parameters such as the cumulative absolute velocity (CAV) or Arias intensity.

- There are strongly shaken thick, clean sand sites that experienced zero ejecta-induced settlement. The CPT tip resistance, groundwater depth, crust thickness, and first liquefiable layer thickness at these sites could be compared with the same parameters at thick, clean sand sites that did have ejecta and were shaken by similar $PGA_{6.1}$. The observed performance of the thick, clean sand sites could be investigated relative to that of the stratified silty soil sites as well as relative to the estimations of the severity of surficial liquefaction effects by liquefaction-induced damage indices.
- Negligible ejecta at residential properties compared to the large amounts of ejecta at adjacent roads were often observed for sites whose properties were at a higher elevation relative to the adjacent roads. Detailed analysis could be conducted for these sites to better understand the migration paths of liquefied soil material toward the lower-elevation roads with storm drains and other crust defects.

3.7 CONCLUSION

In this chapter, the liquefaction ejecta database presented in Chapter 2 was examined to identify general trends associated with the severity of the ejecta-induced settlement, including the effects of the available earthquake characteristics and soil parameters, and to evaluate the efficacy of liquefaction-induced damage indices such as LSN, LPI, and L_D-C_R , as well as the Ishihara (1985) boundary curves. The database is comprised of 58 sites analyzed for the Sep 2010, Feb 2011, Jun 2011, and Dec 2011 earthquakes and 3 additional sites analyzed for the Sep 2010 earthquake only thus 235 case histories in total. The sites are spatially distributed across Christchurch with most sites in the NE quadrant where the ejecta-induced land and light-weight house damage were predominant. Consequently, 66% of sites in the database are characterized by thick, clean sand deposits, while the remaining 34% of sites are characterized by stratified silty soil deposits and gravel-dominated deposits. Each case history has the ejecta-induced settlement, PGA, groundwater depth, crust thickness, first liquefiable soil layer thickness, LPI, LSN, L_D , and C_R estimates.

Although insights can be gleaned from the study of the performance of these sites, there are limitations to consider. There is uncertainty in each of the parameters available in the database. The ejecta-induced settlement used in the analysis of the database represents the best estimate of the areal ejecta-induced settlement for each case history based on the representative settlement assessment area(s) for a site. There were multiple assessment areas for each site to investigate variability. Each site is centered at a selected CPT location, and radial areas of 10 m, 20 m, and 50 m were investigated, with assessment areas being an open field (e.g., a park or playground), a residential area with patches of an open area (e.g., yards), or a road. The ejecta-induced settlement estimates depend on the size of the assessment area and the spatial distribution of ejecta across the assessment area, both of which differ from site to site. Thus, the areal averaging has the potential to obscure the actual ejecta-induced settlement trends among the sites. The quality of the photographs, LiDAR survey data, etc., also affects the ejecta-induced settlement estimates. Furthermore, it is assumed a CPT is representative of a settlement assessment area even though ejecta were not often generated in its close proximity and the spatial variability, both lateral and vertical, in soil conditions is likely, due to the complex depositional environment of

Christchurch. Consequently, the CPT parameters (q_c and I_c) and the CPT-based indices (LPI, LSN, L_D , and C_R) and definitions (the first liquefiable layer and crust thicknesses) may not best describe the soil profile conditions that resulted in the estimated ejecta-induced settlement. There is also uncertainty in the PGA and groundwater depth estimates. Nevertheless, the liquefaction ejecta database provides a unique set of data for the analysis of the occurrence and effects of ejecta.

Liquefaction ejecta occurred for all four main Canterbury earthquakes. The severity of the ejecta-induced settlement ranged from site to site and from earthquake to earthquake. The Feb 2011 earthquake resulted in the most severe and the most frequent ejecta-induced settlement, while the Sep 2010 earthquake resulted in the least severe and the least frequent ejecta-induced settlement. The ejecta-induced settlement ranged from 0 mm to 155 mm for the Feb 2011 earthquake and from 0 mm to 40 mm for the Sep 2010 earthquake. The ejecta-induced settlement ranges for the Jun 2011 and Dec 2011 earthquakes were 0-105 mm and 0-120 mm, respectively. Ejecta were not generated by the Jun 2011 or Dec 2011 earthquake if it were not generated by the Feb 2011 earthquake. For 55% of the studied sites, ejecta did not occur for the Sep 2010 earthquake but did occur for the Jun 2011 earthquake even though their $PGA_{6.1}$, groundwater depths, crust and first liquefiable layer thicknesses did not differ significantly. However, there is a strong correlation between the Feb 2011 ejecta-induced settlement and the Jun 2011 ejecta-induced settlement (as shown in Figure 3.26). It is, therefore, speculated that the Feb 2011 earthquake-induced liquefaction ejecta severely damaged the land forming holes and cracks and thus helping liquefied soil at depth to migrate onto the ground surface more easily for the Jun 2011 earthquake.

The complexity of the formation of ejecta due to the variability in the earthquake ground motions, site conditions, and factors such as the presence of structures and cracks in the crust, etc., uncertainty in estimating the earthquake and site parameters and the ejecta-induced settlement, and inability to control variables in the natural setting may permit a less strict interpretation of the correlation between the ejecta-induced settlement and the $PGA_{6.1}$, groundwater depth, CPT parameters, crust and liquefiable layer thicknesses. $PGA_{6.1} \leq 0.20$ g resulted in < 15 mm of ejecta-induced settlement (typically zero) at the sites regardless of the soil profile characteristics captured by CPT. Sites with silty material in the upper 10 m of the soil profile typically produced no-to-minor ejecta-induced settlement for $PGA_{6.1} < 0.40$ g compared to thick, clean sand sites which tended to experience more severe ejecta-induced settlement relative to the stratified silty soil sites. The severity of ejecta at thick, clean sand sites increased as $PGA_{6.1}$ increased, especially when $PGA_{6.1}$ exceeded 0.40 g. For the Jun 2011 earthquake when $PGA_{6.1} > 0.20$ g, sites with shallower groundwater tables showed considerable tendency to higher ejecta-induced settlement than the ones with deeper groundwater tables. The most notable effect of the crust thickness on the formation of ejecta was for the Jun 2011 and Dec 2011 earthquakes when $PGA_{6.1} > 0.20$ g – the ejecta-induced settlement somewhat decreased as the crust thickness increased. A slight general increase in the ejecta-induced settlement with the increasing thickness of the first liquefiable soil layer was observed, especially for the Feb 2011 earthquake when $PGA_{6.1} = 0.31$ -0.40 g.

The ejecta-induced settlement was compared with the liquefaction-induced damage indices. The Ishihara (1985) boundary curves generally overestimated the liquefaction effects-induced damage for the zero ejecta case histories when the crust and first liquefiable layer thicknesses were both $\lesssim 1$ -2 m and when the first liquefiable layer thickness exceeded

2 m for the crust thickness < 4 m. This trend was most prominent for the Sep 2010 earthquake and least prominent for the Feb 2011 earthquake. The crust thickness versus first liquefiable layer thickness data points corresponding to the non-zero ejecta-induced settlement typically plotted to the left of the Ishihara (1985) boundary curves indicative of damage due to liquefaction effects. LSN and LPI underestimated the severe-to-extreme ejecta-induced settlement in 83% of cases compared to 35% with L_D-C_R . The percent of correctly estimated zero ejecta case histories with L_D-C_R is 83% compared to 72% and 81% with LSN and LPI, respectively. The systematic underestimation of liquefaction effects for clean sand sites highlights the importance of system response effects and the need for their incorporation into the simplified liquefaction triggering procedures.

The liquefaction ejecta database can be improved by adding case histories for 20-30 stratified silty soil sites in Christchurch to balance the number of clean sand sites. It would also benefit from being complemented with case histories from future earthquakes and various geographic regions, and additional parameters such as Arias intensity and cumulative absolute velocity. It is essential that direct, reliable measurements of intact ejecta are taken after future earthquakes and CPTs are conducted in a manner that best captures the soil profile which contributed to the observed spatial distribution of ejecta (e.g., by advancing the cone adjacent to different types of liquefaction ejecta boils). A paleoliquefaction study conducted for the sites in the database could also improve our understanding of differing responses among different sites.

Table 3.1. Distribution of soil deposit types across the geologic quadrants.

Number of sites per soil deposit category				
Quadrant	Thick, clean sand (Category 1)	Partially stratified (Category 2)	Highly stratified (Category 3)	Gravel-dominated (Category 4)
NE	38	2	0	0
SE	3	1	0	0
NW	0	3	3	2
SW	1	3	3	2

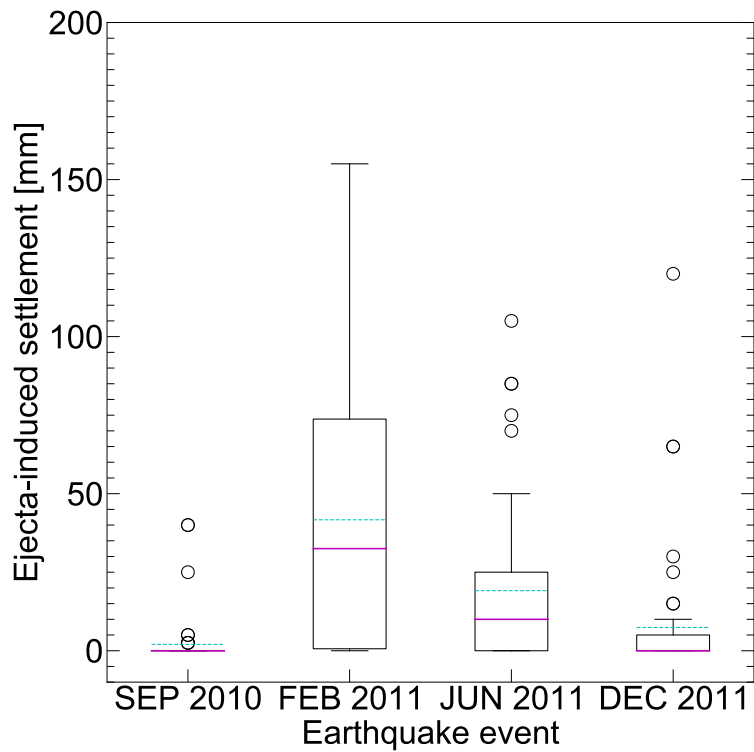


Figure 3.1. Box and whiskers showing distribution of liquefaction ejecta-induced settlement for each of the four main Canterbury earthquakes (magenta = median and cyan = mean).

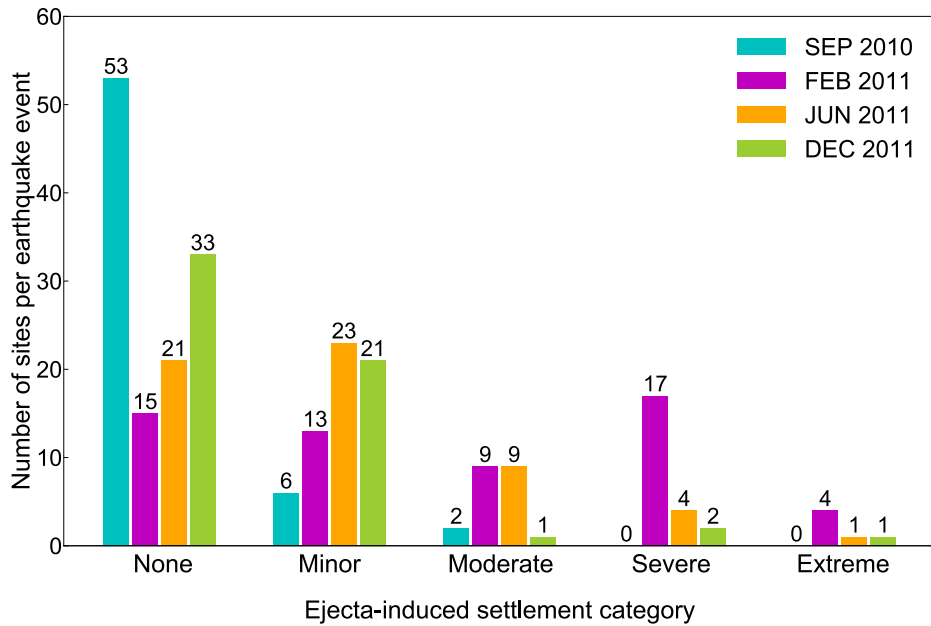


Figure 3.2. The number of sites per liquefaction ejecta-induced settlement category for each of the four main Canterbury earthquakes.

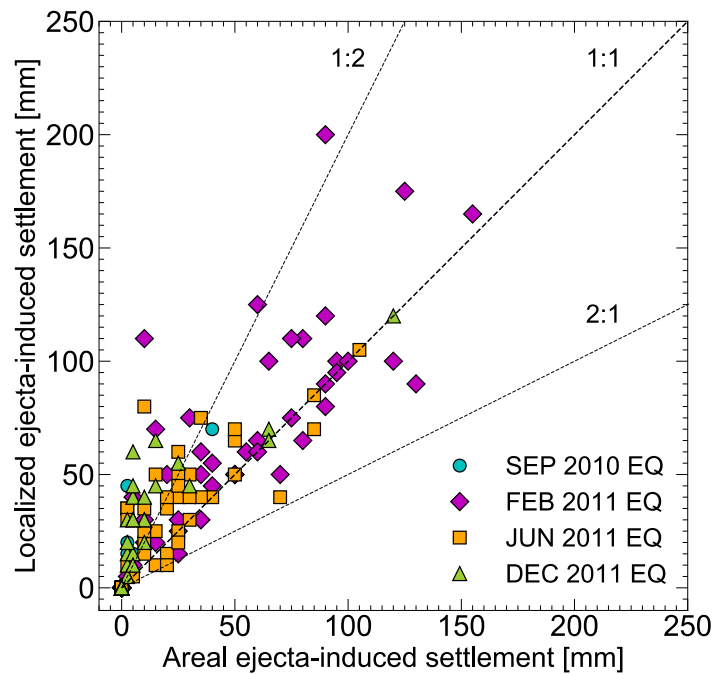


Figure 3.3. Localized versus areal ejecta-induced settlement at each site for each of the four main Canterbury earthquakes.

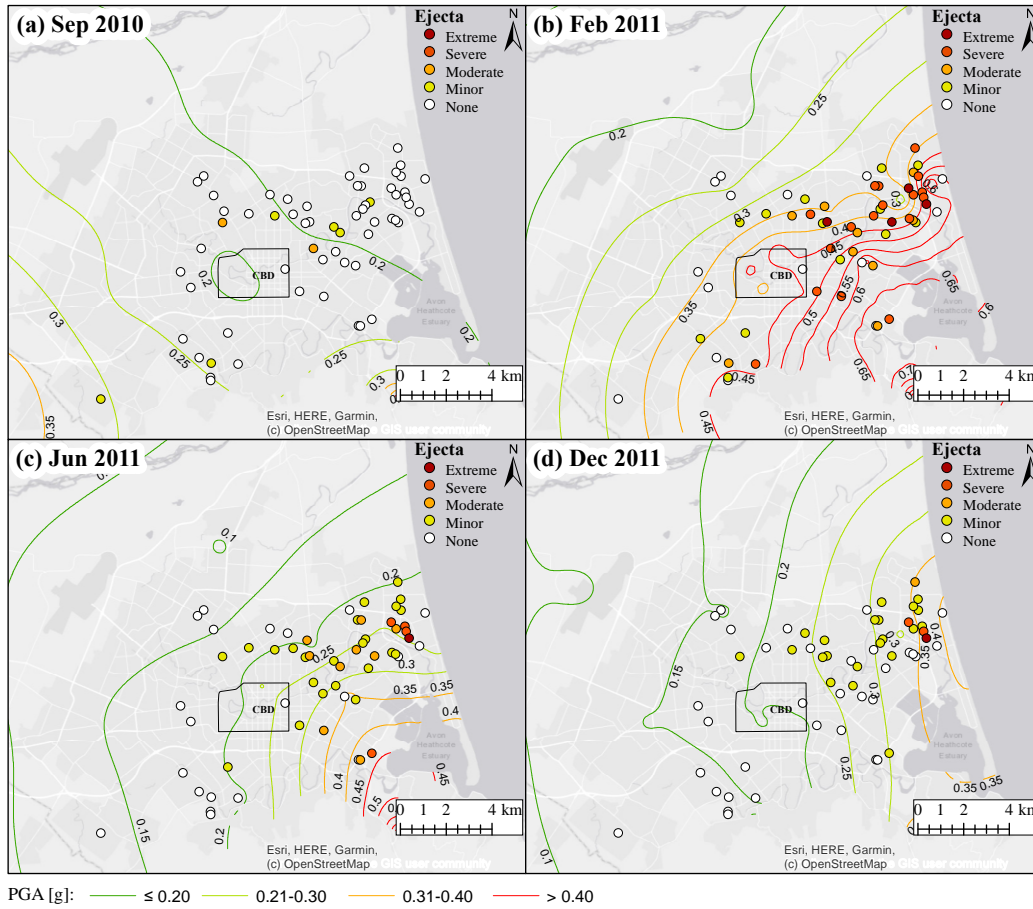


Figure 3.4. Distribution of sites for the (a) Sep 2011, (b) Feb 2011, (c) Jun 2011, and (d) Dec 2011 earthquakes across Christchurch and relative to the Bradley and Hughes (2012) median PGA contours. The ejecta-induced settlement experienced at each site is shown as none (0 mm), minor (1-25 mm), moderate (26-50 mm), severe (51-100 mm), and extreme (> 100 mm).

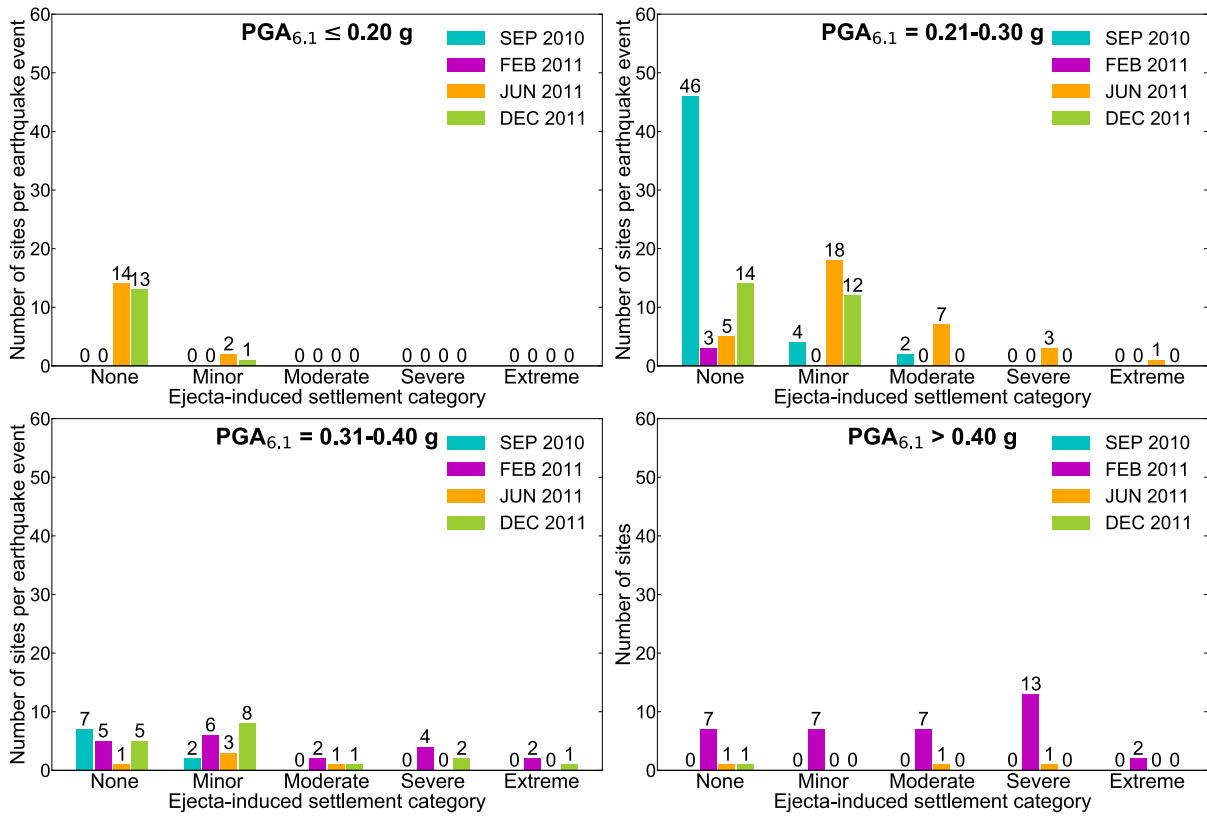


Figure 3.5. The number of sites within each settlement category for each earthquake event and a range of $PGA_{6.1}$.

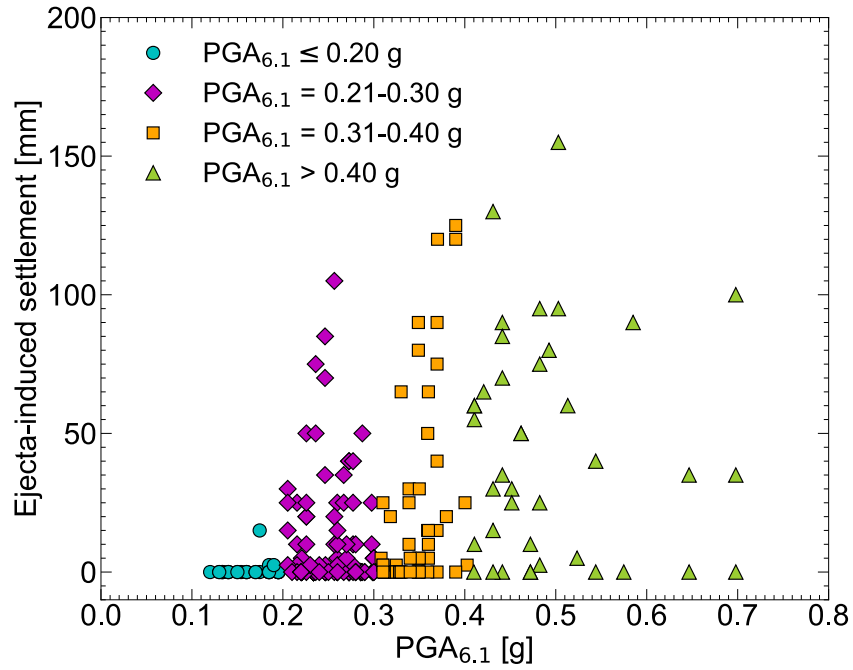


Figure 3.6. The relationship between PGA_{6.1} and liquefaction ejecta-induced settlement for all 235 case histories (Spearman's correlation coefficient = 0.45). Symbols differ for PGA_{6.1} ≤ 0.20, 0.21-0.30, 0.31-0.40, and > 0.40g.

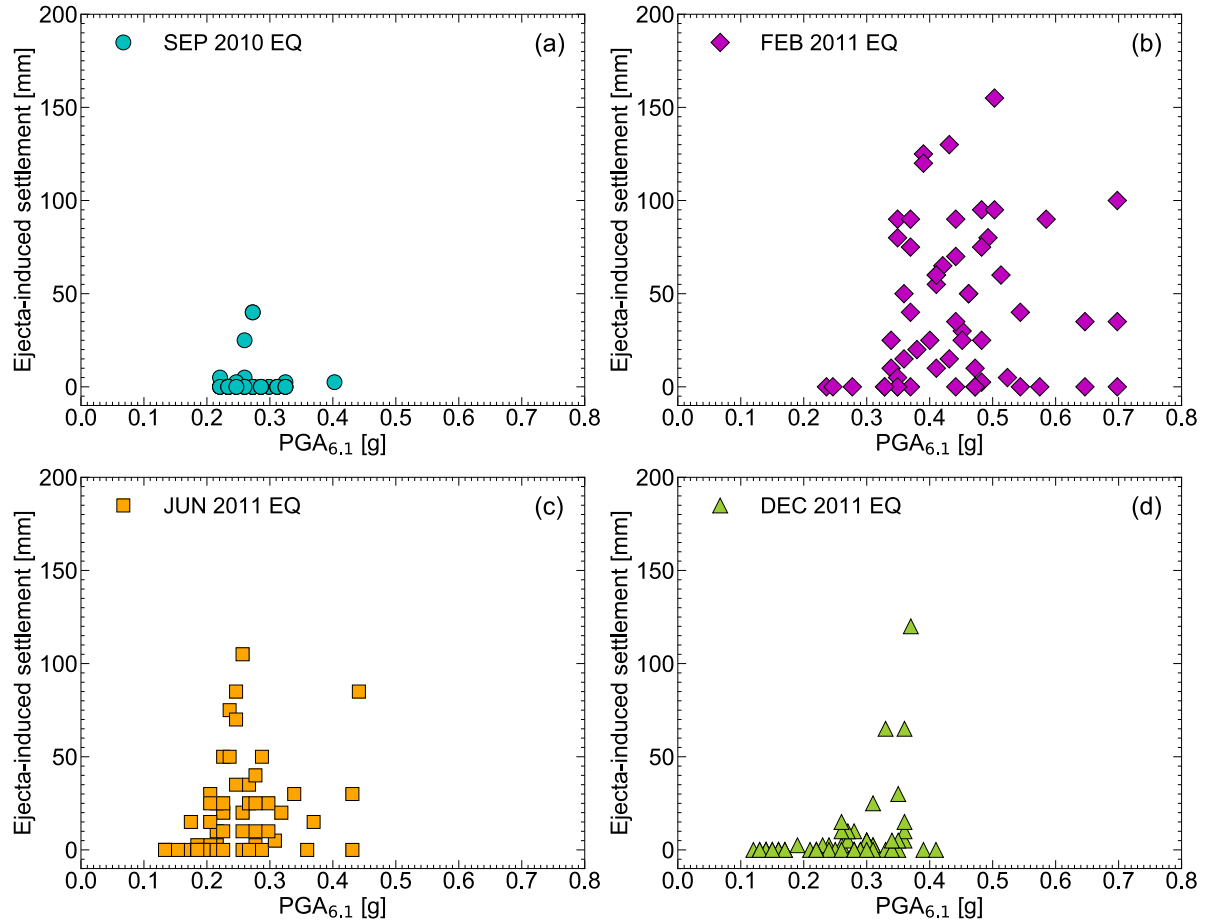


Figure 3.7. Liquefaction ejecta-induced settlement versus $PGA_{6,1}$ for the (a) Sep 2010, (b) Feb 2011, (c) Jun 2011, and (d) Dec 2011 earthquakes. Spearman's correlation coefficients for the Feb 2011, Jun 2011, and Dec 2011 earthquakes are 0.18, 0.47, and 0.50, respectively.

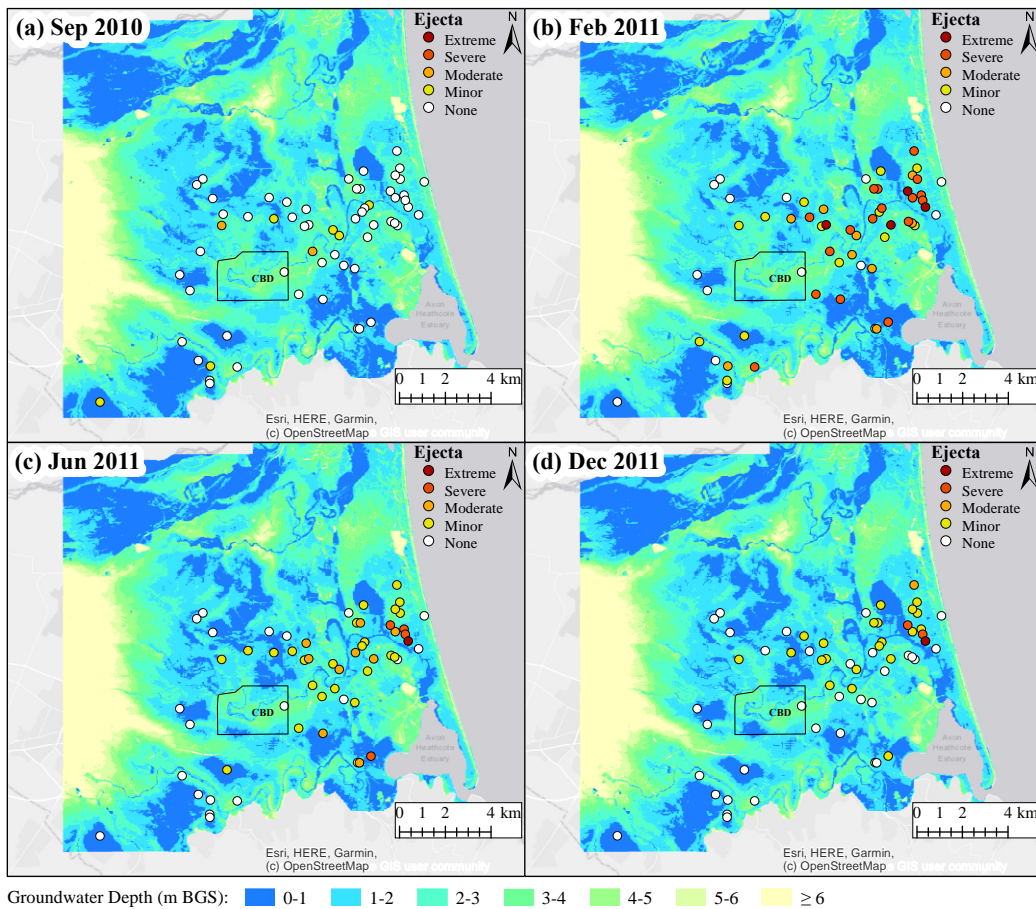


Figure 3.8. Distribution of sites with none (0 mm), minor (1-25 mm), moderate (26-50 mm), severe (51-100 mm), and extreme (>100 mm) ejecta-induced settlement across the regional groundwater depth models for the four main Canterbury earthquakes (T+T 2015).

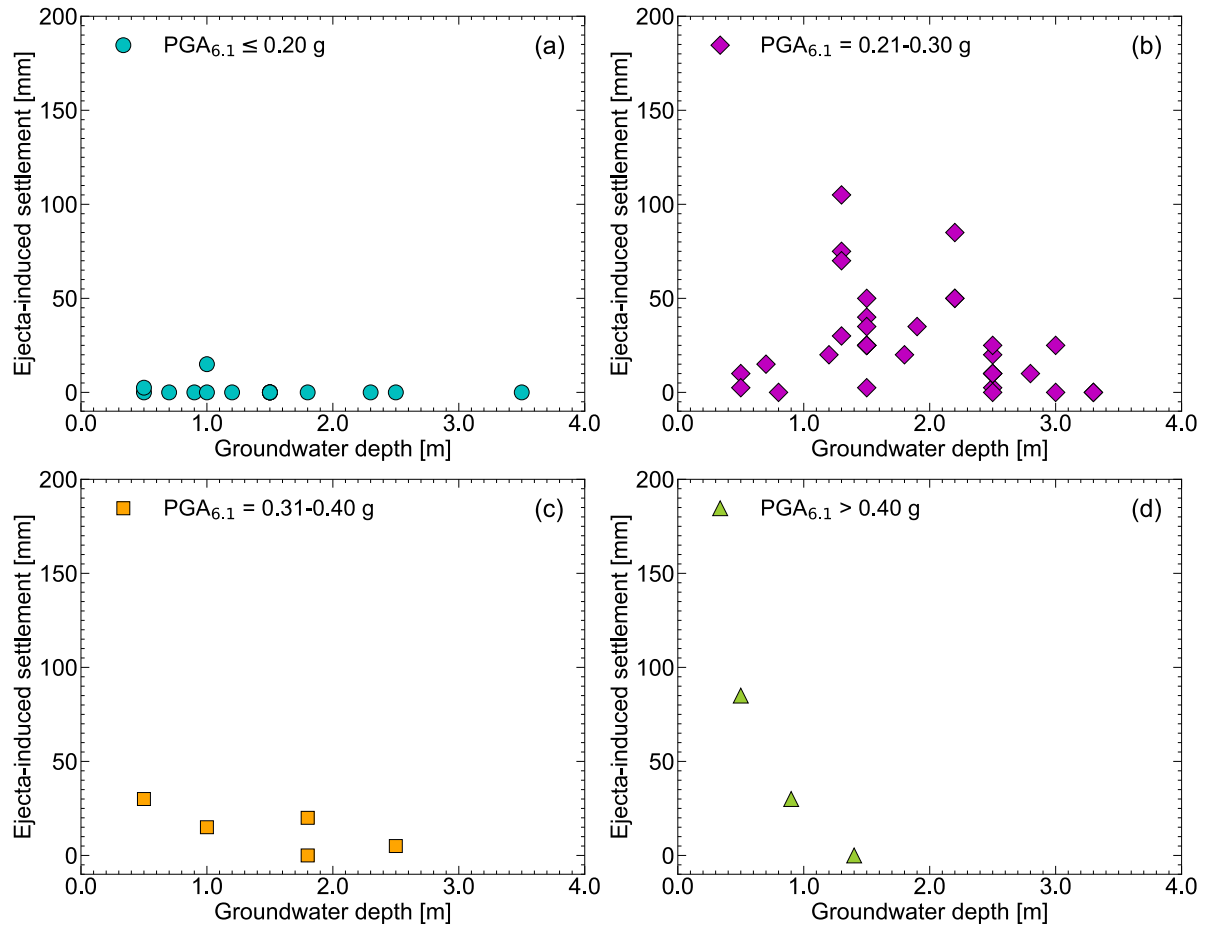


Figure 3.9. Liquefaction ejecta-induced settlement versus groundwater depth for the Jun 2011 earthquake for different $PGA_{6.1}$ ranges: (a) ≤ 0.20 , (b) 0.21-0.30, (c) 0.31-0.40, and (d) > 0.40 g. Spearman's correlation coefficients when $PGA_{6.1} = 0.21-0.30$, 0.31-0.40, and > 0.40 g are -0.32, -0.67, and -1.00, respectively.

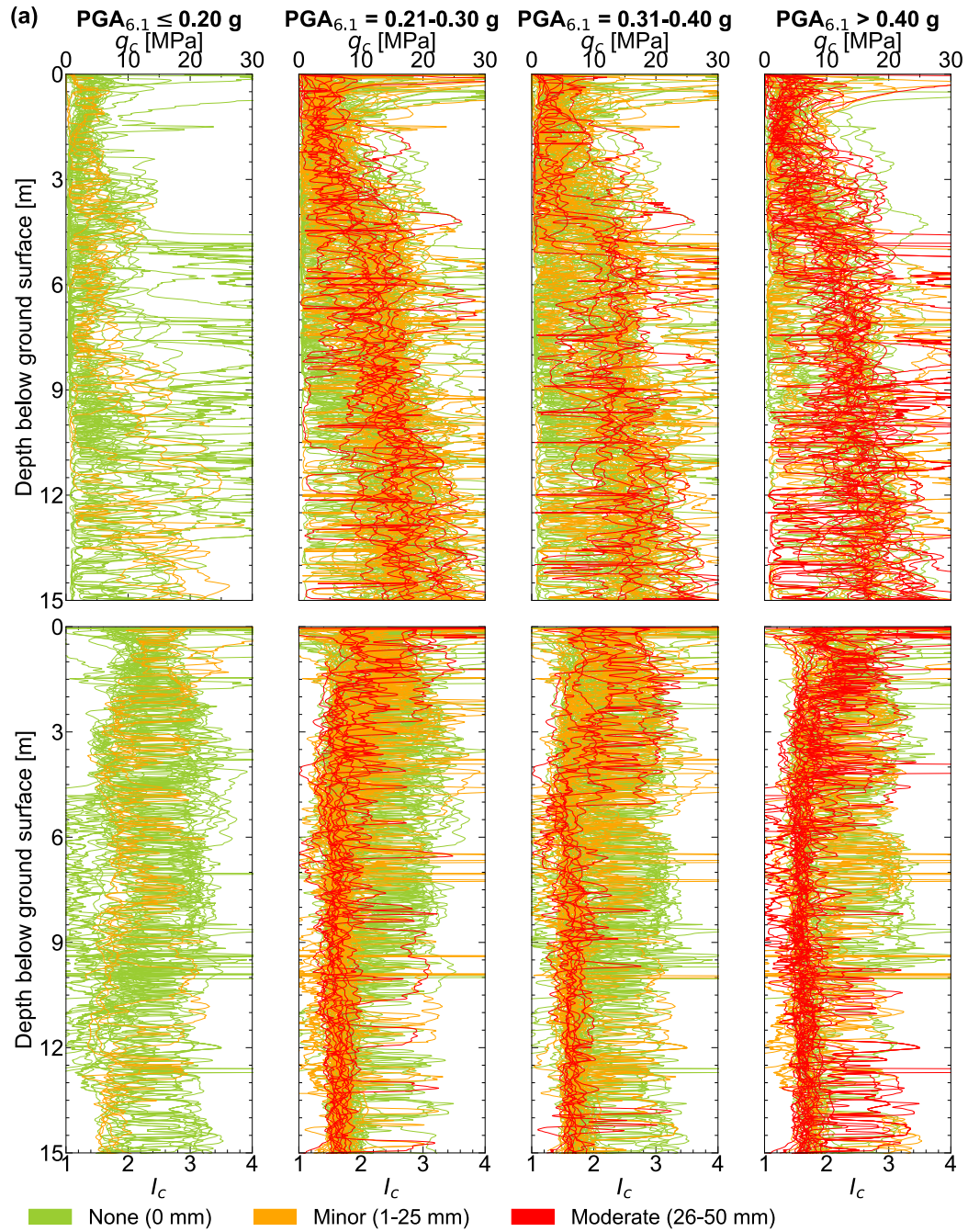


Figure 3.10. (a) CPT tip resistance, q_c , and soil behavior type index, I_c , for case histories with zero, minor (1-25 mm), and moderate (26-50 mm) liquefaction ejecta-induced settlement for $PGA_{6.1} \leq 0.20$, 0.21-0.30, 0.31-0.40, and > 0.40 g.

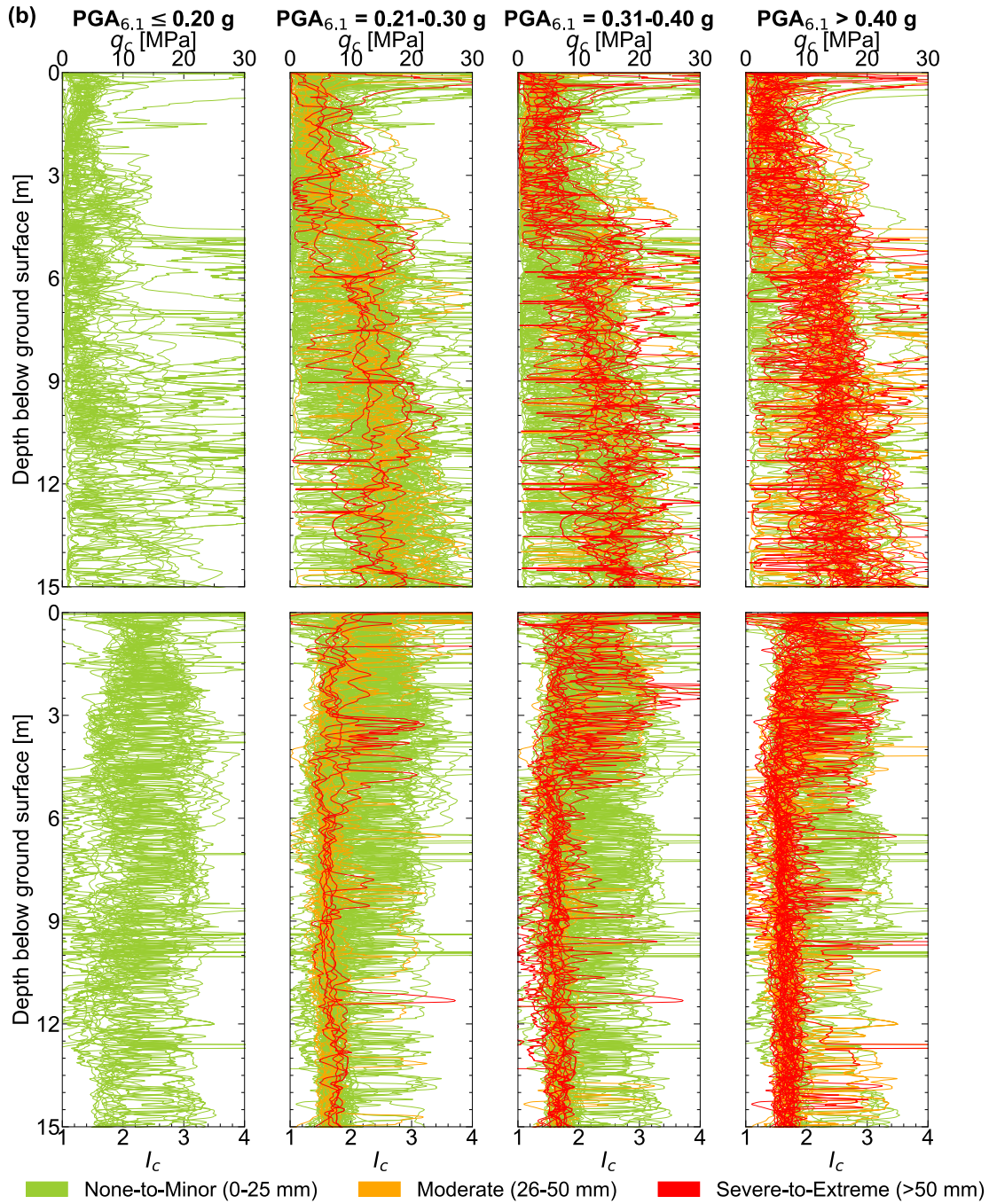


Figure 3.10. (b) CPT tip resistance, q_c , and soil behavior type index, I_c , for case histories with none-to-minor (0-25 mm), moderate (26-50 mm), and severe-to-extreme (> 50 mm) liquefaction ejecta-induced settlement for $PGA_{6.1} \leq 0.20$, 0.21-0.30, 0.31-0.40, and > 0.40 g.

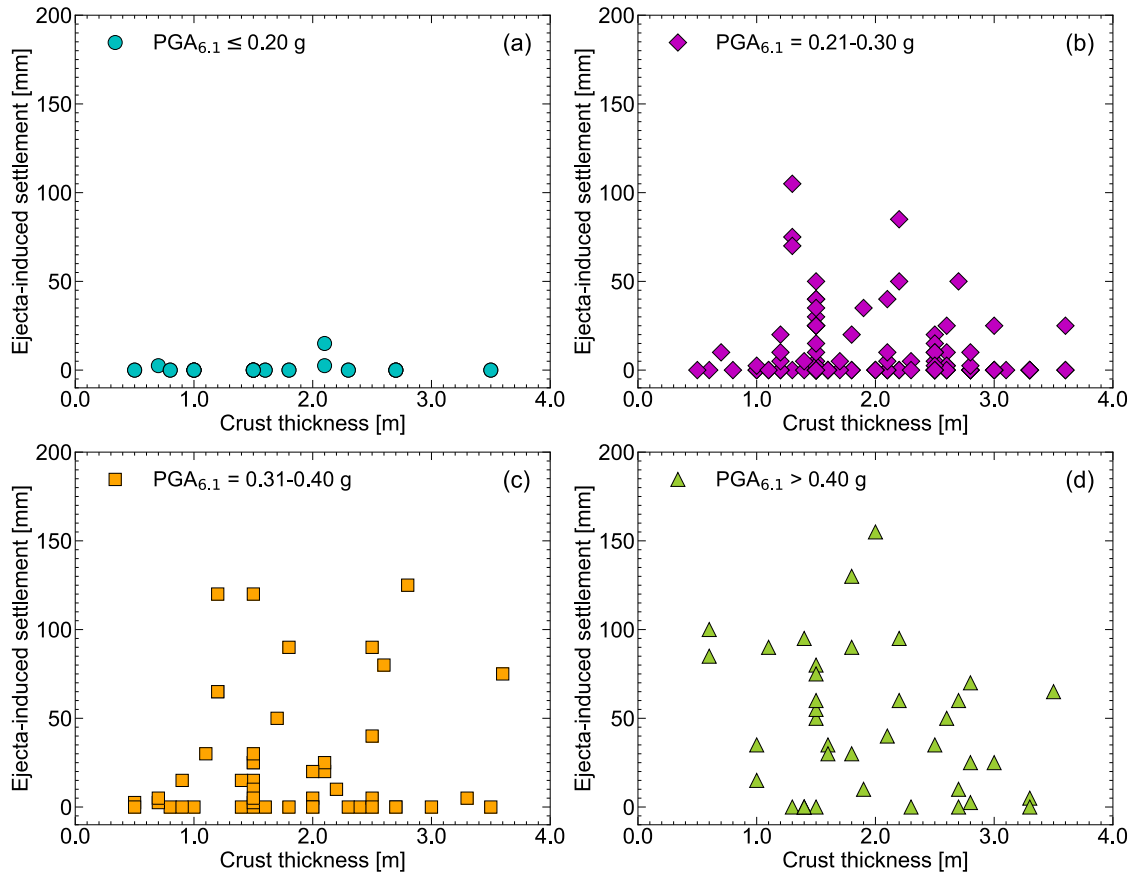


Figure 3.11. The relationship between the ejecta-induced settlement and the I_c -based crust thickness for different $PGA_{6.1}$ ranges: (a) ≤ 0.20 , (b) 0.21-0.30, (c) 0.31-0.40, and (d) > 0.40 g. Spearman's correlation coefficients for $PGA_{6.1} = 0.21-0.30$, 0.31-0.40, and > 0.40 g are -0.17, 0.03, and -0.20, respectively.

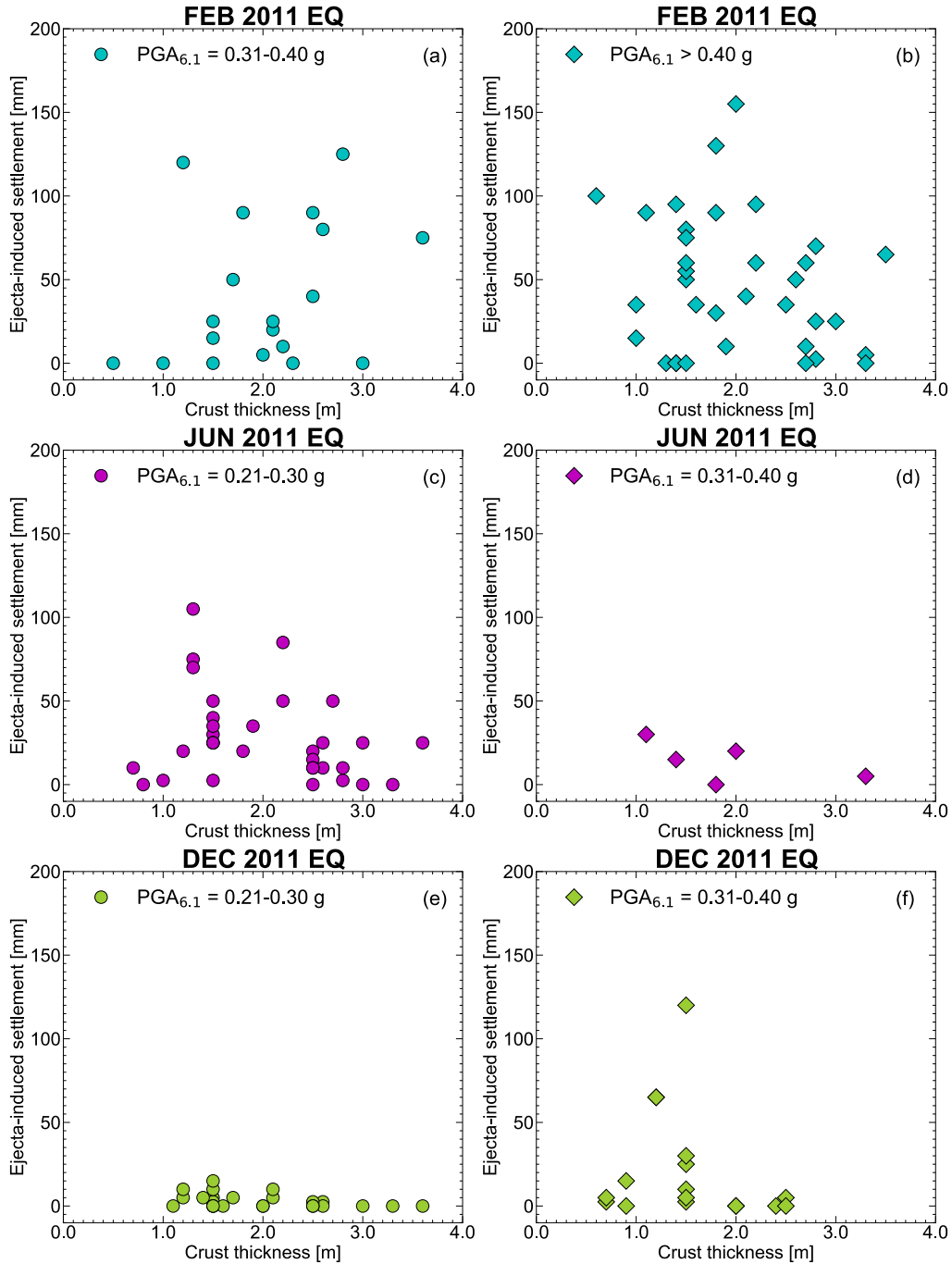


Figure 3.12. The relationship between the ejecta-induced settlement and the I_c -based crust thickness for the (a) Feb 2011 ($PGA_{6.1} = 0.31-0.40$ and > 0.40 g), (b) Jun 2011 ($PGA_{6.1} = 0.21-0.30$ and $0.31-0.40$ g), and (c) Dec 2011 ($PGA_{6.1} = 0.21-0.30$ and $0.31-0.40$ g) earthquakes. Spearman's correlation coefficients are 0.31 and -0.20 for $PGA_{6.1} = 0.31-0.40$ and > 0.40 g, respectively, for the Feb 2011 earthquake, -0.31 and -0.50 for $PGA_{6.1} = 0.21-0.30$ and $0.31-0.40$ g, respectively, for the Jun 2011 earthquake, and -0.42 and -0.35 for $PGA_{6.1} = 0.21-0.30$ and $0.31-0.40$ g, respectively, for the Dec 2011 earthquake.

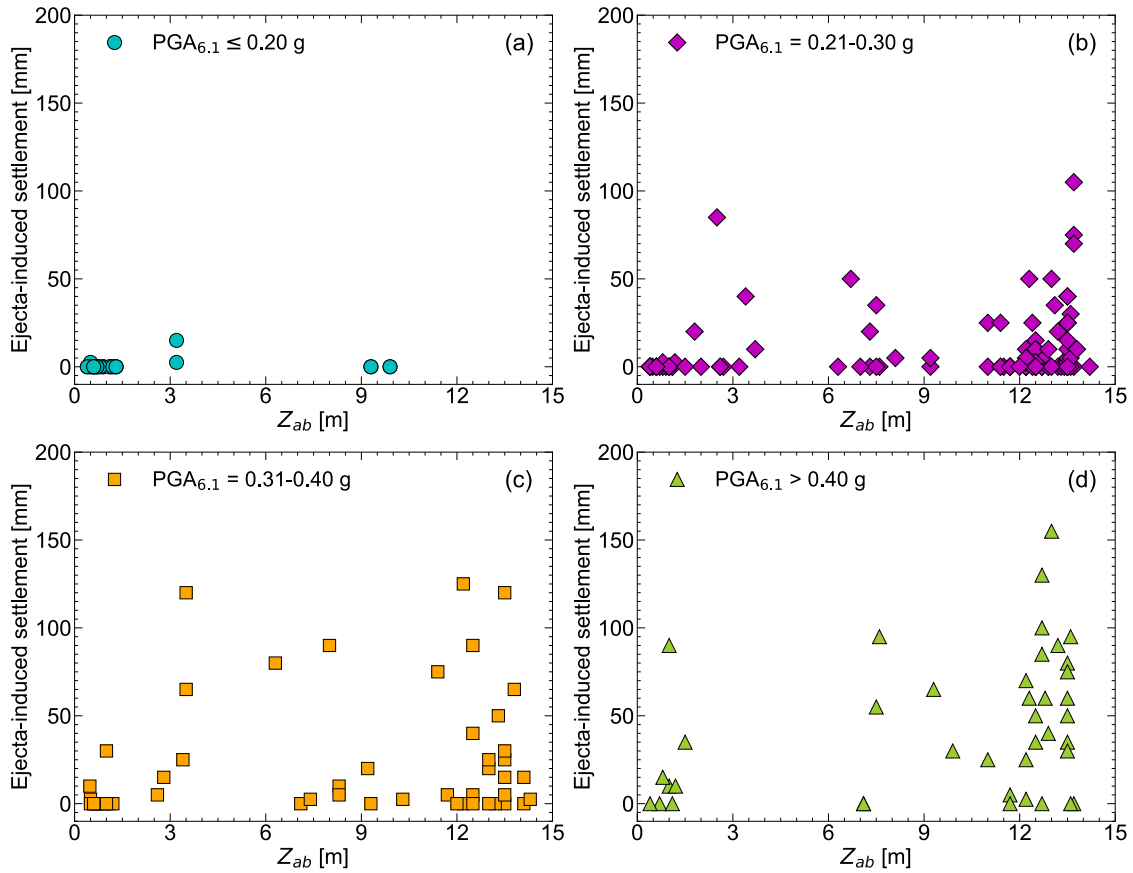


Figure 3.13. The relationship between the ejecta-induced settlement and the first significant liquefiable layer thickness, Z_{ab} , for different $PGA_{6.1}$ ranges: (a) ≤ 0.20 , (b) 0.21-0.30, (c) 0.31-0.40, and (d) > 0.40 g. Spearman's correlation coefficients for $PGA_{6.1} = 0.21-0.30$, 0.31-0.40, and > 0.40 g are 0.37, 0.26, and 0.36, respectively.

FEB 2011 EQ

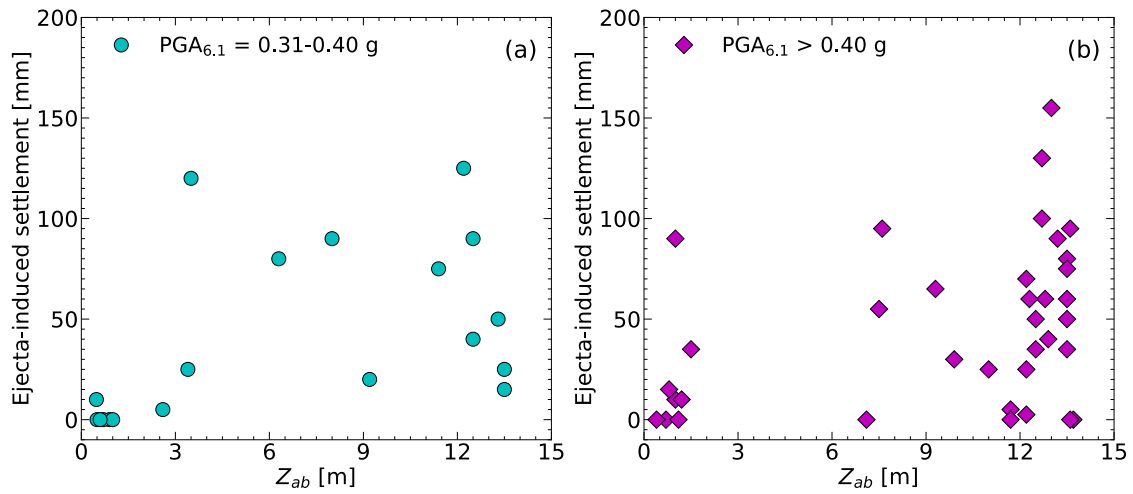


Figure 3.14. The relationship between the ejecta-induced settlement and the first significant liquefiable layer thickness, Z_{ab} , for the Feb 2011 earthquake for (a) $PGA_{6.1} = 0.31-0.40$ g and (b) $PGA_{6.1} > 0.40$ g. Spearman's correlation coefficients for $PGA_{6.1} = 0.31-0.40$ g and $PGA_{6.1} > 0.40$ g are 0.62 and 0.37, respectively.

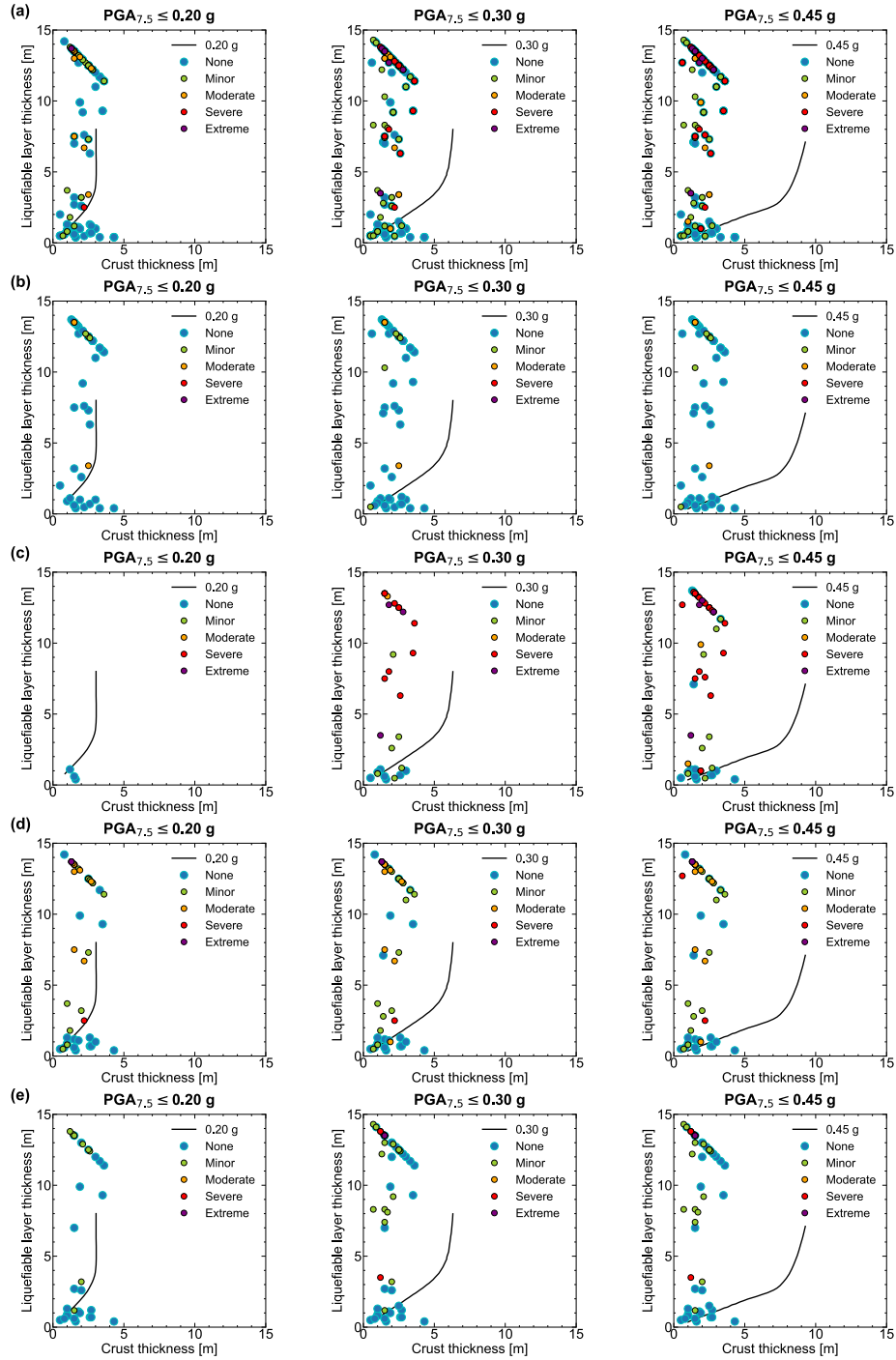


Figure 3.15. Zero, minor (1-25 mm), moderate (26-50 mm), severe (51-100 mm), and extreme (> 100 mm) liquefaction ejecta-induced settlement relative to the Ishihara (1985) boundary curves for (a) all four main Canterbury earthquakes, (b) Sep 2010, (c) Feb 2011, (d) Jun 2011, and (e) Dec 2011 earthquakes. The Ishihara (1985) boundary curves correspond to $PGA_{7.5} = 0.20, 0.30,$ and 0.45 g, while the case histories superimposed on the respective curves correspond to $PGA_{7.5} \leq 0.20, 0.30,$ and 0.45 g.

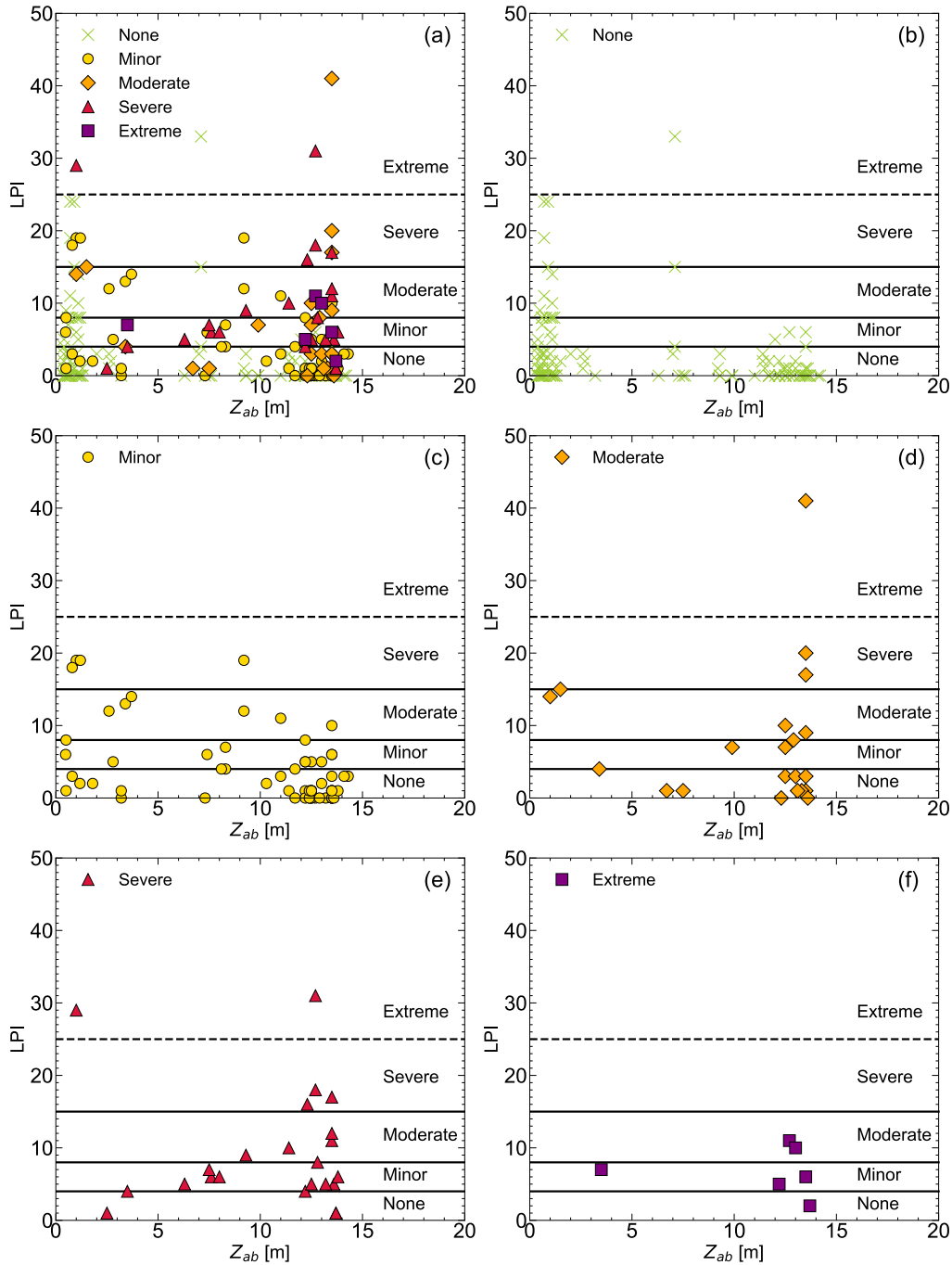


Figure 3.16. Liquefaction potential index, LPI, and thickness of the first liquefiable layer, Z_{ab} , for all case histories relative to the severity of ejecta-induced settlement shown for (a) all ejecta-induced settlement categories, (b) none, (c) minor, (d) moderate, (e) severe, and (f) extreme ejecta-induced settlement categories represented by different symbols.

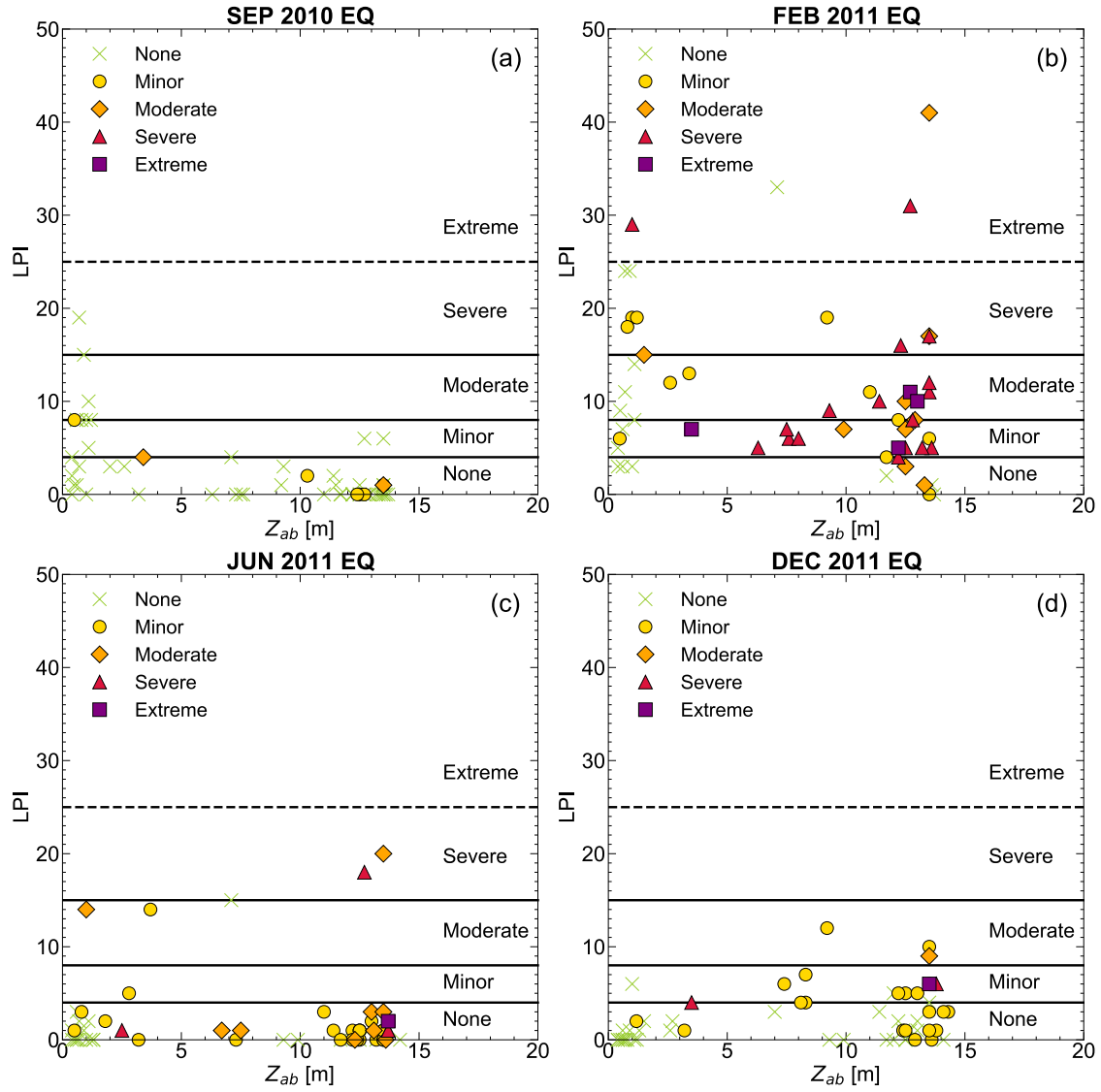


Figure 3.17. Liquefaction potential index, LPI, and thickness of the first liquefiable layer, Z_{ab} , for the (a) Sep 2010, (b) Feb 2011, (c) Jun 2011, and (d) Dec 2011 earthquakes relative to the ejecta-induced settlement categories represented by different symbols.

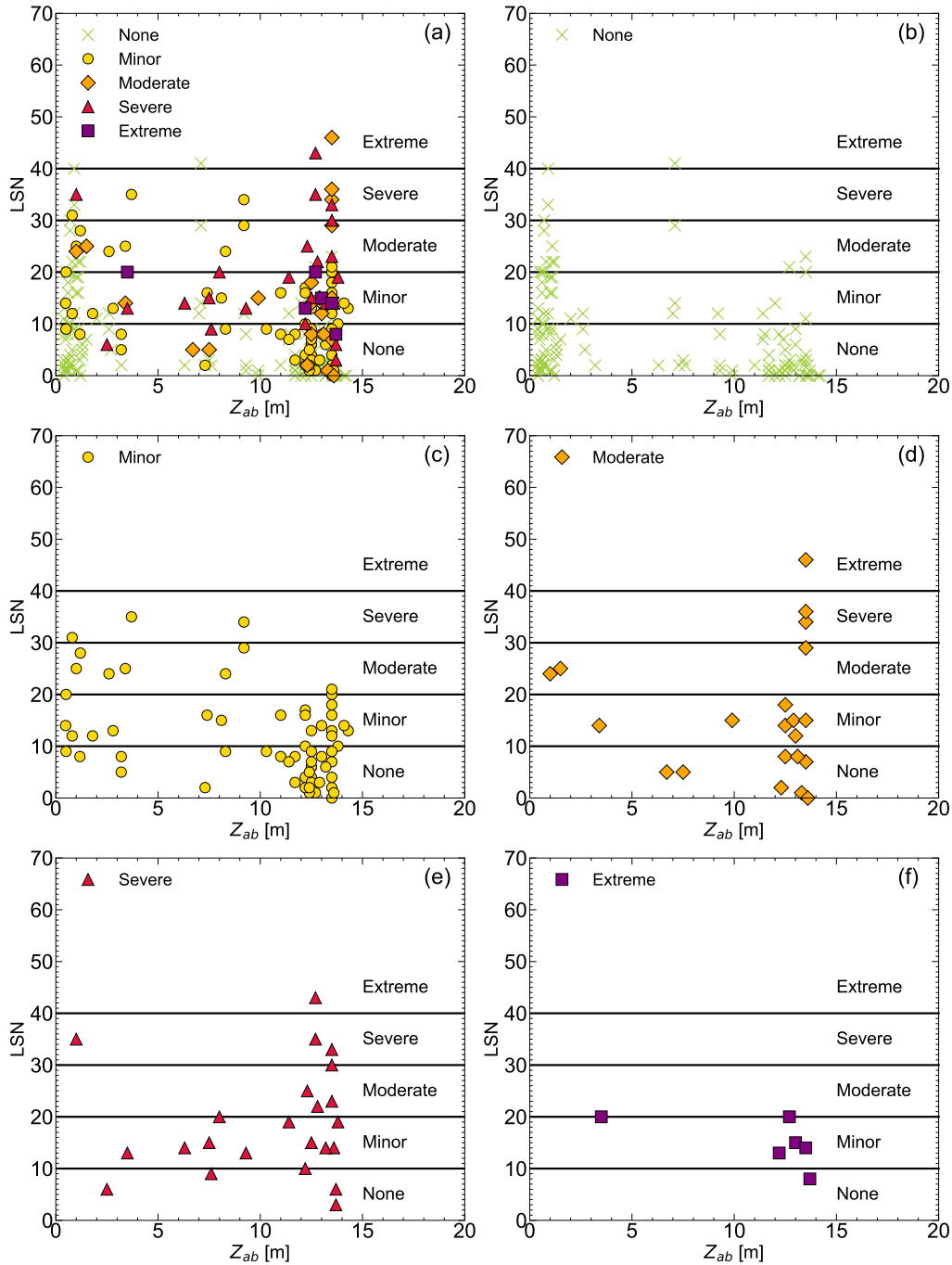


Figure 3.18. Liquefaction severity number, LSN, and thickness of the first liquefiable layer, Z_{ab} , for all case histories relative to the severity of ejecta-induced settlement shown for (a) all ejecta-induced settlement categories, (b) none, (c) minor, (d) moderate, (e) severe, and (f) extreme ejecta-induced settlement categories represented by different symbols.

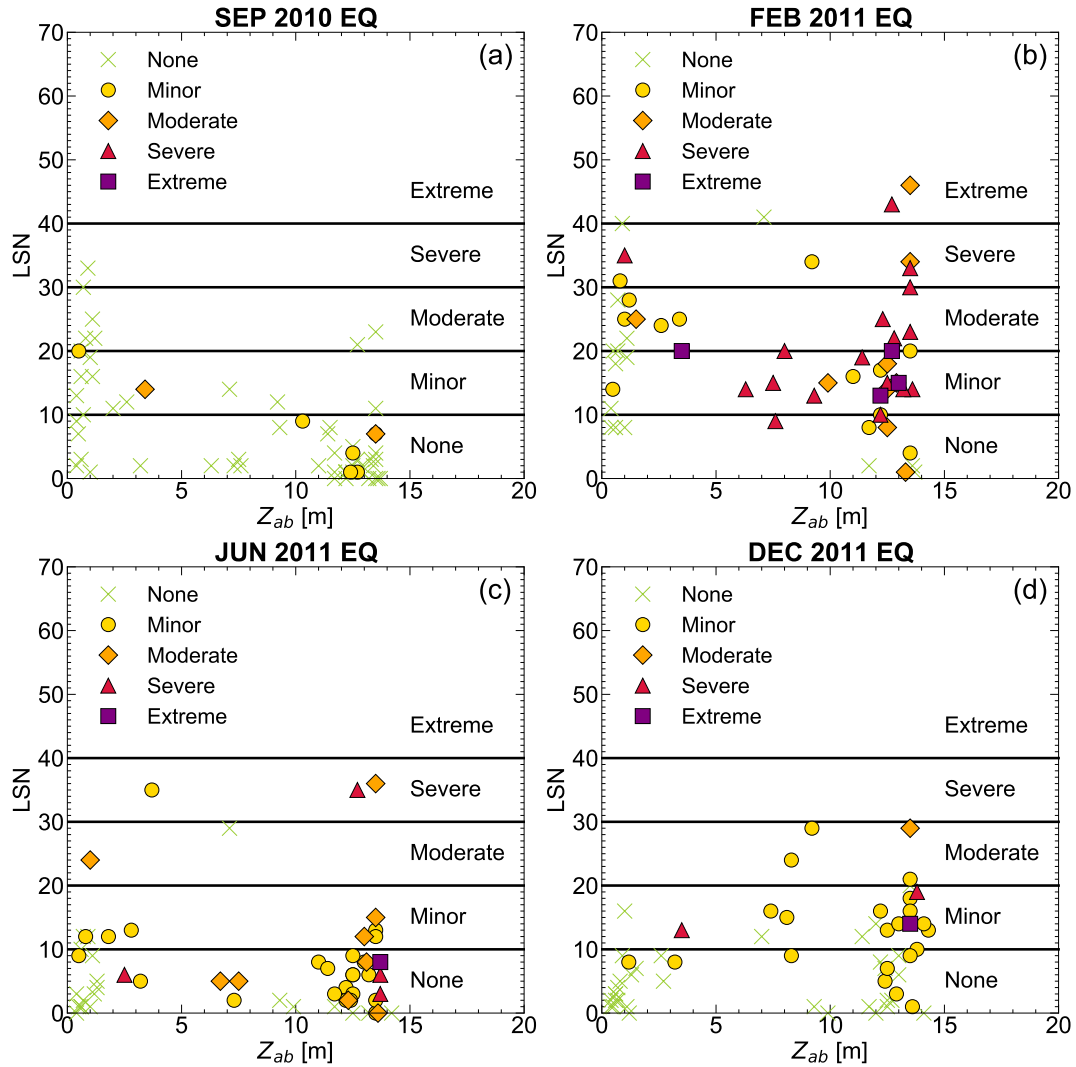


Figure 3.19. Liquefaction severity number, LSN, and thickness of the first liquefiable layer, Z_{ab} , for the (a) Sep 2010, (b) Feb 2011, (c) Jun 2011, and (d) Dec 2011 earthquakes relative to the ejecta-induced settlement categories represented by different symbols.

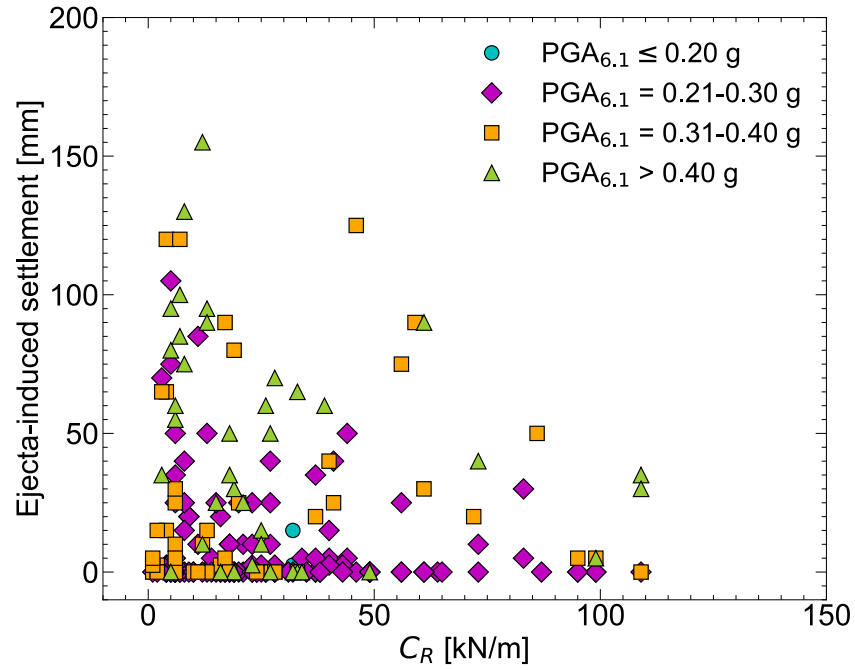


Figure 3.20. Ejecta-induced settlement versus crust resistance, C_R , for all 235 case histories grouped based on their $PGA_{6.1}$. Spearman's correlation coefficient for $PGA_{6.1} = 0.21-0.30$, $0.31-0.40$, and > 0.40 g are -0.13 , 0.10 , and -0.36 , respectively.

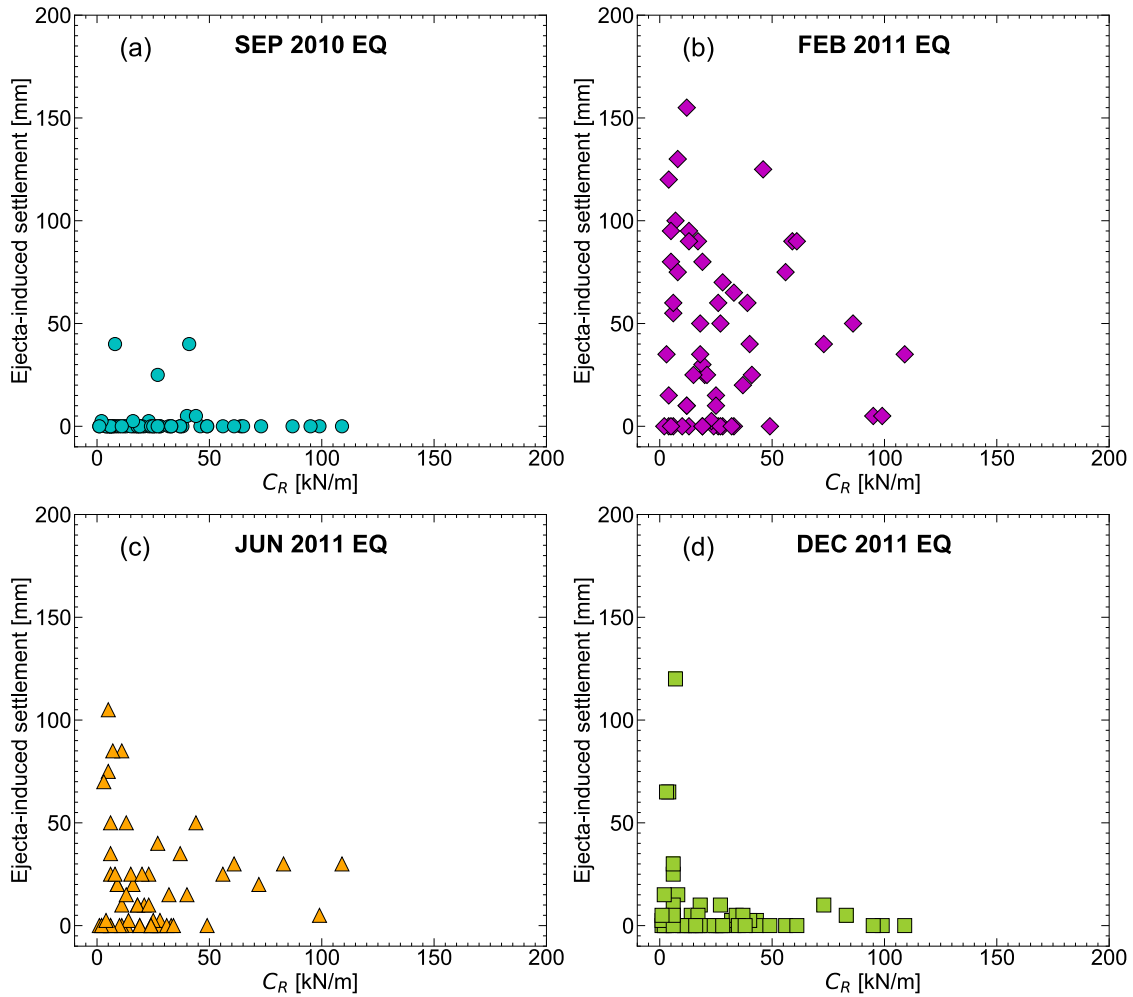


Figure 3.21. The relationship between the ejecta-induced settlement and crust resistance, C_R , for the (a) Sep 2010, (b) Feb 2011, (c) Jun 2011, and (d) Dec 2011 earthquakes.

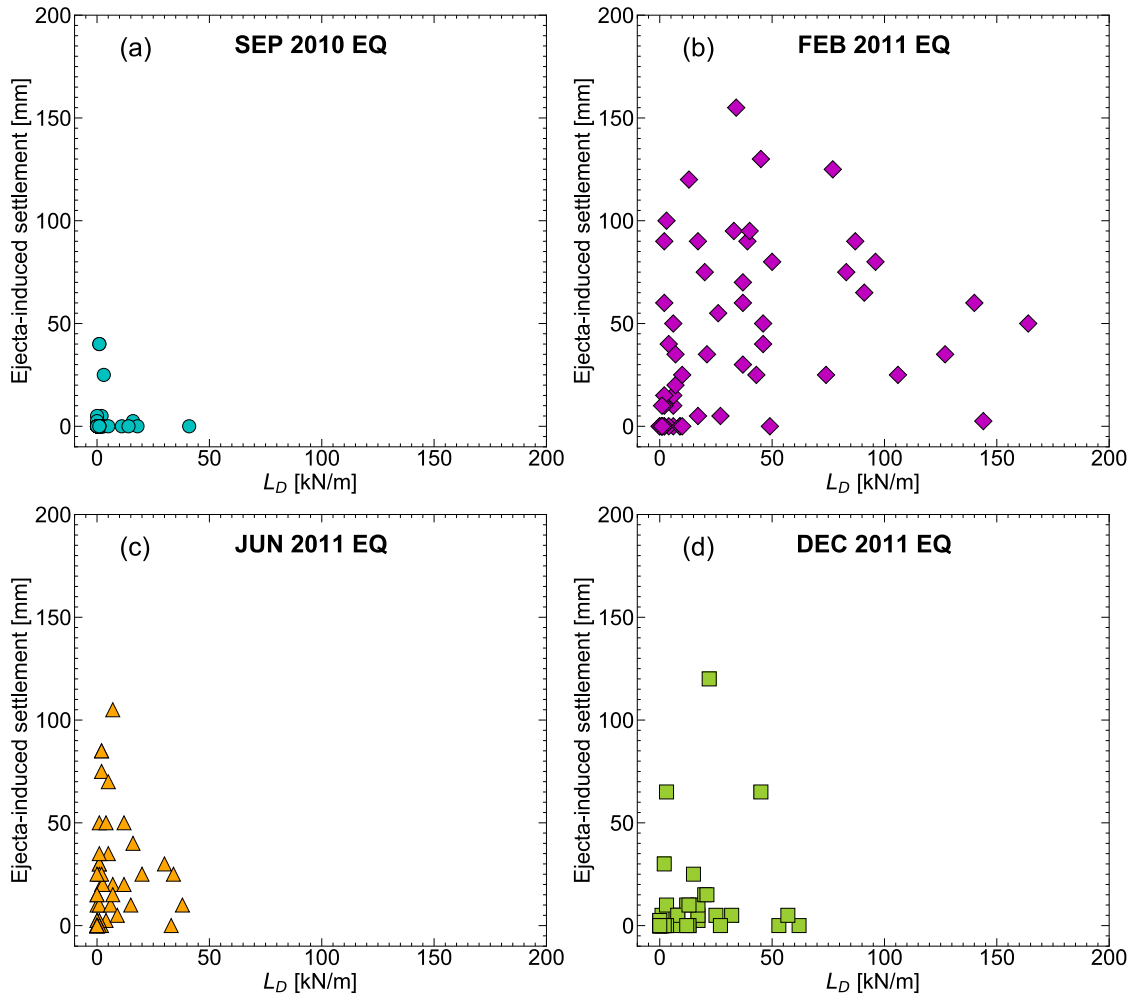


Figure 3.22. The correlation between the ejecta-induced settlement and liquefaction ejecta demand, L_D , for the (a) Sep 2010, (b) Feb 2011, (c) Jun 2011, and (d) Dec 2011 earthquakes. Spearman's correlation coefficients are 0.52, 0.60, and 0.55 for the Feb 2011, Jun 2011, and Dec 2011 earthquakes, respectively.

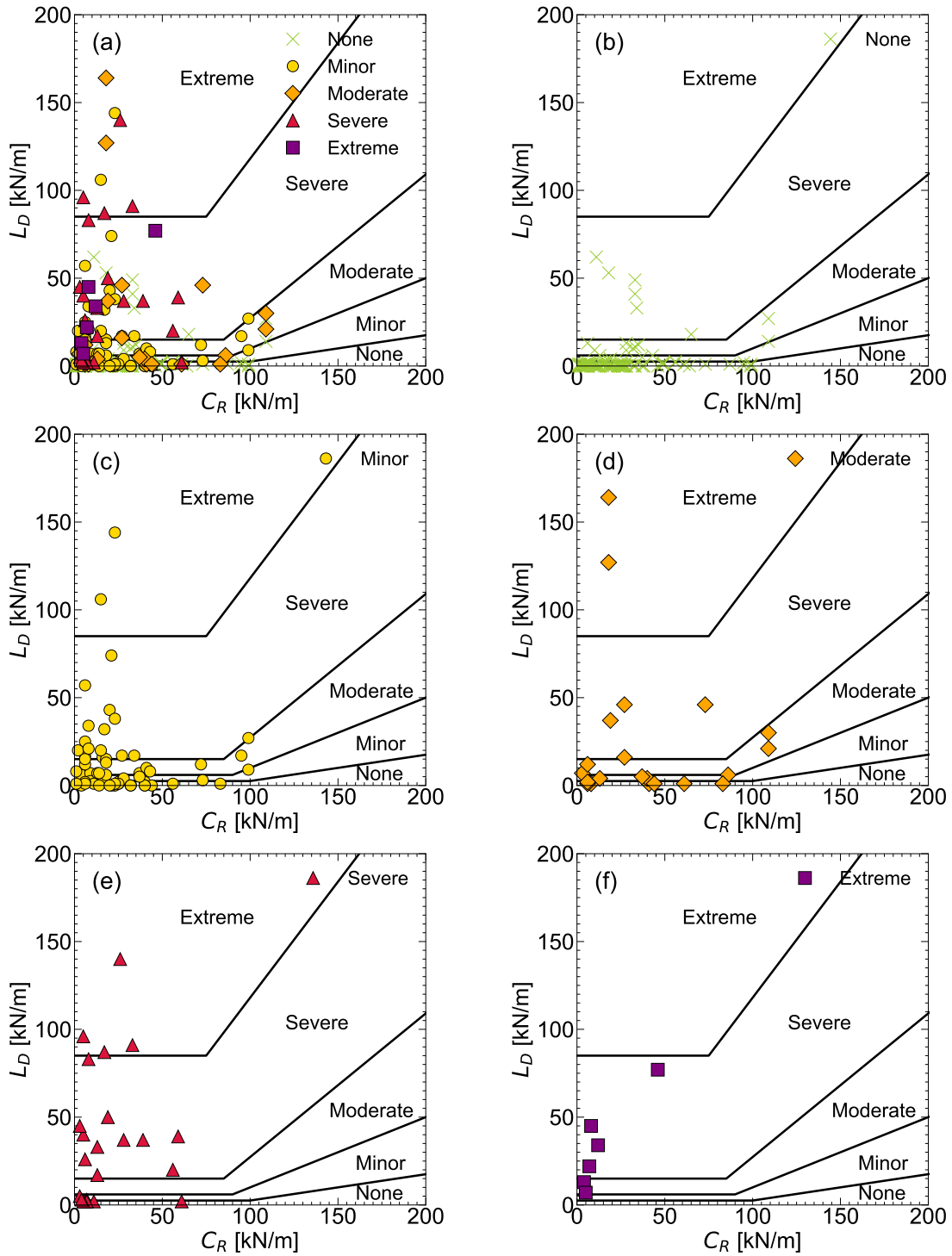


Figure 3.23. Liquefaction ejecta demand, L_D , and crust resistance, C_R , for all case histories relative to the severity of ejecta-induced settlement, shown for (a) all ejecta-induced settlement categories, (b) none, (c) minor, (d) moderate, (e) severe, and (f) extreme ejecta-induced settlement categories represented by different symbols.

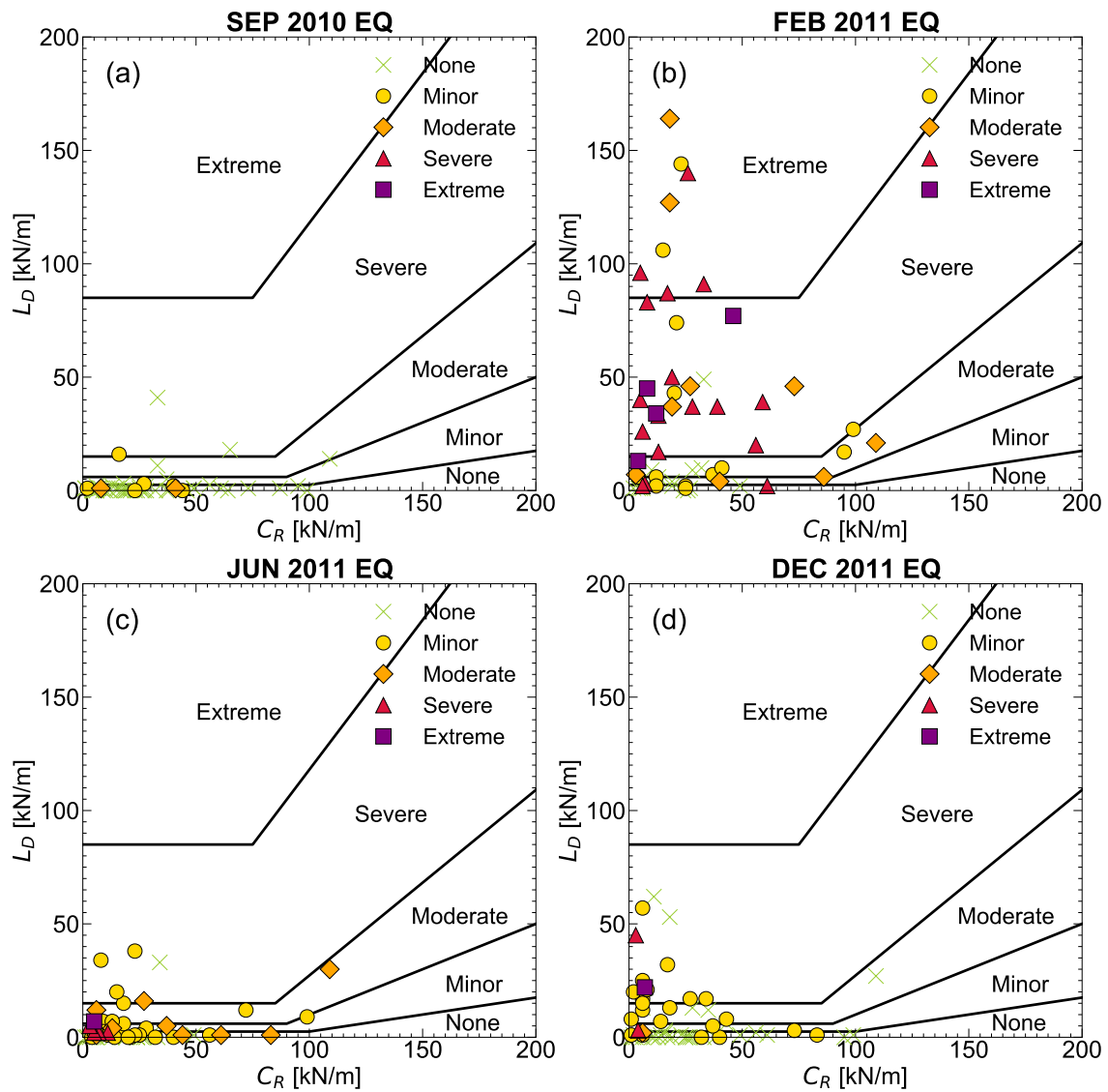


Figure 3.24. Liquefaction ejecta demand, L_D , and crust resistance, C_R , for the (a) Sep 2010, (b) Feb 2011, (c) Jun 2011, and (d) Dec 2011 earthquakes relative to the ejecta-induced settlement categories represented by different symbols.

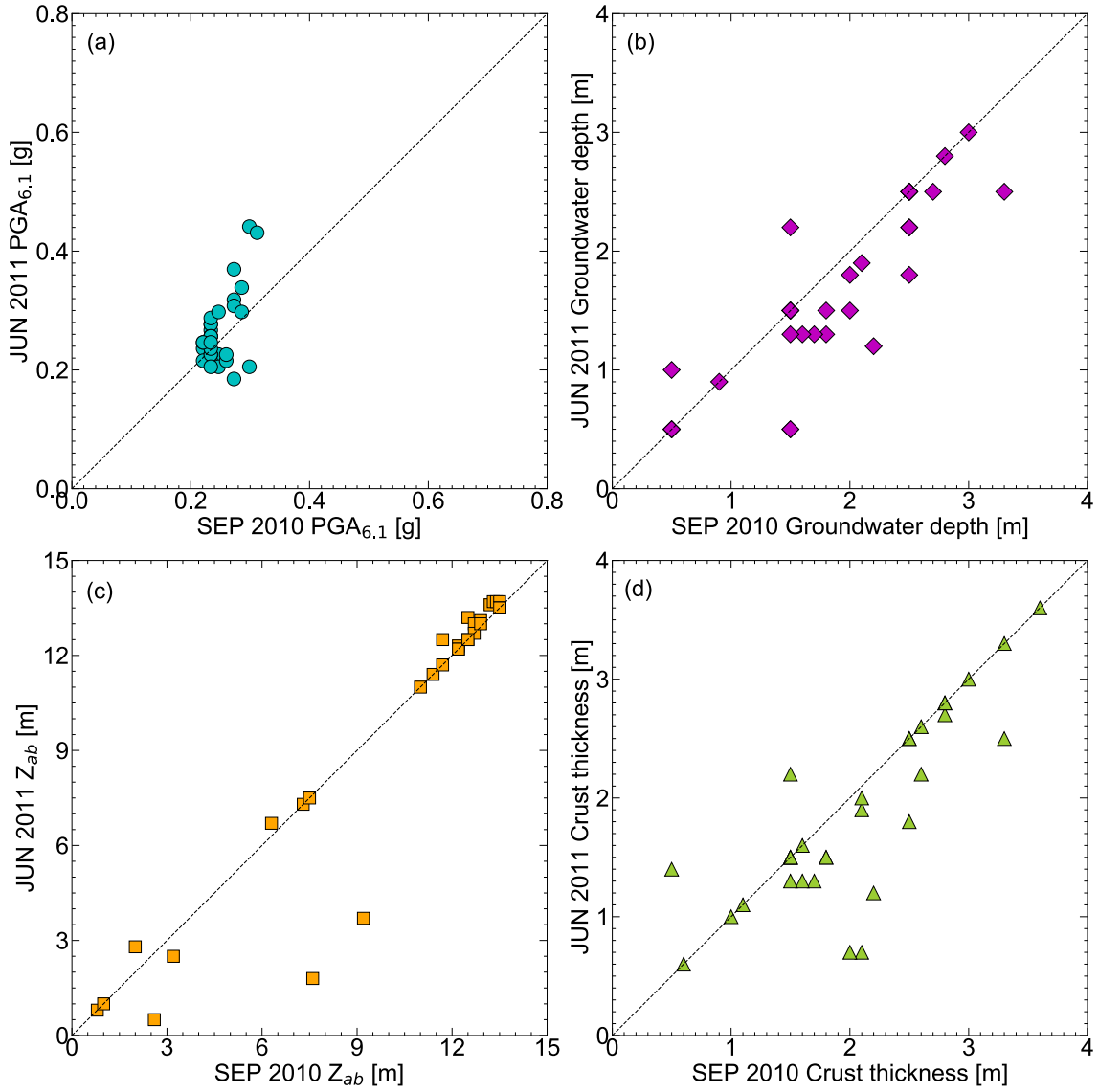


Figure 3.25. Comparison of (a) $PGA_{6.1}$, (b) groundwater depth, (c) first liquefiable soil layer thickness, and (d) crust thickness between the Sep 2010 and Jun 2011 earthquakes at sites that did not have ejecta for the Sep 2010 earthquake but had it for the Jun 2011 earthquake.

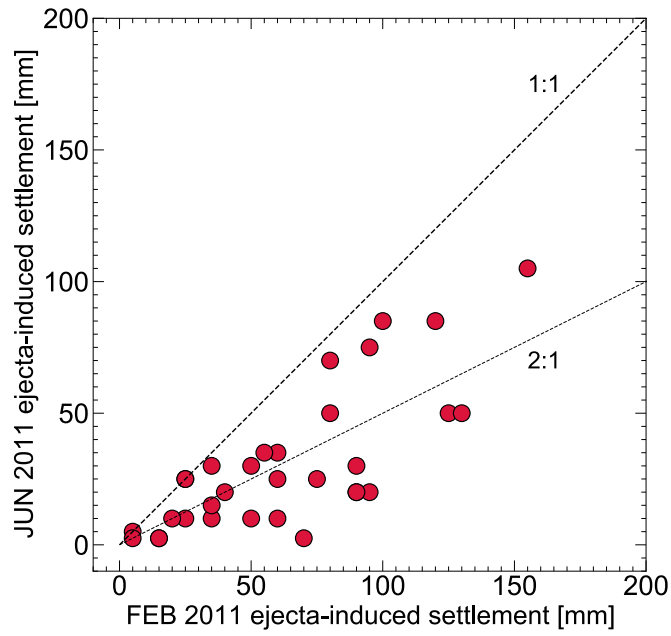


Figure 3.26. The relationship between the ejecta-induced settlement for the Feb 2011 earthquake and the ejecta-induced settlement for the Jun 2011 earthquake. Spearman's correlation coefficient is 0.73.

4 TEST METHOD FOR MINIMUM AND MAXIMUM DENSITIES OF SMALL QUANTITIES OF SOIL

The contents of this chapter are primarily from a journal article published in the Soils and Foundations journal by Mijic, Z., Bray, J. D., Riemer, M. F., Cubrinovski, M., and Rees, S. D., entitled “Test Method for Minimum and Maximum Densities of Small Quantities of Soil.”

4.1 INTRODUCTION

The simple shear test device is useful for evaluating the liquefaction response of retrieved specimens of native soil. In the interpretation of the cyclic simple shear (CSS) and monotonic simple shear (MSS) test results, the minimum and maximum void ratios (e_{\min} and e_{\max} , respectively) are required to establish the relative density of a test specimen. However, conventional-size simple shear test specimens are small and do not have enough material to use the mold specified in the Japanese Standard JIS A 1224:2009 Test Method for Minimum and Maximum Densities of Sands. Unlike reconstituted test specimens prepared from a large batch of soil, only the soil tested in the simple shear device should be used to determine index properties when testing naturally variable soils. Hence, the objective of this study is to develop an alternative test method for evaluating the minimum and maximum densities of soil, which will expand the applicability of the approach adopted in the Japanese Standard method to undisturbed test specimens with small quantities of soil.

4.2 TEST MATERIALS AND METHOD

4.2.1 Test Materials

Soil in this study was retrieved using a hydraulic fixed-piston thin-walled Dames and Moore sampler (Markham et al. 2016) at four sites in Christchurch, New Zealand: Gainsborough Reserve (Site 2), Barrington Park (Site 14), 85 Riccarton Road (Site 23), and 200 Cashmere Road (Site 33). They are highly stratified silty soil sites where liquefaction was not observed at the ground surface during the 2010-2011 Canterbury earthquake sequence. To study the liquefaction potential of the soil from these sites, 42 test specimens, 15-16 mm in height and 61 mm in diameter, were tested at the University of Canterbury (UC) using the 1-D University of California, Berkeley (UCB) simple shear device. The soil samples were then transported to UCB to evaluate index properties such as the fines content (FC), plasticity index (PI), specific gravity (G_s), and minimum and maximum void ratios (e_{\min} and e_{\max}).

The particle size distribution of the tested soil was determined by a combination of wet- and dry-sieving. The gradation curves of 42 soil samples are presented in Figure 4.1. FC (% < 0.075 mm) ranges from 2% to 99% (Table 4.1). All soils are non-plastic (ASTM

D4318). According to the Unified Soil Classification System (USCS), Soil A is poorly graded sand (SP), Soil B, C, D, and E are silty sand (SM), and Soil F (except F-2, which is SM), G, H, I, J, K, L, and M are silt (ML). G_s values (ASTM D854) range from 2.68 for SP to 2.72 for ML with an average of 2.70. Figure 4.1 also shows the gradation curves for eight soil composites obtained by mixing three to four specimens of similar soil from the 42 test specimens.

4.2.2 Development of the Alternative Test Method

Cyclic triaxial (CTX) testing was performed previously on retrieved samples of Christchurch soil. CTX test specimens have enough soil to perform the Japanese Standard JIS A 1224:2009 Test Method so it was used. However, the CSS tests performed on soil specimens in this phase of testing did not have enough soil to fill the JIS A 1224:2009 mold. An alternative test method was required to determine the minimum and maximum densities of a small quantity of soil so the CSS test results could be interpreted and compared with the CTX test results.

In principle, the Japanese Standard method was followed, and alterations were made to the mold size, funnel size, and the distance from which a wooden hammer strikes the sides of the mold to develop an alternative test method to use when only small quantities of soil are available. No changes were made to the number of layers, the manual strike procedure, and the striking tool outlined in the JIS A 1224:2009.

The volume of the Japanese standard-size steel mold is 113 cm³. The total volume of the 61-mm diameter CSS test specimen is only approximately 33 cm³ (based on the smallest mass of solids of 58 g of the 42 soil samples, $G_s = 2.70$, and assuming $e_{\min} = 0.55$). Hence, the amount of soil available is over three times smaller than that required for the JIS A 1224:2009 maximum dry density test method. To develop a test method appropriate for the smaller quantity of soil available, the height and diameter of the standard Japanese mold were scaled down by factors of 1.57 and 1.52, respectively, to manufacture an alternative steel mold. The dimensions of the new steel mold and collar are provided in Figure 4.2. Its volume is 31 cm³. The funnel used for the maximum void ratio test was also downsized from its standard dimensions by a factor of 1.57 (Figure 4.3). It is made of the same material as the funnel used for the Japanese Standard method (i.e., stiff paper reinforced with cellophane tape on the outside). The distance between the initial strike position of a standard 80-g wooden head mallet and the sides of the mold was reduced from 5 cm to 2-3 cm to achieve reliable and consistent results.

Trial tests on Nevada sand were initially performed to assess whether the alternative test method produced results consistent with those using the Japanese Standard JIS A 1224:2009 Test Method for Minimum and Maximum Densities of Sands. The index properties of mined, non-processed Nevada sand vary by batch and within a batch (e.g., Allmond et al. 2015). The minimum and maximum void ratios for a batch available at UCB were evaluated by both the alternative and standard procedures. The difference in the maximum void ratio of Nevada sand between the two methods was negligible (0.8%), while the respective difference for the minimum void ratio was more substantial (7.8%). The test results yielded comparable standard errors for the minimum and maximum void ratios between the two methods (0.003 and 0.004 for the standard and alternative procedures, respectively).

The effect of energy in the alternative procedure was investigated to explore the reasons for the difference in the minimum void ratios between the two methods. The energy was varied by changing the number of layers and blows per layer and the striking tool. The difference between the minimum void ratios of Nevada sand determined by the two methods could be reduced to only 0.8% by applying 1200 blows (six layers and 200 blows/layer) with a plastic handle of a 64-g screwdriver instead of the standard 1000 blows (10 layers and 100 blows/layer) by an 80-g wooden head mallet. However, for 36 of the 42 Christchurch soil samples, a higher maximum dry density value was achieved using the wooden mallet and 1000 blows, and the results were comparable for the remaining six soil samples. Given these results, it was decided to use the wooden mallet and the 1000 blows specified in the Japanese Standard method but with a shorter strike distance to achieve greater consistency between the two methods.

4.2.3 Alternative Test Method

The alternative maximum dry density test consists of 1000 strikes of the smaller mold (Figure 4.2) by a standard 80-g wooden head mallet at a strike distance of 2-3 cm. The total mass of the mallet is 170 g. Its face diameter and head length are 35 mm and 106 mm, respectively, while its wooden handle is 250-mm long. A soil sample is mixed thoroughly before placing each of ten portions of soil in the mold. Five manual strikes are applied at each of five locations along the sides of the mold (the distance between each location corresponds to a central angle of 72°), such that 25 blows overall are applied within 5-6 seconds. The mold is rotated 90° and subjected again to 25 blows. This procedure is repeated two more times resulting in a total of 100 hammer strikes per layer of the soil during a 270° rotation of the mold. The mold is rotated another 90° and the process is repeated for the next layer of soil. This part of the procedure differs slightly from the JIS A 1224:2009, which specifies that the mold is rotated 90° after five strikes. This adjustment did not affect the results and was more efficient and less prone to error, so it was used for both the Japanese Standard method and the alternative method. For the tenth soil layer, the collar is placed on top of the mold; the mold is elevated on a 10-mm thick spacer to accommodate the hammer and is hit 100 times in the manner described previously. The collar is removed, and the excess soil is trimmed with a straight edge tool while firmly holding the mold. The mass of the mold with the soil is then recorded.

The alternative minimum dry density test is performed by placing the smaller funnel (Figure 4.3) on the bottom of the smaller mold, mixing a soil sample meticulously, and filling the funnel slowly with soil using a spoon. Once the funnel is full, it is lifted gradually and continuously while ensuring contact of its tip with the deposited soil beneath it. According to the Japanese Standard method, the funnel should exit the top of the mold in 20-30 seconds; however, this is not possible for soils with higher fines contents which require more time to uniformly deposit through the funnel. The excess soil above the top of the mold is removed carefully. The mold must be held firmly on the table during this process to avoid sudden movements that would densify the soil and lead to an overestimate in the minimum dry density. The mass of the mold and the soil is then recorded.

Once the maximum and minimum void ratios of the 42 individual, small-sized soil samples were determined based on the alternative test method, three to four of these soil samples from the same tube with similar minimum and maximum void ratios were mixed to form a composite soil with three to four times greater volume. Eight composite soil

samples were prepared, which provided enough soil to perform the minimum and maximum dry density testing according to the Japanese Standard JIS A 1224:2009 test method. The minimum and maximum dry densities of the eight soil composites were also evaluated based on the proposed alternative method delineated previously to compare results. Outcomes of the tests are discussed in a subsequent section.

4.2.4 Previous Studies Investigating the Effects of Fines Content

There are challenges to determining the minimum and maximum void ratios of soils with high fines contents. The Japanese Standard method for determining the minimum and maximum void ratios is strictly applicable for sand with up to 5% of fines. However, Cubrinovski and Ishihara (2002) scrutinized the applicability of the Japanese Standard method to obtain the minimum and maximum void ratios of natural soils with the fines content as high as 70%. They found from test results on more than 300 natural soils that the Japanese Standard method produces highly correlated minimum and maximum void ratios for sand with less than about 35% fines. Soil with about 30% fines is at the approximate transition from a sand-dominated particle structure to a fines-controlled particle structure. The minimum void ratio increases slightly as FC increases from 0% to 30%, and it increases more prominently as FC increases above 30% (Cubrinovski and Ishihara 2002). The maximum void ratio increases steadily as the FC increases from 0% to 70% (Cubrinovski and Ishihara 2002). They also recognize that the minimum and maximum void ratios are affected by the particle shape (i.e., these void ratios increase with the increasing particle angularity). Void ratio range ($e_{\max} - e_{\min}$) is an important material parameter because it represents the combined influence of the particle shape and the particle-size composition (Cubrinovski and Ishihara 2002).

Most studies used sand-fines mixtures produced in the laboratory, rather than natural soils, to investigate the influence of the particle-size composition and particle shape on void ratio. Thevanayagam et al. (2002) examined the effect of up to 100% of non-plastic fines on the maximum and minimum void ratios using ASTM D4254 and ASTM D1557, respectively. Yilmaz (2009) evaluated e_{\max} and e_{\min} for 111 soils with FC= 0-100% using ASTM D4254 and ASTM D4253, respectively. Lade et al. (1998) developed a non-standard procedure to determine e_{\max} and e_{\min} of different mixtures of Cambria sand, Nevada sand, and Nevada fines and their relationship with the percentage of fines and the particle shape. In these studies, among others (e.g., Amini and Qi 2000, Salgado et al. 2000, and Murthy et al. 2007), the minimum and maximum void ratios tend to decrease as the content of fines increases from 0% to 20-40% due to the filling of voids in the coarser-grain matrix by fines. As FC changes from 40% to 100%, coarser particles are pushed apart by finer particles such that coarse grains float within the fines, resulting in the increase of the minimum and maximum void ratios. The 20-40% FC is a transition zone between the sand-dominated soil structure and the fines-dominated soil structure. However, it is important to recognize that laboratory-based sand-fines composites may not be representative of the actual packing structure of natural sands with fines due to the presence of wide gaps in grading (Cubrinovski and Ishihara 2002). Regardless, these studies support attempts to determine the minimum and maximum dry densities of high FC non-plastic soil to enable researchers to estimate their relative density for interpreting test results.

4.3 TEST RESULTS AND DISCUSSION

The minimum and maximum void ratios and the void ratio range for 42 Christchurch soil samples are summarized in Table 4.1. The same soil sample used in the CSS and MSS testing was used for the minimum and maximum dry density tests. The consistent CSS and MSS test results, the small dispersion of the results of the repetitive minimum and maximum dry density tests, and the inspection of the soil throughout the test program indicated there was no evidence of significant particle breakage. The e_{\min} values range from 0.564 (Soil I-1) to 0.991 (Soil J-2) while the e_{\max} values range from 1.11 (Soil A-1) to 2.43 (Soil J-2). Void ratio values increase as the FC of these soils increase. Similar e_{\min} and e_{\max} values for silty soils are observed by Cubrinovski and Ishihara (2002). The void ratio is affected by particle shape in addition to FC (e.g., Lade et al. 1998, and Cubrinovski and Ishihara 2002). The Christchurch soils have sub-angular to angular particles, and as such tend to have higher e_{\max} and e_{\min} values than soil with rounded to sub-rounded spherical particles. Moreover, the void ratio range, as a parameter that embodies the combined effects of the particle-size composition and the particle shape, encompasses values from 0.408 (Soil A-1) to 1.44 (Soil J-2).

The effect of fines content on the minimum and maximum void ratios for 42 soil samples is illustrated in Figure 4.4. The maximum void ratio tends to increase as the FC increases, with a higher rate of increase beyond 30% fines. The variability in the maximum void ratio from one soil sample to another appears to be higher for soil samples with nearly 100% fines. Conversely, the minimum void ratio decreases as FC increases from 0% to about 40%. As the FC changes from approximately 40% to 100%, there is a slight increase in the minimum void ratio. Thus, a FC of about 30-40% can be considered a transition point between the sand-dominated particle structure and the fines-dominated particle structure for the tested soils. As FC increases, larger-size particles are pushed apart and gradually replaced by smaller-size particles. As FC exceeds 30-40%, coarse particles begin to float within the soil matrix dominated by fines. This is in agreement with the previous studies (e.g., Lade et al. 1998, Cubrinovski and Ishihara 2002, and Thevanayagam et al. 2002) wherein the 20-40% fines content is observed as a transition zone between the filling-of-voids process and the replacement-of-solids process.

Figure 4.5 shows the influence of the fines content on the void ratio range for 42 soil samples. The void ratio range, a parameter indicative of the compressibility and contractiveness of cohesionless soils, increases continuously as FC increases from 0% to 100%. Scatter in the data tends to increase with increasing FC and becomes more prominent for soil samples with FC > 70% fines.

Table 4.2 summarizes eight soil composites and the individual soil samples that form these composites, as well as the e_{\min} and e_{\max} values of the composites determined in accordance with the proposed alternative test method and the Japanese Standard JIS A 1224:2009 test method. The void ratios of the composite soil samples are also compared with the minimum and maximum void ratios of the individual soil samples determined in accordance with the alternative procedure. The e_{\min} values for the soil composites fall within the range of the values for the individual soil samples (Figure 4.4). The exceptions are the minimum void ratios for soil composites I and M, which are slightly higher than those determined for the individual soil samples. The standard procedure tends to result in the composite e_{\min} values that are lower than the e_{\min} values for the individual soil samples.

Soil composites I and M deviate again from this trend by having somewhat greater minimum void ratios than the individual soil samples. There is good agreement between the values for the composites and the individual soil samples for the e_{\max} values determined in accordance with the alternative method, though soil composites M and K stray from this trend by exhibiting somewhat higher maximum void ratios than the individual soil samples (Figure 4.4). When evaluated by the standard method, the maximum void ratios of the composites generally agree with the maximum void ratios of the individual soil samples. Soil composites F, G, and K are anomalies because they have slightly smaller maximum void ratios than the individual soil samples.

The standard errors presented in Table 4.2 are derived from multiple tests (typically two or three) of the same type performed on the same soil composite. For the alternative test method, the e_{\min} standard errors vary from 0.002 (Soil composite M) to 0.015 (Soil composite K) and the e_{\max} standard errors vary from 0.000 (Soil composite A) to 0.014 (Soil composite K). For the Japanese Standard test method, the e_{\min} standard errors vary from 0.000 (Soil composite E) to 0.029 (Soil composite M), and the e_{\max} standard errors vary from 0.001 (Soil composite E) to 0.018 (Soil composite M). The reliabilities of the alternative and standard methods are comparable.

Re-examination of Figure 4.4 shows that the e_{\min} and e_{\max} values of the soil composites fall within the range of e_{\min} and e_{\max} values of the individual soil samples. The soil composite data do not deviate from the patterns observed for the individual soil samples (e.g., e_{\max} increases slowly as FC increases from 0% to about 30%, after which it increases at a higher rate, and e_{\min} initially decreases slightly as FC increases from 0% to 40% and then increases as FC increases from 40% to 100%). It is evident from Figure 4.4 the e_{\max} values determined by the alternative method are reasonably consistent with the e_{\max} values determined by the standard method for the soil composites with up to 70% fines. The alternative method tends to produce slightly higher e_{\max} values than the standard method for the soil composites with more than 70% fines. There is no systematic difference in the e_{\min} values from the alternative and standard test methods.

The void ratio range values of the soil composites are comparable to those of the individual soil samples using the alternative test method (Figure 4.5). The soil composites follow the same trend as the individual soil samples with void ratio range increasing steadily with increasing FC. However, the void ratio ranges of the soil composites determined in accordance with the alternative and standard test methods differ when FC exceeds 70%. This results largely because the e_{\max} values determined by the two methods differ slightly in a consistent manner when FC exceeds 70% (as shown in Figure 4.4) and because both methods exhibit higher scatter at high FC.

Figure 4.6 compares the minimum and maximum void ratios for eight soil composites determined by the alternative method and the Japanese Standard JIS A 1224:2009 method. Both methods result in the similar e_{\min} for the tested soil. However, the e_{\max} from the alternative method tends to be slightly higher than that from the standard method as the e_{\max} and FC of the tested soil increase. The percent difference between the void ratios determined by the two methods as a function of FC is shown in Figure 4.7. It varies from 0.19% to 7.3% for the minimum void ratio and is not correlated with FC. For the maximum void ratio, the percent difference between the two procedures ranges from 1.4% to 8.9% and tends to increase as FC increases.

4.4 CONCLUSIONS

Based on the Japanese Standard JIS A 1224:2009 Test Method for Minimum and Maximum Densities of Sands, an alternative procedure is proposed for testing small quantities of natural soils, typical for simple shear test specimens. The proposed procedure uses reduced sizes of the mold and funnel and the mallet strike distance of the mold, as compared to the Japanese Standard method. The minimum and maximum void ratios were first determined for 42 individual soil samples using the alternative method and then for eight soil composites with enough soil to employ the Japanese Standard method as well as the alternative method.

The alternative test method produces e_{\min} and e_{\max} values similar to those of the Japanese Standard test method for the identical soil composite mixtures. Additionally, the e_{\min} and e_{\max} of the composites determined by the alternative method agree with the e_{\min} and e_{\max} of the individual soil samples. Fines content does not affect the e_{\min} values obtained by the two methods. However, the alternative method tends to produce slightly higher e_{\max} values than the standard method as FC increases, and hence, as e_{\max} increases. This effect is more pronounced for soil with FC > 70%. The low standard errors from the alternative method testing of the soil composites confirm its good repeatability. Its reliability is comparable to that of the Japanese Standard method. The agreement of the minimum and maximum void ratios of the identical soil composites using both test methods, with comparable standard error estimates, and the agreement of the minimum and maximum void ratios of the individual soil samples with those of the composite soil samples using the alternative test method support the use of the proposed test method to determine e_{\min} and e_{\max} for samples with small quantities of soil. The alternative method enables the relative density of small test specimens to be estimated, which is useful for interpreting soil behavior.

This study also demonstrates the viability of using the standard and alternative test methods to determine the minimum and maximum dry densities of soil with up to 100% non-plastic fines. The e_{\min} and e_{\max} values of the tested soils are within the range of the values observed by Cubrinovski and Ishihara (2002) for the natural soils from Japan with the FC ranging from 0% to 70%. The tested soils exhibit the same e -FC trend as other natural soils (Cubrinovski and Ishihara 2002) and laboratory-prepared sand-fines (e.g., Lade et al. 1998). There is a transition in the data trends at about 30-40% fines where the soil switches from a sand-dominated soil structure to a fines-dominated soil structure. From FC of 0% to 30-40%, there is a slight increase in e_{\max} and a small decrease in e_{\min} . As FC increases from 30-40% to 100%, e_{\max} increases at a faster rate than e_{\min} .

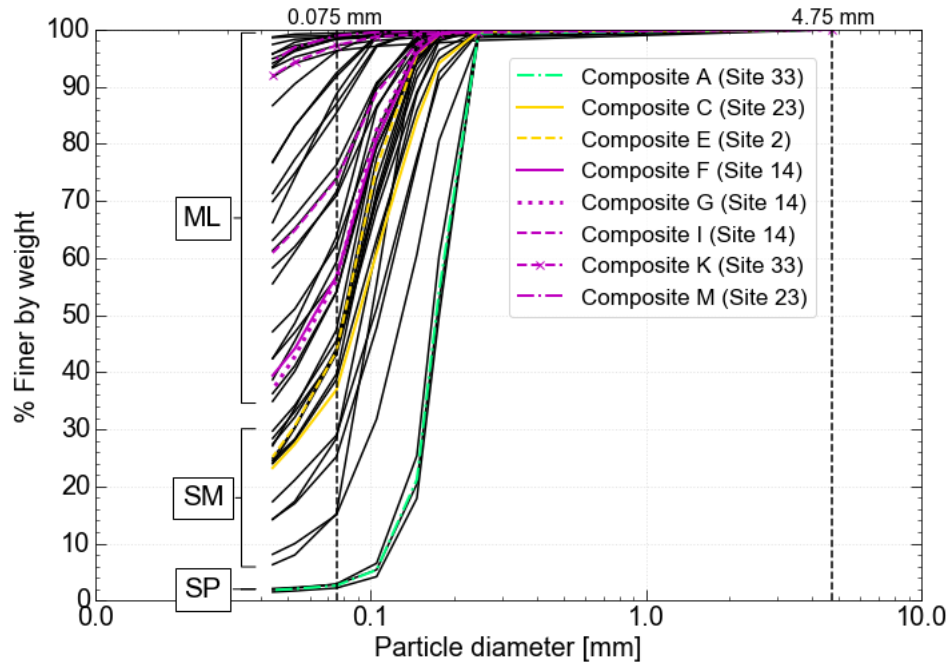


Figure 4.1. Particle size distribution curves for 42 individual soil samples (curves in black) and eight soil composites (curves in green, yellow, and magenta).

Table 4.1. Void ratios of 42 Christchurch soil samples.

Sampling tube (Site No.)	Test specimen No.	Mid-depth [m]	FC [%]	e_{max}	e_{min}	$e_{max} - e_{min}$
A (Site 33)	1	3.322	3	1.11	0.706	0.408
	2	3.341	2	1.14	0.730	0.409
	3	3.359	3	1.16	0.709	0.452
B (Site 33)	1	3.215	28	1.26	0.642	0.616
	2	3.835	15	1.29	0.724	0.566
C (Site 23)	1	7.809	43	1.31	0.565	0.749
	2	7.828	39	1.29	0.575	0.718
	3	7.848	29	1.21	0.577	0.628
	4	7.945	15	1.16	0.635	0.526
D (Site 14)	1	4.740	25	1.20	0.622	0.582
E (Site 2)	1	5.446	43	1.32	0.652	0.666
	2	5.463	44	1.36	0.659	0.698
	3	5.481	47	1.43	0.668	0.757
	4	5.507	40	1.44	0.644	0.795
F (Site 14)	1	4.708	54	1.49	0.641	0.849
	2	4.790	44	1.40	0.612	0.786
	3	4.808	54	1.48	0.612	0.865
	4	4.558	62	1.55	0.619	0.934
G (Site 14)	1	5.160	46	1.40	0.607	0.793
	2	5.302	64	1.51	0.647	0.864
	3	5.319	59	1.47	0.618	0.849
	4	5.008	85	1.78	0.723	1.06
H (Site 2)	1	8.172	72	1.61	0.640	0.971
	2	8.291	87	1.73	0.689	1.04
I (Site 14)	1	6.785	57	1.46	0.564	0.898
	2	6.821	71	1.65	0.641	1.01
	3	6.838	74	1.75	0.626	1.12
	4	6.859	76	1.79	0.644	1.14
J (Site 33)	1	4.387	99	2.17	0.857	1.31
	2	4.419	99	2.43	0.991	1.44
	3	4.439	98	2.17	0.861	1.31
K (Site 33)	1	5.182	99	2.20	0.912	1.29
	2	5.198	97	2.10	0.845	1.25
	3	5.214	98	2.19	0.890	1.30
	4	5.260	96	2.06	0.780	1.28
L (Site 2)	1	2.907	92	1.76	0.703	1.06
	2	2.931	89	1.72	0.687	1.04
	3	2.951	96	1.97	0.802	1.17
M (Site 23)	1	5.146	92	1.81	0.717	1.10
	2	5.203	98	2.06	0.818	1.24
	3	5.253	99	1.91	0.807	1.11
	4	5.316	99	2.05	0.828	1.22

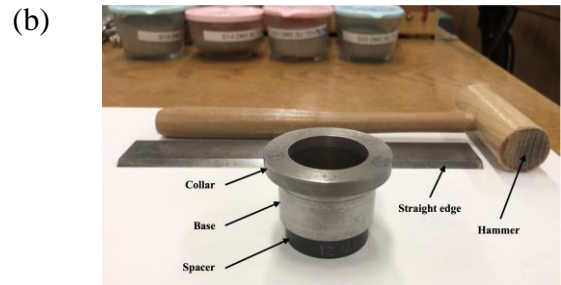
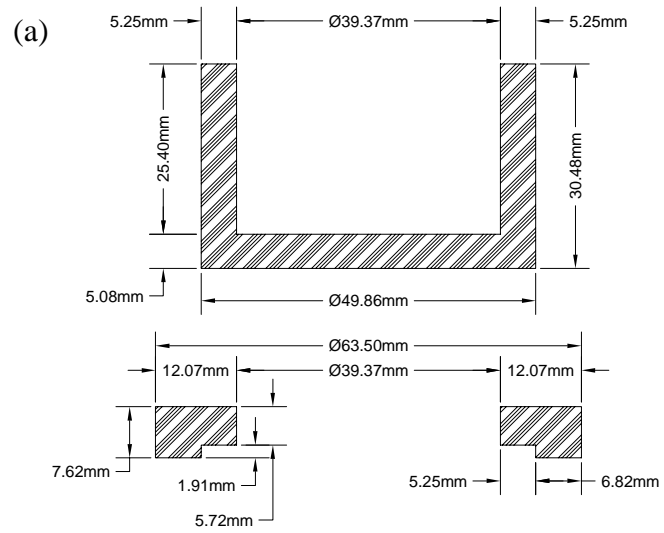


Figure 4.2. (a) Dimensions of the alternative mold and (b) additional tools used to perform the alternative maximum dry density test.

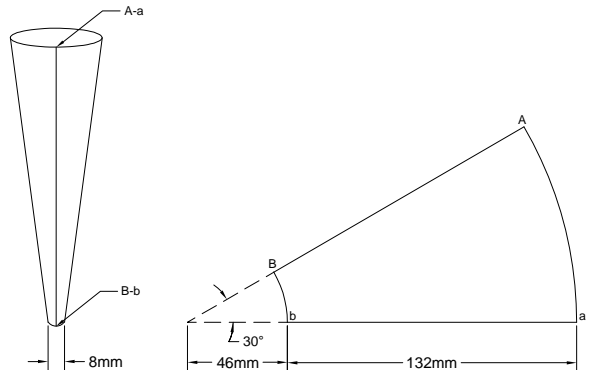


Figure 4.3. Dimensions of the alternative funnel.

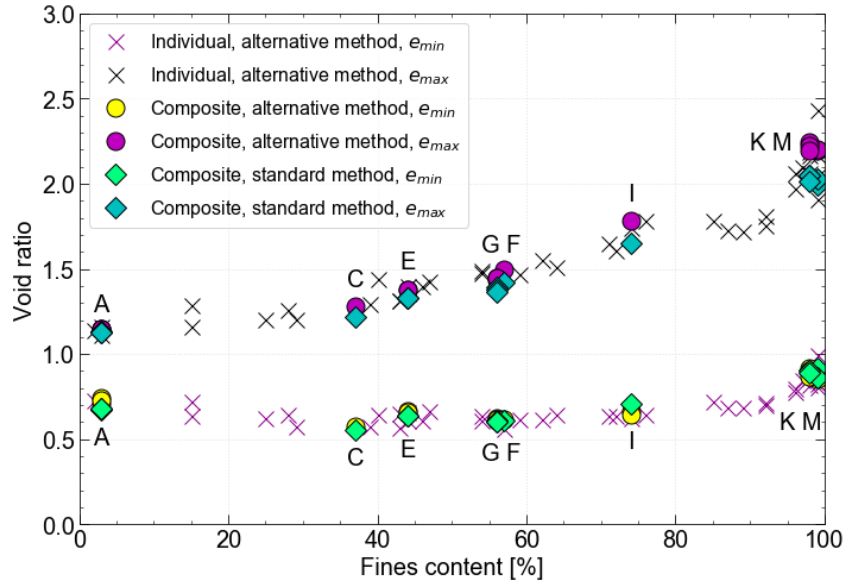


Figure 4.4. Minimum and maximum void ratios as a function of fines content for 42 individual soils and eight soil composites.

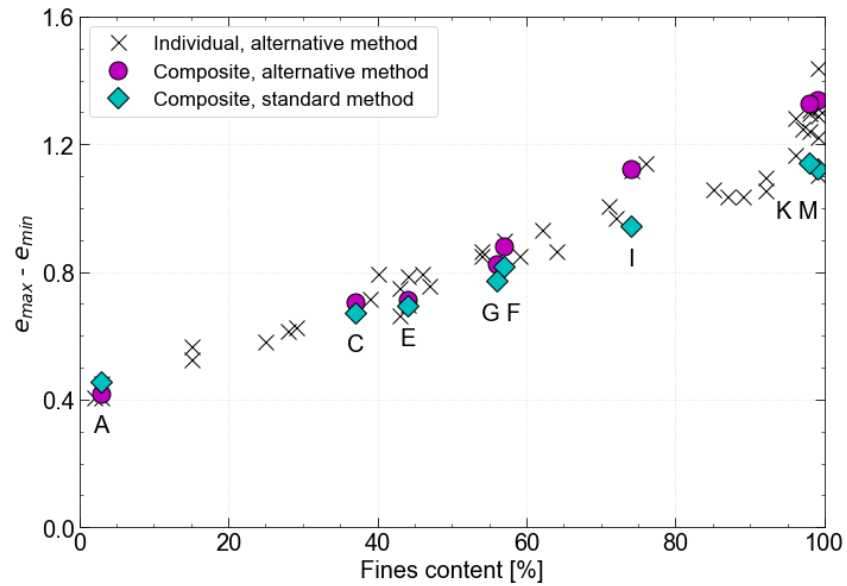


Figure 4.5. Void ratio range as a function of fines content for 42 individual soils and eight soil composites.

Table 4.2. Soil composites and their minimum and maximum void ratios determined by the alternative method and the Japanese Standard method.

Soil composite (FC)	Individual soil sample ID	Alternative Method				Japanese Standard Method	
		$e_{min, individual}$	$e_{max, individual}$	$e_{min, composite} \pm \text{std. error}$	$e_{max, composite} \pm \text{std. error}$	$e_{min, composite} \pm \text{std. error}$	$e_{max, composite} \pm \text{std. error}$
A (3%)	A-1	0.706	1.114	0.727 ± 0.010	1.147 ± 0.000	0.677 ± 0.003	1.131 ± 0.002
	A-2	0.730	1.139				
	A-3	0.709	1.161				
C (37%)	C-1	0.565	1.314	0.572 $\pm NA$	1.279 $\pm NA$	0.551 $\pm NA$	1.220 $\pm NA$
	C-2	0.575	1.293				
	C-3	0.577	1.205				
E (44%)	E-1	0.652	1.318	0.662 ± 0.006	1.376 ± 0.001	0.635 ± 0.000	1.332 ± 0.001
	E-2	0.659	1.357				
	E-3	0.668	1.425				
	E-4	0.644	1.439				
G (56%)	G-1	0.607	1.400	0.619 ± 0.004	1.444 ± 0.005	0.605 ± 0.001	1.379 ± 0.006
	G-2	0.647	1.512				
	G-3	0.618	1.467				
F (57%)	F-1	0.641	1.491	0.614 $\pm NA$	1.496 $\pm NA$	0.607 $\pm NA$	1.423 $\pm NA$
	F-3	0.612	1.477				
	F-4	0.619	1.553				
I (74%)	I-2	0.641	1.649	0.657 ± 0.009	1.781 $\pm NA$	0.707 $\pm NA$	1.650 $\pm NA$
	I-3	0.626	1.745				
	I-4	0.644	1.786				
K (98%)	K-1	0.912	2.202	0.896 ± 0.015	2.224 ± 0.014	0.898 ± 0.004	2.039 ± 0.012
	K-2	0.845	2.096				
	K-3	0.890	2.188				
M (99%)	M-2	0.818	2.060	0.859 ± 0.002	2.197 ± 0.004	0.888 ± 0.029	2.010 ± 0.018
	M-3	0.807	1.912				
	M-4	0.828	2.049				

Note: NA=Not assessed.

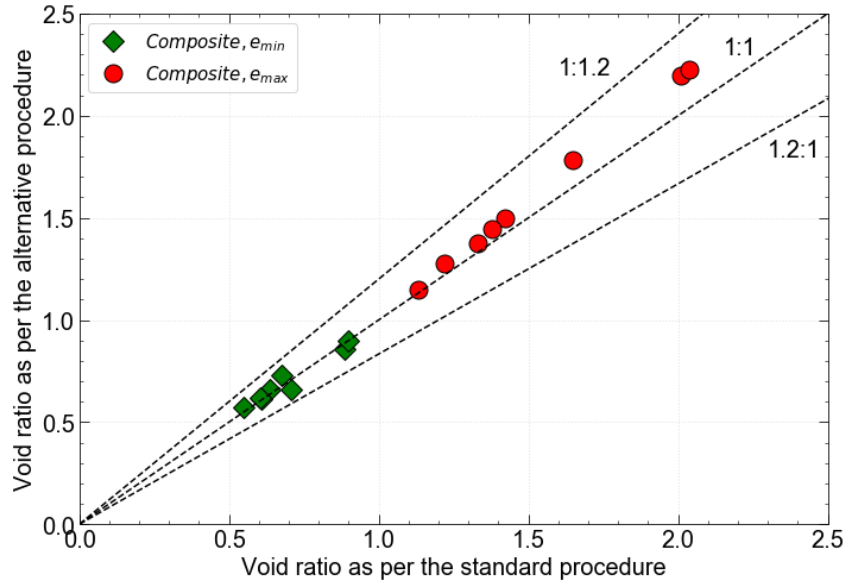


Figure 4.6. Comparison of void ratios between the alternative method and the Japanese Standard method.

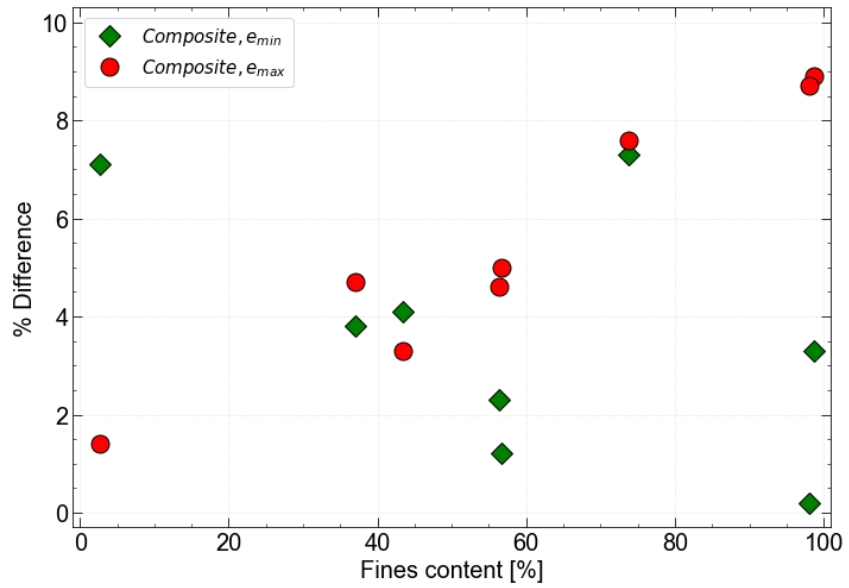


Figure 4.7. Percent difference between the Japanese Standard method and the alternative method as a function of fines content for eight soil composites.

5 CYCLIC AND MONOTONIC SIMPLE SHEAR TESTING OF NATIVE CHRISTCHURCH SILTY SOIL

The contents of this chapter are primarily from a journal article published in the Soil Dynamics and Earthquake Engineering journal by Mijic, Z., Bray, J. D., Riemer, M. F., Cubrinovski, M., and Rees, S. D., entitled “Cyclic and Monotonic Simple Shear Testing of Native Christchurch Silty Soil.”

5.1 INTRODUCTION

The 2010-2011 Canterbury Earthquake Sequence (CES) heavily damaged Christchurch, the second largest city in New Zealand. The main earthquakes in the CES were the 4 September 2010 M_w 7.1 Darfield earthquake, 22 February 2011 M_w 6.2 Christchurch earthquake, 13 June 2011 M_w 5.3 and M_w 6.0 earthquakes, and 23 December 2011 M_w 5.8 and M_w 5.9 earthquakes. The Christchurch earthquake resulted from an oblique-reverse fault in Port Hills (Figure 5.1) and caused the most widespread liquefaction that induced severe damage to land and light-weight structures in much of Christchurch (e.g., Cubrinovski et al. 2011). However, the southwestern, formerly swampy area of Christchurch had no-to-moderate surface evidence of liquefaction (e.g., sediment ejecta, ground deformation, and cracking), even though state-of-practice liquefaction triggering procedures estimated severe ground failure would occur (e.g., Beyzaei et al. 2018a, Beyzaei et al. 2018b). At sites where liquefaction-induced ground failure is overestimated by the liquefaction triggering procedures, expensive ground improvements and robust building foundations are being required, which can potentially waste millions of dollars.

The overestimate of liquefaction manifestation as evidence of liquefaction triggering by the simplified methods may in part be due to the limited content of the existing empirical database used in their development. About 85% of the database used to develop the Boulanger and Idriss (2016) simplified procedure consists of case histories from sites with clean sand deposits and sand deposits with up to 35% of non-plastic fines. Additionally, most of the cyclic testing that forms the basis for our understanding of the cyclic response of soil was performed on reconstituted clean sand test specimens due to the difficulties associated with obtaining “undisturbed” sand specimens and the predominance of case histories from clean sand sites (e.g., Tatsouka et al. 1986, Vaid and Sivathayalan 1996, Wu 2002). The cyclic strength of the reconstituted specimens is generally considered to not reflect the actual response of in-situ soil deposits during earthquakes because reconstituted specimens do not capture the fabric formed under different depositional conditions, age since deposition, and previous seismic strain history (Seed 1979, Ishihara 1996). Hence, tests on high-quality specimens that maintain the effects of those factors to the greatest degree possible are needed to evaluate the cyclic strength of in-situ soil deposits (Seed 1979, Ishihara 1996). Furthermore, observations from recent earthquakes have highlighted the importance of liquefaction in silty soil and have shifted the focus of

liquefaction research to silty soil, i.e., soil with no-to-low plasticity indices, PI, and fines contents, FC, from 35% to 100% (e.g., Bray and Sancio 2006).

Loose, clean sand may be susceptible to “flow liquefaction,” a condition with unlimited strain potential, while dense, clean sand is likely to undergo “cyclic mobility,” which is characterized by the gradual development of excess pore water pressures and limited strain potential under repeated loading. Clean sand, in general, manifests a pore water pressure ratio, r_u , of nearly 100% (Ishihara 1996), where r_u is defined as the ratio of the excess pore water pressure, Δu , to the initial vertical effective stress, σ'_{vo} , acting on the test specimen. In contrast, clay dissipates large amounts of energy through plastic deformation and hysteretic damping. It may cyclically soften and deform but it does not reach a state where the pore water pressure ratio is close to 100%. Between the two extremes represented by loose sand and soft clay, silty soil exhibits an intermediate response. Silt tends to undergo cyclic mobility if liquefaction is triggered and experience the pore water pressure ratio of 90-95% (Ishihara 1996). However, there has been significantly less testing on silt compared to sand or clay, so additional testing of silt is warranted.

As a result of the opportunities presented by the observations of damage and no-damage due to liquefaction following the CES, several studies investigating Christchurch soil were undertaken. Taylor (2015), Markham et al. (2016), Stringer et al. (2016), and Beyzaei et al. (2018b) conducted cyclic triaxial (CTX) tests on “undisturbed” silty soil specimens. There are limitations to CTX testing due to the initially isotropic consolidation state, instantaneous 90° rotation of principal stresses, cyclic axial load application, and necking of a test specimen. Cyclic simple shear (CSS) testing overcomes these limitations, although it too has shortcomings. The lack of complementary shear stresses along the vertical sides of a specimen, non-rigid boundaries, and rocking motions of the specimen’s cap relative to the base all produce some nonuniform stress conditions (Boulanger 1990). However, the limitations are minor compared to the benefits of the CSS test configuration due to a soil element in a K_o -consolidated state experiencing a smooth, continuous rotation of the principal stress directions and a close representation of the earthquake loading conditions in the field. Cappellaro et al. (2021) performed CSS tests on Christchurch soil, but they were limited to tests on reconstituted specimens.

The first CSS tests on high-quality retrieved specimens of Christchurch silty and sandy soil were performed in this study. The focus is on investigating the CSS and monotonic simple shear (MSS) response of “undisturbed” Christchurch silty and sandy soil specimens retrieved from the stratified silty soil deposits that were strongly shaken during the CES and had surface manifestation of liquefaction overestimated by the existing CPT-based liquefaction triggering procedures. The sites, sampling, and test results are described first, and key insights are then shared.

5.2 SITES AND RETRIEVAL OF HIGH-QUALITY SAMPLES

5.2.1 Geological Setting of Christchurch

Christchurch lies on the east coast of New Zealand’s South Island in the northern Canterbury Plains that were formed from coalescing fans of the glacier-fed Waimakariri River and other Canterbury rivers emerging from the Southern Alps (Brown et al. 1995). Christchurch is located just north of the Port Hills of Banks Peninsula, an extinct volcanic

complex formed predominantly by Miocene basalt (Brown et al. 1995). The city is built largely upon gravel, sand, silt, and swamp deposits from the late Quaternary (Brown et al. 1988). The meandering Avon and Heathcote Rivers originate from springs in western Christchurch and form an estuary to the east (Brown et al. 1995).

Due to its complex depositional environment with dominant influences from alluvial and coastal depositional processes, Christchurch can be divided in four geologic quadrants centered on the Christchurch Business District (CBD): southwest (SW), northwest (NW), northeast (NE), and southeast (SE) (Beyzaei et al. 2018a). The SW quadrant is characterized by thick successions of thinly interbedded fine sand and silt swamp deposits and depositional effects from the Port Hills. The NW quadrant is also characterized by silty soil swamp deposits; however, its depositional setting is not influenced by the Port Hills and its sediments are likely younger than those in the SW quadrant due to their closer proximity to the braided Waimakariri River. Additionally, as water spills over onto the floodplain, finer deposits are typically carried a greater distance, resulting in thickening of silt layers and thinning of sand layers away from the avulsing river. By contrast, the NE and SE quadrants contain interchanging layers of coastal and fluvial sediments and did not typically experience inconsistencies between the surficial evidence of liquefaction during the 2010-2011 CES and the estimates generated by the liquefaction triggering procedures. The eastern suburbs contain thicker layers of clean sand, the type of deposits that comprise most of the case histories used in the development of the liquefaction triggering procedures (Beyzaei et al. 2018a).

The shallow surficial geology of Southwest Christchurch consists of Springston Formation that overlies Burnham Formation with a maximum thickness of 20 m, and interfingers with Christchurch Formation to the east (Brown et al. 1988). The Waimakariri River currently flows eastward from the Southern Alps into the South Pacific Ocean, but it used to avulse across the region and deposit alluvial sands, silts, and gravels prior to the European settlement and the flood control measures (Beyzaei et al. 2018a). At times, it flowed through the current location of Christchurch into the Avon-Heathcote Estuary and even into Lake Ellesmere to the south of the Banks Peninsula (Davies 1989). The alluvial sediments are subsequently reworked and redeposited by meandering rivers and streams such as the Avon and Heathcote Rivers.

5.2.2 Sites and Soil Profiles

To study the liquefaction potential of Christchurch silty and sandy soil, four level-ground sites with no potential for lateral spreading were selected for the retrieval of representative samples of silt (ML), silty sand (SM), and clean sand (SP) for advanced laboratory testing. Site 2 – Gainsborough Reserve (-43.5636, 172.6019), Site 14 – Barrington Park (-43.5541, 172.6176), Site 23 – 85 Riccarton Road (-43.5298, 172.6037), and Site 33 – 200 Cashmere Road (-43.5727, 172.6081) are shown in Figure 5.1. Sites 2, 14, and 33 are free-field sites, while Site 23 is occupied by a two-story commercial building and a parking lot. Sites 2, 23, and 33 are in or near formerly swampy areas of Christchurch, whereas Site 14 is located away from them (Beyzaei et al. 2018a). The CES caused no liquefaction at the sites, except Site 14 which experienced moderate manifestation of liquefaction (i.e., 5-20% of the site within a 50-m radius was covered with ejecta) for the Christchurch earthquake (Figure 5.1) (CGD 2012). CPT-based liquefaction triggering

procedures (e.g., Boulanger and Idriss 2016) led to the overestimation of liquefaction manifestation at the ground surface in all cases.

Sites 2, 14, 23, and 33 were selected for this study because they were investigated thoroughly by researchers from the University of Canterbury, University of California, Berkeley, University of Texas at Austin, and Tonkin and Taylor, Ltd., as part of the “silty soils project” (e.g., Stringer et al. 2016). The subsurface conditions at these sites were explored by methods including CPT, Dames and Moore (DM) and Gel-Push (GP) sampling for CTX testing, seismic dilatometer, direct push cross-hole seismic testing, and 20-m borehole sampling (T+T 2015). Additionally, Beyzaei et al. (2018a) performed continuous high-quality sampling and detailed soil logging at Sites 14 and 33 for enhanced characterization of their stratigraphy.

Figure 5.2 presents the CPT tip resistance corrected for unequal-area and thin-layer effects, q_t , and the Robertson (2009) soil behavior type index, I_c , for the upper 10 m of the subsurface profile. The thin-layer correction was performed using the de Greef and Lengkeek (2018) procedure. Its effect on the measured CPT tip resistance is discussed subsequently. The results were exported from the program *CLiq 3.0* (Ioannides 2019). Site 2 consists primarily of clayey silt, silty sand, and non-plastic silt layers. Site 14 contains clayey silt, silty sand, non-plastic silt, and sand strata underlain by gravels. Site 23 is highly stratified with clayey silt, non-plastic silt, sandy silt, and sand. The soil stratigraphy at Site 33 is comprised of silty sand, clayey silt, sand, and non-plastic silt. The groundwater tables in Figure 5.2 were recorded at the time of the CPT investigations. However, the groundwater levels at these sites fluctuate. The typical minimum-maximum groundwater table depths below ground surface for Sites 2, 14, 23, and 33 are 1.0-2.2 m, 0.1-1.8 m, 0.6-1.8 m, and 0.8-2.0 m, respectively, as derived from piezometer readings, sonic boring cores, and compressional wave velocity measurements (Beyzaei et al. 2018a).

5.2.3 Selection of Sampling Depths

The objective of the research was to test a set of high-quality specimens retrieved from non-plastic silt, silty sand, and sand layers in the CSS device. To select soil sample depths, target properties were defined as: ML: $40\% \leq FC \leq 70\%$ and $2.2 \leq I_c \leq 2.6$; SM: $10\% \leq FC \leq 30\%$ and $1.8 \leq I_c \leq 2.2$; and SP: $FC < 5\%$, $I_c < 1.8$, and $q_{t1ncs} > 60$. All target soil layers were well below the abovementioned maximum groundwater table depths and could be considered as fully saturated based on the compression wave measurements, V_p , and absence of iron staining, mottling, root voids, and desiccation at these soil layers (Beyzaei et al. 2018a). Depths with the target I_c and q_{t1ncs} were selected based on the available CPT profiles (Figure 5.2). The continuous DM sampling and detailed logging conducted at Sites 14 and 33 by Beyzaei et al. (2018a) were used to further scrutinize suitable sample depths. Depth intervals with at least 60 mm of similar soil based on the logged description and visual appearance in the images available in Beyzaei (2017), without roots and other defects, were targeted. Lastly, depths from which “undisturbed” retrieved CTX specimens were previously tested by Beyzaei et al. (2018b) and Stringer et al. (2015) were prioritized to support follow-on research comparing the cyclic response of the same soil in different shear conditions. The soil samples discussed herein are shown in Figure 5.2. Their corresponding I_c and q_{t1ncs} values summarized in Figure 5.2 were averaged over a depth range typically from 10 cm above the uppermost test specimen’s mid-depth to 10 cm below the lowermost test specimen’s mid-depth. The q_{t1ncs} was

computed using the Boulanger and Idriss (2016) procedure and C_{FC} of 0.13 developed for Christchurch soil by Maurer et al. (2019). At the specimen origin depths, FC determined in the laboratory and discussed subsequently was used to compute q_{tlncs} .

5.2.3.1 CPT Measurements and Thin-Layer Effects

The CPT, either the 10-cm² conventional CPT or the 5-cm² mini-CPT, cannot adequately capture soil layers that are “only a few millimeters to a few centimeters thick” in these highly stratified soil profiles (Beyzaei et al. 2020). The cone diameter hence the zone of influence is too large compared to the layer thickness, which leads to smearing of CPT measurements (Ahmadi and Robertson 2005). The cone starts to sense a change in material type before it reaches a layer interface boundary and continues to sense a previous layer after it penetrates a new material. The interface influence distance is greater in dilative sand layers than in contractive sand layers (Ahmadi and Robertson 2005). The zone of influence in dilative soil is about 10-20 cone diameters while the zone of influence in soft soil is about 2-3 cone diameters (Ahmadi and Robertson 2005, Lunne et al. 1997). Moreover, the tip resistance of a stiff sand layer embedded in softer, more compressible soil layers is not fully mobilized (Ahmadi and Robertson 2005). As the thickness of the stiff sand layer decreases, the cone senses the softer, more compressible layer sooner and the maximum tip resistance within the dilative sand layer decreases. Consequently, the underestimate in the tip resistance of the thin dilative sand within the thick, soft, compressible soil leads to its incorrect identification as potentially loose. A stratum of highly dilative sand should be at least 28-cone-diameters thick to mobilize its full cone tip resistance (Ahmadi and Robertson 2005).

An attempt was made to correct the CPT tip resistance using the thin-layer correction developed by de Greef and Lengkeek (2018). However, the soil stratification profiles were not much improved. At the test specimen origin depths, the increase in q_t and q_{tln} typically ranged from 0 MPa to 1.5 MPa and from 0 to 20, respectively. This was not unexpected because thin-layer corrections are typically applied to thin (at least 250- to 300-mm thick), stiff layers within thicker, softer layers; they do not work for these highly stratified silty, sandy, and clayey soil profiles because distinct layers of a soil type are too thin and without contrasting stiffnesses.

5.2.4 Dames and Moore Sampling Procedure

A side-discharge tri-cone roller bit was used in combination with heavy bentonite drilling fluid to advance a borehole, which was at least two meters away from previous investigations to avoid disturbance but sufficiently close to them to minimize lateral variability of soil stratigraphy. Casing was kept at a minimum of two times the casing diameter (110 mm) but less than 1 m above the bottom of the borehole to prevent borehole collapse and mud loss (Bray et al. 2016). The DM hydraulic fixed-piston Osterberg-type soil sampler with a thin-walled brass tube was used. The tube has an outside cutting-edge bevel of 60° and the area ratio, C_a , of 7.6%, which is well below the 10-15% C_a recommended by Hvorslev (1949). The C_a is defined as $100 \times (OD^2 - ID^2) / ID^2$, where OD is the outside tube diameter (63.5 mm for the DM tube) and ID is the inside tube diameter (61.2 mm for the DM tube). The inside sampling length of the DM tube is 450 mm. The restricted sample length and the smooth, low-friction brass tube reduce disturbance due to

soil plugging. Additional details on the use and efficacy of the DM sampler in silty soil are provided in Bray and Sancio (2006) and Markham et al. (2016).

High-quality soil samples were retrieved at all sites with typical recoveries of 100% of the theoretical maximum. The retrieved sandy soil samples were allowed to drain through a perforated bottom cap for several hours. The sampling tubes were wrapped in foam, arranged vertically in a cardboard box, and transported carefully on the back seat of a car to the University of Canterbury Soil Mechanics Laboratory. The samples were stored vertically for at most a few weeks, inside the box on a thick layer of polyethylene foam, in a humid environment at the laboratory until extruded for testing. Prior to the removal of soil from a sampling tube, the extrusion length (hence soil disturbance) was minimized by cutting the tube to a height of 270 mm from the bottom of the soil sample. The top 20 mm and the bottom 50 mm of soil in the lower part of the cut tube and the top 50 mm and the bottom 20 mm of soil in the upper part of the cut tube were assumed to be disturbed. The soil was extruded from the tube in the same direction it entered it by a manual hydraulic jack and was inspected visually for disturbance and heterogeneity. Representative uniform specimens were cut by a wire saw to a height of approximately 15.5 mm (Figure 5.3a).

5.2.4.1 Disturbance and Heterogeneity

The soils investigated in this study are ML, SM, and medium dense SP ($q_{t1ncs} > 60$), in which the DM sampler can obtain “relatively undisturbed” samples according to Markham et al. (2016). Potential sample disturbance was evaluated based on observations made during field sampling (e.g., compromised integrity of the brass sample tube), transportation, storage, and laboratory preparation (e.g., movement of sand particles under the wire saw or fingers and specimen abrasion along its sides). Soil specimens that were adversely affected in the period between field sampling and vacuum confinement were not tested.

Each specimen was visually inspected for heterogeneous features, such as fissures, voids, laminations, lenses, roots, and iron-staining. Some degree of heterogeneity is inherent to natural silty soil specimens; thus, a balance between selecting specimens that are representative of a soil stratum as a whole and having sufficient homogeneity to allow for meaningful interpretation of test results was achieved. The uniformity of each specimen was judged based on similarity of soil texture between its top surface and bottom surface (Figure 5.3a). Specimens with a clear interface between two different layers, voids, and similar features that would negatively impact the quality of testing and the interpretation of test results were discarded. Each specimen was split open after testing to evaluate specimen uniformity (Figure 5.3b and 5.3c). The micro-layering in Figure 5.3c was deemed homogenous on the stratum scale. Furthermore, the CSS and MSS specimens from the same sampling tube were reasonably consistent in their features to allow for comparison of their test results. Eventually, 40 soil specimens were tested at the University of Canterbury using the UC Berkeley unidirectional SS device. After SS testing, the specimens were transported to UC Berkeley for scanning electron microscope (SEM) imaging and index property testing.

5.3 CHRISTCHURCH SOIL

5.3.1 SEM Imaging

Particle shape, commonly described by sphericity and roundness, is an inherent soil property that plays an important role in mechanical response of soil (Mitchell and Soga 2005). Sphericity of a particle is the ratio of the surface area of a sphere (with a volume equal to that of the particle) to the surface area of the particle (Wadell 1932). Roundness is a physical property of all sediments that depends on the sharpness of the edges and corners (Powers 1953). It is the ratio of the average radius of curvature of particle's corners and edges to the radius of the maximum sphere that can be inscribed within the particle (Wadell 1932). In short, sphericity refers to the degree to which a particle resembles the shape of a perfect sphere, whereas roundness describes the sharpness of angular protrusions from a particle. Their values range from 0 to 1, 0 indicating elongated and very angular particles and 1 corresponding to highly spherical and well-rounded particles (Powers 1953).

Particle shape affects the minimum and maximum void ratios (Mitchell and Soga 2005). Their values tend to increase with increasing angularity. Particle shape also has an impact on the soil strength. Soil consisting of angular particles are initially less dense than soil with rounded particles. However, angular particles tend to crush and compress more than rounded particles. The collapse of soil structure by particle breakage leads to a soil volume decrease and contractive behavior upon shearing, which is followed by an increase in stiffness and strength. Angular particles typically have more stable contacts than rounded particles and can interlock forming an anisotropic fabric. Furthermore, elongated particles can result in a denser packing and can rotate less than spherical particles. An assembly of elongated particles gives larger values of shear strength and requires more shearing to modify its initial fabric anisotropy to the critical state condition. Fabric anisotropy is a result of depositional and post-depositional processes (e.g., the assembly of non-spherical particles tends to be stiffer in the vertical direction than in the horizontal direction) and can be destroyed during shearing (Mitchell and Soga 2005).

High-quality images of Christchurch soil were obtained by utilizing the Hitachi TM-1000 SEM. Five representative, dry CSS soil specimens with FC ranging from 2% to 99% were selected for the SEM imaging: S33-DM3-1U-T3 (FC=2%), S14-DM3-3U-T5 (FC=44%), S14-DM3-3U-T1 (FC=54%), S14-DM3-6U-T3 (FC=73%), and S33-DM3-4U-T1 (FC=99%). S14-DM3-3U-T1, -T5, and S14-DM3-6U-T3 were wet-sieved through a No. 200 (75- μ m opening) sieve to separate fine particles from coarse particles for imaging. Both fractions were oven-dried, after which a coarse fraction was dry-sieved to eliminate the remaining fines.

Representative images are presented in Figure 5.4. The shape of 50 individual particles in each of these and other images not shown herein were compared against the particle silhouettes in the Powers (1953) chart to characterize the particle shape both qualitatively and quantitatively. The roundness scale is defined by six class intervals and their corresponding geometric means. Each roundness class is further described by high sphericity or low sphericity. To evaluate the roundness, the number of particles in each class is multiplied by the geometric mean of that class and the sum of the products is divided by 50. The average roundness of the eight SEM specimens is in the range from 0.20 to 0.24, as shown in Table 5.1. All specimens belong to the angular class. Low-

sphericity particles predominate for each SEM specimen. The percent of low-sphericity particles ranges from 70 to 90 (Table 5.1).

5.3.2 Index Soil Properties

The specific gravity, G_s , was determined in accordance with ASTM D854. One G_s test was conducted per set of soil, typically on the mid-depth soil specimen of the set. If a soil specimen differed significantly in FC from other soil specimens from the same sampling tube, the specific gravity was evaluated for that soil specimen too (e.g., S14-DM3-4U-T1). The G_s values range from 2.68 for SP to 2.72 for ML with an average of 2.70 (Table 5.2).

The plasticity of soil was evaluated following ASTM D4318. The plastic limit, PL, was determined based on the thread-rolling method, while the liquid limit, LL, was evaluated using the Casagrande cup. In general, the PL values range from 17 to 25 for soil specimens that could be rolled out into a thread (S2-DM2-1U, S2-DM2-6U, S14-DM3-4U-M, S14-DM3-6U, S23-DM2-3U, S33-DM3-3U and -4U) although their corresponding LL values could not be determined due to the problems associated with non-plastic silty soil (e.g., the tendency of soil to slide down in the cup, difficulty in cutting the groove, and the tendency of soil to liquefy in the cup). Therefore, all soil specimens are classified as non-plastic.

Every specimen was wet-sieved through a sieve with a 44- μm opening. A portion of soil with particles greater than 44 μm was then dry-sieved using a mechanical shaker. The resulting gradation curves are summarized in Figure 5.5. Most of the specimens are classified as ML; however, their group names differ depending on the percent of fines they contain (ASTM D2487). There are six sandy-silt specimens (FC = 50-69%), four silt-with-sand specimens (FC = 70-84%), and 15 silt specimens (FC \geq 85%). Three specimens are composed of poorly graded sand (SP) with the coefficient of uniformity of 1.6, and 12 specimens consist of silty sand (SM).

Relative density, D_R , is an important density measure of non-plastic soil. Insights can be obtained using D_R for sand with high fines content because clean sand is the reference material used in liquefaction assessments and the state of sand containing non-plastic fines is often converted to clean-sand-equivalent values when encountered in the field. The D_R of a high FC soil can be used to compare the results of sand with fines, and it can be linked directly to that of clean sand to aid in the interpretation of laboratory studies. The maximum and minimum void ratio tests are typically reserved for soil with less than 5-15% fines. However, Cubrinovski and Ishihara (2002) found the Japanese Standard method, which can accommodate soil with a large range of fines content, yielded consistent e_{\min} and e_{\max} values for non-plastic fines content of up to 35% for a comprehensive database with over 300 native soils. In examining this database further, reasonable e_{\min} and e_{\max} values were obtained for non-plastic soils with even higher fines content. Moreover, Mijic et al. (2021a) found consistent e_{\min} and e_{\max} values were obtained for Christchurch non-plastic silty sand and sandy silt with FC up to at least 70% and their values for non-plastic silt with 100% fines were not unreasonable. Thus, e_{\min} and e_{\max} tests were performed on all non-plastic soil in this study to enable D_R to be estimated for comparison and interpretation of the results. A descriptive name was assigned to each test specimen based on the USCS, FC [%], and D_R [%] (Table 5.2). For instance, ML-57-87

indicates that the test specimen consists of low plasticity silt (ML), 57% fines, and has a relative density of 87%.

The alternative Japanese Standard JIS A 1224:2009 Test Method for Minimum and Maximum Densities of Sands was developed to provide a consistent means for estimating the relative density of each CSS and MSS test specimen, which is too small to provide enough material to utilize the standard-size equipment (Mijic et al. 2021a). The minimum and maximum void ratios of the test specimens are summarized in Table 5.2. The e_{\min} and e_{\max} values range from 0.564 (ML-57-87) to 0.991 (ML-99-92) and from 1.11 (SP-3-84) to 2.43 (ML-99-92), respectively. The minimum void ratio for these soils tends to decrease with increasing FC from 0% to about 30-40%, and it increases only slightly from approximately 40% to 100% fines (Mijic et al. 2021a). The maximum void ratio decreases slightly initially with increasing FC from 0% to about 30%, and then increases with a higher rate of increase with increasing FC beyond 30%. A FC of 30-40% is a transition point between the sand-dominated particle structure and the fines-dominated particle structure for the tested soils (Mijic et al. 2021a). This is in agreement with the previous studies (e.g., Cubrinovski and Ishihara 2002, Thevanayagam et al. 2002) wherein the 20-40% fines content was observed as a transition zone between the filling-of-voids process and the replacement-of-solids process. Christchurch soils are comprised of angular particles, so they tend to have higher e_{\min} and e_{\max} values than soil with rounded to subrounded spherical particles.

5.4 ADVANCED LABORATORY TESTING

The UC Berkeley unidirectional SS device was used for undrained MSS and CSS testing of the saturated “undisturbed” soil specimens. The same device (with a modification to improve system compliance) was employed in the Cappellaro et al. (2021) CSS testing of reconstituted Christchurch soil specimens. A rigid steel cylinder replaced the vertical load cell previously installed directly above the test specimen to reduce rocking motions of the top cap relative to the base in this study. The schematic cross-section of the device is shown in Figure 5.6. The test specimen encased in a plain latex membrane is placed between two flat porous stones tightly fitted in the recesses of two aluminum caps by the means of polytetrafluoroethylene film tape. The caps are firmly affixed to the vertical and horizontal loading tables, which are connected to pneumatic actuators. The specimen is confined laterally by a pressure chamber using compressed air, while vertical confinement is provided by a vertical load actuator. The vertical table and the horizontal base table slide along preloaded, low-friction track bearings, which reduces friction and restricts rocking of the top cap relative to the base.

The device has a set of transducers that measure and record horizontal and vertical load, displacement, cell pressure and effective pressure – thus pore water pressure, and volume change. LVDT4 measures horizontal displacement between the top platen and a vertical post connected to the bottom platen (Figure 5.6). LVDTs 1, 2, and 3 read vertical displacement between the top cap and the bottom platen and are arranged in a manner that allows monitoring of rocking motions of the top cap. All transducers are connected to a signal conditioning system that amplifies the signal prior to data acquisition. The output voltage of the transducers is multiplied by their calibration factors. The graphical output of transducer readings is provided by a program written in *LabView*. The program implements a proportional-integral-derivative (PID) control algorithm integrated into a closed-loop

feedback system. The optimal PID gains for satisfactory performance at a 0.05-Hz frequency in force-controlled tests on soil specimens were determined by trial-and-error.

The soil specimen was tested at its nominal diameter of 61.2 mm and a height of about 15.5 mm, following recommendations for a diameter-to-height ratio of four to minimize the effect of not having complementary shear stresses at the sides of the specimen (Boulanger 1990). Immediately upon trimming, the specimen was weighed, mounted on the bottom cap, encased in a flexible membrane, and confined by the top cap. Vacuum grease and O-rings were used to seal the membrane to the aluminum caps. A differential vacuum of 6 kPa was applied gradually to the specimen as a preliminary method of saturation. A vacuum of 15 kPa was applied to the bottom of the specimen while a vacuum of 21 kPa was applied to the top of the specimen to pull de-aired water up through the specimen. After confirming no leaks were present, the height and the diameter of the specimen were measured, and the specimen was transferred to the chamber. The vacuum was replaced by the cell pressure and the specimen was subjected to backpressure saturation while maintaining a constant effective stress of typically 20-25 kPa.

The specimen was consolidated anisotropically to 1.1 times the estimated in-situ vertical effective stress, assuming a unit weight of 18.5 kN/m³. The nominal K_o values of 0.50, 0.55, and 0.60 were imposed on the SP, SM, and ML specimens, respectively, with the assumption that the soils were normally consolidated. The vertical effective stress at the end of consolidation, σ'_{vo} , and K_o are reported in Table 5.3 for all test specimens. Once the specimen was consolidated to the desired stresses, a final B-check was performed to ensure the degree of specimen saturation was sufficiently high. Considering the stiffness of the silty sand soil, the difficulties with applying an isotropic increment of stress on the SS specimen with big caps and a small membrane area, the friction in the SS system, and the precedence using this SS device, a threshold B value of 0.90 was used to check the test specimen was nearly or fully saturated. Table 5.3 summarizes measured B-values and void ratios at the end of consolidation. The measured volumetric and vertical strains indicated negligible radial strains occurred during consolidation.

At the end of consolidation, the vertical piston was locked in position to maintain a constant specimen height while allowing the total vertical stress to fluctuate (i.e., the “constant-height” test method). The drainage valve was closed to perform undrained MSS/CSS loading. Loading at 1 Hz would not ensure pore water equalization within the test specimen. Thus, the specimen was loaded cyclically by a sinusoidal waveform at a frequency of 0.05 Hz to ensure pore water pressure equalization using the time-to-50%-consolidation (t_{50}) data available from Beyzaei et al. (2018b) and a duration of a loading cycle being at least $16t_{50}$. No change in pore water pressure occurred once the shear loading was stopped. Rate effects for these non-plastic soils were assumed to be negligible; however, it is possible that testing at 1 Hz would produce a slightly steeper stress-strain response for test specimens with high FC and require slightly more cycles to initiate liquefaction (Donahue 2007). For the MSS testing, the specimen was loaded linearly at a rate of 1 N/s until the maximum horizontal displacement of the device was reached. The CSS test specimen was also subjected to undrained MSS testing afterward. The horizontal load and the horizontal displacement were reset to approximately zero before initiating the post-cyclic monotonic test. The specimen was then loaded linearly at a rate of loading of approximately 1 N/s until at least 10% shear strain was reached. After testing, the soil specimen was removed from the SS device and visually inspected for any

heterogeneous features. There was no evidence of significant particle breakage in the tests performed in this study.

5.5 RESULTS AND DISCUSSION

5.5.1 Relative Density

The D_R of the test specimens determined in the laboratory range from 56% to 100% (Table 5.3). The laboratory-based D_R may initially appear to be high compared to the q_{t1n} values presented in Figure 5.2. However, one should consider a D_R - q_{t1n} correlation for a soil of interest based on its particle characteristics (Robertson and Campanella 1983), wherein q_{t1n} represents the normalized CPT tip resistance obtained directly from measured q_t . Most empirical D_R - q_{t1n} correlations were developed for clean sands to allow for an estimate of the in-situ D_R due to the difficulties and high cost associated with retrieving high-quality sand samples (e.g., Schmertmann 1978, Jamiolkowski et al. 2001). In clean sand, $q_{t1n} = q_{t1ncs}$. Calibration chamber test results showed the importance of sand density and compressibility, effective overburden and lateral stress on the cone penetration resistance (Robertson and Cabal 2015). For a given D_R , more compressible sands are less resistant to cone penetration than sands with lower compressibility. The compressibility of sand is affected by the particle size, shape, and mineralogy. Angular mica/carbonate sands tend to be more compressible than sands composed of round quartzitic particles (Robertson and Cabal 2015).

Cubrinovski and Ishihara (1999) developed an empirical correlation between the standard penetration test (SPT) resistance and relative density using data from natural silty sand, sand, and gravel deposits in Japan. They used the void ratio range, the difference between the loosest and densest state of packing of soil as per the Japanese Standard method, to quantify the combined effects of particle size, shape, and size distribution. The void ratio range increased with increasing FC, thus decreasing mean particle size, and increasing angularity of soil (Cubrinovski and Ishihara 1999). Cubrinovski (2019) converted the SPT penetration resistance corrected for the energy ratio of 60% and overburden stress, $(N_1)_{60}$, into q_{t1n} using QNR, a ratio of q_{t1n} to $(N_1)_{60}$, which allows for consideration of particle-size effects. Robertson et al. (1983) showed that QNR increases with the increasing mean particle size, D_{50} .

Figure 5.7 illustrates a range of Cubrinovski and Ishihara (1999) curves for FC = 0, 35, and 100%. To obtain the input $(e_{max}-e_{min})$ values for the three curves, the $(e_{max}-e_{min})$ and FC data for the tested Christchurch soil specimens were fitted linearly, $(e_{max}-e_{min}) = 0.0086 \times FC + 0.388$ (the statistical coefficient of determination, R^2 , equals 0.94). The QNR values were estimated as a function of D_{50} using the corrected Robertson et al. (1983) correlation provided in Cappellaro et al. (2021). The D_{50} values of the CSS and MSS test specimens range from 0.18 mm for SP with FC = 2% to <0.044 mm for ML with FC > 70%. For the FC = 0, 35, and 100% curves, QNR = 4.5, 4.0, and 3.5, respectively, were used. Moreover, the D_R of the CSS and MSS test specimens and their corresponding q_{t1n} as measured over a depth range from 10 cm above to 10 cm below their origin mid-depths are shown in Figure 5.7. Although not directly applicable for the fines-containing soils, the Robertson and Cabal (2015) correlation is included in Figure 5.7 for reference. Robertson and Cabal (2015) modified the Baldi et al. (1986) correlation between the tip resistance and D_R for the Ticino sand, a mixture of subrounded particles composed of quartz, feldspar,

and mica minerals (Robertson and Campanella 1983). This correlation is recommended for normally consolidated, unaged and uncemented sands of moderate compressibility and predominantly quartz mineralogy.

The Cubrinovski and Ishihara (1999) curves in Figure 5.7 show that for a given cone penetration resistance, D_R increases as FC increases (i.e., the mean particle size decreases and the compressibility increases). More detailed analysis revealed that 93% of the laboratory-based D_R values fall within 30% deviation from the in-situ D_R estimated using the Cubrinovski and Ishihara (1999) correlation for the measured q_{t1n} , ($e_{max}-e_{min}$) ranging from 0.408 to 1.44, and approximated QNR of 4.5, 4.0, and 3.5 for $0.10 \text{ mm} < D_{50} < 0.18 \text{ mm}$, $0.044 \text{ mm} < D_{50} < 0.10 \text{ mm}$, and $D_{50} < 0.044 \text{ mm}$, respectively, of the CSS and MSS test specimens. Nearly half of the laboratory-based D_R values are within 20% deviation from the estimated in-situ D_R values. The scatter may stem from the database used to develop the Cubrinovski and Ishihara (1999) correlation containing soils with the maximum void ratio range of 0.870 compared to the maximum void ratio range of 1.44 for the test specimens in this study, effects of fabric not accounted for in the correlation, and the uncertainty associated with the q_{t1n} measurements due to the thin-layer effects. The thickness of these CSS/MSS test specimens is 15-16 mm, whereas each 10-cm² CPT measured tip resistance (assuming a zone of influence of five cone diameters) represents an “average” value over a thickness of 180 mm, which is about 11 times greater than the specimen thickness. The CPT captures the combined influence of multiple thin layers which can lead to misalignment between the CPT measurements and the true nature of the thin in-situ layers. Considering these issues, the laboratory-based D_R values provided in Table 5.3 are reasonable when compared to what is estimated using the D_R - q_{t1n} correlation proposed by Cubrinovski and Ishihara (1999). However, the laboratory-based D_R values of the soils tested in this study are judged to be more indicative of the state of the soil than those suggested by a CPT-based correlation due to the highly stratified nature of the soil deposits. Similarly, the tested soils are all judged to be non-plastic based on the laboratory index tests regardless of the I_c values obtained from the CPT tip and sleeve friction measurements in these highly stratified soil deposits.

5.5.2 Monotonic Simple Shear Testing

The MSS tests were performed on four specimens: SM-15-72, SM-40-66, ML-85-89, and ML-76-98 (the rows without a CSR value in Table 5.3). Their stress-strain responses and stress paths are presented in Figure 5.8. The stress paths (Figure 5.8b) reveal that all specimens generated positive excess pore water pressure initially (15-36 kPa). During this stage of loading, particles tend to move slightly in the direction of shearing, so large shear strains are not mobilized (Ishihara 1996), as shown in Figure 5.8a. Since the LVDT could not capture a very small shear strain that must have occurred due to the generation of positive excess pore water pressure, the initial portion of each MSS stress-strain curve (up to 0.3-0.8% shear strain) was corrected based on the estimated state index (Beyzaei 2017) and the corresponding stress-strain curve (Cubrinovski and Ishihara 1998). SM-15-72 contracted most ($\sigma'_{v,min}/\sigma'_{vo} = 0.63$), while ML-85-89 and ML-76-98 contracted least ($\sigma'_{v,min}/\sigma'_{vo} = 0.78$ for both specimens). The contractiveness of the response is moderately affected by σ'_{vo} , FC, and D_R , as indicated by the positive correlations and R^2 of about 0.5 for $\sigma'_{v,min}$ and σ'_{vo} , $\sigma'_{v,min}/\sigma'_{vo}$ and FC, and $\sigma'_{v,min}/\sigma'_{vo}$ and D_R (plots showing each of these data correlations are not presented for brevity). SM-15-72 is the only MSS

specimen with FC below 30-40%, indicating that it is the only MSS specimen that would have had the potential to experience the filling-of-voids process during shearing and hence the greatest potential to contract. Filling of voids also depends on the relative size of the coarse and fines fractions not analyzed herein. In addition, SM-15-72 was subjected to the highest σ'_{vo} as compared to the other three MSS specimens, which likely exacerbated the contractiveness of its response.

No specimen generated the limited flow condition (i.e., the shear stress did not decrease with decreasing the effective stress), as shown in Figure 5.8b and 5.8c. At the phase transformation (PT) point, the responses of all specimens changed from contractive to dilative due to the change in the mode of particle movement that generated negative excess pore water pressures. Test specimens with higher initial vertical effective stresses exhibited slightly higher shear stresses at their PT states (Figure 5.8b). Specifically, ML-85-89 ($\sigma'_{vo} = 69$ kPa), SM-40-66 ($\sigma'_{vo} = 79$ kPa), ML-76-98 ($\sigma'_{vo} = 88$ kPa), and SM-15-72 ($\sigma'_{vo} = 95$ kPa) experienced the shear stresses of 19.9, 23.2, 26.8, and 26.5 kPa, respectively, at PT. Their respective effective friction angles at PT are 24, 22, 20, and 21 degrees, assuming the horizontal plane is the plane of the maximum stress obliquity, $\tan^{-1}(\tau_{PT}/\sigma'_{v,PT})$.

The soil fabric of high-quality “undisturbed” specimens is affected by particle size, particle shape, particle distribution, and the arrangement of particles, their contacts, and pore spaces through the depositional environment, which are all important factors in addition to relative density. The geologic age and the previous seismic strain history are other key factors that can influence the liquefaction potential of soil, though difficult to quantify, they were likely negligible because the soils were young as they likely liquefied at least once during the CES.

Test specimens ML-76-98 ($\sigma'_{vo} = 88$ kPa), SM-15-72 ($\sigma'_{vo} = 95$ kPa), ML-85-89 ($\sigma'_{vo} = 69$ kPa), and SM-40-66 ($\sigma'_{vo} = 79$ kPa) reached 10% shear strain at 71, 63, 56, and 54 kPa of shear stress, respectively (Table 5.3). When the shear stress at 10% shear strain is normalized by σ'_{vo} , the mobilized normalized shear stress of the soils decreases in the following order: ML-85-89 ($\tau_{\gamma=10\%}/\sigma'_{vo} = 0.82$), ML-76-98 ($\tau_{\gamma=10\%}/\sigma'_{vo} = 0.81$), SM-40-66 ($\tau_{\gamma=10\%}/\sigma'_{vo} = 0.69$), and SM-15-72 ($\tau_{\gamma=10\%}/\sigma'_{vo} = 0.66$). The higher mobilized normalized shear stress of the first two test specimens may be explained by the higher D_R (89% and 98% of ML-85-89 and ML-76-98, respectively, versus 66% and 72% of SM-40-66 and SM-15-72, respectively). However, they cannot be compared directly in terms of D_R because ML-85-89 and ML-76-98 have higher FC than SM-40-66 and SM-15-72 (85% and 76%, respectively, versus 40% and 15%, respectively). Finally, at 10% shear strain, ML-76-98, SM-15-72, ML-85-89, and SM-40-66 have similar effective friction angles: 30, 31, 29, and 30 degrees, respectively (Table 5.3), as calculated under the assumption of the horizontal plane being the plane of the maximum stress obliquity, $\tan^{-1}(\tau_{\gamma=10\%}/\sigma'_{v,\gamma=10\%})$.

5.5.3 Cyclic Simple Shear Testing

In the interpretation of the CSS test results, liquefaction triggering is defined by the point in which 5% single-amplitude (SA) shear strain developed. The liquefaction triggering criterion of the pore water pressure ratio (r_u) reaching nearly 100% for clean sands or approximately 95% for silty soil (Ishihara 1996) is also examined. The applied cyclic stress ratio, CSR, and the number of loading cycles to trigger liquefaction, $N_{c,5\%SA}$, are reported in Table 5.3.

Representative responses of five specimens (i.e., SP-2-88, SM-43-76, SM-43-56, ML-64-82, and ML-74-100) subjected to the CSR of 0.16, 0.17, 0.20, 0.20, and 0.18, respectively, are shown in Figure 5.9. These SM and ML specimens originate from the same sampling tubes as the MSS test specimens. The SP specimen was added for reference.

In the first quarter cycle of the CSS test, the test specimens developed positive excess pore water pressures, and the vertical effective stress decreased progressively, similarly to their MSS responses (Figs. 8 and 9). The largest drop in the vertical effective stress in the cyclic tests occurred during the first loading cycle. The vertical effective stresses decreased by 29, 33, 41, 42, and 34% relative to σ'_{vo} for SP-2-88, SM-43-76, SM-43-56, ML-64-82, and ML-74-100, respectively. SP-2-88, SM-43-76, and ML-74-100 reached a reduction in σ'_{vo} by 50% in the third cycle of loading, while SM-43-56 and ML-64-82 specimens reached a 50% decrease in σ'_{vo} in the second cycle of loading. The vertical effective stress eventually reached nearly zero in the CSS test specimens indicating liquefaction was triggered based on the r_u criterion discussed previously.

The cyclic response experienced by the dense, clean sand and silty soil specimens in this study is characterized by cyclic mobility with limited strain potential (herein called cyclic mobility) as opposed to the condition with unlimited strain potential (i.e., flow liquefaction). SP-2-88, SM-43-76, SM-43-56, ML-64-82, and ML-74-100 developed 5% SA shear strain in the 11th, 12th, 9th, 15th, and 14th cycles of loading, respectively (Figure 5.9). The number of cycles to liquefaction triggering tends to increase moderately with increasing FC and increasing D_R . ML-64-82 and ML-74-100 have 64% and 74% fines, respectively, as compared to SM-43-76 and SM-43-56, both with 43% fines. ML-64-82 and ML-74-100 also have higher D_R than SM-43-76 and SM-43-56 (82% and 100%, respectively, versus 76% and 56%, respectively). Even though SP-2-88 has only 2% fines, its relatively high D_R of 88% underlines the importance of D_R for the cyclic response of clean sands. Unlike the other four test specimens that gradually developed the shear strain under repeated loading, SP-2-88 started accumulating a considerable amount of shear strain after the 4th loading cycle such that the SA shear strain increased by about 3.6% through the 8th loading cycle, after which a shear strain increment decreased and the test specimen continued developing the shear strain in a fairly steady manner. It is also noteworthy that the shear strain developed at a slower rate for ML-64-82 than for the other four CSS specimens even though it was subjected to the highest CSR and did not have the highest D_R (or FC). The somewhat weak correlation between the soil parameters, such as D_R , and the soil's cyclic resistance suggests other unquantified factors, such as soil fabric, were important in these high-quality "undisturbed" soil specimens.

Figure 5.10 indicates that the general stress-strain response of the five CSS specimens in the second loading cycle is characterized by relatively high stiffness. The differences in the hysteresis loops among the five specimens are subtle in both the second cycle and the liquefaction-triggering cycle, as defined by 5% SA shear strain. However, the soil stiffness and strength degraded significantly in the liquefaction-triggering cycle relative to the second cycle of loading. In the third cycle following the liquefaction triggering, the soil stiffness and strength degraded further. SP-2-88 and ML-64-82 experienced less shear strain accumulation in the third post-liquefaction-triggering cycle than SM-43-76, SM-43-56, and ML-74-100 (10% and 11%, respectively, of double-amplitude (DA) shear strain as compared to 14, 15, and 15%, respectively, of DA shear strain). This difference cannot be explained by a single soil parameter. SP-2-88 was

subjected to the lowest σ'_{vo} (55 kPa) and CSR (0.16), while ML-64-82 was subjected to the same CSR as SM-43-56 (0.20) and σ'_{vo} that was only slightly lower than that of SM-43-56 (71 kPa versus 79 kPa, respectively).

The r_u - N_c curves in Figure 5.11 show the pore water pressure development within the five CSS specimens during the first ten cycles of loading. The excess pore water pressures generated by the CSS test specimens are generally similar in both the pattern and magnitude. The first peak in the pore pressure ratio occurs at the end of the first cycle because the contractive response dominated throughout the entire cycle, which yielded to the greatest amount of excess pore water pressure development during a cycle of loading. The contractive response of the CSS test specimens is consistent with that observed for the MSS test specimens. In the subsequent cycles, the positive and negative loading with stress ratios above the PT points caused the CSS test specimens to experience the dilative response and generate negative excess pore water pressures, as manifested by the troughs, while the positive and negative unloading, i.e., stress ratios below their PT points, resulted in the contractive response and positive excess pore water pressures, as displayed by the peaks. The excess pore water pressure polarity changed at approximately load reversal points.

All five CSS specimens tended to experience more contractive than dilative response, which resulted in accumulation of positive excess pore water pressures with each loading cycle. SP-2-88 experienced the negligible dilative response in the first two cycles of loading. In the third loading cycle, its dilative response became more prominent; however, it was still small relative to its contractive response and significantly smaller than the dilative response of the other four CSS specimens. The significant increase in r_u for SP-2-88 began with the fourth cycle and the specimen reached $r_u=0.90$ at the end of the fifth cycle. By comparison, SM-43-56 and ML-64-82 attained $r_u=0.90$ at the end of the sixth cycle, SM-43-76 at the end of the seventh cycle, and ML-74-100 at the end of the eighth cycle. Moreover, during the first three cycles of loading, the r_u is higher for SM-43-56 and ML-64-82 than for SP-2-88, SM-43-76, and ML-74-100. This trend may be due to the slightly higher CSR imposed on SM-43-56 and ML-64-82 (0.20) than on SP-2-88, SM-43-76, and ML-74-100 (0.16, 0.17, and 0.18, respectively). The CSS test specimens attained r_u of 0.93 to 0.96 after ten loading cycles. Additional cycles of loading did not increase the final r_u value appreciably (i.e., $r_{u,final} = 0.95$ to 0.98).

The cyclic resistance ratio, CRR, curves for the eleven soil sets were fitted to the CSR- $N_{c,5\%SA}$ data points using the shapes of typical CRR curves (e.g., Tatsouka et al. 1986). As shown in Figure 5.12, the CRR curves are fairly steep at N_c values less than about 10, which is typical for dense, dilative soil. The relative densities of the test specimens are at least 80% except for two soil sets with the average D_R of 75% and 60%, so this might have been expected. The angularity of the soil particles may be one of the many factors contributing to the dilative soil behavior thus the steep shape of the CRR curves. Moreover, the overall shapes of the CRR curves are similar. The influence of minor changes in D_R or σ'_{vo} on differences in the shapes are difficult to discern. However, there is a slight tendency of CRR at the 15th loading cycle (an equivalent to a M_w 7.5 earthquake) to increase for soils with higher D_R . The CRR curve can also be described by the slope, i.e., the non-linear least-square fitting parameter, b-value, which is given in Table 5.3. The b-values range from 0.23 to 0.42, with one high value of 0.52. Within the relatively small range of D_R of most of these test specimens and the variation in the range of cycles among

the soil sets over which the slope was fit, there was not a systematic increase in b with increasing D_R . Unlike uniform reconstituted test specimens of similar materials, the inherent variability of the native soil test specimens and their different fabric, etc., obscured expected trends.

5.5.3.1 Silty Sand and Sandy Silt Responses

The use of fines content in the USCS to classify soil as either coarse-grained or fine-grained is not expected to differentiate soil response for these uniform sand and silt soils. To explore this issue, the CSS responses of a silty sand specimen (SM with FC=44% and PI=0, SM-44-80) and sandy silt specimen (ML with FC=54% and PI=0, ML-54-74) are compared in Figure 5.13. The test specimens were taken from the same sampling tube and have similar relative densities (i.e., SM: 80% and ML: 74%). They are strikingly similar in their particle size and shape (Figure 5.4a and 5.4b). The average roundness values of the silty sand coarse-fraction and fines-fraction specimens are 0.21 (angular) and 0.22 (angular), respectively. The average roundness values of the sandy silt coarse-fraction and fines-fraction specimens are 0.20 (angular) and 0.24 (angular), respectively. Both soils are composed predominantly of low-sphericity particles (i.e., SM coarse-fraction and fines-fraction specimens both have 80% of low-sphericity particles and ML coarse-fraction and fines-fraction specimens have 80% and 70%, respectively, of particles with low sphericity). The mean particle size, D_{50} , values of the SM and ML are also comparable (i.e., 0.08 mm and 0.07 mm, respectively).

The SM and ML test specimens shown in Figure 5.13 (with additional details in Table 5.3) were subjected to practically the same CSR (0.215 and 0.210, respectively) after consolidation to essentially the same initial mean effective stress (45-46 kPa). Liquefaction was triggered in both specimens at $N_{c,5\%SA}=11$. In the first loading cycle, both specimens exhibited the contractive responses and developed positive excess pore water pressures at the same rate. Near the end of testing, at the end of the 14th loading cycle, the silty sand reached a r_u value of 0.99, whereas the sandy silt reached a r_u value of 0.95. The silty sand tended to generate slightly higher positive excess pore water pressures in each cycle, which led to its stress path being offset slightly to the left relative to the stress path of the sandy silt. However, the difference in the vertical effective stress drop/increase at the same point in a loading cycle did not exceed 6%, which is negligible considering that two natural soil specimens are not identical. Both specimens developed nearly equal shear strains and their stiffness degraded to almost the same level with each loading cycle. The DA shear strain of 12% was developed in the final 14th cycle by both specimens.

These test results indicate that the cyclic response of soil with 40-60% of non-plastic fines responds similarly regardless of the differing UCSC classifications of SM and ML. The silty sand (SM) with FC exceeding the transitional FC of 30-40% responds similarly to the sandy silt (ML) because both soils have about the same relative density, soil fabric, stress history, and initial effective stress. The cyclic responses of the SM and ML soils are controlled by the fines fraction of the soil. The amount passing the No. 200 sieve does not change anything fundamental in the cyclic response of a uniform, very fine sand with silt and a uniform, very coarse silt with sand.

5.5.4 Post-Cyclic Monotonic Simple Shear Testing

The post-cyclic monotonic tests on the CSS test specimens display responses like those observed in the last loading cycle of the CSS tests, as shown in the normalized stress path and normalized stress-strain plots in Figure 5.14. The test specimens dilated and generated negative excess pore water pressures. Test specimens SP-2-88, SM-43-76, SM-43-56, and ML-64-82 attained $\sigma'_v/\sigma'_{v0} = 1.0$ (where σ'_{v0} is the vertical effective stress at the end of consolidation, prior to CSS testing) at 21.4, 13.4, 18.8, and 12.9 % shear strain, respectively. Only ML-74-100 did not regain its initial vertical effective stress as a result of post-cyclic monotonic loading ($\sigma'_v/\sigma'_{v0} = 0.58$ at $\gamma = 22\%$).

In general, higher post-cyclic stiffness is observed for specimens with lower cyclic stiffness degradation. Figure 5.14b illustrates the variability in post-cyclic stiffness among the five test specimens. The highest stiffness in the post-cyclic MSS loading was experienced by ML-64-82, a test specimen with the stiffest response in the last cycle of loading (considering both positive and negative loading/unloading together), while the lowest post-cyclic stiffness was displayed by ML-74-100, a test specimen with the lowest stiffness over the last loading cycle. At 10% shear strain, the values of the post-cyclic monotonic shear stress normalized by the initial vertical effective stress (τ/σ'_{v0}) for ML-64-82 and ML-74-100 are 0.42 and 0.18, respectively. The post-cyclic stiffness of SM-43-76 is only slightly smaller than that experienced by ML-64-82 (at 10% shear strain, τ/σ'_{v0} is 0.37 as compared to 0.42), even though its stiffness in the last loading cycle is relatively lower. Moreover, SP-3-84 experienced the highest post-cyclic stiffness, $\tau/\sigma'_{v0} = 1.73$ at 10% shear strain (Table 5.3). This test specimen, subjected to the CSR of 0.33 in the CSS test, accumulated 12% DA shear strain in ten loading cycles. By comparison, two test specimens with the same FC, SP-2-88 and SP-3-78, responded to the post-cyclic monotonic shearing with significantly less dilation and generation of negative excess pore water pressures. Their τ/σ'_{v0} at 10% shear strain are 0.28 and 0.14, respectively. They were loaded with CSR of 0.16 and 0.15, respectively, and were loaded with 19 and 22 cycles, respectively, in total, during which they both accumulated 14% of DA shear strain.

The effective friction angles at 10% shear strain, $\phi'_{\gamma=10\%}$, evaluated as $\tan^{-1}(\tau_{\gamma=10\%}/\sigma'_{v,\gamma=10\%})$, are practically identical for the post-cyclic test results shown in Figure 5.14 (i.e., 34-35 degrees). These values are higher than those developed in the MSS in similar soil by only several degrees (Table 5.3). However, as expressed through τ/σ'_{v0} at 10% shear strain, the stiffness of the post-cyclic test specimens was significantly lower than those experienced by the MSS test specimens (Table 5.3). The initial effective stresses of the post-cyclic test specimens were nearly zero, while the initial effective stresses of the MSS test specimens were much higher (the mean effective stress ranged from 48 kPa to 64 kPa). Also, the previous cyclic loading of the test specimens lowered their stiffness and the stiffness resulting from the initial fabric of the “undisturbed” specimens was erased by deformation during the CSS loading.

Lastly, Figure 5.14b indicates that the post-cyclic stress-strain curve of ML-74-100 begins to plateau at approximately 16% shear strain. The stress-strain curves of SP-2-88, SM-43-76, and SM-43-56 exhibit minor bending, while the stress-strain curve of ML-64-82 displays no bend. The non-negative values of the actual pore water pressure inside the specimens suggest that cavitation did not occur. The observed bending of the stress-strain curve may be due to yielding of soil as it approached steady state. Similarly, the MSS test

results show slight bending at large shear strains for SM-15-72, SM-40-66, and ML-76-98 and almost no bending for ML-85-89 (Figure 5.8a).

5.5.5 Comparison of Field-Corrected Laboratory-Based CRR with CPT-Based CRR

The laboratory-based CRR values that correspond to the 15th loading cycle (equivalent to a M_w 7.5 earthquake) were corrected by a factor of 0.9 to account for multidirectional shaking of representative soil elements in the field during earthquakes (Seed 1979). The obtained CRR_{CSS} values are compared with the cyclic resistance values derived from the CPT-based Boulanger and Idriss (2016) liquefaction triggering procedure, CRR_{BI16} , using the I_c -FC correlation with C_{FC} of 0.13 as suggested by Maurer et al. (2019) for Christchurch soil and the laboratory-based FC available only for the test specimen origin depths (Figure 5.15). The demand on the soil induced by the 2010 Darfield, 2011 Christchurch, and 2011 June earthquakes was corrected for the duration of shaking (through an earthquake magnitude scaling factor, MSF) and the effective overburden stress (through a K_σ factor) to a reference M_w 7.5 and $\sigma'_v=1$ atm (Boulanger and Idriss 2016). The June 2011 earthquake was modeled as a M_w 6.2 earthquake to account for the excess pore water pressure at the time of the second M_w 6.0 June 2011 earthquake that resulted from the first M_w 5.3 June 2011 earthquake (van Ballegooy et al. 2014). The CSR_{BI16} for the three earthquakes is also shown in Figure 5.15. The additional input parameters were the peak ground acceleration, PGA, by Bradley and Hughes (2012), probability of liquefaction, P_L , of 50% (the actual response of the site is compared to the median CPT-based estimate to remove bias), I_c cutoff value of 2.6 as a threshold between liquefiable and non-liquefiable soil (Lees et al. 2015), and the groundwater table depths at the time of the earthquakes (CGD 2014).

The CRR_{CSS} values for the 11 soil sets range from 0.14 to 0.19 (Table 5.3). These values are generally consistent with CRR_{BI16} . A difference between CRR_{CSS} and CRR_{BI16} is observed for the test set of ML-99-86, ML-99-92, and ML-98-82 (S33-DM3-3U). CRR_{BI16} indicates that this soil is not susceptible to liquefaction based on $I_c > 2.6$, whereas $CRR_{CSS} = 0.15$. If the Bray and Sancio (2006) liquefaction susceptibility criterion of $PI \leq 12$ and $w_c/LL \geq 0.85$ (where w_c is natural water content) is applied, this soil is susceptible to liquefaction because its $PI=0$ and $w_c/LL > 0.85$. The increase of the I_c cutoff to 2.9 for this soil results in the CRR_{BI16} of 0.13, which is comparable with the CRR_{CSS} of 0.15. Another dissimilarity between the CRR_{CSS} and CRR_{BI16} occurs in part for the test set of SM-43-76, SM-39-79, and SM-29-71 (S23-DM2-6U). The CRR_{BI16} averaged over a depth range from 10 cm above to 10 cm below these test specimens is 0.21, which is higher than the CRR_{CSS} of 0.14. However, the higher CRR_{BI16} value is influenced significantly by a thin layer with $FC = 43\%$, which increases CRR_{BI16} significantly because of the large increase in q_{t1ncs} as a function of FC. As discussed previously, the CSS specimens are about 15-mm thick, and the resolution of CPT is not sufficiently high to adequately characterize such thin layers. The CPT captures a combined influence of multiple thin layers at these highly stratified silty soil sites so “smeared” CPT measurements do not reflect the actual scale and nature of in-situ layering at the studied sites.

For all four sites, the greatest earthquake-induced demand on soil, CSR_{BI16} , is due to the Christchurch event, the intermediate CSR_{BI16} is due to the Darfield event, and the lowest CSR_{BI16} is due to the June 2011 event (Figure 5.15). For the June 2011 earthquake, the laboratory- and CPT-based FS_L values are generally comparable; however, they are

often marginal ($FS_L = 1.0 \pm 0.1$), meaning it is not clear from the CPT-based approach whether liquefaction was triggered and whether liquefaction effects would be estimated to manifest at the ground surface. Due to the greater uncertainty inherent in its assessment of liquefaction triggering, the June 2011 event was not considered in assessing potential inconsistencies between liquefaction observations at the sites and FS_L calculated using the laboratory-based or CPT-based CRR values.

The laboratory-based FS_L values for the Darfield earthquake range from 0.45 to 0.67, while CPT-based FS_L for the Darfield earthquake include values from 0.47 to 0.88. For the Christchurch earthquake, the range of the laboratory-based FS_L values is from 0.35 to 0.51, whereas the CPT-based FS_L values range from 0.31 to 0.60. The calculated FS_L for both the laboratory and field methods are consistent and well below 1.0 for both earthquakes, indicating liquefaction at all four sites was triggered at the element level.

The CSS test results in this study suggest that all four sites liquefied during the Darfield and Christchurch earthquakes. Therefore, the cyclic resistances evaluated by CSS testing do not explain the absence of surface manifestation of liquefaction at the sites. The element-scale laboratory CSS test specimens do not capture the mitigating effects of liquefaction at the sites such as communication between layers in their dynamic response and pore water pressure redistribution (e.g., Cubrinovski et al. 2019, Hutabarat and Bray 2021). The presence of a soil layer with hydraulic conductivity lower than that of a soil layer below has the potential to impede the propagation of excess pore water pressures toward the ground surface. However, these test results provide useful insights and simple shear mode deformation data that can be used to calibrate simple shear constitutive models to support effective stress analysis of the sites to investigate the reasons for the observed field responses.

5.6 CONCLUSIONS

Cyclic and monotonic simple shear testing of high-quality “undisturbed” test specimens was performed to evaluate the cyclic response of silty soils at sites that did not typically manifest liquefaction effects at the ground surface for the intense Christchurch earthquake, though simplified CPT-based methods indicated liquefaction was triggered. The first cyclic simple shear testing of “undisturbed” native soil specimens of Christchurch soils was performed in this study. Through high-quality DM sampling, important effects such as soil fabric were preserved in addition to relative density.

The key findings of the study are:

- The D_R evaluated for test specimens with 2-99% non-plastic fines ranged from 56% to 100%. These values are reasonable compared with the in-situ D_R estimated using the D_R - q_{tln} correlation for fines-containing soil and considering the uncertainties associated with the thin-layer effects on CPT measurements and the correlation itself.
- The MSS test specimens generated positive excess pore water pressures initially, after which they passed through the phase transformation point and developed negative excess pore water pressures. The MSS effective stress paths indicated the soil response would likely be cyclic mobility with limited strain potential. The test specimens did not reach the steady state of deformation.

- In the CSS tests, the specimens exhibited a fully contractive response in the first cycle of loading during which they lost a significant percent of the initial vertical effective stress. In the subsequent cycles, the specimens generated both positive and negative excess pore water pressures until their vertical effective stresses reduced to nearly zero and liquefaction was triggered according to the $r_u \approx 95\text{-}100\%$ criterion. The excess pore water pressures induced the gradual shear strain development and all specimens experienced cyclic degradation. The observed response of the CSS specimens was indeed cyclic mobility.
- Though the CSS test specimens had 2-99% fines, the differences in the cyclic responses of the tested soil were subtle and could not be attributed to the variation in FC.
- The cyclic response of silty sand (SM) with less than 50% non-plastic fines did not differ from the cyclic response of non-plastic sandy silt (ML) with more than 50% fines. Both soil specimens had more than 30-40% fines, indicating their cyclic responses are controlled by the fines fraction of the soil. The amount passing the No. 200 sieve does not change anything fundamental in the cyclic response of a uniform, fine sand with silt and a uniform, coarse silt with sand.
- The cyclic resistances evaluated by CSS testing do not explain the absence of surface manifestation of liquefaction at the studied sites. The CSS laboratory-based field-corrected cyclic resistances were generally consistent with the cyclic resistances estimated by CPT-based liquefaction-triggering procedures. The calculated factors of safety against liquefaction using both cyclic resistances were well below one for the Darfield and Christchurch earthquakes indicating these soils liquefied during these earthquakes. The element-scale laboratory CSS test specimens cannot capture the in-situ system response associated with interaction between soil strata in their seismic response, pore water pressure redistribution, and flow of water.
- The post-cyclic MSS test effective stress paths and stress-strain responses mirrored those associated with the last loading cycle of the CSS tests. Specimens with higher stiffness degradation in the last cycle of loading typically responded with less stiffness in post-cyclic monotonic loading. The soil stiffness in post-cyclic monotonic tests was significantly lower than that in MSS tests, likely due to the large difference in the initial effective stress between the two types of tests, cyclic degradation, and the loss of fabric resulting from deformation during cyclic loading.
- The 15-mm thick test specimens in this study originate from sites whose subsurface profiles are complex systems comprised of thin layers (often only a few mm thick). The CPT cannot capture the true scale and nature of such thin layers so one should be mindful when comparing the laboratory-based soil properties with the CPT measurements as the CPT measurements reflect a combined influence of multiple in-situ thin layers. The instance of a difference between CRR_{CSS} of the soil susceptible to liquefaction and CRR_{BI16} of the “corresponding” soil layer with $I_c > 2.6$ underlines the importance of thin-layer effects, high-quality sampling, detailed soil logging, and laboratory testing at these highly stratified silty soil sites.

- The variations in parameters such as D_R and σ'_{vo} could not explain well the subtle differences in the cyclic stress paths and stress-strain responses observed in these tests. The differences in particle shape among specimens were too marginal to aid in categorizing the transitional responses discretely. Contacts of the angular, elongated particles in these soils likely contributed to dilative soil behavior. The liquefaction resistance of the high-quality “undisturbed” soil specimens was also affected by soil fabric formed by deposition, among other factors, which could not be quantified. Therefore, the subtle differences in the responses of the intermediate Christchurch soil are believed to be a result of the combined effects of confinement, relative density, particle shape, and soil fabric, among other factors.

The high-quality CSS test results provide important insights in the silty soil response during earthquakes and enhance our understanding of the liquefaction phenomenon. The natural silty soil specimens have varying degrees of heterogeneity due to their depositional environments (overbank deposits and swamps), which cannot be replicated with laboratory-prepared specimens. Some heterogeneity within a specimen is acceptable as long as the quality of testing is not adversely affected and the primary characteristics of a soil stratum are captured. The research study yields valuable data that can be incorporated into the existing international dataset to help improve empirical correlations regarding soil parameters, liquefaction triggering, and its consequential effects. Importantly, these test results provide guidance for calibrating simple shear-based soil constitutive models for use in dynamic effective stress analysis.

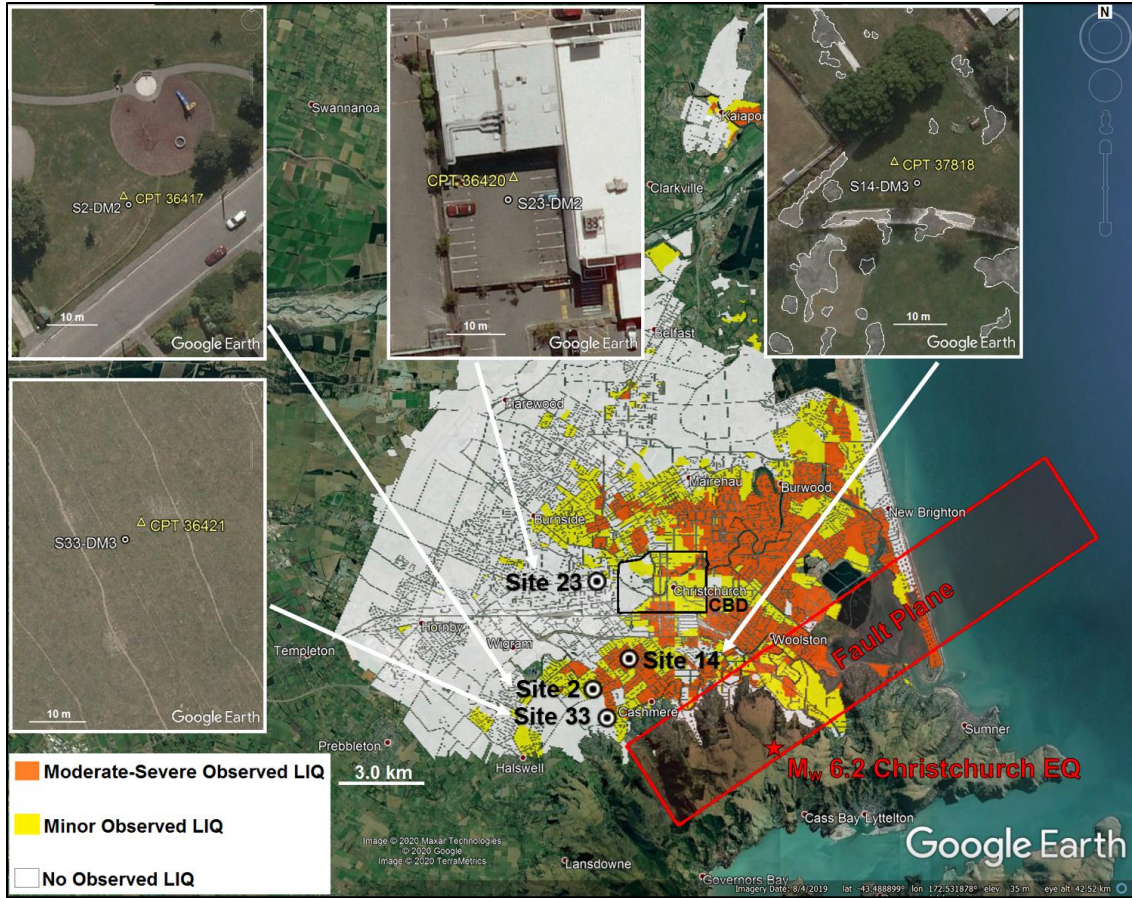


Figure 5.1. Site locations and liquefaction observations following the 2011 Christchurch earthquake; aerial photographs show absence of liquefaction ejecta at Sites 2, 23, and 33 and presence of moderate liquefaction ejecta at Site 14.

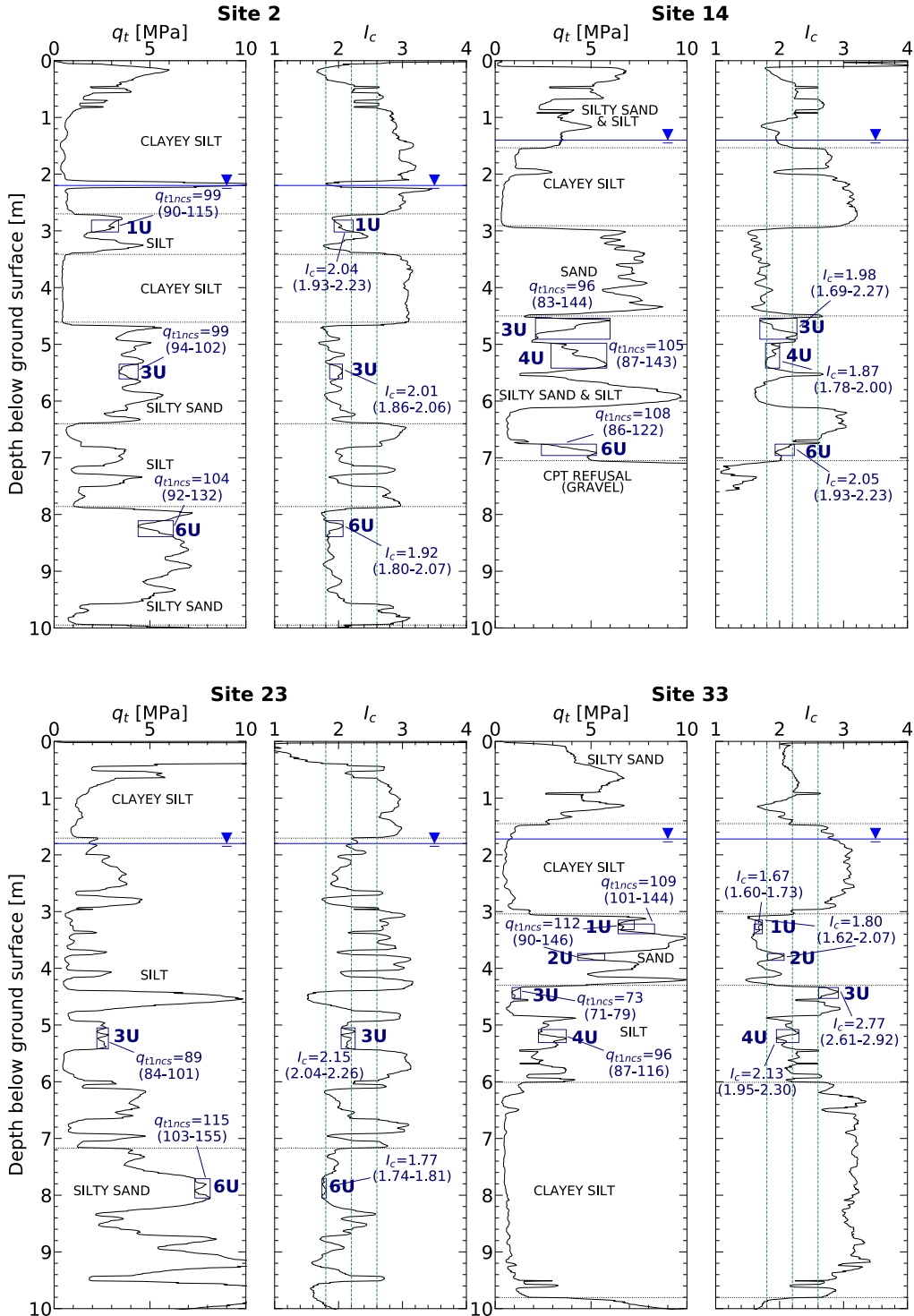


Figure 5.2. CPT tip resistance corrected for thin-layer effects and soil behavior type index profiles for sites 2, 14, 23, and 33. The q_{t1ncs} and I_c range for each set of specimens is based on q_{t1ncs} and I_c values that correspond to CPT measurements 10 cm above and below the specimen's mid-depth as well as agreement between I_c and the retrieved soil; q_{t1ncs} was computed using the I_c -FC correlation with $C_{FC} = 0.13$ and laboratory-based FC; q_{t1ncs} for S33-DM3-3U is with the application of $I_{c,cutoff} = 2.9$.



Figure 5.3. Test specimen appearance: (a) S14-DM3-4U-M (ML) before testing, (b) S23-DM2-6U-T3 (SM) after testing, and (c) S33-DM3-3U-T5 (ML) after testing.

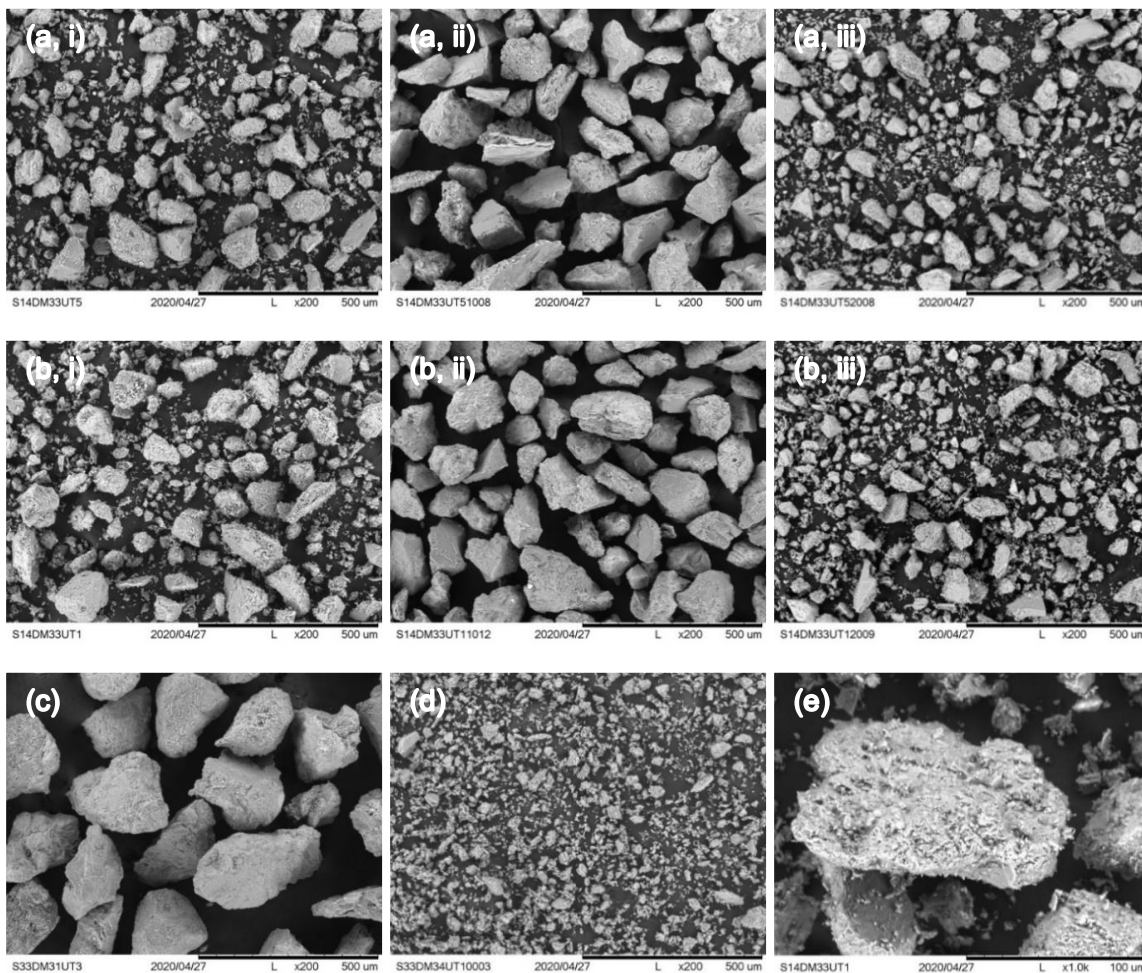


Figure 5.4. SEM images of soil [enlarged 200x except (e) which is enlarged 1000x]: (a) S14-DM3-3U-T5 (FC=44%): (i) “as-is” (coarse plus fines fraction), (ii) coarse fraction (particles $\geq 75\mu\text{m}$), and (iii) fines fraction (particles $\leq 75\mu\text{m}$); (b) S14-DM3-3U-T1 (FC=54%): (i) “as-is”; (ii) coarse fraction, and (iii) fines fraction; (c) S33-DM3-1U-T3 (FC=2%): “as-is”; (d) S33-DM3-4U-T1 (FC=99%): “as-is”; and (e) S14-DM3-3U-T1 (FC=54%): “as-is”.

Table 5.1. Particle shape characteristics of eight soil specimens.

Soil Specimen	FC [%]	Photographed Fraction	Average Roundness	Roundness Class	% of Low-Sphericity Particles
S33-DM3-1U-T3	2	Coarse	0.24	Angular	74
S14-DM3-3U-T5	44	Coarse	0.21	Angular	78
		Fines	0.22	Angular	78
S14-DM3-3U-T1	54	Coarse	0.20	Angular	80
		Fines	0.24	Angular	70
S14-DM3-6U-T3	74	Coarse	0.21	Angular	90
		Fines	0.22	Angular	74
S33-DM3-4U-T1	99	Fines	0.22	Angular	74

Table 5.2. Test specimen characteristics.

Specimen Name	Specimen Designation	Mid-depth [m]	USCS	FC [%]	G _s	e _{max}	e _{min}
SP-3-84	S33-DM3-1U-T2	3.322	SP	3	2.68	1.11	0.706
SP-2-88	S33-DM3-1U-T3	3.341	SP	2	2.68	1.14	0.730
SP-3-78	S33-DM3-1U-T4	3.359	SP	3	2.68*	1.16	0.709
SM-28-85	S33-DM3-1U-T1	3.215	SM	28	2.68	1.26	0.642
SM-15-75	S33-DM3-2U-T1	3.835	SM	15	2.70*	1.29	0.724
SM-43-76	S23-DM2-6U-T1	7.809	SM	43	2.69	1.31	0.565
SM-39-79	S23-DM2-6U-T2	7.828	SM	39	2.69*	1.29	0.575
SM-29-71	S23-DM2-6U-T3	7.848	SM	29	2.69	1.21	0.577
SM-15-72	S23-DM2-6U-M	7.945	SM	15	2.70*	1.16	0.635
SM-43-56	S2-DM2-3U-T1	5.446	SM	43	2.70	1.32	0.652
SM-44-58	S2-DM2-3U-T2	5.463	SM	44	2.70*	1.36	0.659
SM-47-65	S2-DM2-3U-T3	5.481	SM	47	2.70	1.43	0.668
SM-40-66	S2-DM2-3U-M	5.507	SM	40	2.70	1.44	0.644
ML-54-74	S14-DM3-3U-T1	4.708	ML	54	2.71	1.49	0.641
SM-44-80	S14-DM3-3U-T5	4.790	SM	44	2.71	1.40	0.612
ML-54-82	S14-DM3-3U-T6	4.808	ML	54	2.71*	1.48	0.612
ML-62-83	S14-DM3-3U-T7	4.558	ML	62	2.71	1.55	0.619
SM-46-76	S14-DM3-4U-T1	5.160	SM	46	2.69	1.40	0.607
ML-64-82	S14-DM3-4U-T2	5.302	ML	64	2.69*	1.51	0.647
ML-59-81	S14-DM3-4U-T3	5.319	ML	59	2.69	1.47	0.618
ML-85-89	S14-DM3-4U-M	5.008	ML	85	2.72*	1.78	0.723
ML-72-89	S2-DM2-6U-T1	8.172	ML	72	2.71	1.61	0.640
ML-87-84	S2-DM2-6U-T2	8.291	ML	87	2.71*	1.73	0.689
ML-57-87	S14-DM3-6U-T1	6.785	ML	57	2.69	1.46	0.564
ML-71-99	S14-DM3-6U-T2	6.821	ML	71	2.69*	1.65	0.641
ML-74-100	S14-DM3-6U-T3	6.838	ML	74	2.69	1.75	0.626
ML-76-98	S14-DM3-6U-M	6.859	ML	76	2.69	1.79	0.644
ML-99-86	S33-DM3-3U-T4	4.387	ML	99	2.71	2.17	0.857
ML-99-92	S33-DM3-3U-T5	4.419	ML	99	2.71*	2.43	0.991
ML-98-82	S33-DM3-3U-T6	4.439	ML	98	2.71	2.17	0.861
ML-99-94	S33-DM3-4U-T1	5.182	ML	99	2.70	2.20	0.912
ML-97-85	S33-DM3-4U-T2	5.198	ML	97	2.70	2.10	0.845
ML-98-89	S33-DM3-4U-T3	5.214	ML	98	2.70*	2.19	0.890
ML-92-82	S2-DM2-1U-T1	2.907	ML	92	2.71	1.76	0.703
ML-89-77	S2-DM2-1U-T2	2.931	ML	89	2.71*	1.72	0.687
ML-96-93	S2-DM2-1U-T3	2.951	ML	96	2.71	1.97	0.802
ML-92-97	S23-DM2-3U-T1	5.146	ML	92	2.69	1.81	0.717
ML-98-99	S23-DM2-3U-T2	5.203	ML	98	2.69	2.06	0.818
ML-99-91	S23-DM2-3U-T3	5.253	ML	99	2.69*	1.91	0.807
ML-99-91	S23-DM2-3U-T5	5.316	ML	99	2.69	2.05	0.828

Notes: The specimen designation is based on sampling, while the specimen name is based on the USCS, FC [%], and D_R [%]; G_s values without * are inferred from G_s* values for test specimens from the same sampling tube determined according to ASTM D854.

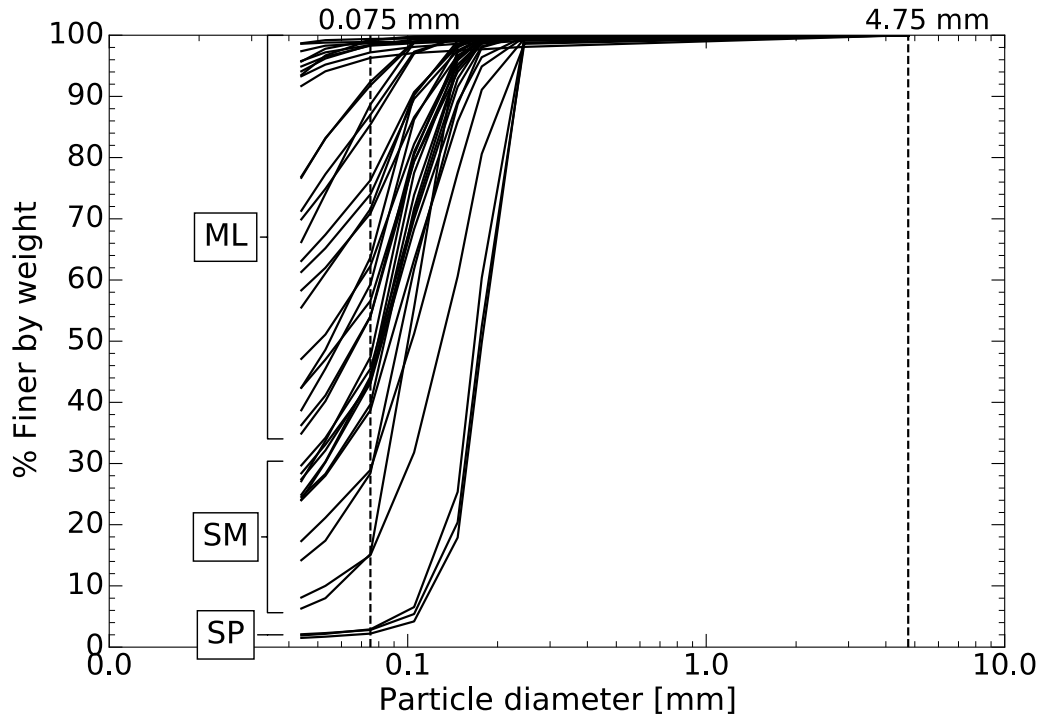


Figure 5.5. Particle size distribution curves for the test specimens.

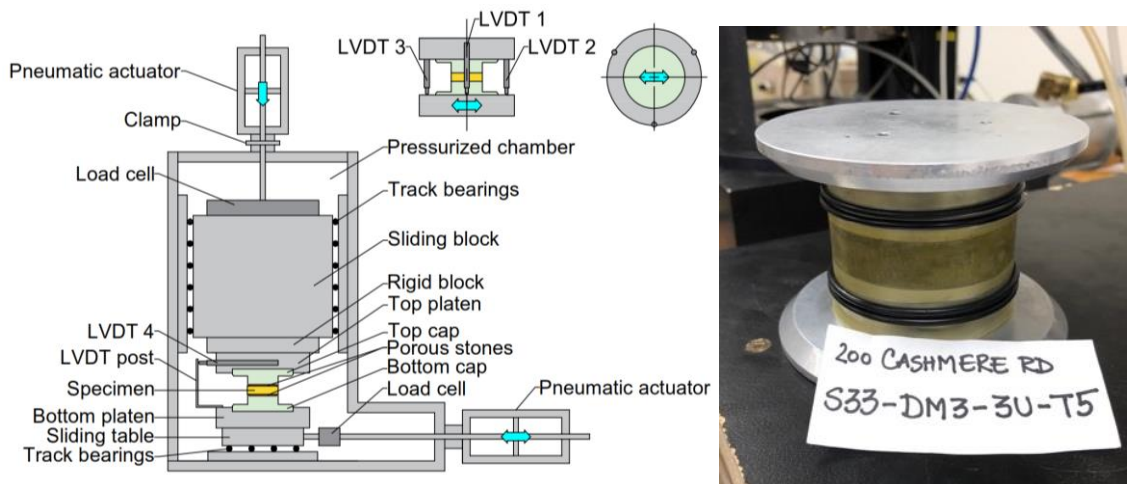


Figure 5.6. (a) UC Berkeley unidirectional simple shear device and arrangement of vertical LVDTs (modified after Cappellaro et al. (2021), not drawn to scale), and (b) simple shear test specimen encased in plain latex membrane and subjected to vacuum pressure.

Table 5.3. CSS, MSS, and post-cyclic MSS test results.

Specimen	B	e _c	D _R [%]	σ _{vo} ' [kPa]	K _o	CSR	N _{c,5%SA}	b	CRR _{CSS}	τ _{v=10%} [kPa]	φ' _{v=10%} [deg]
SP-3-84	0.91	0.771	84	53.3	0.50	0.33	6	-	-	92	34
SP-2-88	0.94	0.781	88	54.6	0.50	0.16	11			15	35
SP-3-78	0.91	0.808	78	55.6	0.50	0.15	10			8	35
SM-28-85*	0.96	0.733	85	53.8	0.51	0.17	24	0.30	0.17	12	40
SM-15-75	0.92	0.866	75	59.5	0.53	0.22	10			14	37
SM-43-76	0.99	0.749	76	95.2	0.50	0.17	12	0.42	0.14	35	34
SM-39-79	0.98	0.727	79	96.1	0.50	0.27	4			27	34
SM-29-71	0.96	0.761	71	95.1	0.51	0.14	19			10	38
SM-15-72	0.94	0.781	72	95.1	0.51	--	--	--	--	63	31
SM-43-56	0.95	0.946	56	78.5	0.55	0.20	9	0.33	0.15	21	34
SM-44-58	0.93	0.956	58	77.1	0.56	0.31	3			23	32
SM-47-65	0.94	0.934	65	78.6	0.55	0.14	37			20	34
SM-40-66	0.93	0.915	66	78.5	0.55	--	--	--	--	54	30
ML-54-74	0.90	0.861	74	65.4	0.55	0.21	11	0.35	0.17	34	33
SM-44-80	0.91	0.766	80	63.7	0.57	0.22	11			19	35
ML-54-82	0.92	0.772	82	65.5	0.55	0.28	7			34	34
ML-62-83	0.95	0.775	83	66.0	0.55	0.15	41			NA	NA
SM-46-76	0.94	0.798	76	68.6	0.55	0.30	5	0.38	0.17	12	36
ML-64-82	0.91	0.807	82	71.2	0.56	0.20	15			30	35
ML-59-81	0.92	0.782	81	72.0	0.56	0.15	31			9	40
ML-85-89	0.98	0.843	89	68.5	0.55	--	--	--	--	56	29
ML-72-89	0.99	0.751	89	103	0.55	0.22	7	0.33	0.15	5	37
ML-87-84	0.97	0.859	84	105	0.55	0.19	10			11	35
ML-57-87	0.93	0.684	87	85.7	0.60	0.26	9	0.34	0.17	28	33
ML-71-99	0.93	0.648	99	85.8	0.60	0.30	4			9	35
ML-74-100	0.93	0.629	100	86.9	0.60	0.18	14			16	34
ML-76-98	0.94	0.663	98	87.9	0.60	--	--			--	71
ML-99-86	0.95	1.05	86	61.7	0.61	0.22	6	0.24	0.15	13	33
ML-99-92	0.95	1.11	92	64.2	0.59	0.16	23			15	32
ML-98-82	0.94	1.10	82	65.1	0.59	0.18	11			9	33
ML-99-94	0.99	0.995	94	72.6	0.59	0.18	19	0.28	0.17	14	34
ML-97-85	0.93	1.04	85	73.0	0.60	0.25	8			5	36
ML-98-89	0.94	1.03	89	73.0	0.59	0.31	3			15	33
ML-92-82	0.93	0.890	82	53.8	0.56	0.20	8	0.52	0.15	8	33
ML-89-77	0.96	0.922	77	54.9	0.55	0.14	20			4	44
ML-96-93	0.96	0.888	93	55.4	0.55	0.28	5			6	39
ML-92-97	0.94	0.746	97	70.2	0.60	0.23	19			43	34
ML-98-99	0.93	0.828	99	73.5	0.60	0.18	29	0.23	0.19	29	34
ML-99-91	0.93	0.910	91	70.9	0.60	0.34	3			12	34
ML-99-91	0.94	0.938	91	71.4	0.60	0.25	5			6	42

Notes: Reported CRR_{CSS} values are derived from the CRR curves shown in Figure 5.12 and corrected for field conditions; τ_{v=10%} values correspond to post-cyclic monotonic and monotonic simple shear tests; the effective friction angles at 10% shear strain are calculated assuming the horizontal plane was the plane of the maximum stress obliquity, i.e., φ' = tan⁻¹(τ/σ'_v); * denotes a test specimen that might have been unintentionally overconsolidated during vacuum saturation to the maximum overconsolidation ratio of 1.9; NA = Not assessed.

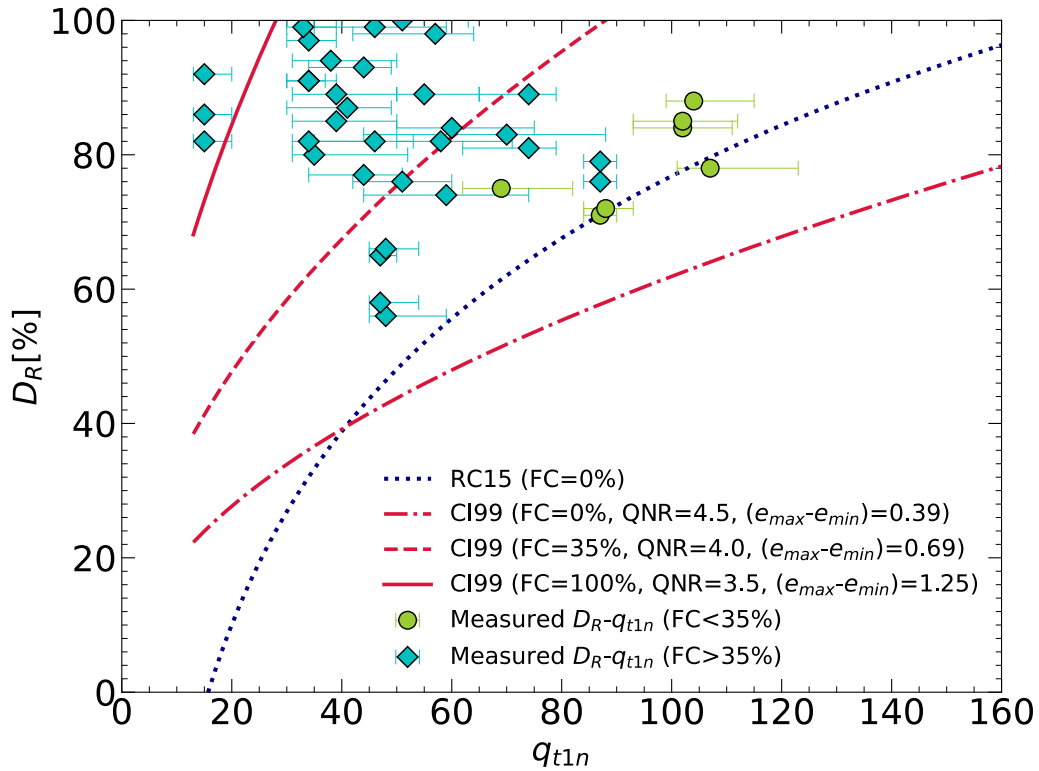


Figure 5.7. Comparison between laboratory-based D_R and in-situ D_R estimated using the Cubrinovski and Ishihara (1999) and Robertson and Cabal (2015) correlations. The horizontal bars correspond to the upper and lower q_{t1n} values measured over a depth range typically 10 cm above and below the specimen's mid-depth.

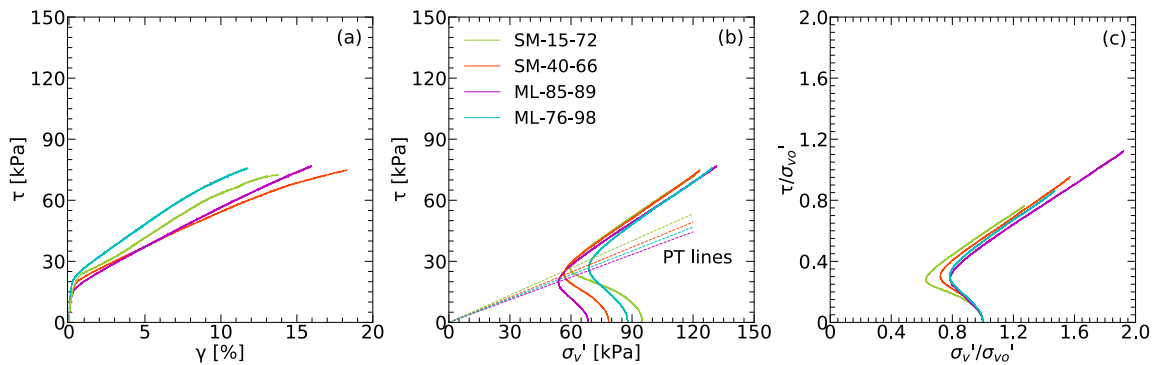


Figure 5.8. Monotonic simple shear response of four test specimens with the dashed lines representing phase transformation lines for the test specimens.

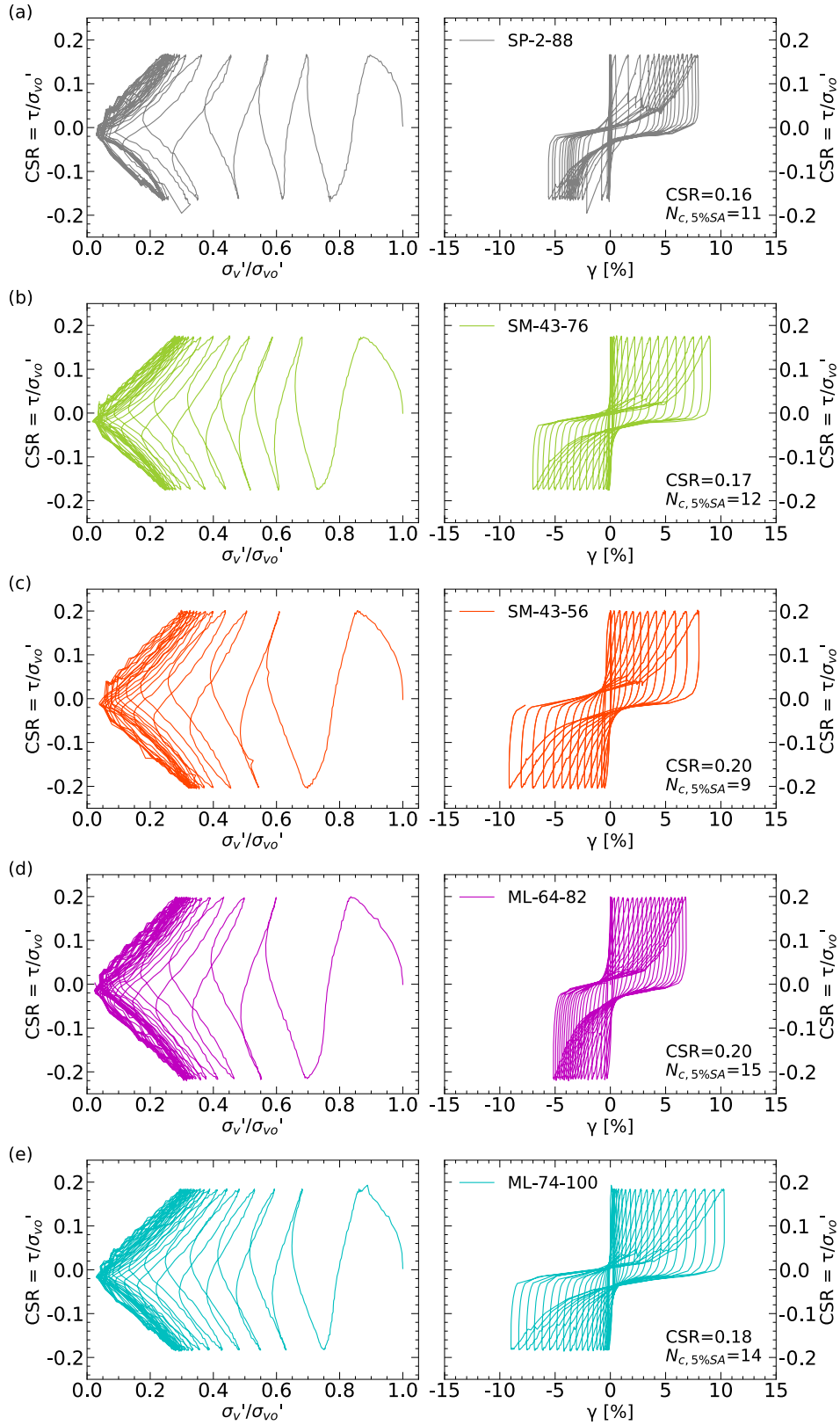


Figure 5.9. Cyclic simple shear response of test specimens: (a) SP-2-88, (b) SM-43-76, (c) SM-43-56, (d) ML-64-82, and (e) ML-74-100.

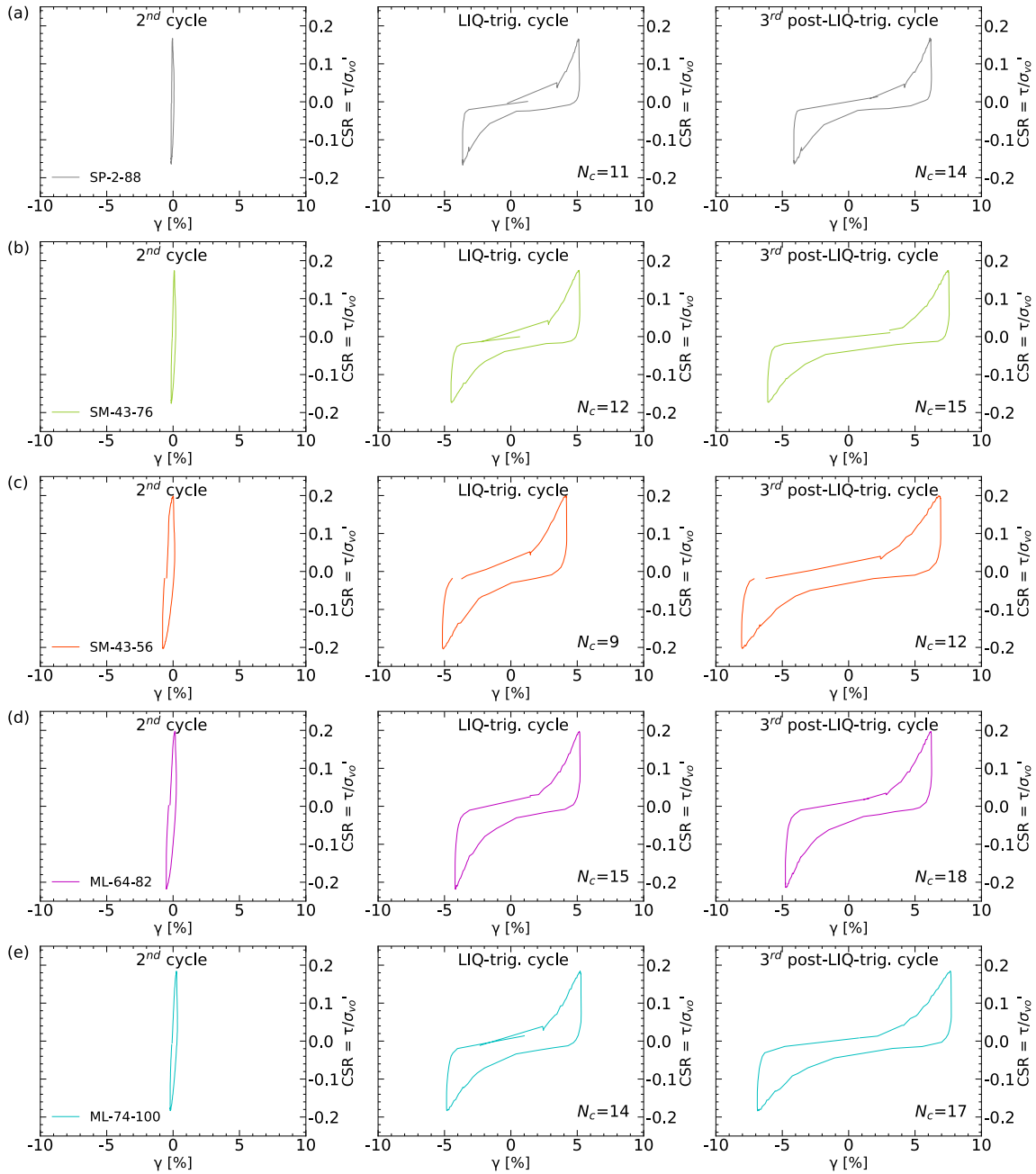


Figure 5.10. Shear stress-strain response in the second, liquefaction-triggering, and third post-liquefaction-triggering cycle: (a) SP-2-88, (b) SM-43-76, (c) SM-43-56, (d) ML-64-82, and (e) ML-74-100.

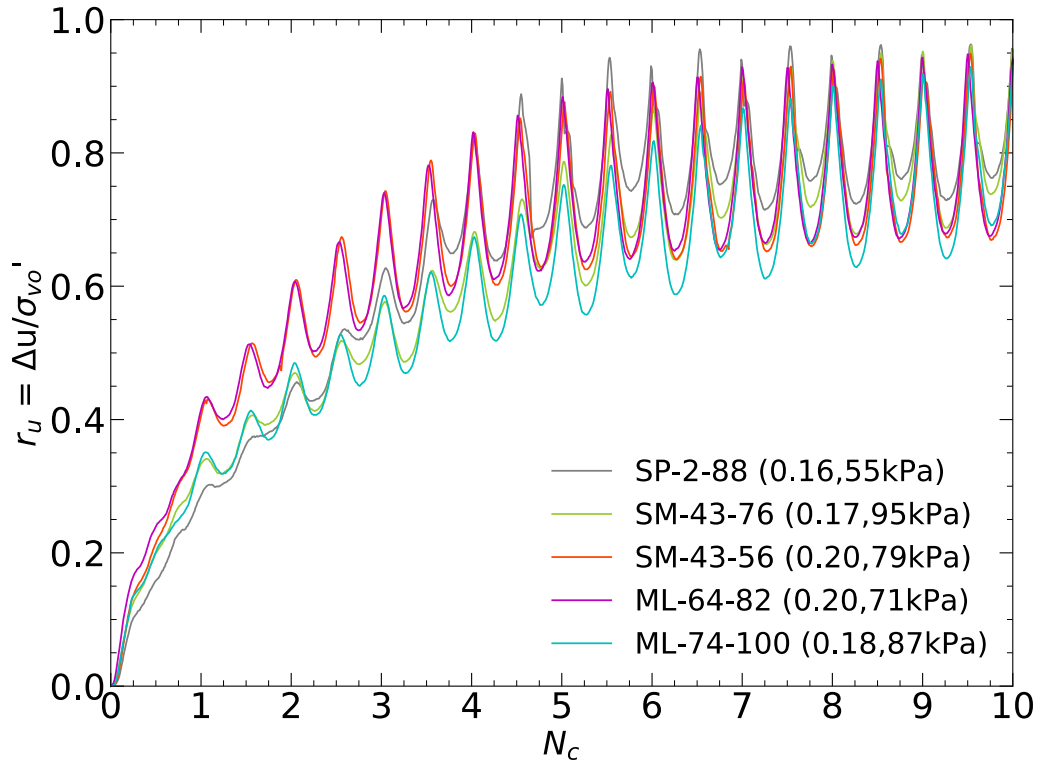


Figure 5.11. Excess pore water pressure generation during the first ten loading cycles for test specimens: SP-2-88, SM-43-76, SM-43-56, ML-64-82, and ML-74-100; values in parentheses correspond to CSR and σ'_{vo} , respectively.

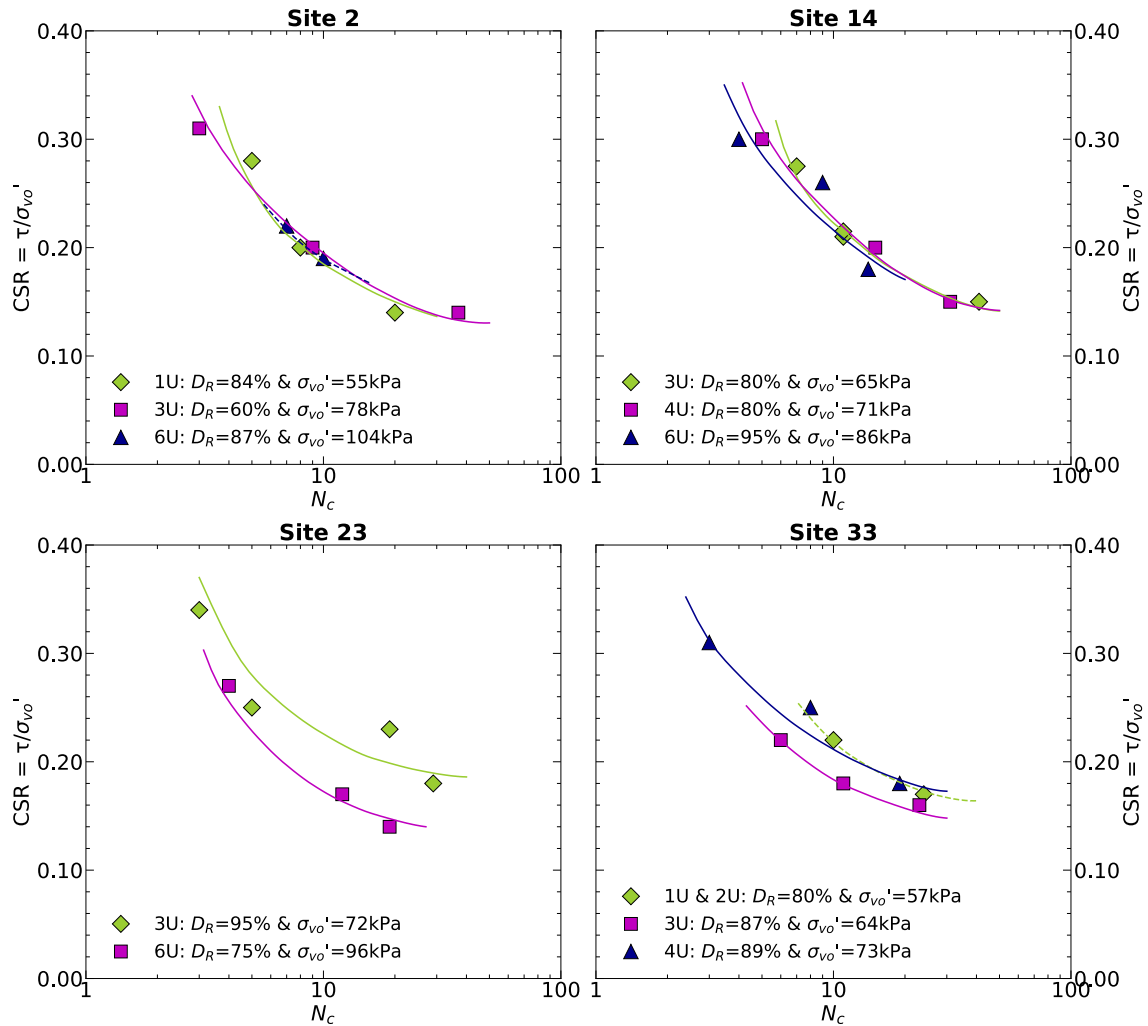


Figure 5.12. Cyclic resistance ratio curves for the simple shear test specimens; the provided D_R and σ'_{vo} represent an average for a set of test specimens.

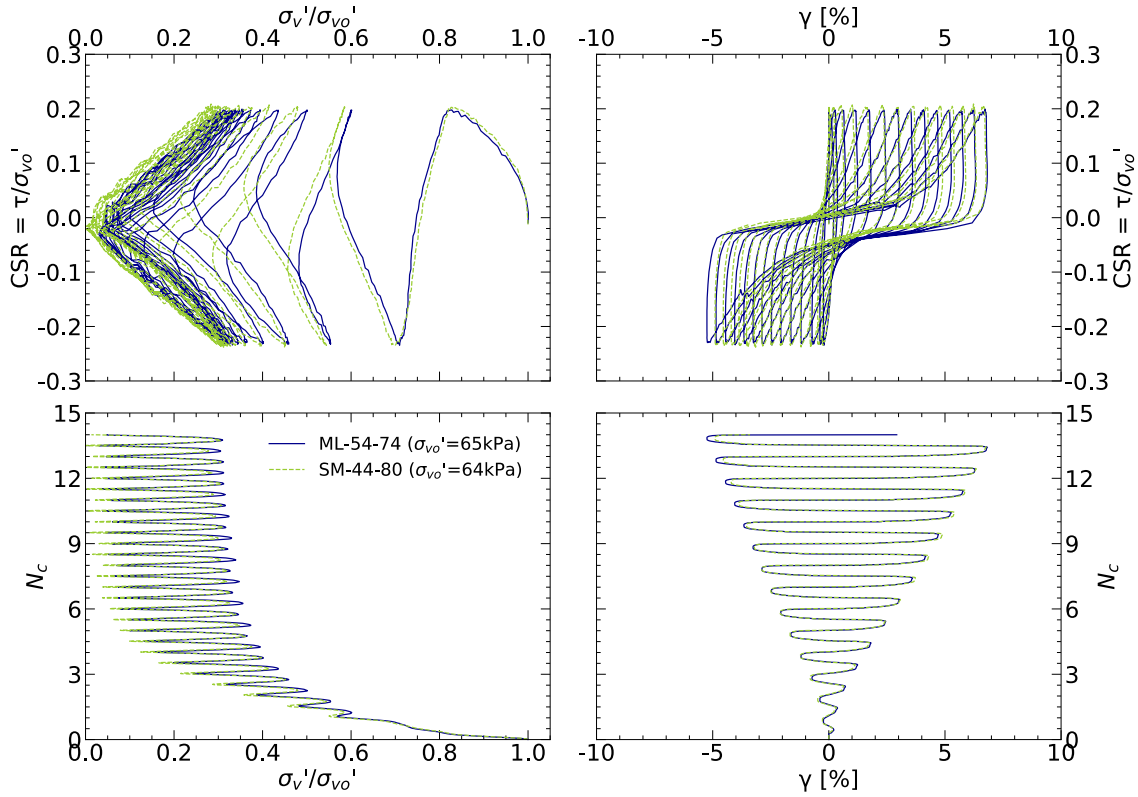


Figure 5.13. Comparison of cyclic simple shear responses of soil with 44% fines (SM-44-80) and 54% fines (ML-54-74).

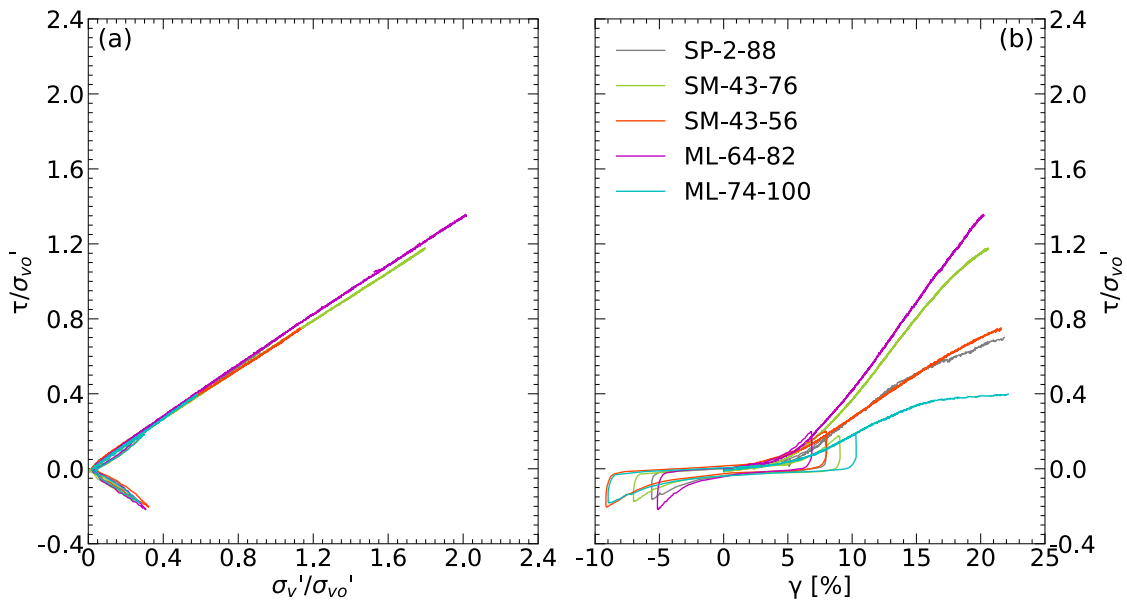


Figure 5.14. Post-cyclic monotonic simple shear response of the test specimens.

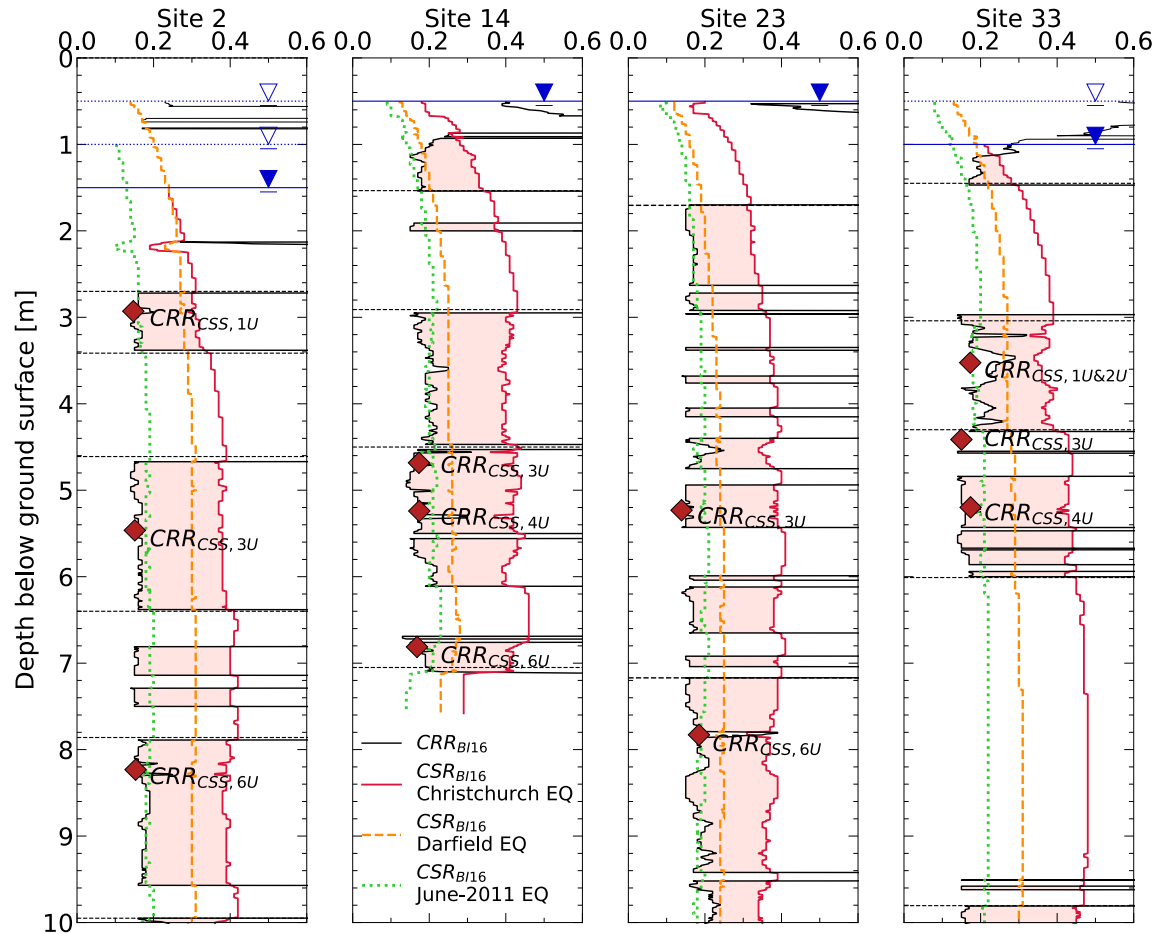


Figure 5.15. Comparison of the field-adjusted laboratory-based cyclic resistance ratio (CRR_{CSS}) and the Boulanger and Idriss (2016) estimated cyclic resistance (CRR_{BI16}) based on the I_c -FC correlation and laboratory-based FC at the test specimen origin depths with the cyclic stress ratio (CSR_{BI16}) adjusted for $M_w = 7.5$ and $\sigma'_{vo} = 1$ atm for the 2010 Darfield, 2011 Christchurch, and June 2011 earthquakes. Layers with $FS_L < 1$ for the Christchurch event are shaded.

6 CONCLUSIONS

6.1 SUMMARY

Through this research, liquefaction ejecta effects observed in Christchurch during the 2010-2011 Canterbury earthquake sequence were investigated and the liquefaction potential of silty soil deposits in Christchurch were investigated by performing advanced laboratory testing. The Canterbury earthquakes produced widespread and varying amounts of liquefaction ejecta in a modern urban setting. Sites throughout Christchurch experienced differing levels of ground shaking generated by four main earthquakes of the Canterbury earthquake sequence, i.e., the 4 Sep 2010 M_w 7.1, 22 Feb 2011 M_w 6.2, 13 Jun 2011 equivalent- M_w 6.2, and 26 Dec 2011 equivalent- M_w 6.1 earthquakes, and various levels of liquefaction ejecta-induced land damage, including no ejecta when state-of-the-practice methods indicated there should have been severe liquefaction-induced ground failure. The careful, comprehensive documentation of liquefaction and its effects in Christchurch, which resulted in part due to land being insured from natural disasters by the New Zealand Earthquake Commission, provided an unparalleled opportunity to study liquefaction triggering and its effects.

This research effort developed the first liquefaction ejecta case histories database by taking advantage of and adding to the comprehensive Canterbury geotechnical database, and it tested for the first time native “undisturbed” silty soil test specimens in the cyclic simple shear test device. The summary of objectives, methods, and key findings for the two primary research thrusts of this effort – (1) liquefaction ejecta case histories and (2) liquefaction of silty soils – are provided in Sections 6.2.1 and 6.2.2, respectively. Future research recommendations are delineated in Section 6.3.

6.2 FINDINGS

6.2.1 Liquefaction Ejecta Case Histories Database

Sediment ejecta triggered by the 2010-2011 Canterbury earthquakes were a key mechanism of liquefaction-induced land and lightweight house damage in the greater Christchurch area. However, there are no procedures for estimating the settlement due to liquefaction ejecta. To address this issue and advance our understanding of the formation, occurrence, and effects of liquefaction ejecta, the first liquefaction ejecta database was developed, building upon the comprehensive New Zealand geotechnical database.

The liquefaction ejecta-induced settlement was estimated using the photographic evidence- and LiDAR-based approaches because direct measurements of liquefaction ejecta were not conducted after the Canterbury earthquakes. The two estimates were weight-averaged for the best final estimate of ejecta-induced settlement. The analyses were performed for 58 sites for the Sep 2010, Feb 2011, Jun 2011, and Dec 2011 earthquakes and 3 additional sites for the Sep 2010 earthquake. Therefore, 235 liquefaction ejecta case histories were compiled into the database. Each case history contains the estimates of PGA and groundwater depth, among other details. The CPT profiles available at the sites were used to identify the soil deposit type (i.e., a thick, clean sand site, partially or highly stratified silty soil site, or gravel-dominated site), crust and first significant liquefiable layer

thicknesses, and to evaluate several liquefaction-induced damage indices. The database is available to other researchers to use to explore liquefaction ejecta through the data provided in this dissertation. It will also be available through a more widely circulated journal publication.

The compiled database was examined to identify general trends associated with the severity of liquefaction ejecta-induced settlement and to evaluate the efficacy of some of the liquefaction-induced damage indices. About 70% of the sites in the database are characterized with at least a 3-m thick sand layer below the groundwater table in the top 10 m of the soil profile. These sites are referred to as thick, clean sand sites. The remaining sites were primarily stratified silty soil sites. The key findings from this examination are:

- Liquefaction ejecta occurred for all four main Canterbury earthquakes; however, the amount of settlement it induced differed from site to site and from earthquake to earthquake. The most severe and most frequent ejecta-induced settlement was observed for the Feb 2011 earthquake (up to 155 ± 45 mm), while the least severe and the least frequent ejecta-induced settlement was observed for the Sep 2010 earthquake (up to 40 ± 10 mm).
- If a site did not manifest liquefaction ejecta for the Feb 2011 earthquake, the Jun 2011 and Dec 2011 earthquakes also did not produce ejecta-induced settlement.
- More than 50% of the studied sites had no ejecta-induced settlement for the Sep 2010 earthquake but did have it for the Jun 2011 earthquake even though their equivalent $M_w = 6.1$ PGA ($PGA_{6.1}$) values, groundwater depths, non-liquefiable crust thickness, and first liquefiable layer thickness did not differ significantly. However, a strong correlation between the Feb 2011 ejecta-induced settlement and the Jun 2011 ejecta-induced settlement suggests the severely damaged land by the Feb 2011 liquefaction ejecta formed cracks and defects in the non-liquefiable crust which liquefied soil at depth could exploit to form ejecta at the ground surface during the Jun 2011 earthquake.
- Intensities of $PGA_{6.1} \leq 0.20$ g resulted in < 15 mm of ejecta-induced settlement (typically zero) at the studied sites regardless of CPT q_c and I_c values. The severe-to-extreme ejecta-induced settlement was more pronounced at sites where clean sand layers dominated the soil profile, a trend that became more apparent as $PGA_{6.1}$ increased, especially beyond 0.40 g. Sites with interbedded silty material in the top 10 m of the soil profile typically had no-to-minor ejecta-induced settlement. This trend was more pronounced for $PGA_{6.1} < 0.40$ g.
- During the Jun 2011 earthquake, sites with shallower groundwater tables had a slight tendency to experience more severe ejecta-induced settlement than the sites with deeper groundwater tables. There was a slight increase in the ejecta-induced settlement as the first significant liquefiable soil layer increased in thickness, which was most pronounced for the Feb 2011 earthquake and $PGA_{6.1} > 0.30$ g.
- The ejecta-induced settlement documented at the sites in the database was used to examine some of the available liquefaction damage indices. LSN (van Ballegooy et al. 2014) and LPI (Iwasaki et al. 1978) underestimated the ejecta-induced settlement in 83% of case histories with severe-to-extreme ejecta-induced settlement compared to 35% in case of the L_D - C_R chart of Hutabarat

and Bray (2022). The percent of correctly estimated zero ejecta case histories using the L_D-C_R chart is 83% compared to 72% and 81% with LSN and LPI, respectively.

6.2.2 Liquefaction Potential of Stratified Silty Soil Deposits

6.2.2.1 Test Method for Minimum and Maximum Void Ratio for Small Quantities of Natural Soil

An alternative procedure based on the Japanese Standard JIS A 1224:2009 Test Method for Minimum and Maximum Densities of Sands is proposed for testing small quantities of natural soils. The alternative procedure is required for determining the minimum and maximum void ratios for small test specimens of natural soil, such as when performing simple shear tests on retrieved “undisturbed” test specimens. It uses reduced sizes of the mold and funnel and the mallet strike distance of the mold, as compared to the Japanese Standard method. The minimum and maximum void ratios were first determined for 42 individual soil samples with 2% to 99% non-plastic fines using the alternative method and then for eight soil composites with enough soil to employ the Japanese Standard method as well as the alternative method. The key findings from this part of the study are:

- The e_{min} and e_{max} produced by the alternative test method are similar to those of the Japanese Standard test method for the identical soil composite mixtures. The e_{min} and e_{max} of the composites determined by the alternative method agree with the e_{min} and e_{max} of the individual soil samples.
- Fines content (FC) does not affect the e_{min} obtained by the two methods. However, the alternative method tends to produce slightly higher e_{max} values than the standard method as FC increases (i.e., primarily observable when $FC > 70\%$), and hence, as e_{max} increases.
- At about 30-40% fines, the soil switches from a sand-dominated soil structure to a fines-dominated soil structure, as demonstrated by the transition in the data trends. From FC of 0% to 30-40%, there is a slight increase in e_{max} and a small decrease in e_{min} . As FC increases from 40% to 100%, e_{max} increases at a faster rate than e_{min} .
- Using the standard and alternative test methods to determine the minimum and maximum dry densities of soil with up to 100% non-plastic fines is viable. The alternative method enables the relative density of small test specimens to be estimated, which is useful for interpreting soil behavior.

6.2.2.2 Simple Shear Testing of High-Quality Silty and Sandy Soil Specimens

Silty soil deposits in southwest Christchurch were strongly shaken during the Feb 2011 earthquake but most of these deposits did not manifest liquefaction at the ground surface despite the estimations of severe ground failure by state-of-practice liquefaction triggering methods. To explore potential reasons for the discrepancy between the observations and the manifestations, the first cyclic simple shear (CSS) and monotonic simple shear (MSS) tests were performed on high-quality “undisturbed” specimens retrieved from the silty soil sites using the Dames and Moore hydraulic fixed-piston

smooth-wall sampler, which preserves soil fabric in addition to other important effects. The key findings from this part of the study are:

- The relative density evaluated for test specimens with 2%-99% non-plastic fines ranged from 56% to 100% and were deemed reasonable compared to the in-situ D_R estimated using the D_R - q_{t1n} correlation for fines-containing soil and considering the uncertainties associated with the thin-layer effects on CPT measurements and the correlation itself.
- The MSS test specimens generated positive excess pore water pressure initially, after which they passed through the phase transformation point and developed negative excess pore water pressure. The MSS effective stress paths indicated the soil response would likely be cyclic mobility with limited strain potential. The test specimens did not reach the steady state of deformation.
- The CSS test specimens generated excess pore water pressure which induced the gradual shear strain development and cyclic degradation. The observed response of the CSS specimens was cyclic mobility with limited strain potential, as indicated by the MSS tests.
- The differences in the responses of CSS test specimens with 2-99% fines were subtle and could not be attributed to variations in FC.
- The CSS laboratory-based field-corrected cyclic resistances were generally consistent with the cyclic resistances estimated by CPT-based liquefaction-triggering procedures. Thus, the cyclic resistances evaluated by CSS testing do not explain the absence of surface manifestation of liquefaction at the studied sites. The element-scale laboratory CSS test specimens cannot capture the in-situ system response associated with interaction between soil layers in their seismic response, pore water pressure redistribution, and flow of water.
- The post-cyclic MSS test effective stress paths and stress-strain responses mirrored those associated with the last loading cycle of the CSS tests. The soil stiffness in post-cyclic monotonic tests was significantly lower than that in MSS tests, likely due to the large difference in the initial effective stress between the two types of tests, cyclic degradation, and the loss of fabric resulting from deformation during cyclic loading.

6.3 FUTURE RESEARCH RECOMMENDATIONS

Future research recommendations arise from the research presented in this dissertation and are aimed at advancing the state of knowledge and practice related to the liquefaction phenomenon, including the development of a robust procedure to estimate the liquefaction ejecta-induced settlement in an earthquake. Future research recommendations are:

- Expand the liquefaction ejecta database by developing additional case histories for the 2010-2011 Canterbury earthquakes and for other earthquakes in other regions of the world. The initial focus in Christchurch should be on stratified silty soil sites to balance the number of thick, clean sand sites in the newly developed database.
- Add field case histories with direct, robust measurements of ejecta to the liquefaction ejecta database. This can be accomplished by utilizing terrestrial

LiDAR, structure-from-motion photogrammetry, or conventional land surveys, photographs, and hand measurements immediately after future earthquakes while all related evidence remains intact. For regional assessment of liquefaction-induced damage, strict control of ground points is recommended.

- Include additional ground motion parameters, such as Arias intensity and cumulative absolute velocity, to the database and investigate their efficacy in estimating liquefaction effects.
- Conduct paleoliquefaction studies for some of the sites in the liquefaction ejecta database to improve our understanding of the differing responses among different sites.
- Use the liquefaction ejecta case histories to develop methods to estimate ejecta effects.
- Employ the simple shear test results from this study to calibrate soil constitutive models which can be used in dynamic effective stress analysis to explore details about the system response of stratified silty soil deposits.

REFERENCES

- Ahmadi, M. M., and Robertson P. K. (2005). Thin-layer effects on the CPT q_c measurement. *Canadian Geotechnical Journal*, 42, 1302-1317. doi: 10.1139/T05-036
- Allmond, J., Kutter, B. L., Bray, J. D., and Hayden, C. (2015). A new database for foundation and ground performance in liquefaction experiments. *Earthquake Spectra, EERI*, 31(4), 2485-2509. doi: 10.1193/072814EQS120.
- Amini, F., and Qi, G. Z. (2000). Liquefaction testing of stratified silty sands. *ASCE J. of Geotechnical and Geoenvironmental Engineering*, 126(3), 208-217.
- Ang, A. S., and Tang, W. H. (2007). *Probability concepts in engineering: Emphasis on applications to civil and environmental engineering* (2nd ed). Wiley.
- Arduino, P., Ashford, S. A., Asimaki, D., Bray, J. D., Eldridge, T., Frost, J. D., Hashash, Y. M. A., ... Zoa, N. (2010). *Geo-engineering reconnaissance of the 2010 Maule, Chile earthquake*. GEER Report No. GEER-022, Version 2.
- ASTM Standards. D2487 (Classification of Soils for Engineering Purposes – USCS), D422 (Particle-Size Analysis of Soils), D854 (Specific Gravity of Soil Solids by Water Pycnometer), D1557 (Laboratory Compaction Characteristics of Soil Using Modified Effort (56,000 ft-lbf/ft³ (2,700 kN-m/m³))), D4253 (Maximum Index Density and Unit Weight of Soils Using a Vibratory Table), D4254 (Minimum Index Density and Unit Weight of Soils and Calculation of Relative Density), D4318 (Liquid Limit, Plastic Limit, and Plasticity Index of Soils).
- Audemard, F.A., and de Santis, F. (1991). Survey of liquefaction structures induced by recent moderate earthquakes. *Bulletin of the International Association of Engineering Geology*, 44, 5-16.
- Baldi, G., Belotti, R., Ghionna, N., Jamiolkowski, M., and Pasqualini, E. (1986). Interpretation of CPT and CPTU; 2nd part: drained penetration of sands. *Fourth International Geotechnical Seminar*, 143-156, Nanyang Technological Institute, Singapore.
- Beyzaei, C. Z. (2017). *Fine-Grained Soil Liquefaction Effects in Christchurch, New Zealand* (Doctoral dissertation, Univ. of California, Berkeley).
- Beyzaei, C. Z., Bray, J. D., van Ballegooy, S., Cubrinovski, M., and Bastin, S. (2018a). Depositional environment effects on observed liquefaction performance in silt swamps during the Canterbury earthquake sequence. *Soil Dynamics and Earthquake Engineering*, 107, 303-321. doi: 10.1016/j.soildyn.2018.01.035
- Beyzaei, C.Z., Bray, J. D., Cubrinovski, M., Riemer, M., and Stringer, M. (2018b). Laboratory-based characterization of shallow silty soils in southwest Christchurch. *Soil Dynamics and Earthquake Engineering*, 110, 93-109. doi.org/10.1016/j.soildyn.2018.01.046
- Beyzaei, C. Z., Bray J. D., Cubrinovski, M., Bastin, S., Stringer, M., Jacka, M., van Ballegooy S., Riemer, M., and Wentz, R. (2020). Characterization of silty soil thin layering and groundwater conditions for liquefaction assessment. *Canadian Geotechnical Journal*, 57(2), 263-276. doi: 10.1139/cgj-2018-0287
- Boulanger, R. W. (1990). *Liquefaction Behavior of Saturated Cohesionless Soils Subjected to Uni Directional and Bi-Directional Static and Cyclic Simple Shear Stresses* (Doctoral dissertation, Univ. of California, Berkeley).

- Boulanger, R. W., and Idriss, I. M. (2016). CPT-based liquefaction triggering procedure. *Journal of Geotechnical and Geoenvironmental Engineering*, 142(2), 04015065—1-11. doi: 10.1061/(asce)gt.1943-5606.0001388
- Bradley, B., and Hughes, M. (2012). *Conditional peak ground accelerations in the Canterbury earthquakes for conventional liquefaction assessment*. Technical Report prepared for the Department of Building and Housing, New Zealand.
- Bray, J. D., Sancio, R. B., Durgunoglu, T., Onalp, A., Youd, T. L., Stewart, J. P., Seed, R. B., Cetin, O. K., Bol, E., Baturay, M. B., Christensen, C., and Karadayilar, T. (2004). Subsurface characterization at ground failure sites in Adapazari, Turkey. *Journal of Geotechnical and Geoenvironmental Engineering*, 130(7), 673–685. [https://doi.org/10.1061/\(asce\)1090-0241\(2004\)130:7\(673\)](https://doi.org/10.1061/(asce)1090-0241(2004)130:7(673))
- Bray, J. D., and Sancio, R. B. (2006). Assessment of the liquefaction susceptibility of fine-grained soils. *Journal of Geotechnical and Geoenvironmental Engineering*, 132(9), 1165–1177. doi: 10.1061/(asce)1090-0241(2006)132:9(1165)
- Bray, J. D., and Dashti, S. (2014). Liquefaction-induced building movements. *Bulletin of Earthquake Engineering*, 12, 1129–56. doi.org/10.1007/s10518-014-9619-8
- Bray, J. D., Beyzaei, C. Z., Cubrinovski, M., Riemer, M. F., Markham, C., Stringer, M. E., Jacka, M., Wentz, F. J., and Haycock, I. (2016). *Recommendations for high-quality field sampling procedures using the Dames & Moore (DM) hydraulic fixed-piston thin-walled tube sampler*. Technical Report prepared for New Zealand Ministry of Business, Innovation and Employment.
- Bray, J.D. and Macedo, J. (2017). 6th Ishihara Lecture: Simplified Procedure for Estimating Liquefaction-Induced Building Settlement. *Soil Dynamics and Earthquake Engineering*, 102, 215-231.
- Brown, L. J., Beetham, R. D., Paterson, B. R., and Weeber, J. H. (1995). Geology of Christchurch, New Zealand. *Environmental and Engineering Geoscience*, 1(4), 427-488. doi:10.2113/gseegeosci.I.4.427
- Brown, L. J., Wilson, D. D., Moar, N. T., and Mildenhall, D. C. (1988). Stratigraphy of the late Quaternary deposits of the northern Canterbury Plains, New Zealand. *New Zealand Journal of Geology and Geophysics*, 31(3), 305-335. doi: 10.1080/00288306.1988.10417779
- Canterbury Earthquake Recovery Authority. (2014). “Verification of LiDAR acquired before and after the Canterbury Earthquake Sequence,” Technical Specification, retrieved May 2022 from <https://canterburygeotechnicaldatabase.projectorbit.com>
- Canterbury Geotechnical Database (2012a) "Aerial Photography", Map Layer CGD0100 - 1 Jun 2012, retrieved Jul 2018 – Jul 2021 from <https://canterburygeotechnicaldatabase.projectorbit.com/>
- Canterbury Geotechnical Database (2012b) "Vertical Ground Surface Movements", Map Layer CGD0600 - 23 Jul 2012, retrieved Jul 2018 – Jul 2021 from <https://canterburygeotechnicaldatabase.projectorbit.com/>
- Canterbury Geotechnical Database (2014) "Event Specific Groundwater Surface Elevations", Map Layer CGD0800 - 10 Jun 2014, retrieved Jul 2018 – Jul 2021 from <https://canterburygeotechnicaldatabase.projectorbit.com/>
- Canterbury Geotechnical Database (2015) "Conditional PGA for Liquefaction Assessment", Map Layer CGD5110 - 20 Jul 2015, retrieved Jul 2018 – Jul 2021 from <https://canterburygeotechnicaldatabase.projectorbit.com/>

- Cappellaro, C., Cubrinovski, M., Bray, J. D., Chiaro, G., Riemer, M. F., and Stringer, M. E. (2021). Liquefaction resistance of Christchurch sandy soils from direct simple shear tests. *Soil Dynamics and Earthquake Engineering*, 141. doi.org/10.1016/j.soildyn.2020.106489.
- Cubrinovski, M., and Ishihara, K. (1998). Modelling of sand behaviour based on state concept. *Soils and Foundations*, 38(3), 115-127. https://doi.org/10.3208/sandf.38.3_115
- Cubrinovski, M., and Ishihara, K. (1999). Empirical correlation between SPT N-value and relative density for sandy soils. *Soils and Foundations*, 39(5), 61-71.
- Cubrinovski, M., and Ishihara, K. (2002). Maximum and Minimum Void Ratio Characteristics of Sands. *Soils and Foundations*, 42(6), 65-78. doi: 10.3208/sandf.42.6_65
- Cubrinovski, M., Bradley, B., Wotherspoon, L., Green, R., Bray, J., Wood, C., . . . Wells, D. (2011). Geotechnical aspects of the 22 February 2011 Christchurch earthquake. *Bulletin of the New Zealand Society for Earthquake Engineering*, 44(4), 205-226. doi:10.5459/bnzsee.44.4.205-226
- Cubrinovski, M., Rhodes, A., Ntritsos, N., and van Ballegooy, S. (2017a). System response of liquefiable deposits. In *Proceedings of the 3rd International Conference on Performance-based Design in Earthquake Geotechnical Engineering*, 16-19 Jul, Vancouver, BC.
- Cubrinovski, M., Bray, J. D., De La Torre, C., Olsen, M. J., Bradley, B. A., Chiaro, G., Stocks, E., and Wotherspoon, L. (2017b). Liquefaction effects and associated damages observed at the Wellington CentrePort from the 2016 Kaikoura earthquake. *Bulletin of the New Zealand Society for Earthquake Engineering*, 50(2), 152-173. <https://doi.org/10.5459/bnzsee.50.2.152-173>
- Cubrinovski, M. (2019). "Some important considerations in the engineering assessment of soil liquefaction." Retrieved 26 Feb 2021 from <https://www.nzgs.org/library/some-important-considerations-in-the-engineering-assessment-of-soil-liquefaction/>
- Cubrinovski, M., Rhodes, A., Ntritsos, N., and van Ballegooy, S. (2019). System response of liquefiable deposits. *Soil Dynamics and Earthquake Engineering*, 124, 212-229. doi: 10.1016/j.soildyn.2018.05.013
- Davies, L. J. (1989). *The landforms of the Christchurch lowland* (Doctoral dissertation, Univ. of Canterbury, New Zealand).
- de Greef, J., and Lengkeek, H. J. (2018). Transition and thin layer corrections for CPT based liquefaction analysis. In *Proceedings of the 4th International Symposium on Cone Penetration Testing (CPT'18)*, 21-22 Jun, 2018, Delft, The Netherlands.
- Donahue, J. L. (2007). *The liquefaction susceptibility, resistance, and response of silty and clayey soils* (Doctoral dissertation, Univ. of California, Berkeley).
- Forthofer, R. N., Lee, E.S., and Hernandez, M. (2007). *Biostatistics (2nd ed): 3 - Descriptive methods*. Academic Press. <https://doi.org/10.1016/B978-0-12-369492-8.50008-X>.
- GNS Science. (2021). "The most recent aftershock map." Retrieved 1 Aug 2021 from <https://www.gns.cri.nz/Home/Our-Science/Natural-Hazards-and-Risks/Recent-Events/Canterbury-quake/Recent-aftershock-map>
- Green, R. A., Cubrinovski, M., Wotherspoon, L., Allen, J., Bradley, B. A., Bradshaw, A., Bray, J. D. . . . Winkley, A. (2012). Geotechnical aspects of the M_w 6.2 2011

- Christchurch, New Zealand Earthquake. *2012 Annual Congress of the Geo-institute of ASCE*, 25-29 Mar 2012, Oakland, CA, USA.
- Hutabarat, D., and Bray, J. D. (2021). Effective Stress Analysis of Liquefiable Sites to Estimate the Severity of Sediment Ejecta. *Journal of Geotechnical and Geoenvironmental Engineering, ASCE*, 147(5). 10.1061/(ASCE)GT.1943-5606.0002503.
- Hutabarat, D., and Bray J. D. (2022). Estimating the severity of liquefaction ejecta using the cone penetration test. *Journal of Geotechnical and Geoenvironmental Engineering, ASCE*, 148(3), 04021195. doi: 10.1061/(ASCE)GT.1943-5606.0002744.
- Hvorslev, M. J. (1949). "Subsurface exploration and sampling of soils for civil engineering purposes." Waterways Experiment Station, Vicksburg, MS.
- Idriss, I. M., and Boulanger, R.W. (2008). *Soil liquefaction during earthquakes*. EERI Monograph MNO-12.
- Ioannides, J. T. (2019). *Cliq v.3.0.3.2 – CPT soil liquefaction software*. Greece: Geologismiki.
- Ishihara, K. (1985). Stability of natural deposits during earthquakes. In *Proceedings of the 11th International Conference on Soil Mechanics and Foundation Engineering*, 376–321, International Society of Soil Mechanics and Foundation Engineering, London, UK.
- Ishihara, K. (1996). *Soil Behaviour in Earthquake Geotechnics*. Great Britain: Oxford Univ. Press.
- Ishihara, K., and Yoshimine, M. (1992). Evaluation of settlements in sand deposits following liquefaction during earthquakes. *Soils and Foundations*, 32(1), 173–188. <https://doi.org/10.3208/sandf1972.32.173>.
- Iwasaki, T., Tatsuoka, F., Tokida, K., and Yasuda, S. (1978). A practical method for assessing soil liquefaction potential based on case studies at various sites in Japan. In *Proceedings of the 2nd International Conference on Microzonation*, 885-896, National Science Foundation, Washington, DC.
- Jamiolkowski, M., Lo Presti, D. C. F., and Manassero, M. (2001). Evaluation of relative density and shear strength of sands from CPT and DMT. *ASCE Geotechnical Special Publication*, 119, 201-238.
- Lade, P. V., Liggio, C. D., and Yamamuro, J. A. (1998). Effects of non-plastic fines on minimum and maximum void ratios of sand. *Geotechnical Testing Journal, GTJODJ*, 21(4), 336-347.
- Land Damage Assessment Team (LDAT). (2021). *LDAT Reports Data Entry (Database)*. Retrieved from <https://tracker.projectorbit.com/Sites/LDAT/EQCFieldReportFormExtra.aspx>
- Lees, J., van Ballegooy, S., and Wentz, F. J. (2015). Liquefaction susceptibility and fines content correlations of Christchurch soils. *6th International Conference on Earthquake Geotechnical Engineering*, 1-4 Nov 2015, Christchurch, New Zealand.
- Lunne, T., Berre, T., and Strandvik, S. (1997). Sample disturbance effects in soft low plastic Norwegian clay. *Symposium on Recent Developments in Soil and Pavement Mechanics*, 25-27 June 1997, Rio de Janeiro, Brazil.
- Markham, C. S., Bray, J.D., Riemer, M. F., and Cubrinovski, M. (2016). Characterization of shallow soils in the Central Business District of Christchurch, New Zealand.

- Geotechnical Testing Journal*, 39(6), 922-937.
<http://dx.doi.org/10.1520/GTJ20150244>.
- Markham, C. S., Bray, J. D., Cubrinovski, M., and Riemer, M. F. (2018). Liquefaction resistance and steady-state characterization of shallow soils within the Christchurch Central Business District. *Journal of Geotechnical and Geoenvironmental Engineering*, 144(6), 04018032. [https://doi.org/10.1061/\(asce\)gt.1943-5606.0001823](https://doi.org/10.1061/(asce)gt.1943-5606.0001823)
- Maurer, B. W., Green, R. A., Cubrinovski, M., and Bradley, B. A. (2014). Evaluation of the liquefaction potential index for assessing liquefaction hazard in Christchurch, New Zealand. *Journal of Geotechnical and Geoenvironmental Engineering*, 140(7), 04014032-1-11. doi:10.1061/(asce)gt.1943-5606.0001117
- Maurer, B. W., Green, R. A., Cubrinovski, M., and Bradley, B. (2015). Assessment of CPT-based methods for liquefaction evaluation in a liquefaction potential index framework. *Géotechnique*, 65(5), 328–336. <https://doi.org/10.1680/geot.SIP.15.P.007>.
- Maurer, B., Green, R., van Ballegooy, S., and Wotherspoon, L. (2019). Development of region-specific soil behavior type index correlations for evaluating liquefaction hazard in Christchurch, New Zealand. *Soil Dynamics and Earthquake Engineering*, 117, 96-105.
- Mijic, Z., Bray, J. D., Riemer, M. F., Cubrinovski, M., and Rees, S. D. (2021a). Test method for minimum and maximum densities of small quantities of soil. *Soils and Foundations*, 61(2), 533-540. <https://doi.org/10.1016/j.sandf.2020.12.003>
- Mijic, Z., Bray, J. D., Riemer, M. F., Rees, S. D., and Cubrinovski, M. (2021b). Cyclic and monotonic simple shear testing of native Christchurch silty soil. *Soil Dynamics and Earthquake Engineering*, 148, 106834. <https://doi.org/10.1016/j.soildyn.2021.106834>
- Mijic, Z., Bray, J. D., and van Ballegooy, S. Liquefaction Ejecta Case Histories For 2010-11 Canterbury Earthquakes. (2022). *ISSMGE Journal of Geoengineering Case Histories*, under review.
- Mitchell, J. K., and Soga, K. (2005). *Fundamentals of Soil Behavior* (3rd ed.). Hoboken, NJ: Wiley.
- Murthy, T. G., Loukidis, D., Carraro, J. A., Prezzi, M., and Salgado, R. (2007). Undrained monotonic response of clean sand and silty sands. *Géotechnique*, 57(3), 273-288. <https://doi.org/10.1680/geot.2007.57.3.273>
- Obermeier, S. F. (1989). *The New Madrid earthquakes; An engineering-geologic interpretation of relict liquefaction features*. US Geological Survey Professional Paper 1336-B.
- Obermeier, S. F. (1996). Use of liquefaction-induced features for paleoseismic analysis. *Engineering Geology*, 44, 1-76.
- Powers, M. C. (1953). A new roundness scale for sedimentary particles. *Journal of Sedimentary Petrology*, 23 (2), 117-119.
- Robertson, P. K., and Campanella, R. G. (1983). Interpretation of cone penetration tests. Part I: Sand. *Canadian Geotechnical Journal*, 20(4), 718-733. <https://doi.org/10.1139/t83-078>
- Robertson, P. K., Campanella, R. G., and Wightman, A. (1983). SPT-CPT correlations. *Journal of Geotechnical Engineering, ASCE*, 109(11), 149-1459. doi.org/10.1061/(ASCE)0733-9410(1983)109:11(1449)
- Robertson, P.K. (2009). Interpretation of cone penetration tests – a unified approach. *Canadian Geotechnical Journal*, 46, 1337-1355.

- Robertson, P. K., and Cabal, K. L. (2015). *Guide to Cone Penetration Testing for Geotechnical Engineering*. Signal Hill, CA: Greg Drilling and testing, Inc.
- Rogers, N., van Ballegooy, S., Williams, K., and Johnson, L. (2015). Considering post-disaster damage to residential building construction - Is our modern building construction resilient? *6th International Conference on Earthquake Geotechnical Engineering*, Christchurch, New Zealand.
- Russell, J., and van Ballegooy, S. (2015). *Canterbury Earthquake Sequence: Increased Liquefaction Vulnerability Assessment Methodology*. T+T Report 0028-1-R-JICR-2015 prepared for the Earthquake Commission.
- Salgado, R., Bandini, P., and Karim, A. (2000). Shear strength and stiffness of silty sand. *ASCE Journal of Geotechnical and Geoenvironmental Engineering*, 126(5), 451-462.
- Schmertmann, J. H. (1978). *Guidelines for cone penetration test, performance and design*. Report FHWA-TS-78-209, U.S. Depart. of Transportation, Federal Highway Admin.
- Schober, P., Boer, C., and Schwarte, L. A. (2018). Correlation Coefficients: Appropriate Use and Interpretation. *Anesthesia and Analgesia*, 126(5), 1763–1768. <https://doi.org/10.1213/ANE.0000000000002864>
- Seed, H. B., and Idriss, I. M. (1967). Analysis of soil liquefaction: Niigata earthquake. *Journal of the Soil Mechanics and Foundations Division, ASCE*, 93(SM3), 83-108.
- Seed, R. B., Riemer, M. F., and Dickenson, S. E. (1991). Liquefaction of Soils in the 1989 Loma Prieta Earthquake. *2nd International Conferences on Recent Advances in Geotechnical Earthquake Engineering and Soil Dynamics*, St. Louis, MO.
- Seed, H. B. (1979). Soil liquefaction and cyclic mobility evaluation for level ground during earthquakes. *Journal of the Geotechnical Engineering Division*, 105(GT2), 201-255. doi: 10.1016/0148-9062(79)91243-9
- Soga, K. (1998). Soil liquefaction effects observed in the Kobe earthquake of 1995. *Proceedings of the Institution of Civil Engineers-Geotechnical Engineering*, 131(1), 34-51. <https://doi.org/10.1680/igeng.1998.30004>
- Stringer, M. E., Beyzaei, C. Z., Cubrinovski, M., Bray, J. D., Riemer, M. F., Jacka, M., and Wentz, F. (2015). Liquefaction Characteristics of Christchurch Silty Soils: Gainsborough Reserve. *Sixth International Conference on Earthquake Geotechnical Engineering*, 1-4 Nov 2015, Christchurch, New Zealand.
- Stringer, M. E., Beyzaei, C. Z., Cubrinovski, M., Bray, J. D., and Riemer, M. F. (2016). *Geotechnical Data Report: Site2 - Gainsborough Reserve*. Technical Report prepared for New Zealand Ministry of Business, Innovation and Employment.
- Tatsuoka, F., Ochi, K., Fujii, S., and Okamoto, M. (1986). Cyclic undrained triaxial and torsional shear strength of sands for different sample preparation methods. *Soils and Foundations*, 26(3), 23-41.
- Taylor, M. L. (2015). *The geotechnical characterisation of Christchurch sands for advanced soil modelling* (Doctoral dissertation, Univ. of Canterbury, New Zealand).
- Thevanayagam, S. Shenthana, T., Mohan, S., and Liang, J. (2002). Undrained fragility of clean sands, silty sands and sandy silts. *ASCE Journal of Geotechnical and Geoenvironmental Engineering*, 128(10), 849-859.
- Tonkin and Taylor Ltd. (T+T). (2013). *Liquefaction vulnerability study - Report to Earthquake Commission*. Report 52020.0200/v1.0, <https://www.nzgd.org.nz>

- Tonkin and Taylor, Ltd. (2015). *Tonkin and Taylor Geotechnical Database: Canterbury Maps* (Database). Retrieved from <https://canterburygeotechnicaldatabase.projectorbit.com/>
- Upadhyaya, S., Green, R. A., Maurer, B. W., Rodriguez-Marek, A., and van Ballegooy, S. (2022). Limitations of surface liquefaction manifestation severity index models used in conjunction with simplified stress-based triggering models. *ASCE Journal of Geotechnical and Geoenvironmental Engineering*, 148(3), 04021194.
- Vaid, Y. P. and Sivathayalan, S. (1996). Static and cyclic liquefaction potential of Fraser Delta sand. *Canadian Geotechnical Journal*, 33, 281–289.
- van Ballegooy, S., Malan, P., Lacrosse, V., Jacka, M.E., Cubrinovski, M., Bray, J.D., O'Rourke, T.D., Crawford, S.A., and Cowan, H. (2014). Assessment of liquefaction-induced land damage for residential Christchurch. *Earthquake Spectra*, 30(1), 31-55. doi: 10.1193/031813EQS070M
- Wadell, H. (1932). Volume, shape and roundness of rock particles. *Journal of Geology*, 40, 443-451.
- Wu, J. (2002). *Liquefaction Triggering and Post-Liquefaction Deformation of Monterey 0/30 Sand Under Uni-Directional Cyclic Simple Shear Loading* (Doctoral dissertation, Univ. of California, Berkeley).
- Yilmaz, Y. (2009). A study on the limit void ratio characteristics of medium to fine mixed graded sands. *Engineering Geology*, 104(3-4), 290-294. <https://doi.org/10.1016/j.enggeo.2008.11.009>
- Zhang, G., Robertson, P. K., and Brachman, R. W. I. (2002). Estimating liquefaction-induced ground settlements from CPT for level ground. *Canadian Geotechnical Journal*, 39, 1168-1180. doi: 10.1139/T02-047

Appendix A

Liquefaction Ejecta Case Histories

- Liquefaction ejecta case histories for 61 sites listed herein are provided as supplemental electronic files.
- *EjectaCaseHistories_FlatFile.xlsx* is provided as an electronic supplement.

Raw CPT data are publicly available through the New Zealand Geotechnical Database (NZGD).

- A.1 Shirley Intermediate School – VsVp 57203
- A.2 Rydal Reserve – VsVp 57190
- A.3 Rawhiti Domain – VsVp 57188
- A.4 Caulfield Ave – VsVp 38175
- A.5 70 Langdons Rd – VsVp 57142
- A.6 Vivian St – CPT 5586
- A.7 50 Eureka St – VsVp 57195
- A.8 Parnwell St & Bassett St – CPT 27709
- A.9 Vangelis Ln & Fernbrook Pl – CPT 49582
- A.10 Pinewood Ave – CPT 61991
- A.11 Carisbrooke Playground – VsVp 57193
- A.12 Avondale Playground – VsVp 57062
- A.13 Bower Ave – CPT 3937
- A.14 Wattle Dr – CPT 90678
- A.15 Warrington St – CPT 44959
- A.16 Hunt Ln – CPT 4674

- A.17 Sandown Cres – CPT 15498
- A.18 Travis Country Dr – CPT 29778
- A.19 Aldershot St – CPT 5261
- A.20 1/19 Chardale St – VsVp 57320
- A.21 15b Royds Pl – VsVp 57326
- A.22 31 Landy St – CPT 44439
- A.23 Normans Rd/Papanui Rd – VsVp 57200
- A.24 St. Teresa's School – VsVp 57191
- A.25 Kaiwara Reserve – VsVp 57182
- A.26 Ti Rakau Reserve – VsVp 57186
- A.27 Avondale Park – VsVp 57187
- A.28 Sabina Playground – VsVp 57192
- A.29 Barrington Park – VsVp 38172
- A.30 Shortland St – CPT 6551
- A.31 Mark Treffers Dr – CPT 62594
- A.32 Shirley Primary School – CPT 54376

- A.33 Cashmere High School – CPT 33732
- A.34 Dunarnan St – CPT 17908
- A.35 Baker St – CPT 14070
- A.36 Randolph St – CPT 44440
- A.37 Woodham Rd – CPT 25514
- A.38 Rudds Rd – CPT 5687
- A.39 Palmers Rd – CPT 27040
- A.40 Willryan Ave – CPT 2168
- A.41 Bideford Pl – CPT 17200
- A.42 Wharenui School – VsVp 57165
- A.43 Heaton Normal Intermediate School – VsVp 57181
- A.44 Hillmorton High School – VsVp 57201
- A.45 St. Albans Catholic School – VsVp 57180
- A.46 113A Palmers Rd – CPT 29740
- A.47 Hurst Pl – CPT 25981
- A.48 Shirley Boys High School – CPT 56468

- A.49 Bracken St – CPT 59661
- A.50 Palinurus Rd 1 – VsVp 57185
- A.51 Palinurus Rd 2 – CPT 62761
- A.52 Nursery Rd – CPT 17262
- A.53 Gainsborough Reserve – VsVp 38176
- A.54 55 Papanui Rd – VsVp 57189
- A.55 Keers Rd – CPT 28986
- A.56 200 Cashmere Rd – VsVp 38171
- A.57 Armagh St – CPT 45795
- A.58 Lakewood Dr – CPT 54736
- A.59 Kensington Ave – CPT 88252
- A.60 Tonks St – CPT 128494
- A.61 Marblewood Reserve – VsVp 57155

Appendix B

Site Investigations

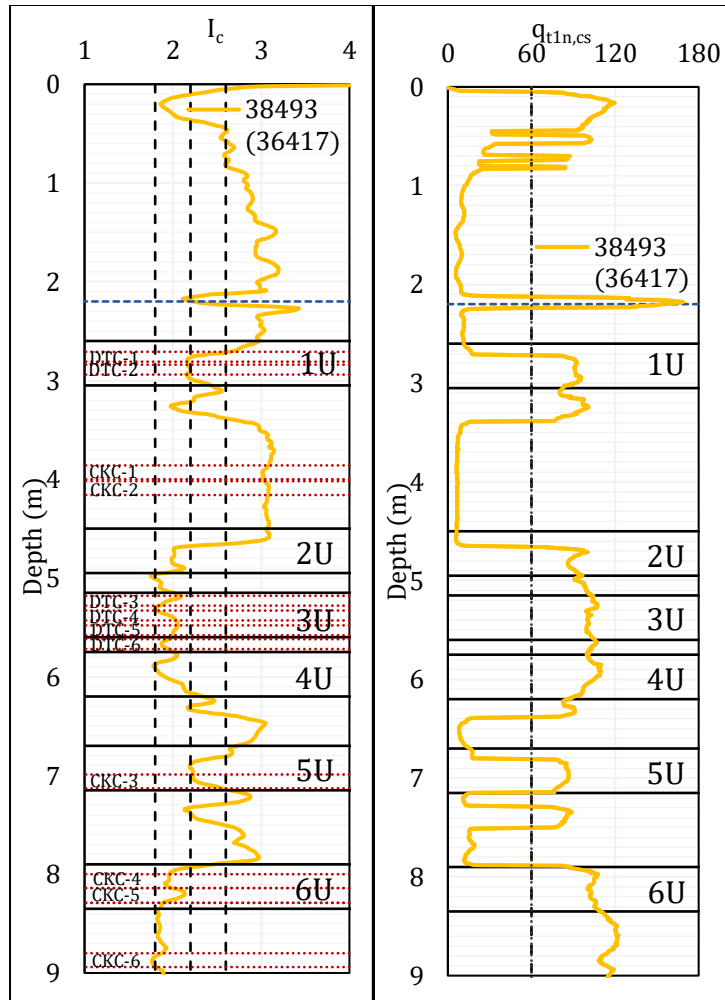


Figure B.1.1.3. I_c and $q_{t1n,cs}$ profiles at the Gainsborough Reserve site with Dames and Moore sampling depths for the simple shear testing program and depths of cyclic triaxial test specimens from previous research studies.

Table B.1.1.1. Dames and Moore sampling depths at Site 2 – Gainsborough Reserve.

Sample ID	Sampling Depth Range (m)
S2-DM2-1U	2.60-3.05
S2-DM2-2U	4.50-4.95
S2-DM2-3U	5.15-5.60
S2-DM2-4U	5.75-6.20
S2-DM2-5U	6.70-7.15
S2-DM2-6U	7.90-8.35

B.1.2 Site 14 – Barrington Park



Figure B.1.2.1. Plan view of the Barrington Park site with the Dames and Moore sampling location (S14-BH3_DM) relative to the locations of previous investigations.



Figure B.1.2.2. Photographs of the Barrington Park site (date: 23 May 2019; the 2nd day of sampling).

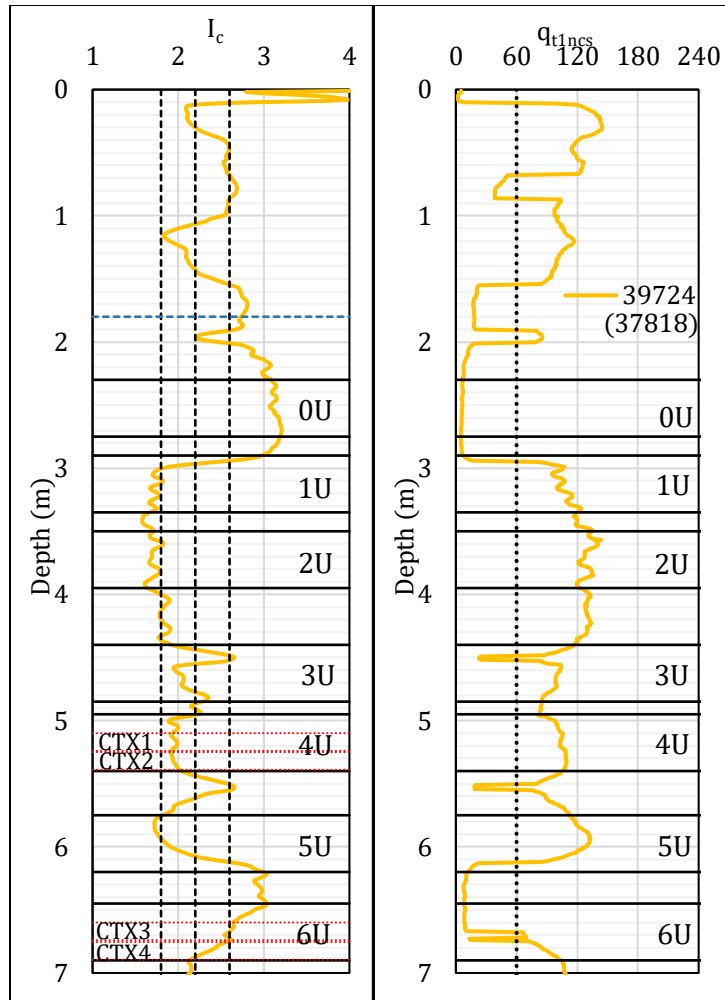


Figure B.1.2.3. I_c and q_{t1ncs} profiles at the Barrington Park site with Dames and Moore sampling depths for the simple shear testing program and depths of cyclic triaxial test specimens from previous research studies.

Table B.1.2.1. Dames and Moore sampling depths at Site 14 – Barrington Park.

Sample ID	Sampling Depth Range (m)
S14-DM3-0U	2.30-2.75
S14-DM3-1U	2.90-3.35
S14-DM3-2U	3.50-3.95
S14-DM3-3U	4.40-4.85
S14-DM3-4U	4.95-5.40
S14-DM3-5U	5.75-6.20
S14-DM3-6U	6.45-6.90

B.1.3 Site 23 – 85 Riccarton Road

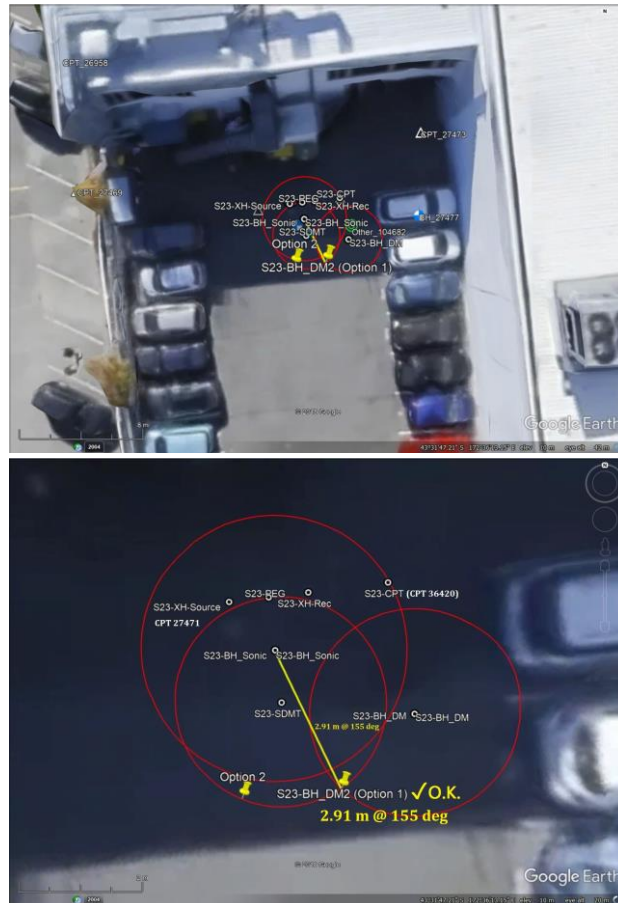


Figure B.1.3.1. Plan view of the 85 Riccarton Road site with the Dames and Moore sampling location (S23-BH_DM2) relative to the locations of previous investigations.

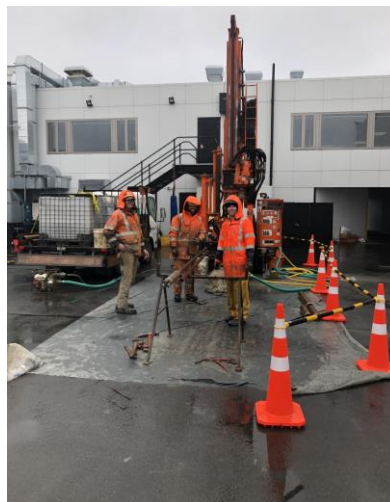


Figure B.1.3.2. Photograph of the 85 Riccarton Road site (date: 20 July 2019).

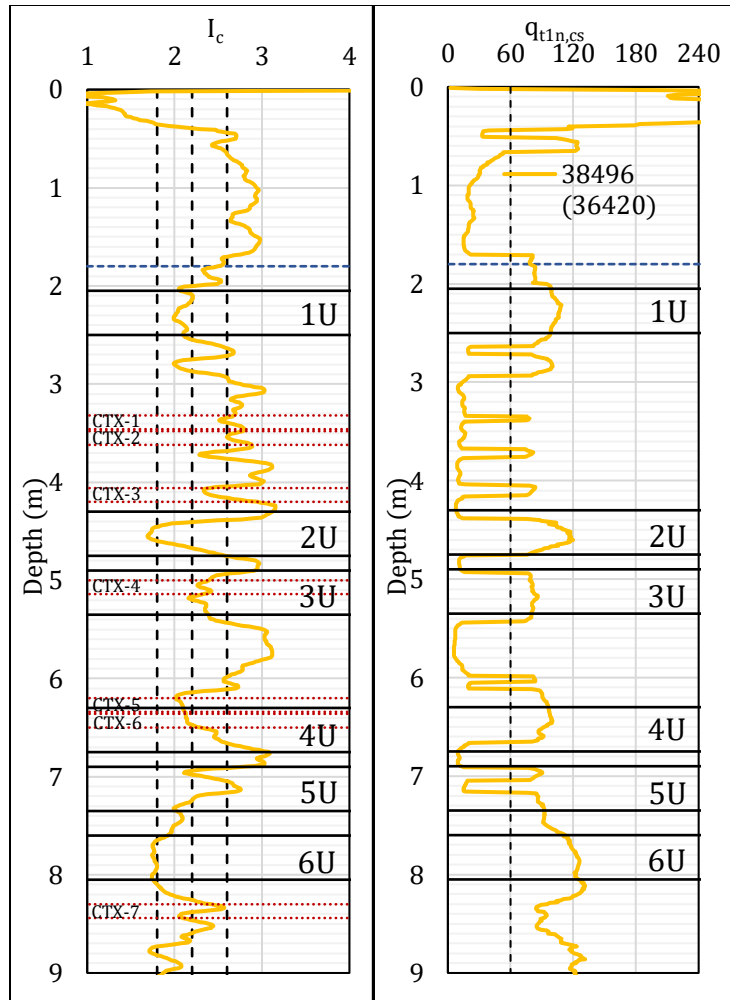


Figure B.1.3.3. I_c and $q_{t1,ncs}$ profiles at the 85 Riccarton Road site with Dames and Moore sampling depths for the simple shear testing program and depths of cyclic triaxial test specimens from previous research studies.

Table B.1.3.1. Dames and Moore sampling depths at Site 23 – 85 Riccarton Road.

Sample ID	Sampling Depth Range (m)
S23-DM2-1U	2.05-2.50
S23-DM2-2U	4.30-4.75
S23-DM2-3U	4.90-5.35
S23-DM2-4U	6.30-6.75
S23-DM2-5U	6.90-7.35
S23-DM2-6U	7.60-8.05

B.1.4 Site 33 – 200 Cashmere Road

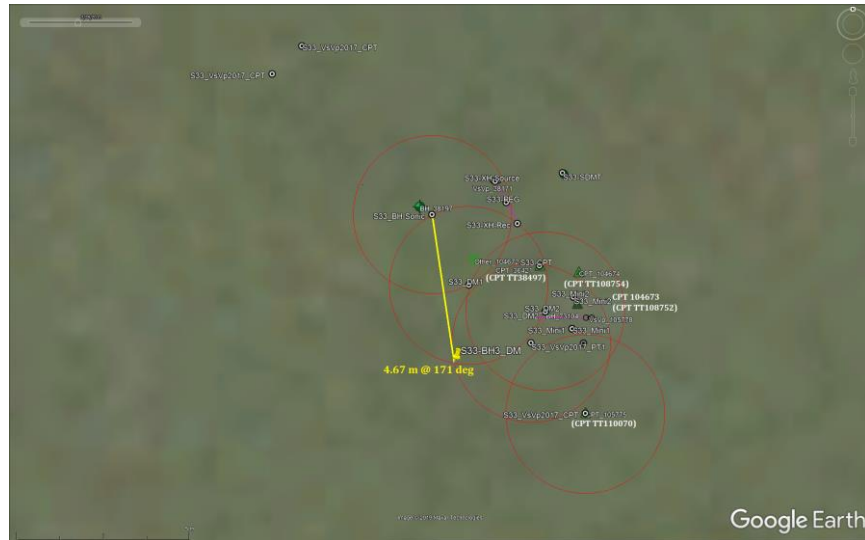


Figure B.1.4.1. Plan view of the 200 Cashmere Road site with the Dames and Moore sampling location (S23-BH_DM2) relative to the locations of previous investigations.



Figure B.1.4.2. Photographs of the 200 Cashmere Road site (date: 21 May 2019).

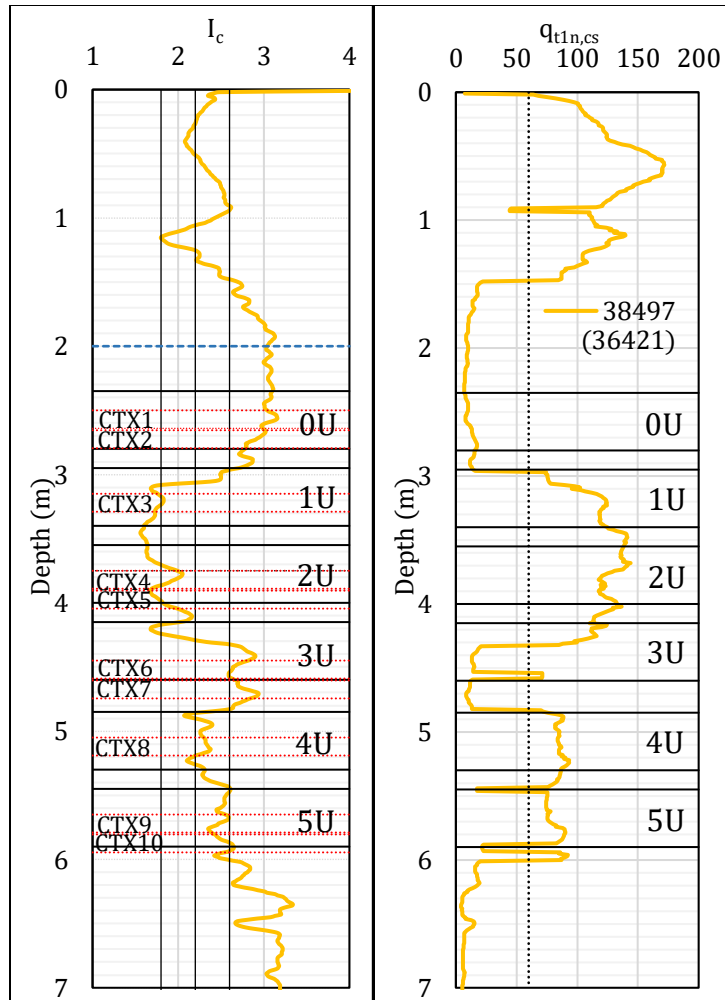



Figure B.1.4.3. I_c and $q_{t1n,cs}$ profiles at the 200 Cashmere Road site with Dames and Moore sampling depths for the simple shear testing program and depths of cyclic triaxial test specimens from previous research studies.

Table B.1.4.1. Dames and Moore sampling depths at Site 33 – 200 Cashmere Road.


Sample ID	Sampling Depth Range (m)
S33-DM2-0U	2.35-2.80
S33-DM2-1U	2.95-3.40
S33-DM2-2U	3.55-4.00
S33-DM2-3U	4.15-4.60
S33-DM2-4U	4.85-5.30
S33-DM2-5U	5.45-5.90

B.2 Boring Logs for Dames and Moore Sampling


B.2.1 Site 2 – Gainsborough Reserve

		SOIL BORING LOG			Page	1/1
		Project Name Silty Soils Project		Boring Number DM-2		
General Comments:		Dames & Moore (DM) sampling for simple shear testing program				
Location:		Site 2 – Gainsborough Reserve		Drilling Contractor:		McMillan Drilling Services
Elevation:		-		Drilling Method and Equipment:		Mud-rotary, Hurjin DB8
Start/Finish Date:		18-07-19 (Thur)		Casing Diameter (mm):		123 (OD)
Logger		Zorana Mijic (UC Berkeley)		Mud Level:		-
Depth below GS (m)	Sample				Soil Description	Comments
	Interval (m)	Number & Type	DM Sampling pressure (psi)	Recovery (%)	(from samples extruded in the lab)	Casing Depth, Drilling Rate, Fluid Loss, Tests & Instrumentation
1.0						
2.0						
3.0	2.60-3.05	1U	125	99 ø56mm/ø63mm		Casing depth = 2.30 m
4.0						
5.0	4.50-4.95	2U	235	98 ø54mm/ø63mm		Casing depth = 4.20 m
6.0	5.15-5.60	3U	150	99 ø59mm/ø63mm		Casing depth = 4.20 m
7.0	5.75-6.20	4U	175	100 ø65mm/ø63mm		Casing depth = 5.20 m
8.0	6.70-7.15	5U	140	100 ø64mm/ø63mm		Casing depth = 6.20 m
	7.90-8.35	6U	200	100 ø64mm/ø63mm		Casing depth = 7.20 m


B.2.2 Site 14 – Barrington Park

		SOIL BORING LOG			Page 1/1	
		Project Name Silty Soils Project		Boring Number DM-3		
		General Comments:		Dames & Moore (DM) sampling for simple shear testing program		
Location:		Site 14 -- Barrington Park		Drilling Contractor:		McMillan Drilling Services
Elevation:		--		Drilling Method and Equipment:		Mud-rotary, Hunjin DB8
Start/Finish Date:		22-05-19 (Wed) - 23-05-19 (Thur)		Casing Diameter (mm):		110
Logger		Zorana Mijic (UC Berkeley)		Mud Level:		--
Depth below GS (m)	Sample			DM Sampling Pressure	Soil Description	Comments
	Interval (m)	Number & Type	Recovery (%)	(psi)	(from samples extruded in the lab)	Casing Depth, Drilling Rate, Fluid Loss, Tests & Instrumentation
1.0						
2.0						
2.30-2.75	0U	94 435mm/463mm	150			Casing depth = 2.00 m; Sudden pressure drop
2.90-3.35	1U	101 467mm/463mm	220			Casing depth = 2.33 m; Sample was drained overnight; High suction at top
3.50-3.95	2U	100 461mm/463mm	200			Casing depth = 3.00 m; Sample was drained overnight; High suction at top
4.0						Wed: casing at 4.00 m BGS, BH depth = 4.00 m Thur: casing at 4.00 m BGS, BH depth = 3.85 m
4.40-4.85	3U	100 463mm/463mm	150			Casing depth = 4.00 m
4.95-5.40	4U	101 466mm/463mm	175			Casing depth = 4.00 m
5.0						
5.75-6.20	5U	98 453mm/463mm	190			Casing depth = 5.45 m (pulled down by bit from 5.33-m to 5.45-m depth)
6.0						
6.45-6.90	6U	100 465mm/463mm	230			Casing depth = 6.15 m
7.0						

B.2.3 Site 23 – 85 Riccarton Road

		SOIL BORING LOG			Page	1/1
		Project Name Silty Soils Project		Boring Number DM-2		
General		Dames & Moore (DM) sampling for simple shear testing program				
Comments:						
Location:		Site 23 -- 85 Riccarton Road			Drilling Contractor: McMillan Drilling Services	
Elevation:		-			Drilling Method and Equipment: Mud-rotary, Hurjin DB8	
Start/Finish Date:		20-07-19 (Saturday)			Casing Diameter (mm): 123 (OD)	
Logger:		Zorana Mijic (UC Berkeley)			Mud Level: -	
Depth below GS (m)	Sample				Soil Description	Comments
	Interval (m)	Number & Type	DM Sampling pressure (psi)	Recovery (%)	(from samples extruded in the lab)	Casing Depth, Drilling Rate, Fluid Loss, Tests & Instrumentation
1.0						
2.0						
2.05-2.50	1U	350	94	436mm/463mm		Casing depth = 1.30 m
3.0						
4.0						
4.30-4.75	2U	175	94	433mm/463mm		Casing depth = 3.90 m
5.0						
4.90-5.35	3U	140	97	451mm/463mm		Casing depth = 3.90 m
6.0						
6.30-7.75	4U	290	98	456mm/463mm		Casing depth = 6.00 m
7.0						
6.90-7.35	5U	200	100	461mm/463mm		Casing depth = 6.00 m
8.0						
7.60-8.05	6U	290	101	466mm/463mm		Casing depth = 6.60 m

B.2.4 Site 33 – 200 Cashmere Road

		SOIL BORING LOG			Page 1/1		
		Project Name Silty Soils Project		Boring Number DM-3			
		General Comments:		Dames & Moore (DM) sampling for simple shear testing program			
Location:		Site 33 -- 200 Cashmere Road		Drilling Contractor:		McMillan Drilling Services	
Elevation:		--		Drilling Method and Equipment:			Mud-rotary, Hunjin DB8
Start/Finish Date:		21-05-19 (Tuesday)		Casing Diameter (mm):			110
Logger		Zorana Mijic (UC Berkeley)		Mud Level:			--
Depth below GS (m)	Sample			DM Sampling Pressure (psi)	Soil Description (from samples extruded in the lab)	Comments (Casing Depth, Drilling Rate, Fluid Loss, Tests & Instrumentation)	
	Interval (m)	Number & Type	Recovery (%)				
1.0							
2.0							
2.35-2.80	0U	98 452mm/463mm	150			Casing depth = 2.00 m; Sudden pressure drop	
2.95-3.40	1U	97 451mm/463mm	200			Casing depth = 2.60 m; Gradual pressure drop	
3.55-4.00	2U	95 438mm/463mm	230			Casing depth = 2.60 m; Gradual pressure drop; High suction at top 15 cm	
4.15-4.60	3U	100 463mm/463mm	100			Casing depth = 3.80 m; Gradual pressure drop	
4.85-5.30	4U	99 456mm/463mm	120			Casing depth = 3.80 m; Gradual pressure drop	
5.45-5.90	5U	99 456mm/463mm	200			Casing depth = 4.50 m; Sudden pressure drop	
7.0							

B.3 Dames and Moore Sampling and Soil Sample Extrusion



Figure B.3.1. Tri-cone roller bit and thin-walled brass tube attached to the Dames and Moore sampler.

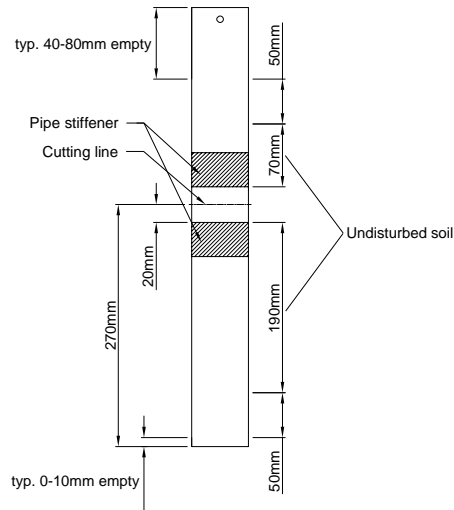


Figure B.3.2. Brass tube cutting prior to soil extrusion.

Appendix C

Index Testing and Scanning Electron Microscope Images

C.1 Particle Size Distribution

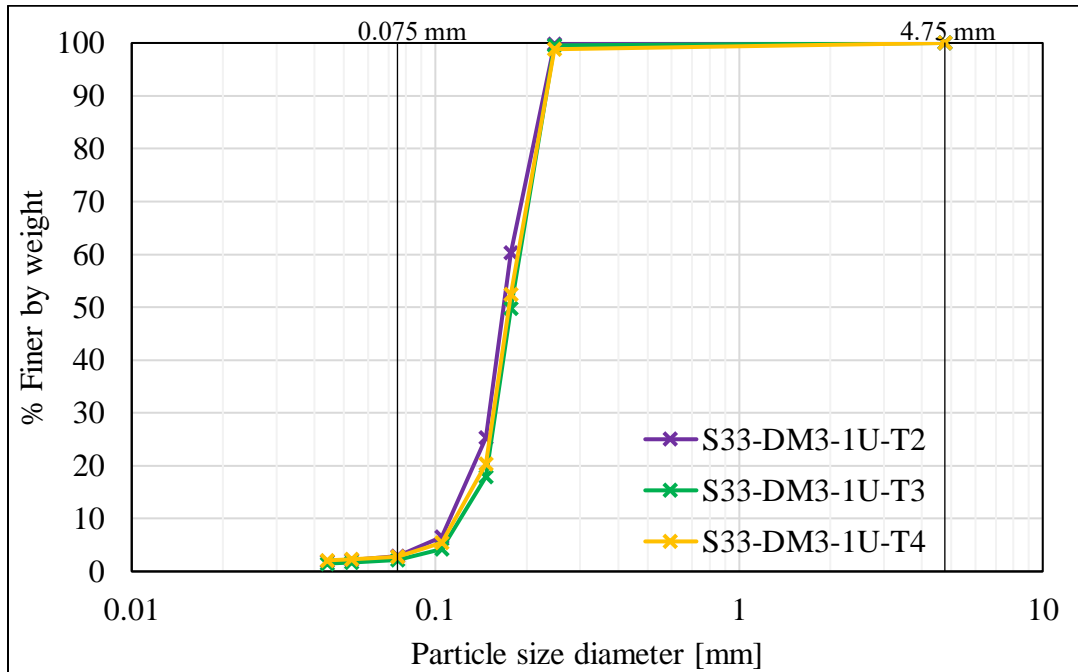


Figure C.1.1. Particle size distribution curves for S33-DM3-1U-T2, -T3, and -T4.

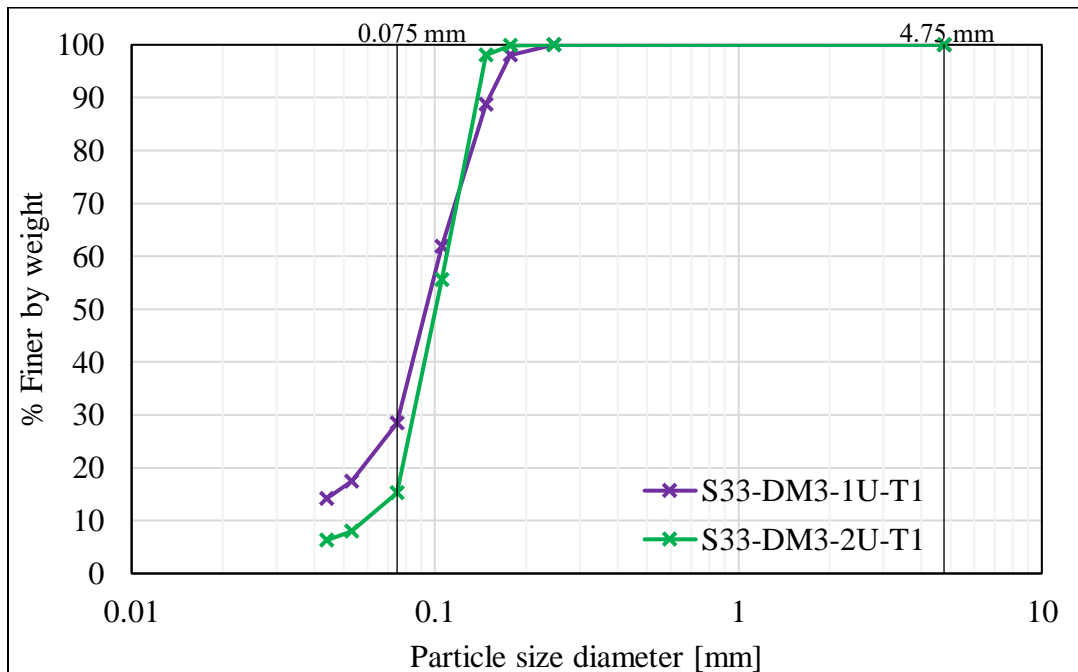


Figure C.1.2. Particle size distribution curves for S33-DM3-1U-T1 and S33-DM3-2U-T1.

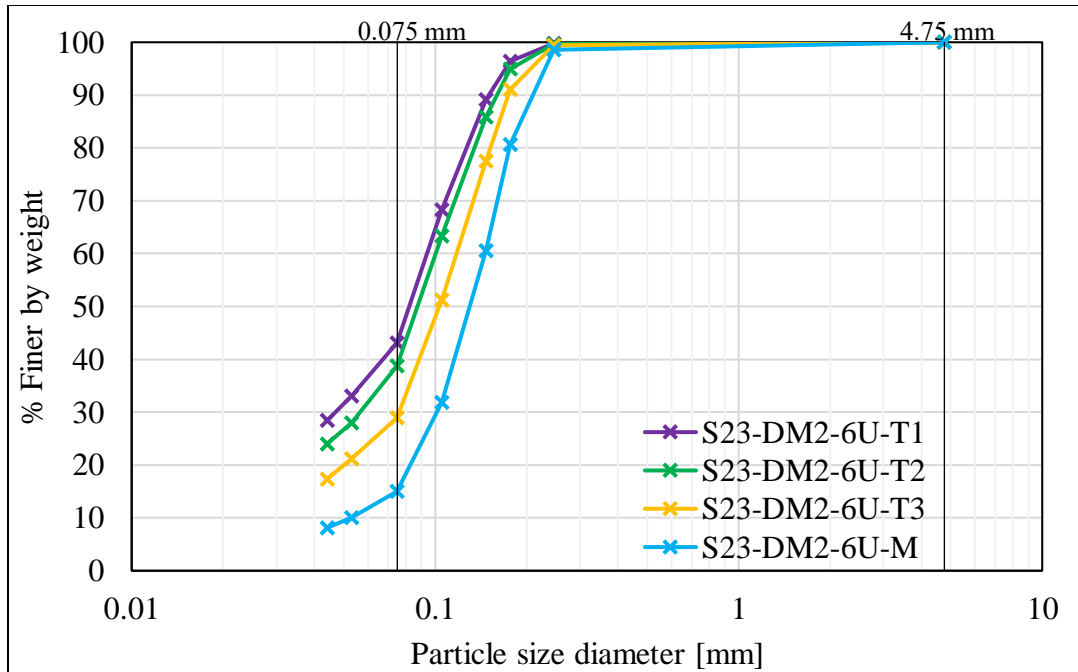


Figure C.1.3. Particle size distribution curves for S23-DM2-6U-T1, -T2, -T3, and -M.

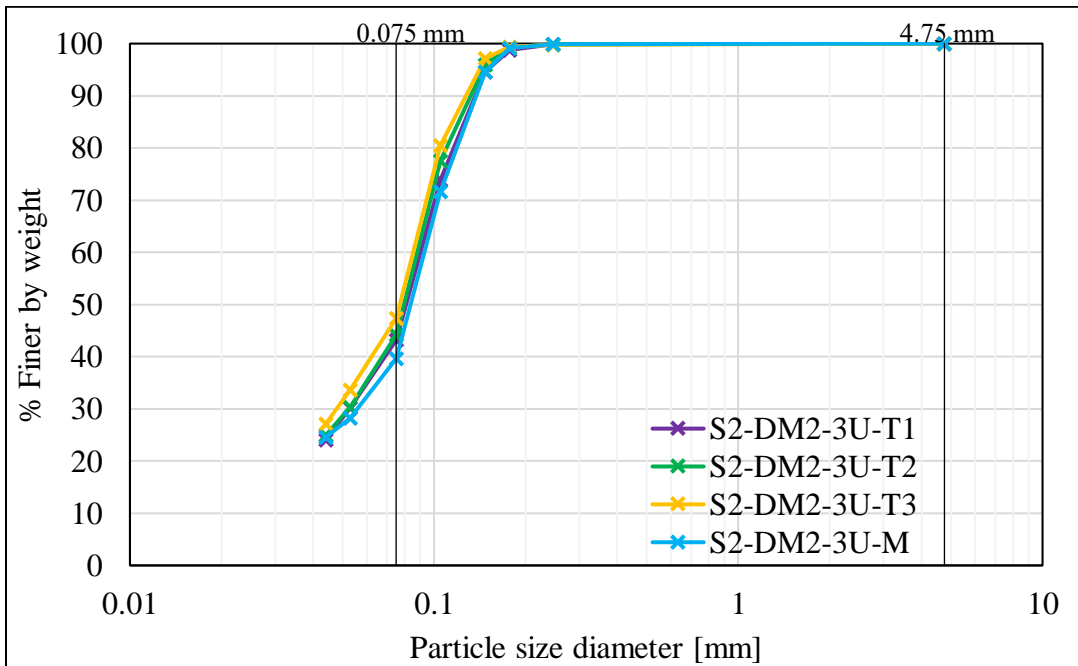


Figure C.1.4. Particle size distribution curves for S2-DM2-3U-T1, -T2, -T3, and -M.

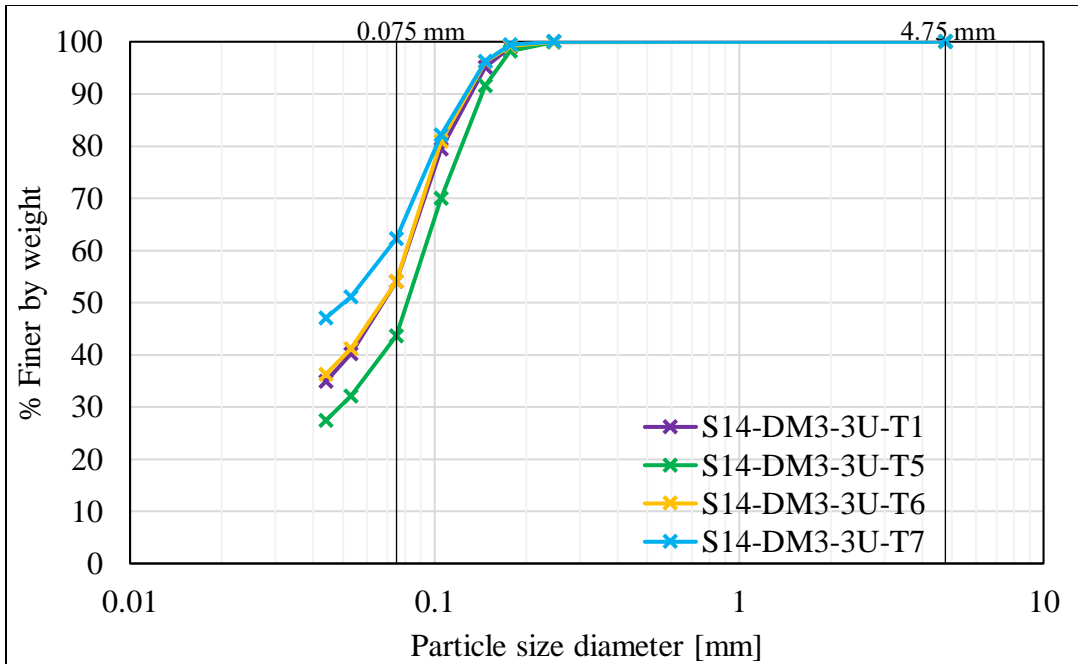


Figure C.1.5. Particle size distribution curves for S14-DM3-3U-T1, -T5, -T6, and -T7.

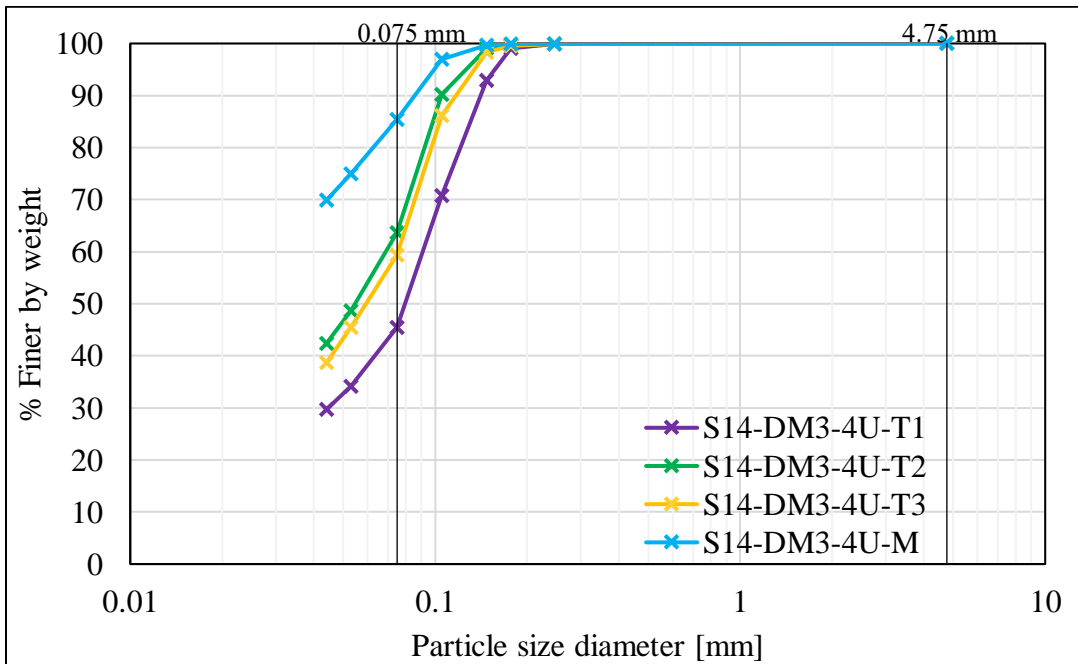


Figure C.1.6. Particle size distribution curves for S14-DM3-4U-T1, -T2, -T3, and -M.

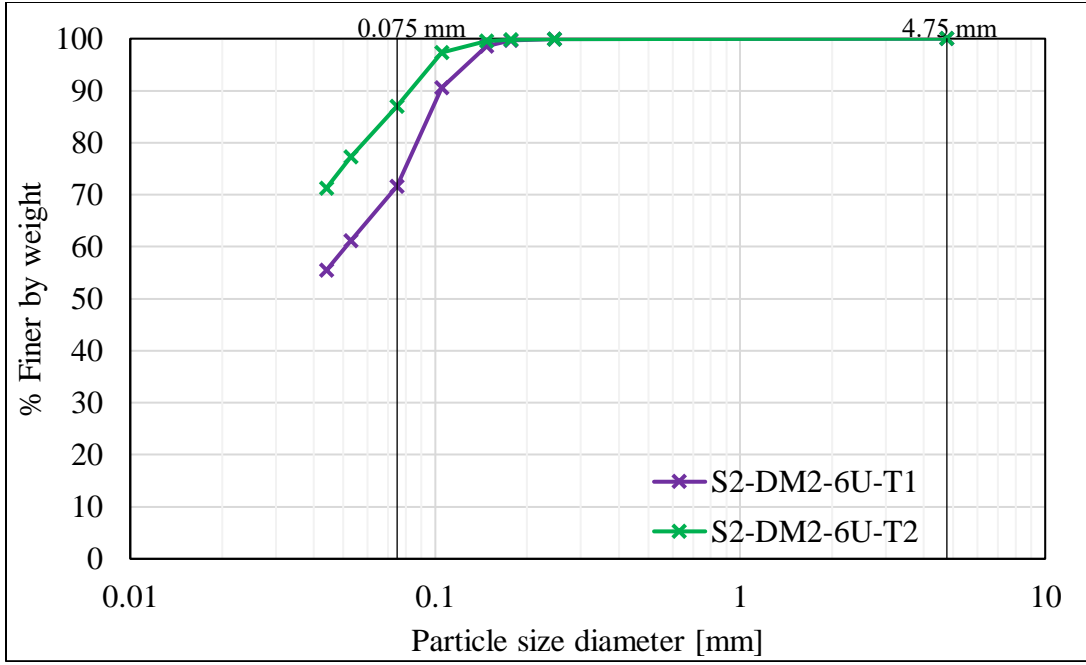


Figure C.1.7. Particle size distribution curves for S2-DM2-6U-T1 and -T2.

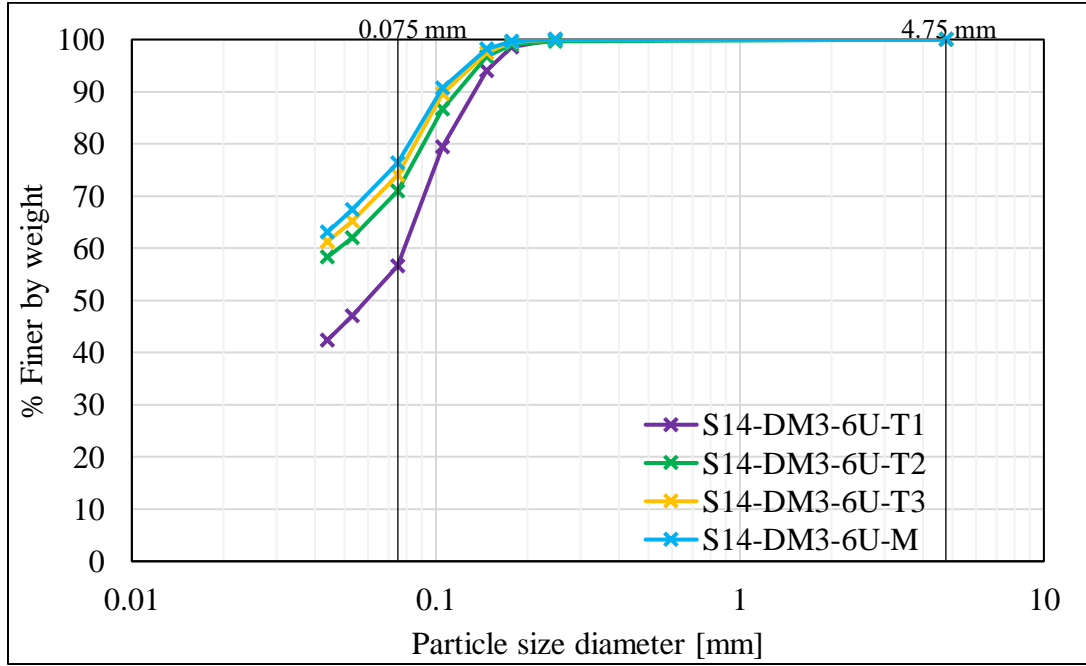


Figure C.1.8. Particle size distribution curves for S14-DM3-6U-T1, -T2, -T3, and -M.

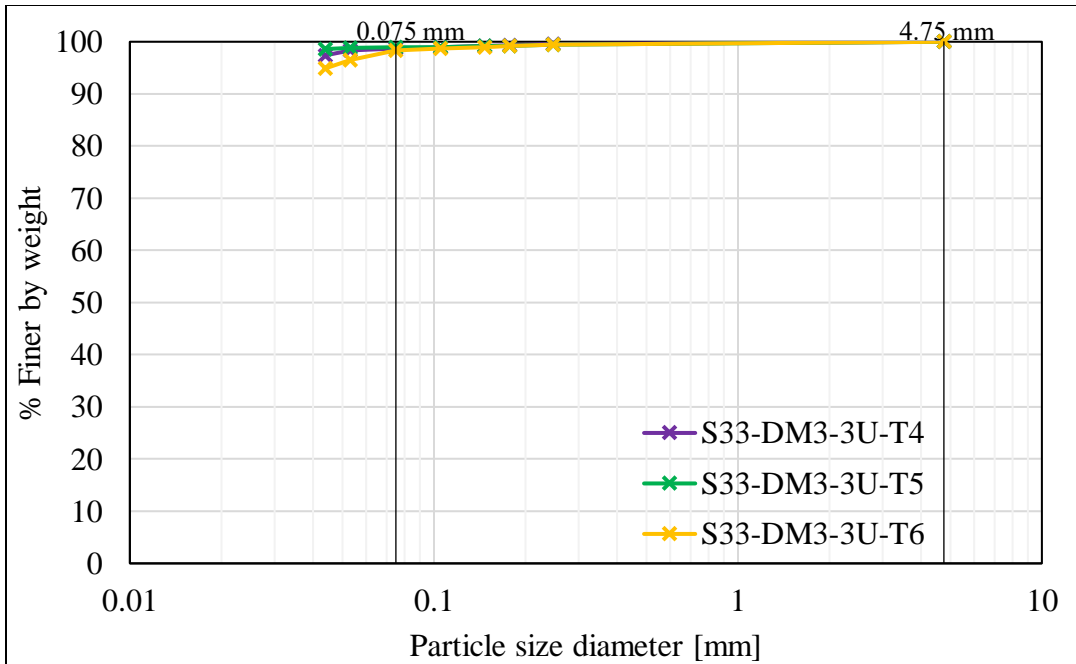


Figure C.1.9. Particle size distribution curves for S33-DM3-3U-T4, -T5, and -T6.

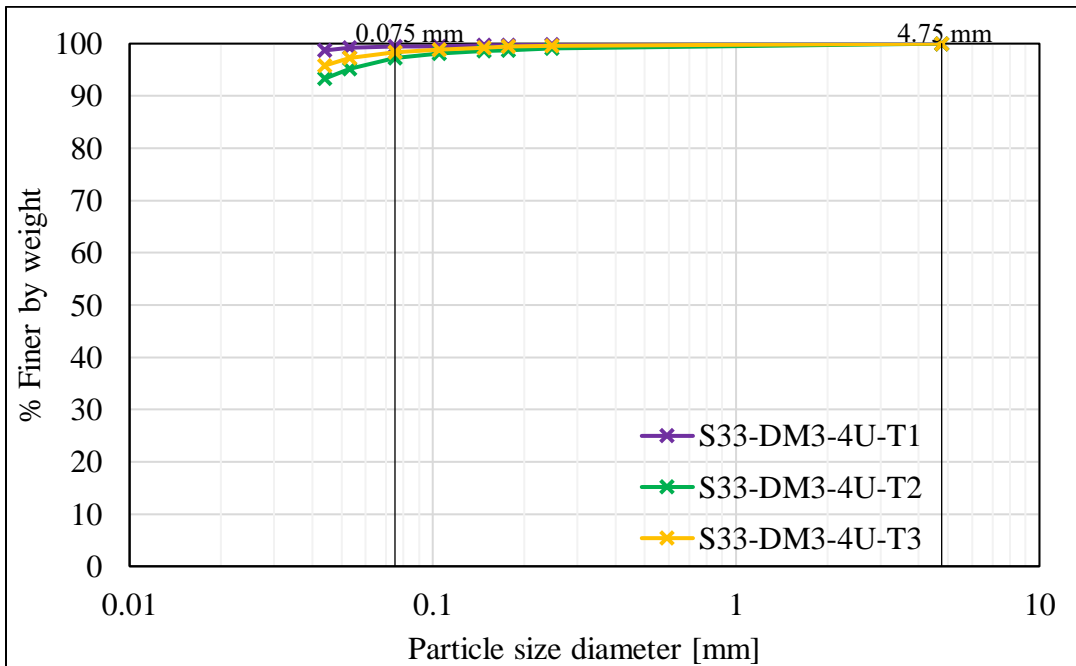


Figure C.1.10. Particle size distribution curves for S33-DM3-4U-T1, -T2, and -T3.

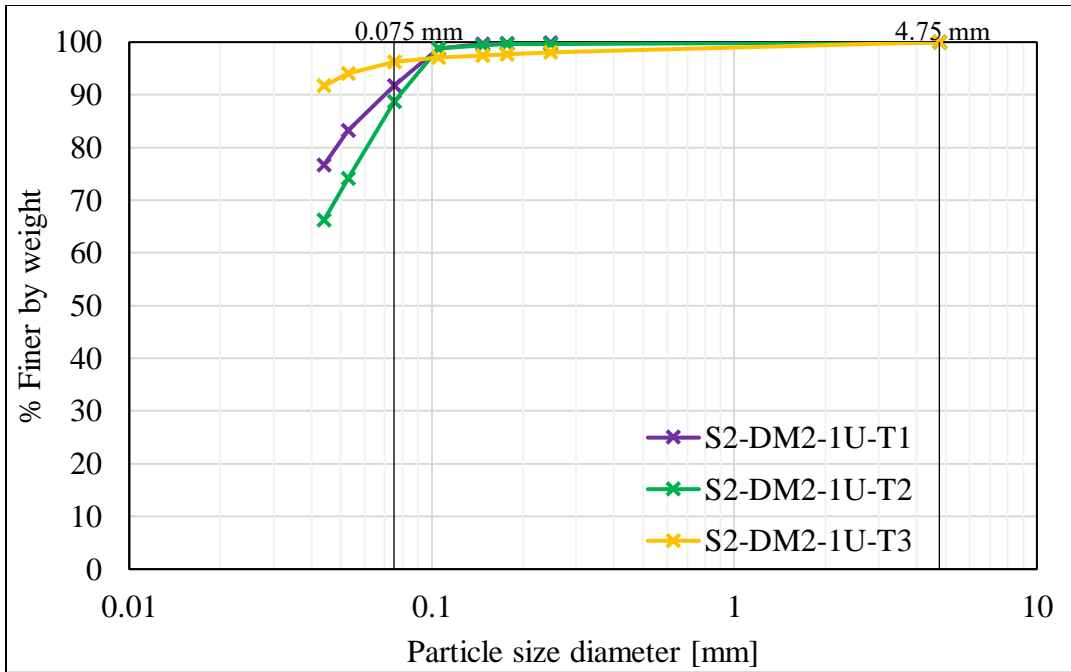


Figure C.1.11. Particle size distribution curves for S2-DM2-1U-T1, -T2, and -T3.

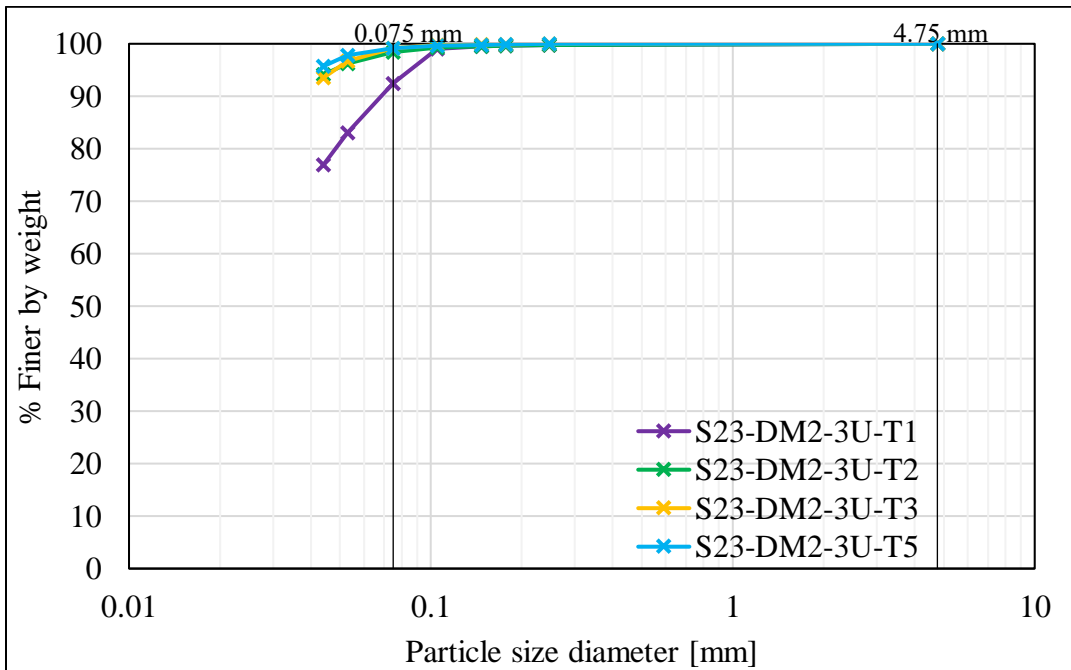


Figure C.1.12. Particle size distribution curves for S23-DM2-3U-T1, -T2, -T3, and -T5.

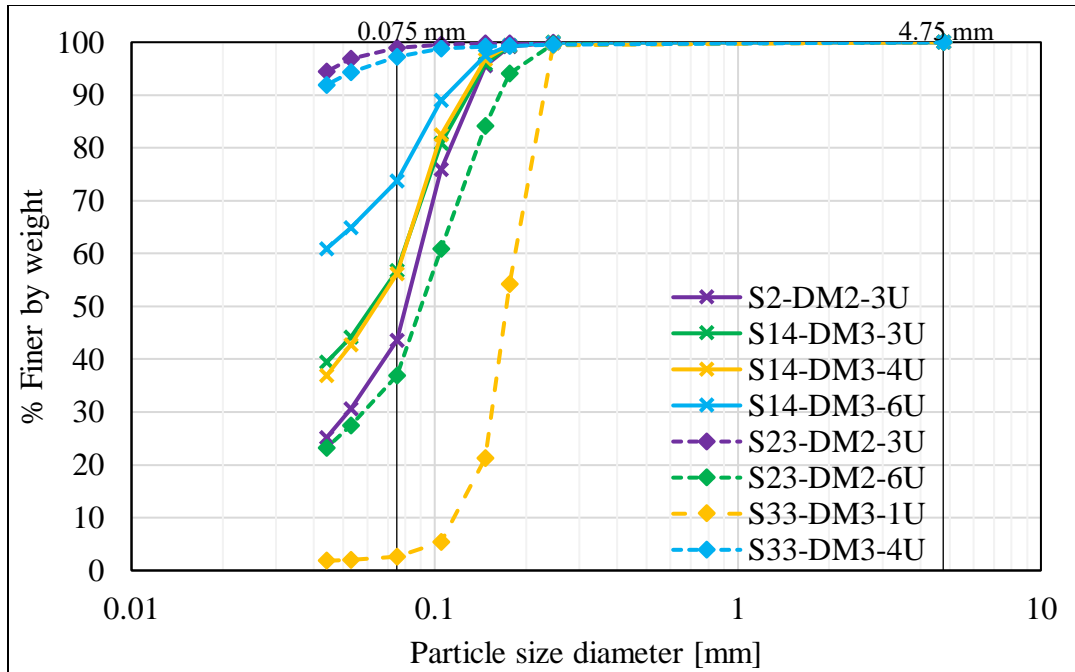


Figure C.1.13. Particle size distribution curves for soil composites: S2-DM2-3U, S14-DM3-3U, S14-DM3-4U, S14-DM3-6U, S23-DM2-3U, S23-DM2-6U, S33-DM3-1U, and S33-DM3-4U.

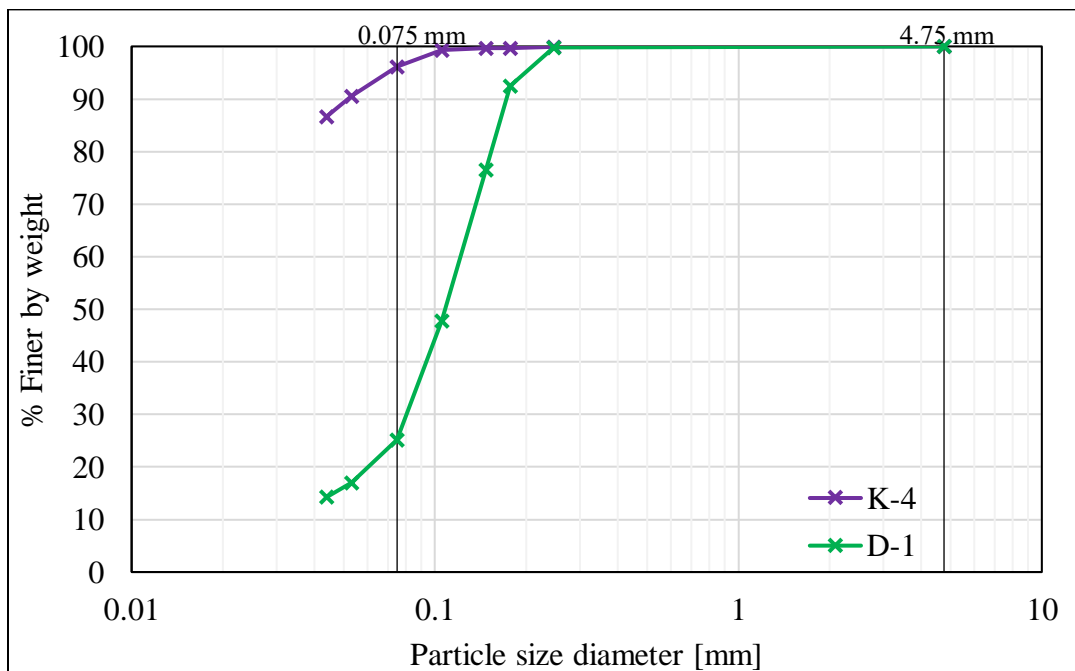


Figure C.1.14. Particle size distribution curves for D-1 and K-4 (Table 4.1). D-1 is an equivalent of S14-DM3-3U-T2 not presented in Chapter 5.

C.2 Plasticity Index per ASTM D4318 and NGI Fall Cone Test

The first step in determining the plasticity of soil was a plastic limit test in accordance with ASTM D4318, which consisted of rolling out a thread of soil until it broke apart at a diameter of 3.2 mm [1/8 in]. Soils that could not be rolled out into a thread and down to the specified diameter were considered non-plastic and were not tested for the liquid limit. Soils whose plastic limit could be determined were subsequently subjected to the liquid limit testing as per ASTM D4318, which utilizes the percussion cup (also known as the Casagrande cup). The soil is said to reach its liquid limit when 25 drops of the cup cause the groove to close over a distance of 12.7 mm [1/2 in]. However, all of the tested soils closed the groove over the specified distance at less than 25 drops of the cup when their moisture contents were close to their plastic limits. This can be interpreted in two ways: (1) soils are non-plastic because the liquid limit is equal to or less than the plastic limit or (2) the liquid limit of these soils hence their plasticity index cannot be determined by the Casagrande's method because of the testing difficulties associated with these soils.

When a soil was too dry, i.e., its moisture content was below its plastic limit, it crumbled during its placement in the cup and cutting of the groove and slid down relative to the surface of the cup (Figure C.2.1). Once the groove was made with multiple passes of a grooving tool, the dry soil bounced off the cup's surface as the cup was dropped. When a moisture content of a soil was at a plastic limit or above it by even 1%, the soil slid out of the cup and exhibited thin water films on its surface during its placement in the cup (Figure C.2.2). The groove was cut with multiple strokes of the grooving tool. Even though extreme care was exercised during the cutting process, tearing of the soil and sliding of the soil pat relative to the surface of the cup could not be prevented (Figure C.2.2).

For soils whose liquid limit could not be evaluated using the Casagrande's method, the fall cone test (FCT) was used too to assess the liquid limit. The FCT tends to have better accuracy and repeatability than the Casagrande's method (Campbell and Blackford 1984; O'Kelly et al. 2018). For low plasticity soils, it eliminates problems associated with the Casagrande's method, such as the difficulty in cutting the groove and the tendency of soil to slide down in the cup (Sowers et al. 1960; Sherwood and Ryley 1970; Mitchell 1961). However, the FCT does not address the problem of low plasticity soils that tend to liquefy in the Casagrande cup. Once placed in the fall cone cup, these low plasticity soils tend to liquefy near the surface.

The cone type and the cone penetration depth used to determine the liquid limit of the soil vary among different countries. Canada, Japan, Sweden, and Norway utilize a cone that has a mass of 60 g and an apex angle of 60°, whereas a 30°-80 g cone is used in the UK, Australia, New Zealand, and France (Shimobe 2010, Kang et al. 2017). The Japanese Geotechnical Society defines the liquid limit as the moisture content at which the 60°-60 g cone penetrates a depth of 11.5 mm, while the standards in Canada, Sweden, and Norway specify the penetration depth of 10 mm by the same 60°-60 g cone (Kang et al. 2017). The British standard defines the liquid limit as the moisture content at which the 30°-80 g cone penetrates a depth of 20 mm. It appears that countries concerned with low-to-medium plasticity clays have adopted a 10-mm penetration depth, while countries interested in testing high-plasticity clays prefer a larger penetration depth (Kuomoto and Houlsby 2001). Koumoto and Houlsby (2001) propose the adoption of the 10-mm penetration depth to eliminate differences in the standards worldwide. They also advocate the use of the 60°-60

g cone due to (1) better agreement between the theoretical understanding of this cone and the experimental results, (2) lower sensitivity to variations in cone roughness hence greater repeatability between geotechnical laboratories, and (3) resistance of the blunter tip of the 60° cone to wear. They acknowledge the larger penetration depth for the 30° cone results in higher accuracy; however, they still consider the 60° cone to be superior to the 30° cone due to the aforementioned advantages. O’Kelly et al. (2018) propose the 30° cone as a choice for international standardization due to its much wider use.

The fall cone test device available at the geotechnical laboratory at UC Berkeley is designed by the Norwegian Geotechnical Institute and manufactured by Roctest, Canada. It utilizes a 60°-60 g cone. A cylindrical soil container has a diameter of 39.4 mm [1.55 in] and a depth of 25.5 mm [1.00 in] to accommodate the amount of soil available for testing. The liquid limit is defined as the moisture content at which the cone impression is 10 mm (Karlsson 1961). Accordingly, all tested soils in this study exhibited liquid limits higher than their plastic limits determined by the ASTM D4318 thread-rolling method so their plasticity indices range from 4 to 9 (Table C.2.1). The plasticity index was calculated as the difference between the FCT-based liquid limit and the ASTM-based plastic limit. The Norwegian Standard reports the thread-rolling technique as a standard test method for determining the plastic limit of soil (NS 1982).

O’Kelly et al. (2018) reviewed the fall cone approach as an alternative method for determining the plastic limit and concluded the true plastic limit could not be measured by these shear strength-based methods because they do not measure the onset of brittleness. These approaches can be useful if the variability of undrained strength with changing water content is of interest rather than the brittle-ductile state transition. However, if a 30°-80 g and fall cone set-up is used, they suggested reporting PL₂₅, the moisture content at which the shear strength is 25 times the strength mobilized at the fall cone-based liquid limit for inorganic soils. The PL₂₅ corresponds to a 4-mm penetration depth (one-fifth of the 20-mm penetration depth at the liquid limit). O’Kelly et al. (2018) consider PL₂₅ to be superior to PL₁₀₀ because it requires only a minor extrapolation of cone penetration depth against moisture content. Importantly, the PL₁₀₀ moisture content is often lower than the moisture content corresponding to the Atterberg’s PL, meaning the soil is often tested in a brittle rather than a plastic state, and the strain-rate dependence is expected to differ significantly for the two states.

Shimobe (2010), Feng (2000), and Harrison (1988) defined the plastic limit based on the 30°-80g fall cone test as a moisture content at which a cone penetration depth is 2 mm. This value stems from the correlation between the undrained shear strength and the penetration depth and the assumption of the ratio between the undrained shear strength at the plastic limit and the undrained shear strength at the liquid limit. Considering the penetration depth is inversely proportional to the square root of the undrained shear strength (Hansbo 1957) and assuming a 100-fold variation between the undrained shear strength at the plastic limit and the undrained shear strength at the liquid limit, the cone penetration depth at the plastic limit (2 mm) corresponds to one-tenth of the cone impression depth at the liquid limit (20-mm). The 2-mm penetration depth is also reported in the People’s Republic of China standard for determining the plastic limit by a 30°-76 g fall cone (Shimobe 2010). The UK, France, Australia, New Zealand, Sweden, Norway, Canada, and Japan do not have a standardized cone penetration depth at the plastic limit (Shimobe 2010).

For a 60°-60g cone and a penetration depth of 10 mm, the undrained shear strength at the liquid limit is 1.83 kPa (Koumoto and Houlsby 2001). If 100 times the undrained shear strength at the liquid limit and one-tenth of the penetration depth at the liquid limit are assumed, then a 1-mm penetration depth would be expected at the plastic limit. However, Koumoto and Houlsby (2001) considered a penetration depth of 1 mm to be “unrealistic” because it is rarely achieved for clays and as such requires extrapolation to the plastic limit from higher water contents and “serious consideration” of setting a plastic limit threshold. Hence, they recommended the plastic limit be redefined based on a suitable combination of cone mass and penetration depth. Koumoto and Houlsby (2001) also redefined a plasticity index, $PI_{FC} = \ln(LL_{FC}) - \ln(PL_{FC})$, where LL_{FC} and PL_{FC} are the fall cone-based liquid limit and the fall cone-based plastic limit, respectively.

The fall cone-based plastic limits for the penetration depth of 1 mm, PL_{FC} , and the plasticity indices as per Koumoto and Houlsby (2001), PI_{FC} , are reported in Table C.2.1. Clearly, the plastic limits determined by the fall cone method are lower than the plastic limits determined by the thread-rolling method, PL_{ASTM} . Likewise, the plasticity indices calculated using the equation of Koumoto and Houlsby (2001) for PI_{FC} are lower than $PI_{FC/ASTM}$, the plasticity indices evaluated based on the ASTM plastic limit, PL_{ASTM} , or as the difference between the fall-cone based liquid limit, LL_{FC} , and the PL_{ASTM} .

Importantly, the liquid and plastic limit values deduced using the ASTM Casagrande cup and thread-rolling methods were used for the development of the standard plasticity chart (ASTM 2020). If it is insisted on absolute adherence to this traditional approach, then the fall cone-based liquid limit and/or the fall cone-based plastic limit should not be used for soil classification purposes. Although a change in the liquid limit and/or the plastic limit with respect to the testing method may not represent a fundamental change in soil behavior, it may affect the soil classification due to the precise thresholds of the liquid limit and the plasticity index.



Figure C.2.1. Soil is too dry so its liquid limit cannot be determined using the Casagrande's method.



Figure C.2.2. Soil is at its plastic limit yet above its liquid limit according to the Casagrande's method.

Table C.2.1. Liquid limit, plastic limit, and plasticity index using ASTM D4318 and fall cone test method.

Specimen	FC [%]	PL _{ASTM}	PL _{FC}	LL _{ASTM}	LL _{FC}	PI _{ASTM}	PI _{FC/ASTM}	PI _{FC}
S14-DM3-4U-M	85	23	11	≤23	28	0	5	1
S2-DM2-6U-T1	72	22	13	≤22	25	0	3	1
S2-DM2-6U-T2	87	21	13	≤21	27	0	6	1
S14-DM3-6U-T1	57	20	7	≤20	24	0	4	1
S14-DM3-6U-T2	71	17	14	≤17	23	0	6	1
S14-DM3-6U-T3	74	18	8	≤18	22	0	4	1
S14-DM3-6U-M	76	17	9	≤17	23	0	6	1
S33-DM3-3U-T4	99	24	11	≤24	31	0	7	1
S33-DM3-3U-T5	99	25	19	≤25	32	0	7	1
S33-DM3-3U-T6	98	24	17	≤24	30	0	6	1
S33-DM3-4U-T1	99	24	22	≤24	31	0	7	0
S33-DM3-4U-T2	97	24	19	≤24	30	0	6	1
S33-DM3-4U-T3	98	21	16	≤21	30	0	9	1
S2-DM2-1U-T1	92	20	6	≤20	27	0	7	2
S2-DM2-1U-T2	89	23	11	≤23	30	0	7	1
S2-DM2-1U-T3	96	19	7	≤19	27	0	8	1
S23-DM2-3U-T1	92	21	12	≤21	28	0	7	1
S23-DM2-3U-T2	98	21	18	≤21	30	0	9	1
S23-DM2-3U-T3	99	22	15	≤22	30	0	8	1
S23-DM2-3U-T5	99	23	18	≤23	31	0	8	1

Notes: PL_{ASTM} = Plastic limit as per ASTM D4318 (the thread-rolling method), PL_{FC} = Plastic limit based on the fall cone test method (Koumoto and Houlsby 2001); LL_{ASTM} = Liquid limit as per ASTM D 4318 (the Casagrande's method), LL_{FC} = Liquid limit based on the fall cone test method (Karlsson 1961); PI_{ASTM} = Plasticity index as the difference between LL_{ASTM} and PL_{ASTM} (used for USCS); PI_{ASTM/FC} = Plasticity index as the difference between LL_{FC} and PL_{ASTM}; PI_{FC} = Plasticity index as the difference between ln(LL_{FC}) and ln(PL_{FC}) (Koumoto and Houlsby 2001).

References

- ASTM Standard. (2018). ASTM D4318-17e1: Standard test methods for liquid limit, plastic limit, and plasticity index of soils. West Conshohocken, PA, USA: ASTM International.
- ASTM Standard. (2020). ASTM D2487-17e1: Standard practice for classification of soils for engineering purposes (unified soil classification system). West Conshohocken, PA, USA: ASTM International.
- Campbell, D. A., and Blackford, J. W. (1984). *Fall cone method used to determine the liquid limit of soil*. Retrieved from <https://www.usbr.gov/tsc/techreferences/research/GR8411.pdf>
- Feng, T. W. (2000). Fall-cone penetration and water content relationship of clays. *Géotechnique*, 50(2), 181-187.
- Hansbo, S. (1957). A new approach to the determination of the shear strength of clay by the fall-cone test. In *Proceedings of the Royal Swedish Geotechnical Institute SGI*, Vol. 14, 7-47.
- Harrison, J. A. (1988). Using BS cone penetrometer for the determination of plastic limit of soils. *Géotechnique*, 38(3): 433–438.
- Kang, G., Tsuchida, T., Tang, T.X., and Kalim, T. P. (2017). Consistency measurement of cement-treated marine clay using fall cone test and Casagrande liquid limit test. *Soils and Foundations*, 57(5), 802-814. <https://doi.org/10.1016/j.sandf.2017.08.010>
- Karlsson, R. (1961). Suggested improvements in the liquid limit test, with reference to flow properties of remoulded clays. In *Proceedings of the 5th International Conference on Soil Mechanics and Foundation Engineering*, Paris, France, Vol. 1, 171-184.
- Koumoto, T. and Houlsby, G. T. (2001). Theory and practice of the fall cone test. *Géotechnique*, 51(8), 701–712. <https://doi.org/10.1680/geot.2001.51.8.701>
- Mitchell, J. E. (1961). *Determination of liquid and plastic limits of soils by the cone penetration method*. U.S. Army Engineer Waterways Experiment Station, Miscellaneous Paper No. 3-478, Report 4.
- Norsk Standard 8003. (1982). *Geoteknisk prøving. Laboratoriemetoder. Plastisitetsgrensen*. Norges Standardiseringsforbund.
- O'Kelly, B. C., Vardanega, P. J., and Haigh, S. K. (2018). Use of fall cones to determine Atterberg limits: A review. *Géotechnique*, 68(10), 843-856. doi:10.1680/jgeot.17.r.039
- Sherwood, P. T., and Ryley, M. D. (1970). An investigation of a cone-penetrometer method for the determination of the liquid limit. *Géotechnique*, 20, 203-208.
- Shimobe, S. (2010). Determination of index properties and undrained shear strength of soils using the fall-cone test. In *Proceedings of the 7th international symposium on lowland technology, ISLT2010*, Saga, Japan, 51–59.
- Sowers, G. F., A. Vesic, and M. Grandolfi, (1960). Penetration tests for liquid limit. *ASTM Special Technical Publication*, No. 254, 216-224.

C.3 Scanning Electron Microscope Images

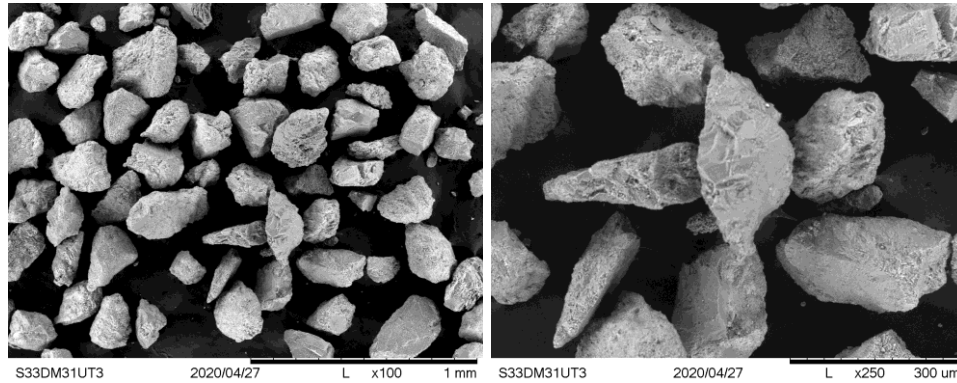


Figure C.3.1. SEM images of S33-DM3-1U-T3 (FC = 2%) enlarged 100 and 250 times. The one enlarged 100 times was used to assess the particle shape (Table 5.1).

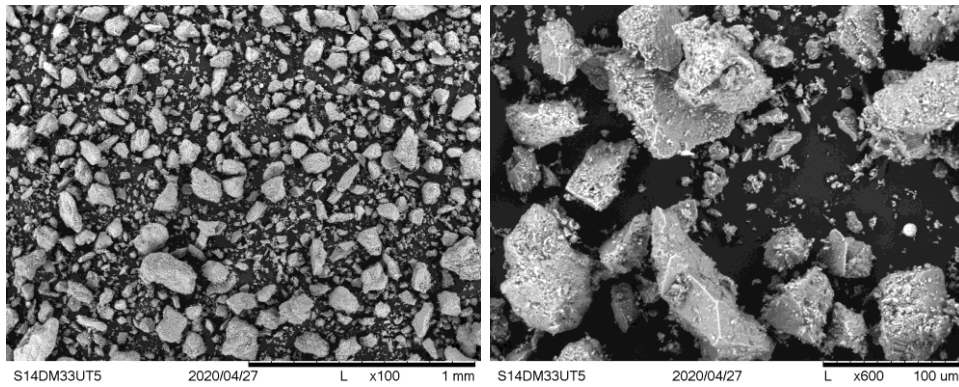


Figure C.3.2. SEM images of S14-DM3-3U-T5 (FC = 44%) fines + coarse fractions (“as-is”) enlarged 100 and 600 times.

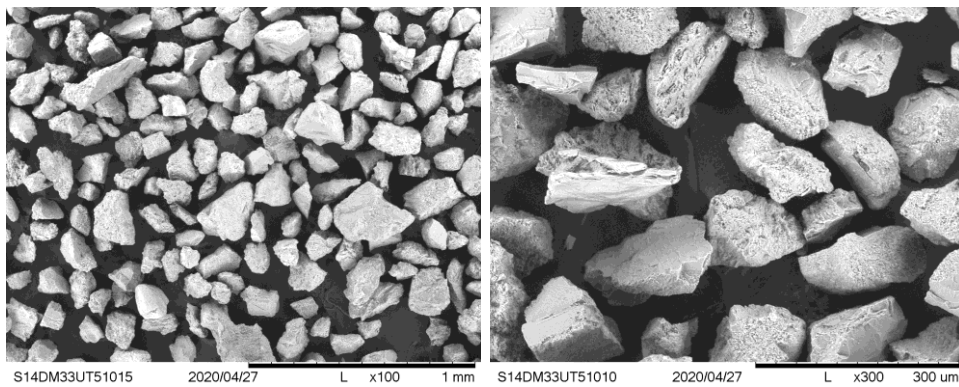


Figure C.3.3. SEM images of S14-DM3-3U-T5 coarse fraction enlarged 100 and 300 times. The one enlarged 100 times was used to assess the particle shape (Table 5.1).

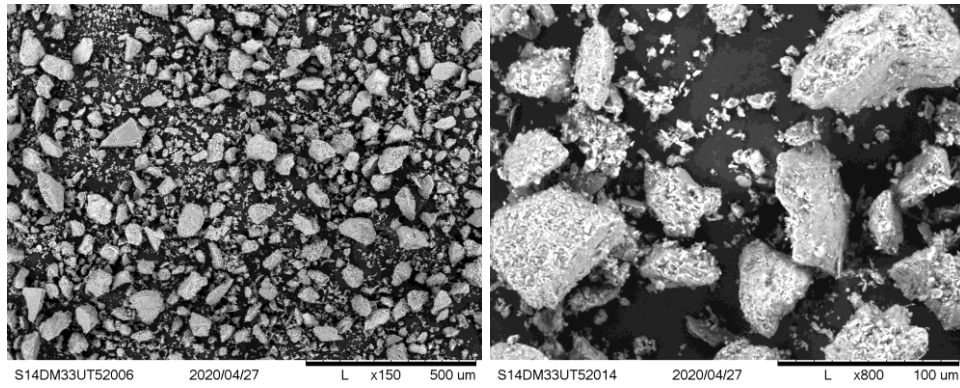


Figure C.3.4. SEM images of S14-DM3-3U-T5 fines fraction enlarged 150 and 800 times. The one enlarged 150 times was used to assess the particle shape (Table 5.1).

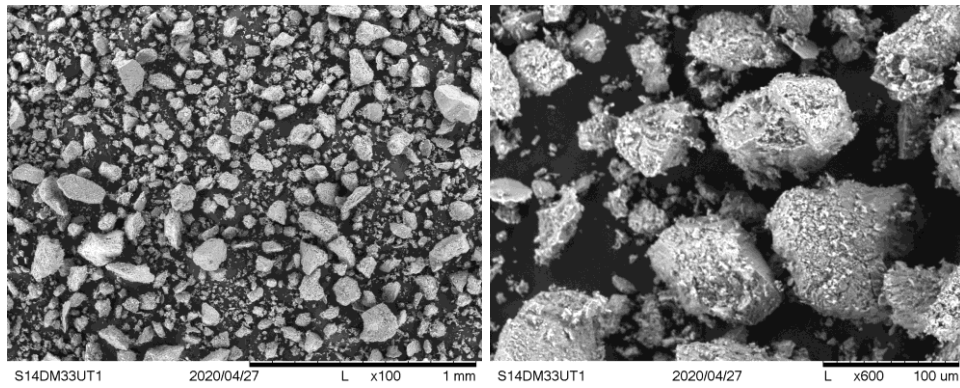


Figure C.3.5. SEM images of S14-DM3-3U-T1 (FC = 54%) coarse + fines fractions ("as-is") enlarged 100 and 600 times.

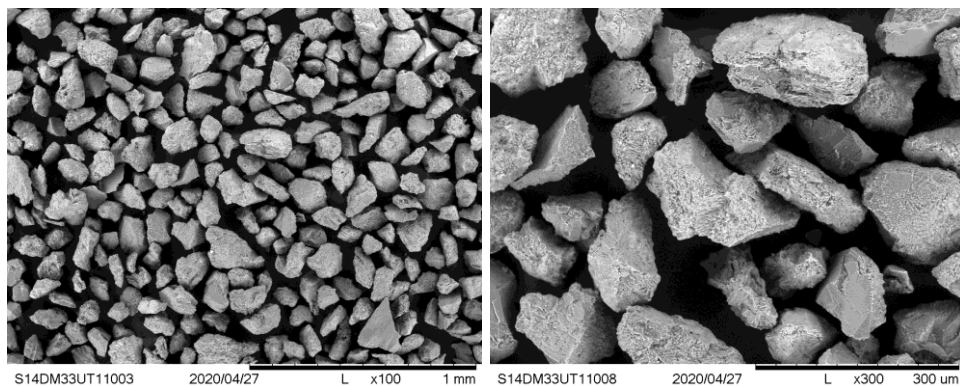


Figure C.3.6. SEM images of S14-DM3-3U-T1 coarse fraction enlarged 100 and 300 times. The one enlarged 100 times was used to assess the particle shape (Table 5.1).

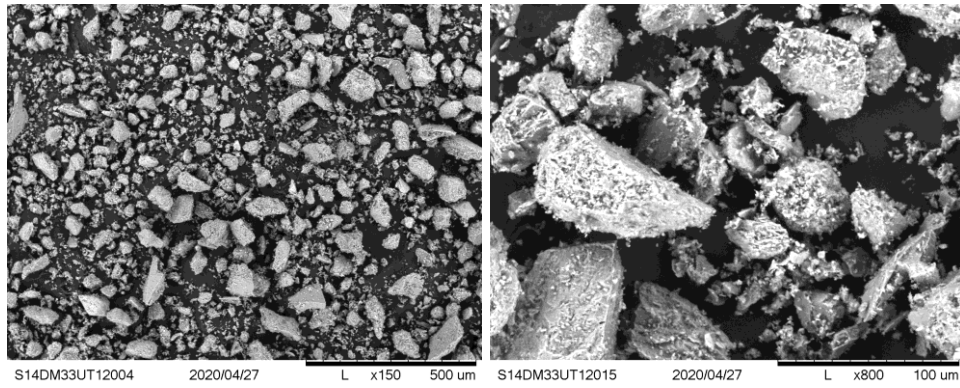


Figure C.3.7. SEM images of S14-DM3-3U-T1 fines fraction enlarged 150 and 800 times. The one enlarged 150 times was used to assess the particle shape (Table 5.1).

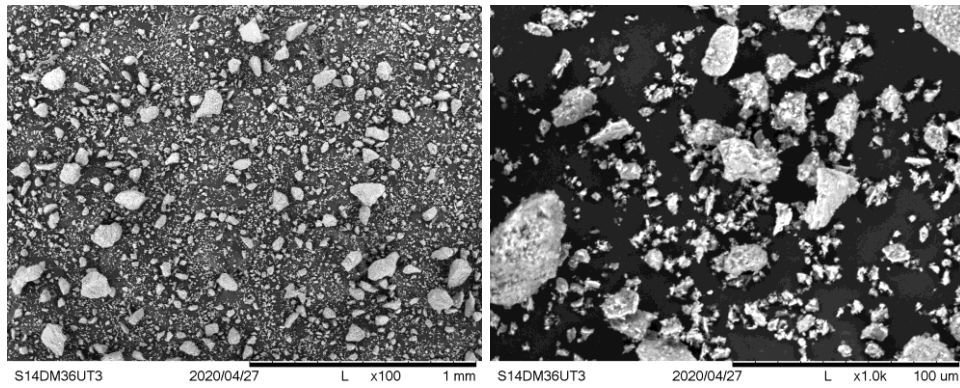


Figure C.3.8. SEM images of S14-DM3-6U-T3 (FC = 74%) coarse + fines fractions ("as-is") enlarged 100 and 1000 times.

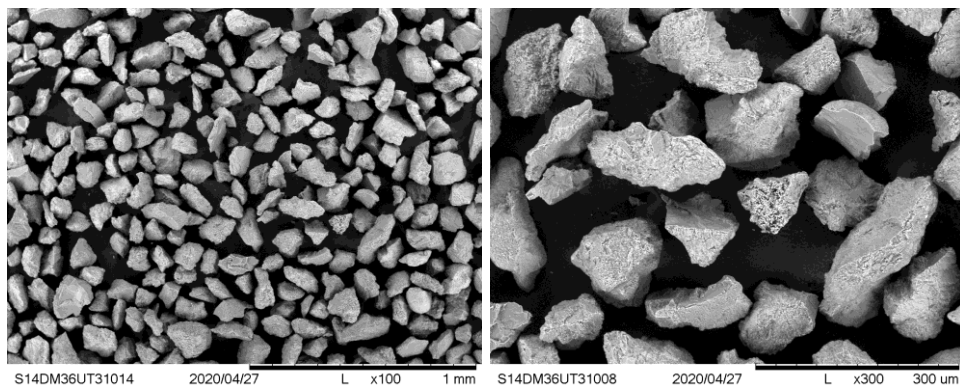


Figure C.3.9. SEM images of S14-DM3-6U-T3 coarse fraction enlarged 100 and 300 times. The one enlarged 100 times was used to assess the particle shape (Table 5.1).

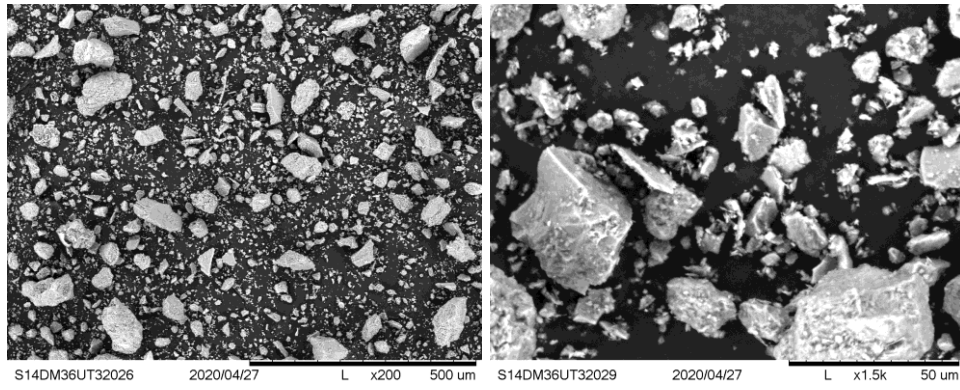


Figure C.3.10. SEM images of S14-DM3-6U-T3 fines fraction enlarged 200 and 1500 times. The one enlarged 200 times was used to assess the particle shape (Table 5.1).

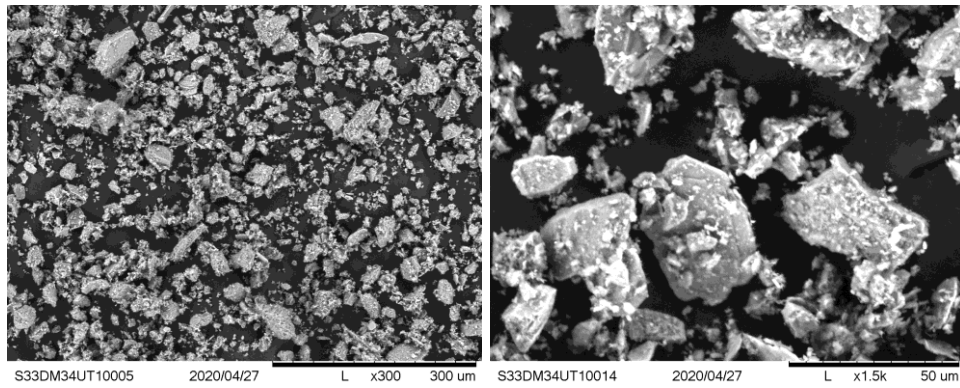


Figure C.3.11. SEM images of S33-DM3-4U-T1 (FC = 99%) enlarged 300 and 1500 times. The one enlarged 300 times was used to assess the particle shape (Table 5.1).

Appendix D

Supporting Data and Information for Monotonic, Cyclic, and Post-cyclic Monotonic Simple Shear Testing Program

Data used to generate plots in Appendix D.2 are provided as an electronic supplement.

D.1 Cyclic and Monotonic Simple Shear Test Specimen Photographs



Figure D.1.1. S33-DM3-1U-T2 before and after CSS testing.



Figure D.1.2. S33-DM3-1U-T3 before and after CSS testing.



Figure D.1.3. S33-DM3-1U-T4 before and after CSS testing.



Figure D.1.4. S33-DM3-1U-T1 before and after CSS testing.



Figure D.1.5. S33-DM3-2U-T1 before and after CSS testing.



Figure D.1.6. S23-DM2-6U-T1 before and after CSS testing.



Figure D.1.7. S23-DM2-6U-T2 before and after CSS testing.



Figure D.1.8. S23-DM2-6U-T3 before and after CSS testing.



Figure D.1.9. S23-DM2-6U-M before and after MSS testing.



Figure D.1.10. S2-DM2-3U-T1 before and after CSS testing.

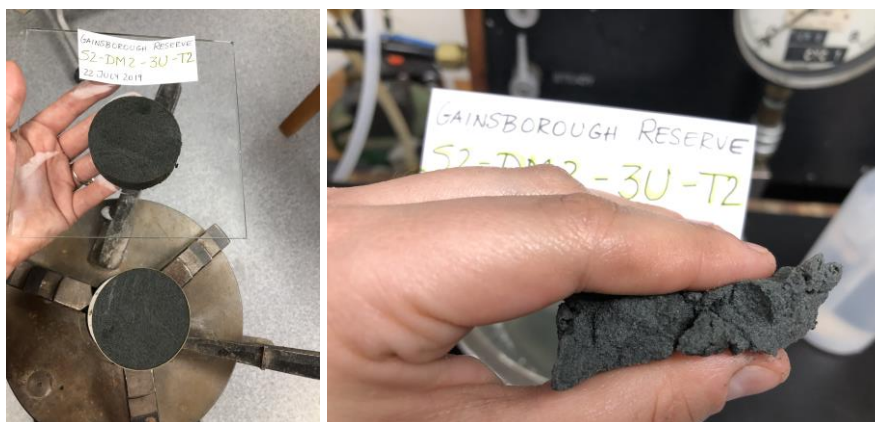


Figure D.1.11. S2-DM2-3U-T2 before and after CSS testing.



Figure D.1.12. S2-DM2-3U-T3 before and after CSS testing.



Figure D.1.13. S2-DM2-3U-M before and after MSS testing.



Figure D.1.14. S14-DM3-3U-T1 before and after CSS testing.



Figure D.1.15. S14-DM3-3U-T5 before and after CSS testing.



Figure D.1.16. S14-DM3-3U-T6 before and after CSS testing.



Figure D.1.17. S14-DM3-3U-T7 before and after CSS testing.



Figure D.1.18. S14-DM3-4U-T1 before and after CSS testing.



Figure D.1.19. S14-DM3-4U-T2 before and after CSS testing.



Figure D.1.20. S14-DM3-4U-T3 before and after CSS testing.



Figure D.1.21. S14-DM3-4U-M before and after MSS testing.



Figure D.1.22. S2-DM2-6U-T1 before and after CSS testing.



Figure D.1.23. S2-DM2-6U-T2 before and after CSS testing.



Figure D.1.24. S14-DM3-6U-T1 before and after CSS testing.

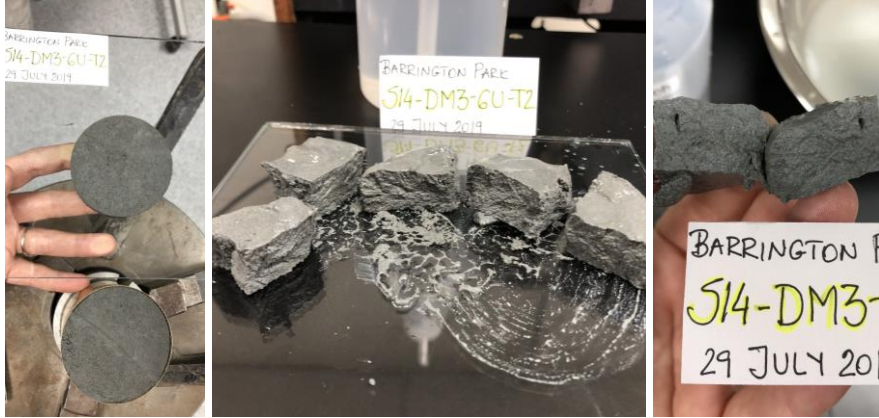


Figure D.1.25. S14-DM3-6U-T2 before and after CSS testing.



Figure D.1.26. S14-DM3-6U-T3 before and after CSS testing.



Figure D.1.27. S14-DM3-6U-M before and after MSS testing.



Figure D.1.28. S33-DM3-3U-T4 before and after CSS testing.



Figure D.1.29. S33-DM3-3U-T5 before and after CSS testing.



Figure D.1.30. S33-DM3-3U-T6 before and after CSS testing.



Figure D.1.31. S33-DM3-4U-T1 before and after CSS testing.



Figure D.1.32. S33-DM3-4U-T2 before and after CSS testing.



Figure D.1.33. S33-DM3-4U-T3 before and after CSS testing.



Figure D.1.34. S2-DM2-1U-T1 before and after CSS testing.



Figure D.1.35. S2-DM2-1U-T2 before and after CSS testing.



Figure D.1.36. S2-DM2-1U-T3 before and after CSS testing.



Figure D.1.37. S23-DM2-3U-T1 before and after CSS testing.



Figure D.1.38. S23-DM2-3U-T2 before and after CSS testing.



Figure D.1.39. S23-DM2-3U-T3 before and after CSS testing.



Figure D.1.40. S23-DM2-3U-T5 before and after CSS testing.



Figure D.1.41. S14-DM3-3U-T2 before and after CSS testing. This test specimen is not presented in Chapter 5.

D.2 Processed Monotonic, Cyclic, and Post-Cyclic Monotonic Simple Shear Data

D.2.1 Monotonic Simple Shear Test Results

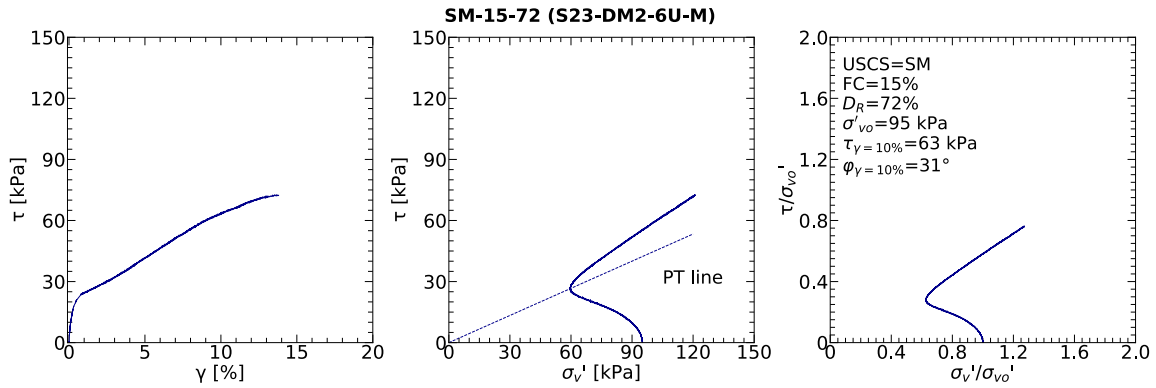


Figure D.2.1.1. MSS test results for SM-15-72 (S23-DM2-6U-M).

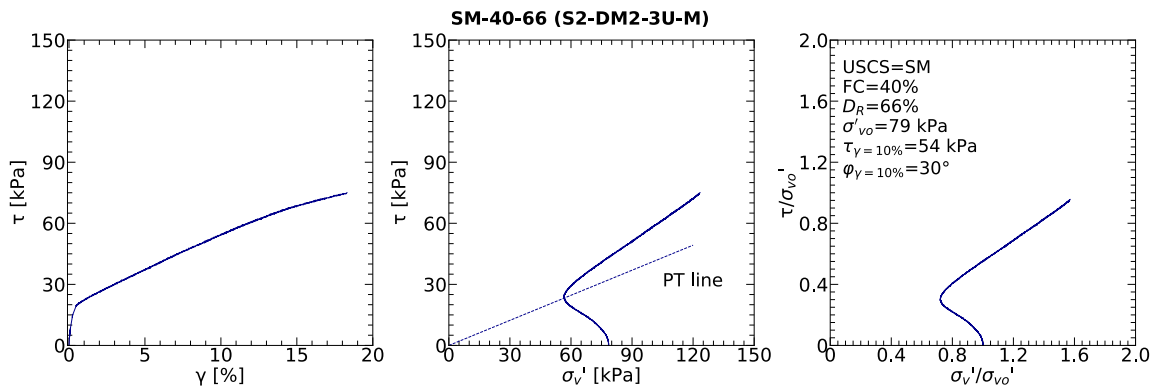


Figure D.2.1.2. MSS test results for SM-40-66 (S2-DM2-3U-M).

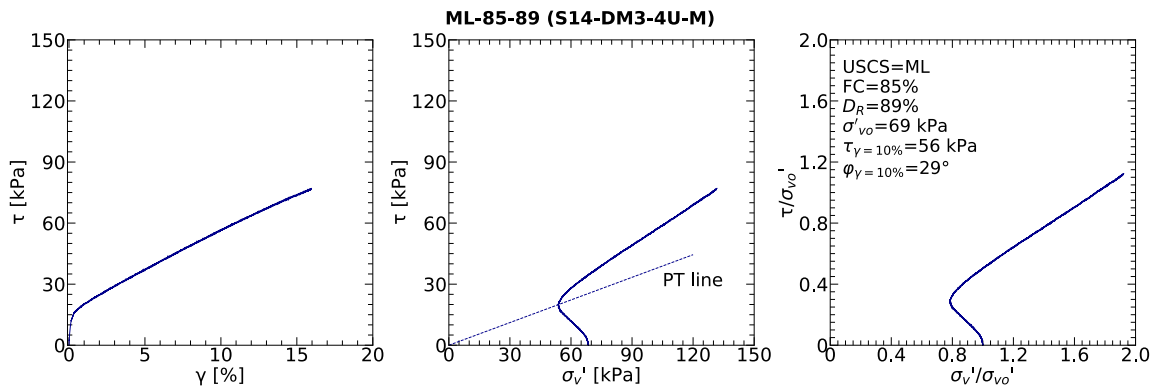


Figure D.2.1.3. MSS test results for ML-85-89 (S14-DM3-4U-M).

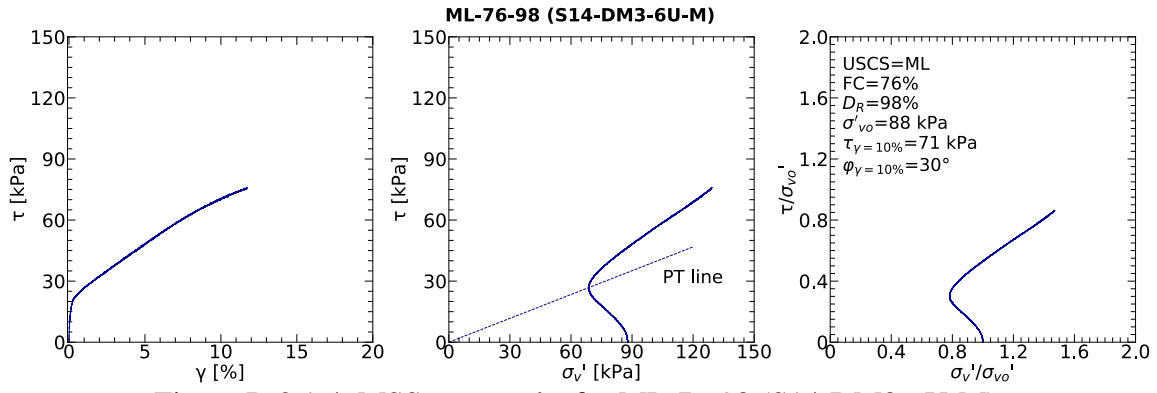


Figure D.2.1.4. MSS test results for ML-76-98 (S14-DM3-6U-M).

D.2.2 Cyclic Simple Shear Test Results

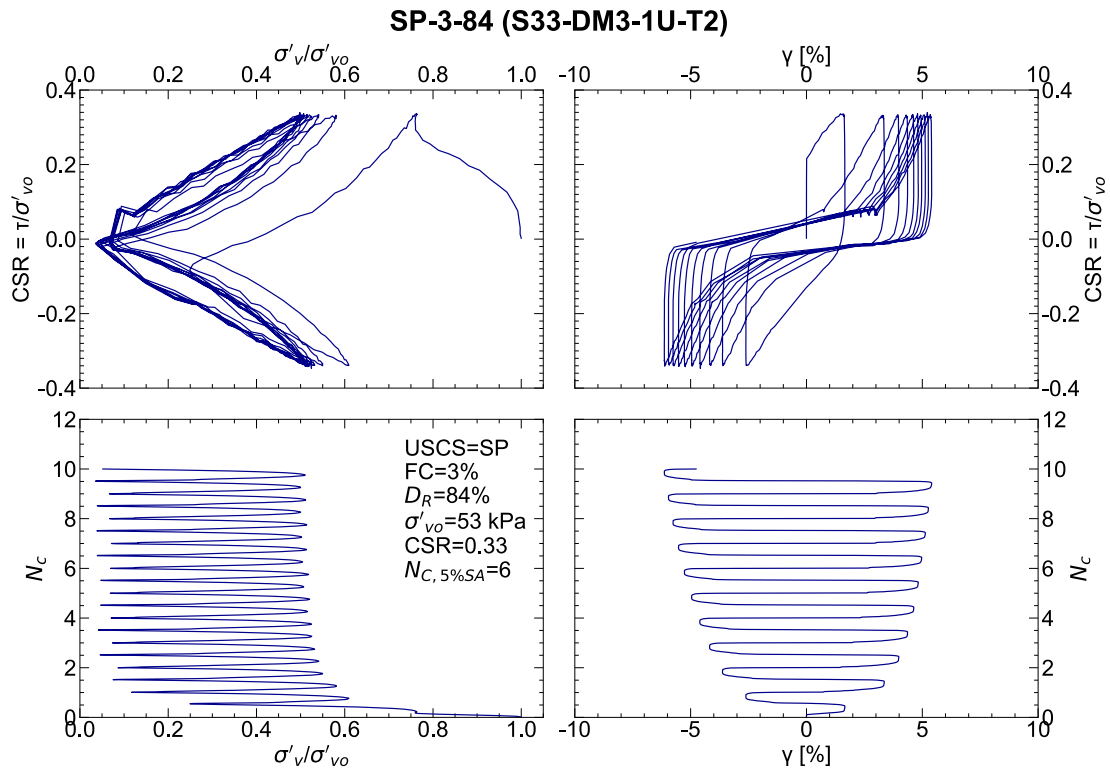


Figure D.2.2.1. CSS test results for SP-3-84 (S33-DM3-1U-T2).

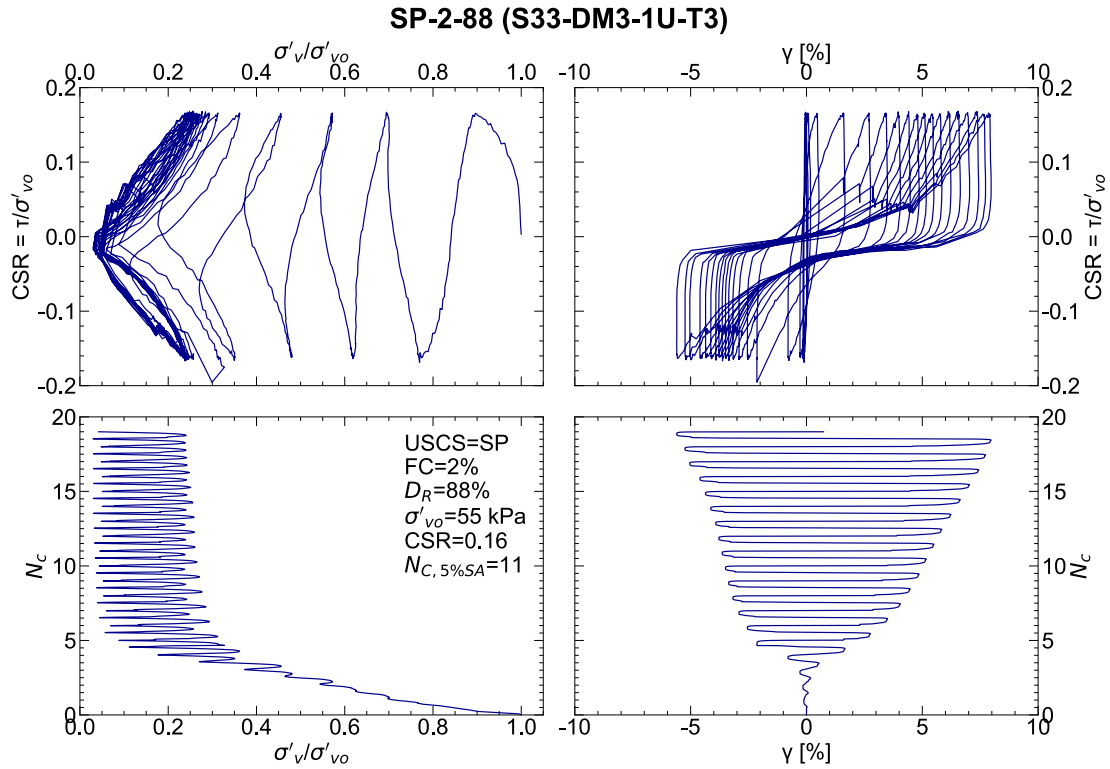


Figure D.2.2.2. CSS test results for SP-2-88 (S33-DM3-1U-T3).

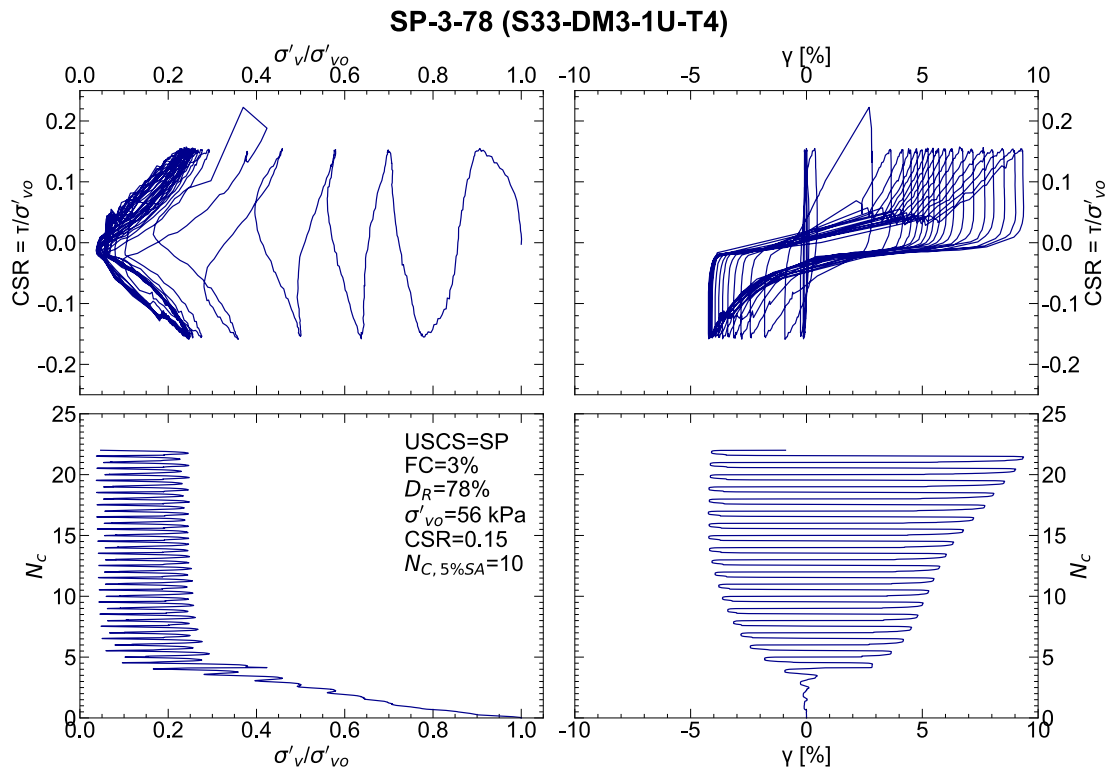


Figure D.2.2.3. CSS test results for SP-3-78 (S33-DM3-1U-T4).

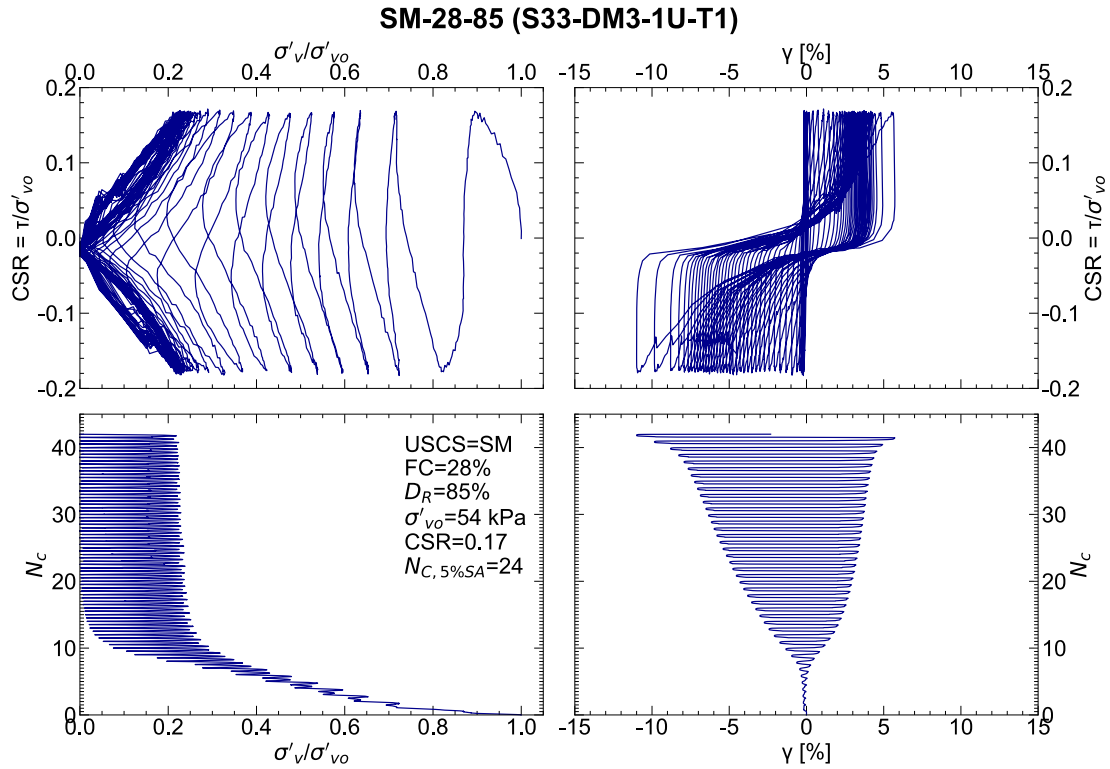


Figure D.2.2.4. CSS test results for SM-28-85 (S33-DM3-1U-T1).

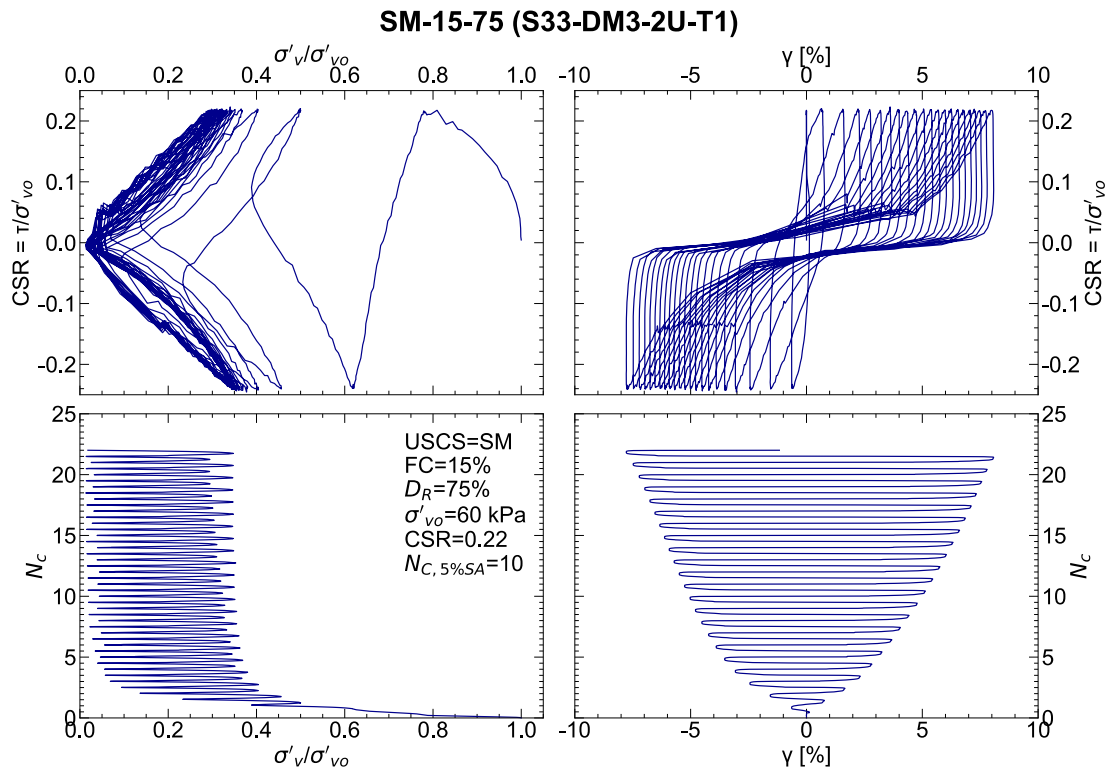


Figure D.2.2.5. CSS test results for SM-15-75 (S33-DM3-2U-T1).

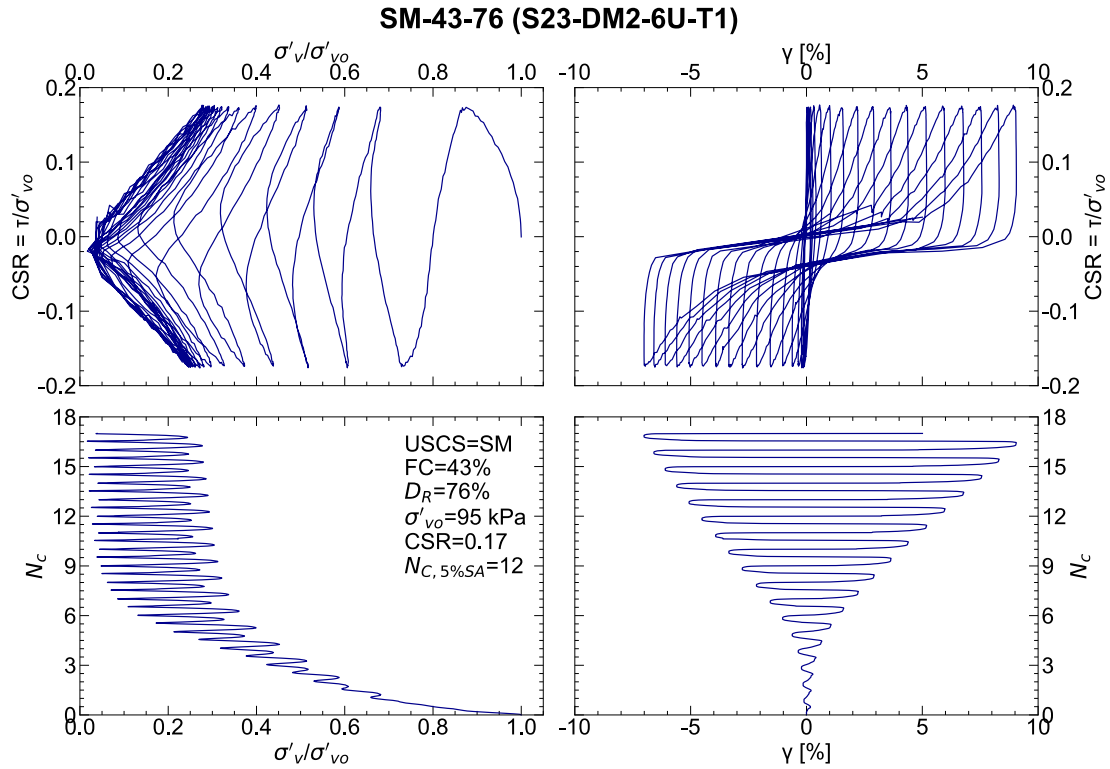


Figure D.2.2.6. CSS test results for SM-43-76 (S23-DM2-6U-T1).

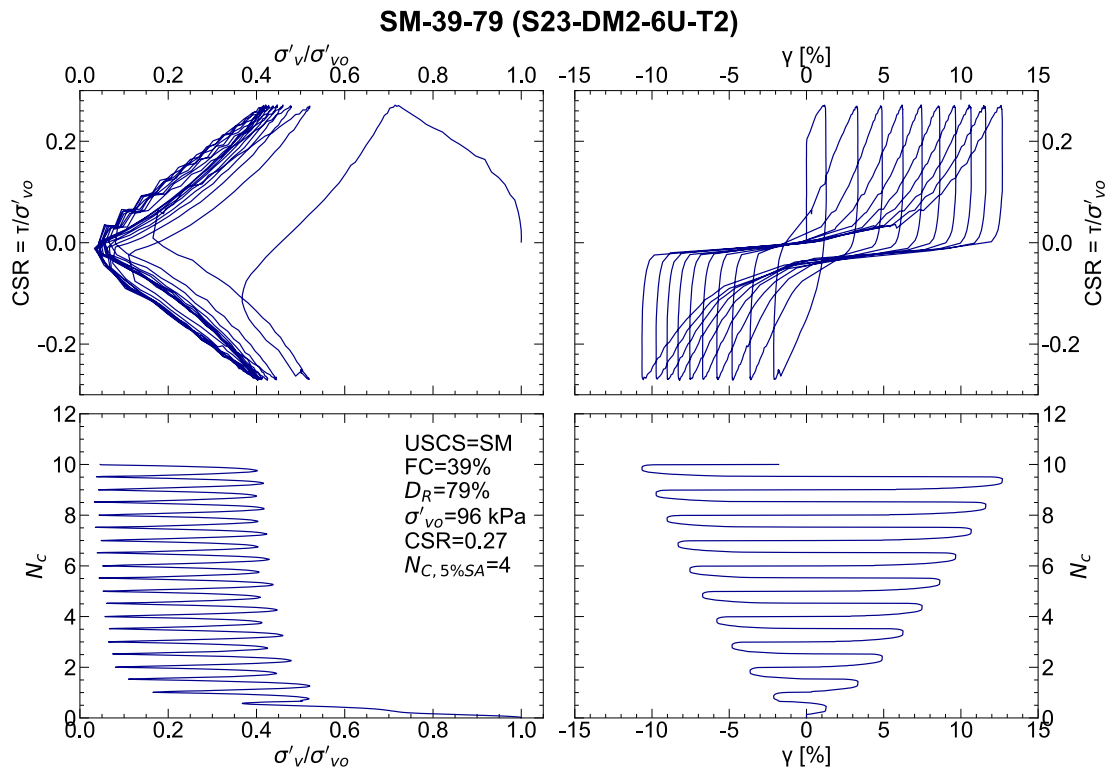


Figure D.2.2.7. CSS test results for SM-39-79 (S23-DM2-6U-T2).

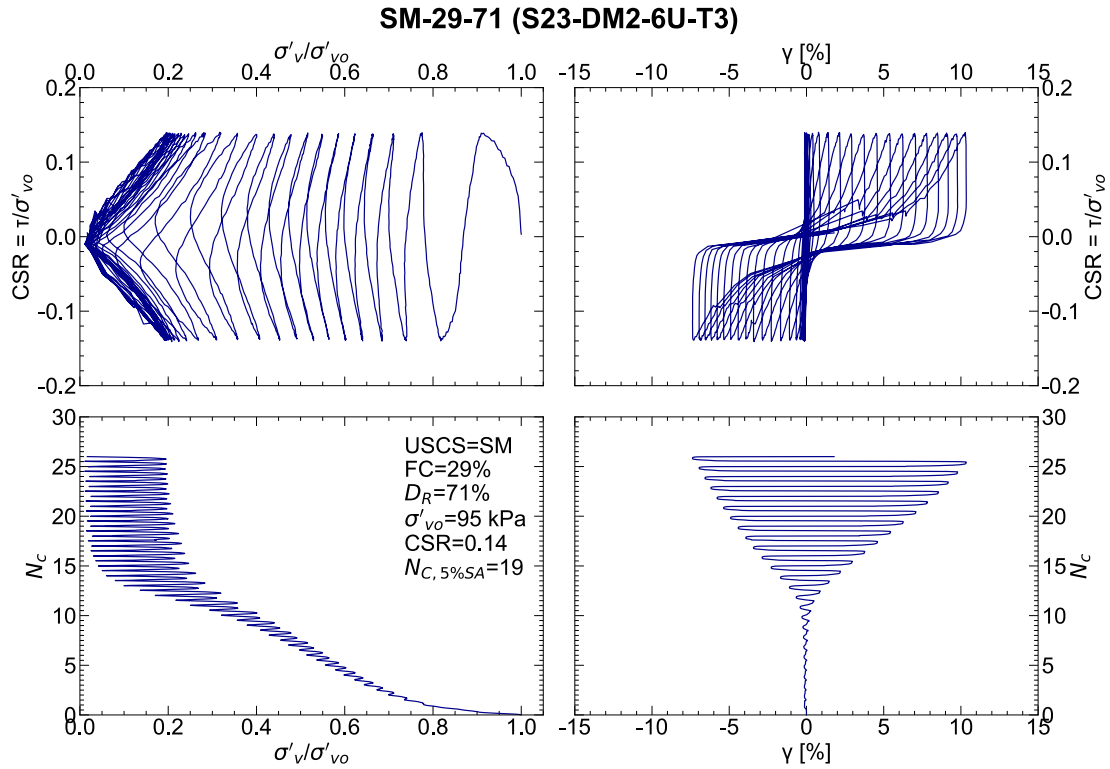


Figure D.2.2.8. CSS test results for SM-29-71 (S23-DM2-6U-T3).

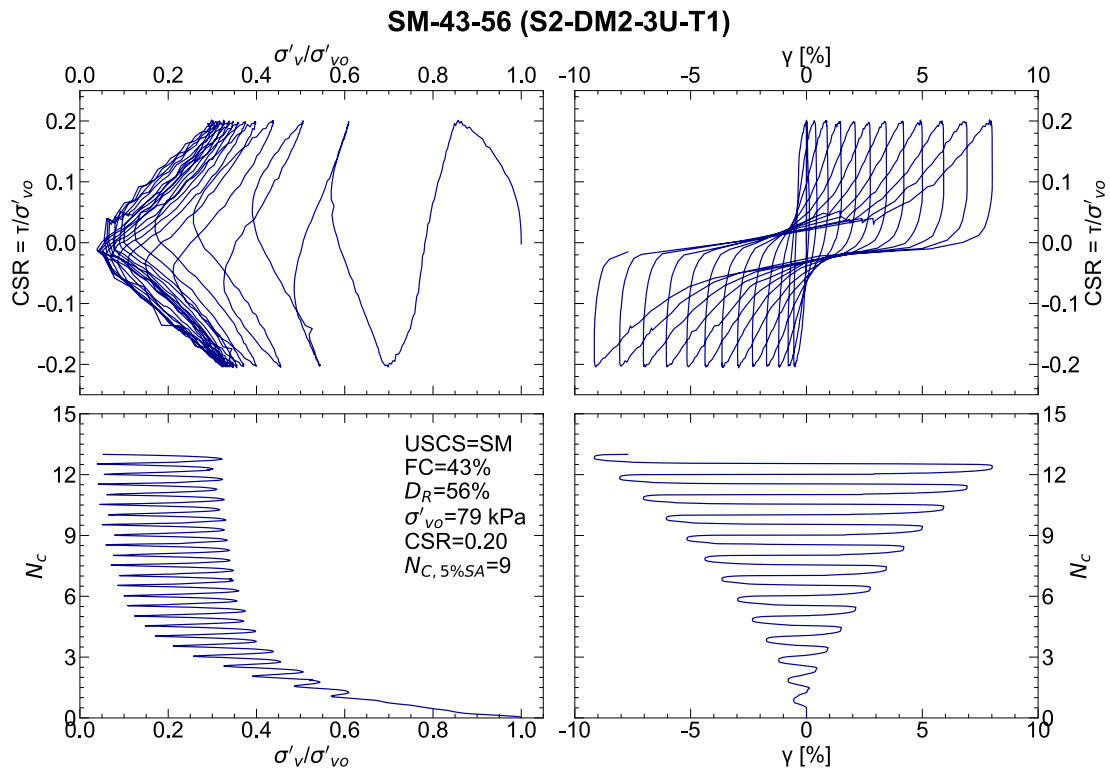


Figure D.2.2.9. CSS test results for SM-43-56 (S2-DM2-3U-T1).

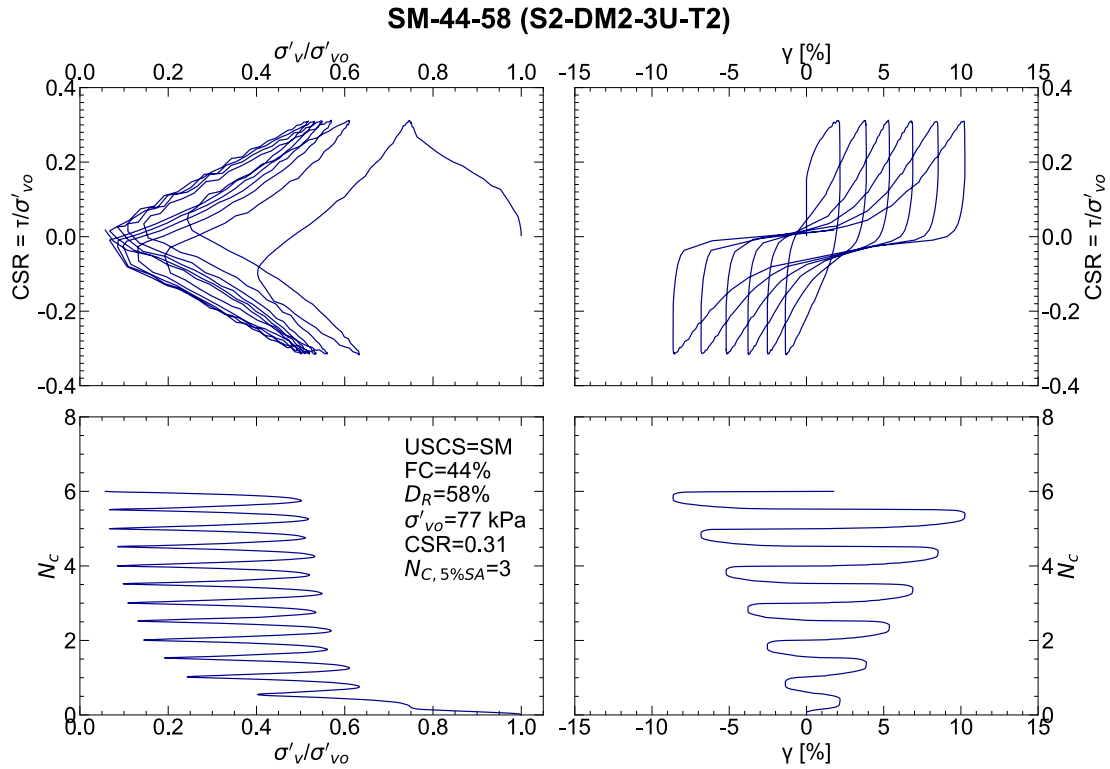


Figure D.2.2.10. CSS test results for SM-44-58 (S2-DM2-3U-T2).

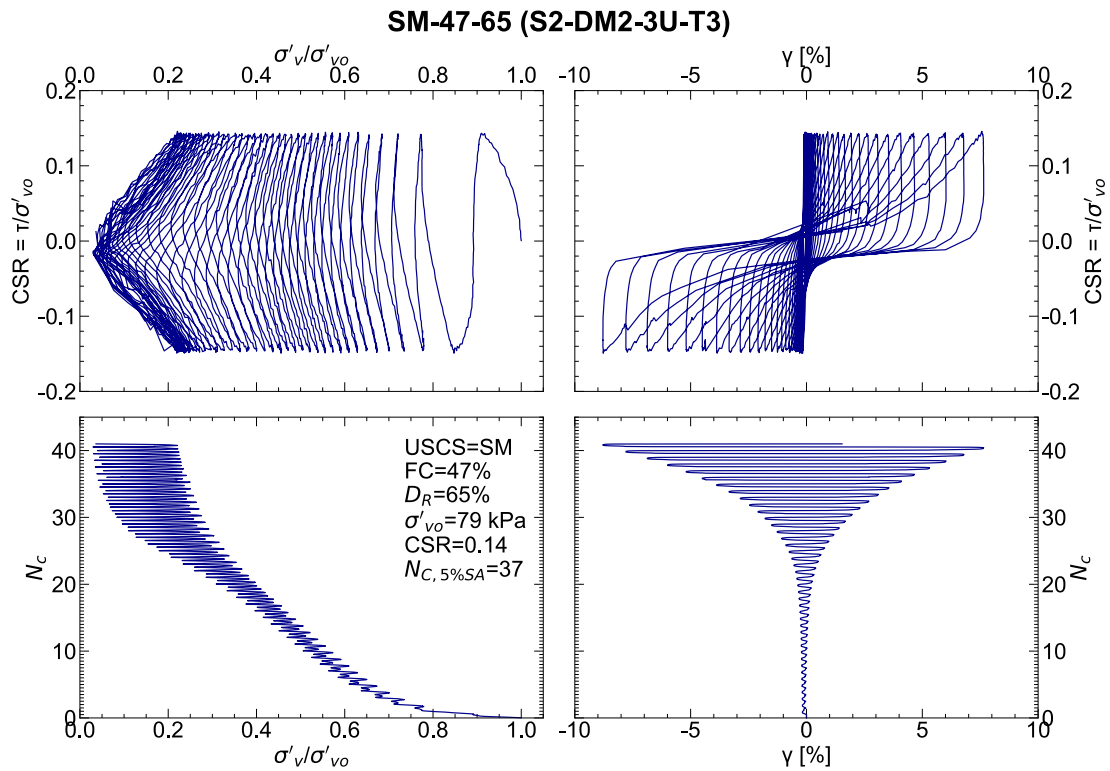


Figure D.2.2.11. CSS test results for SM-47-65 (S2-DM2-3U-T3).

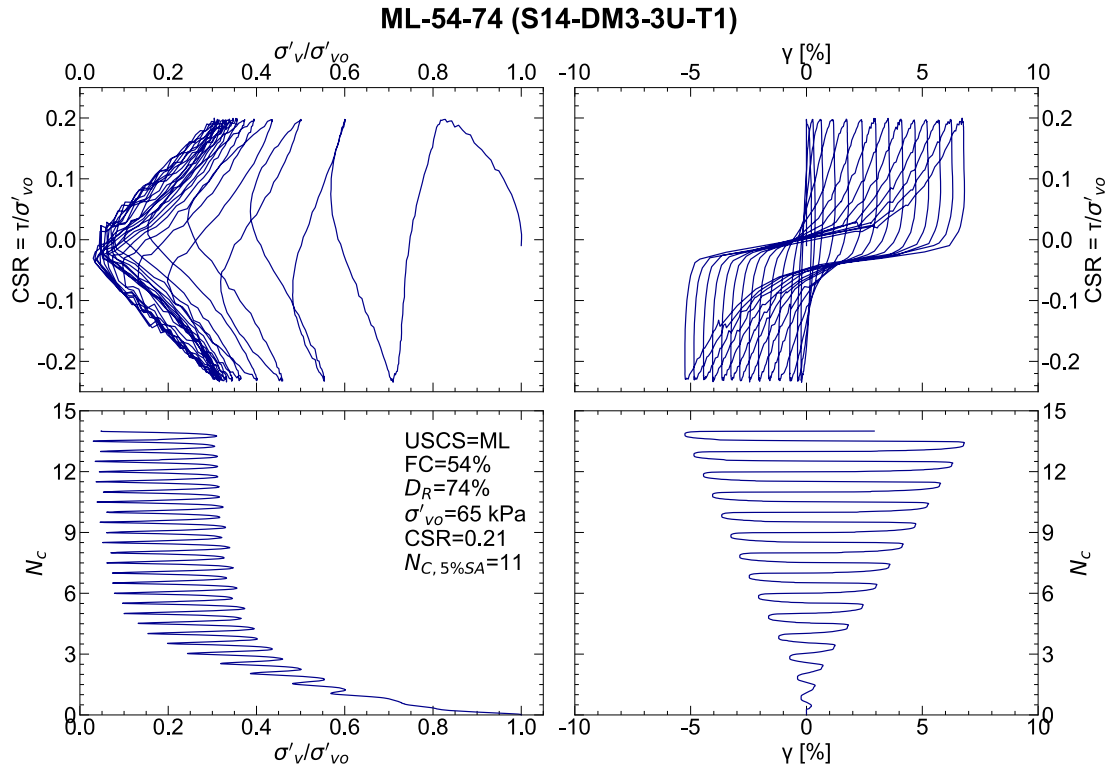


Figure D.2.2.12. CSS test results for ML-54-74 (S14-DM3-3U-T1).

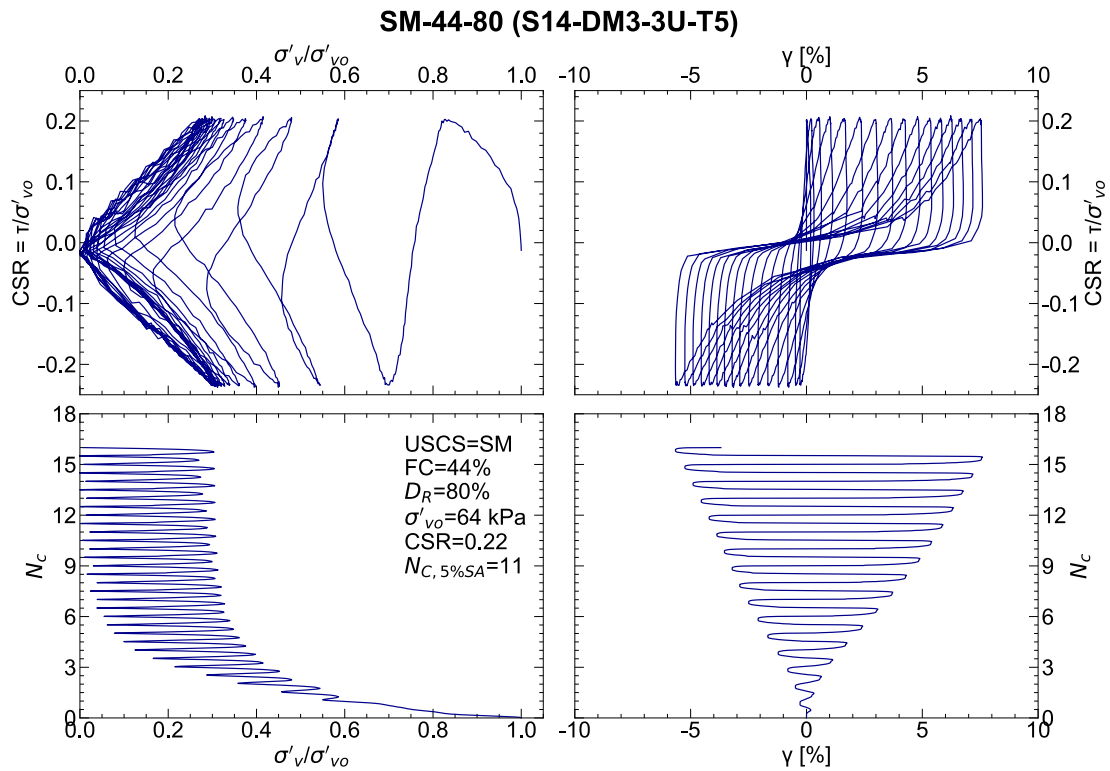


Figure D.2.2.13. CSS test results for SM-44-80 (S14-DM3-3U-T5).

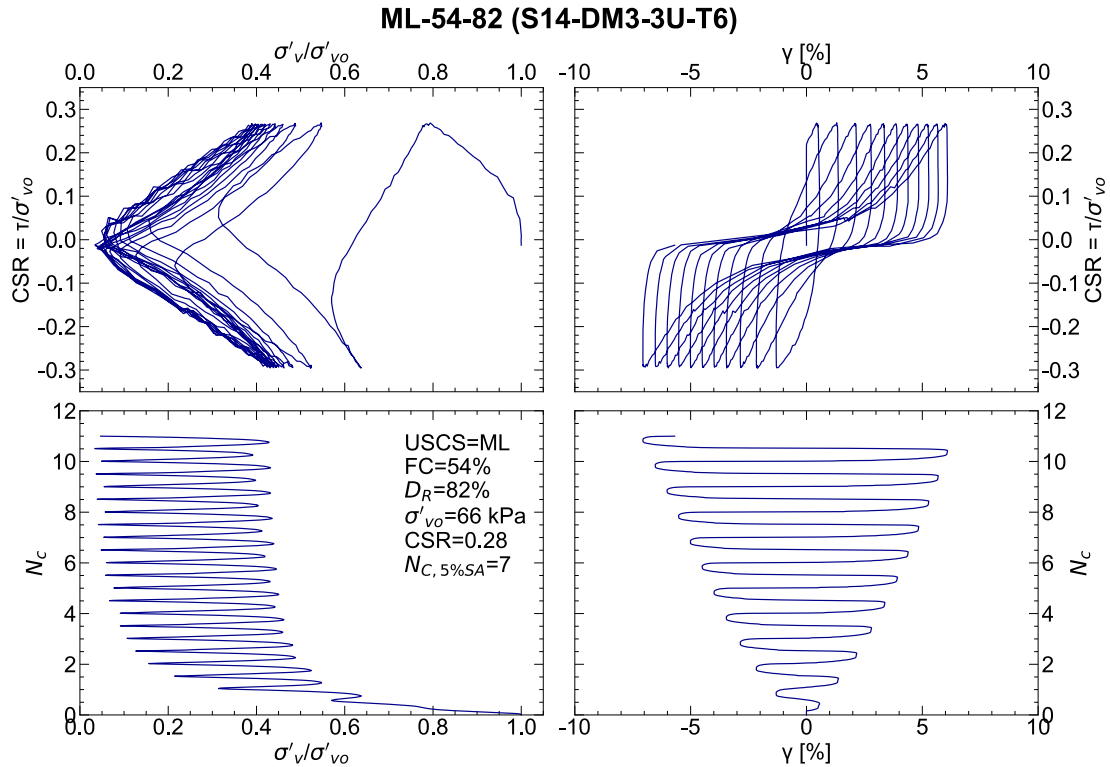


Figure D.2.2.14. CSS test results for ML-54-82 (S14-DM3-3U-T6).

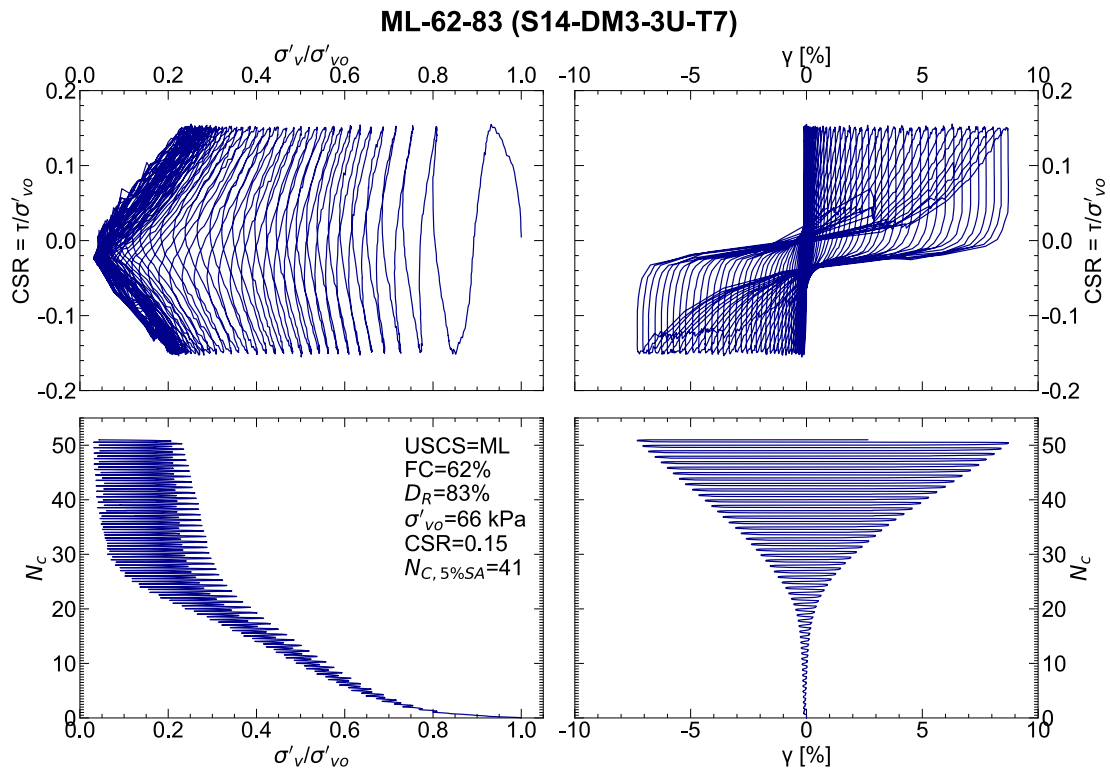


Figure D.2.2.15. CSS test results for ML-62-83 (S14-DM3-3U-T7).

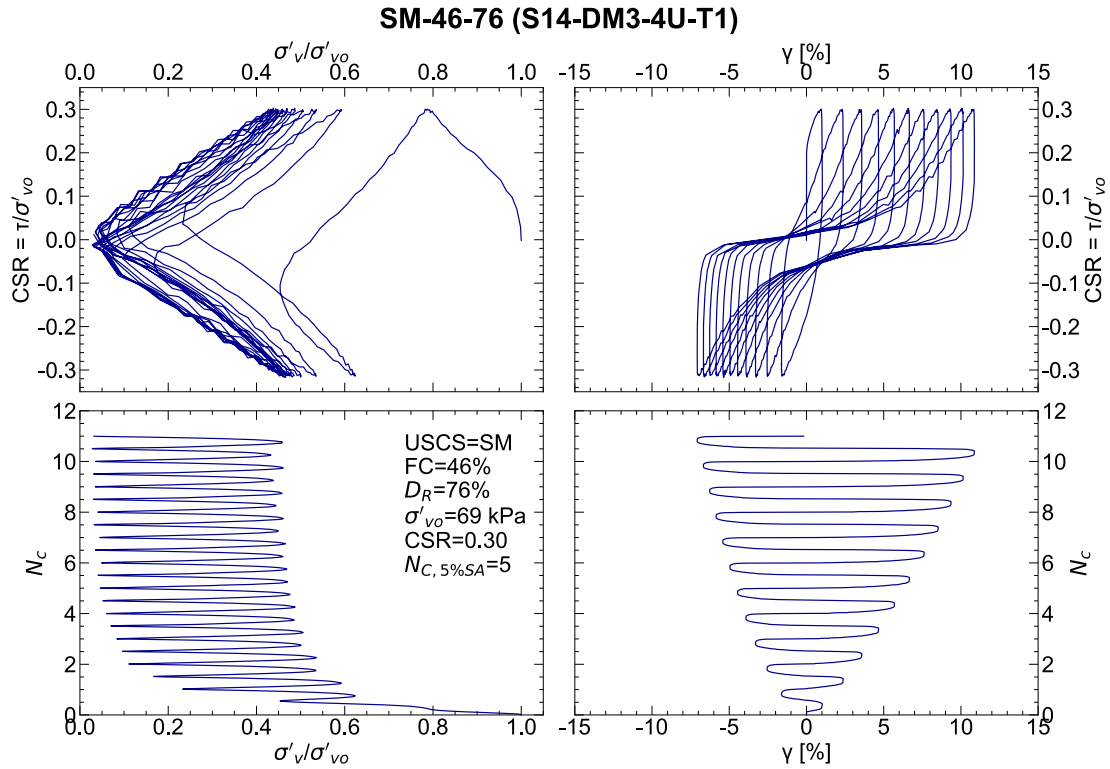


Figure D.2.2.16. CSS test results for SM-46-76 (S14-DM3-4U-T1).

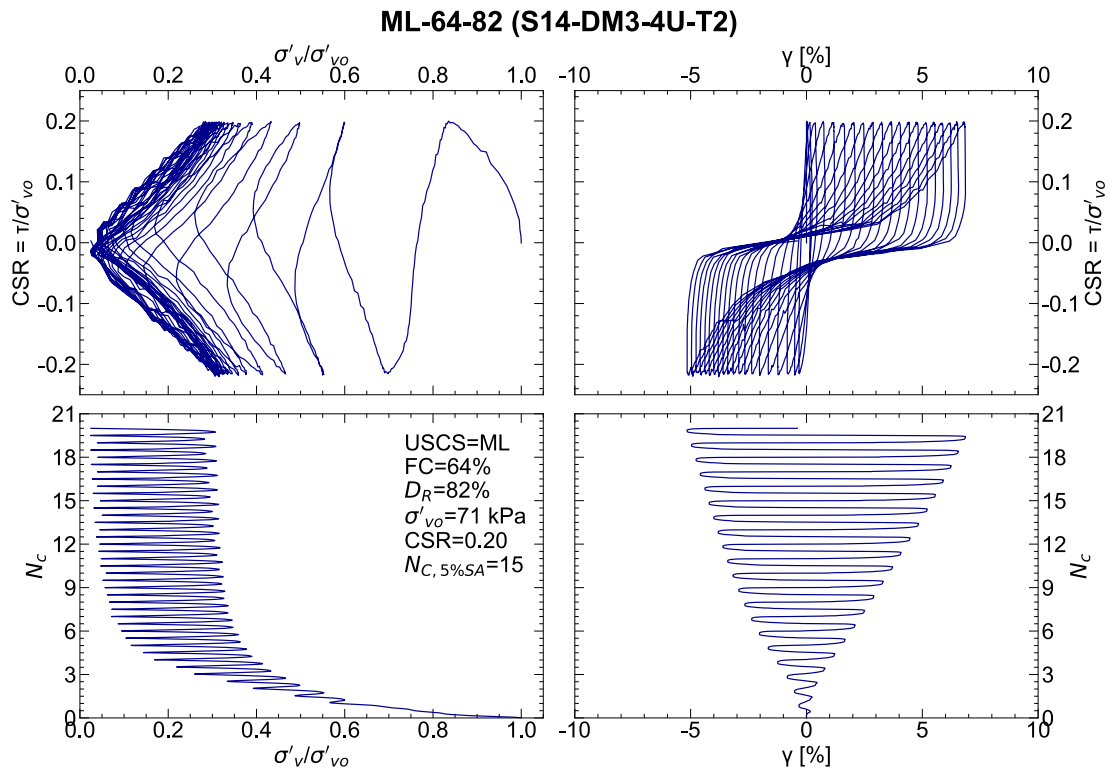


Figure D.2.2.17. CSS test results for ML-64-82 (S14-DM3-4U-T2).

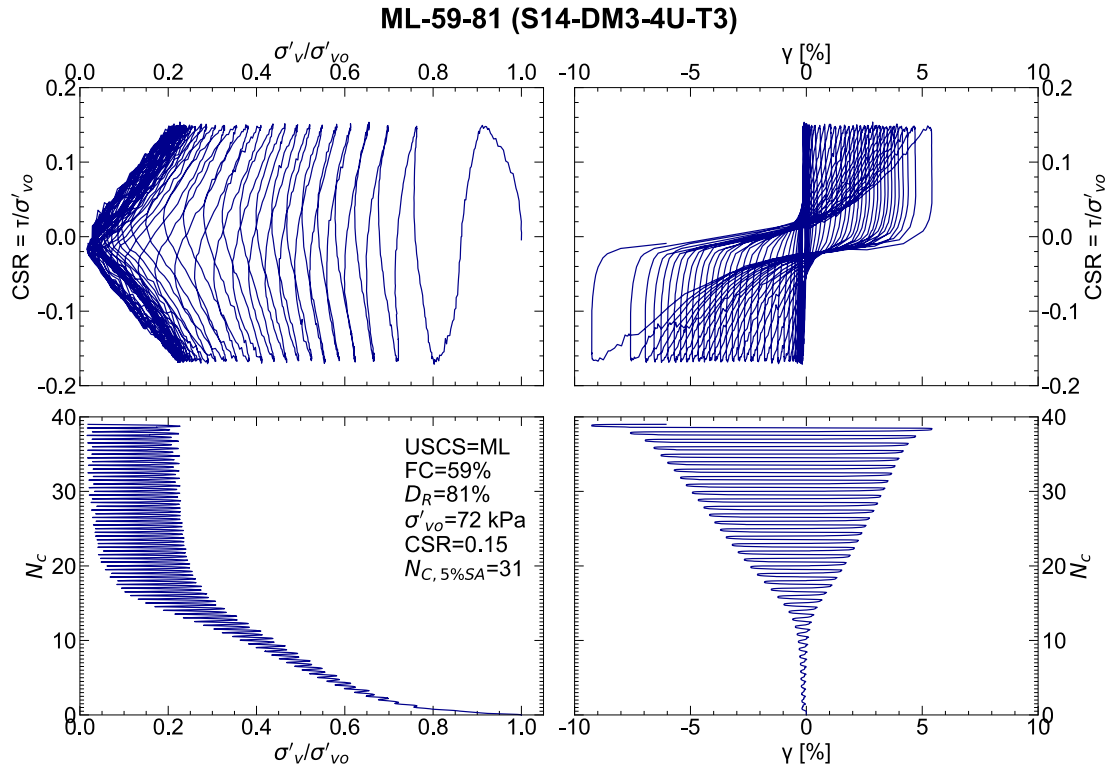


Figure D.2.2.18. CSS test results for ML-59-81 (S14-DM3-4U-T3).

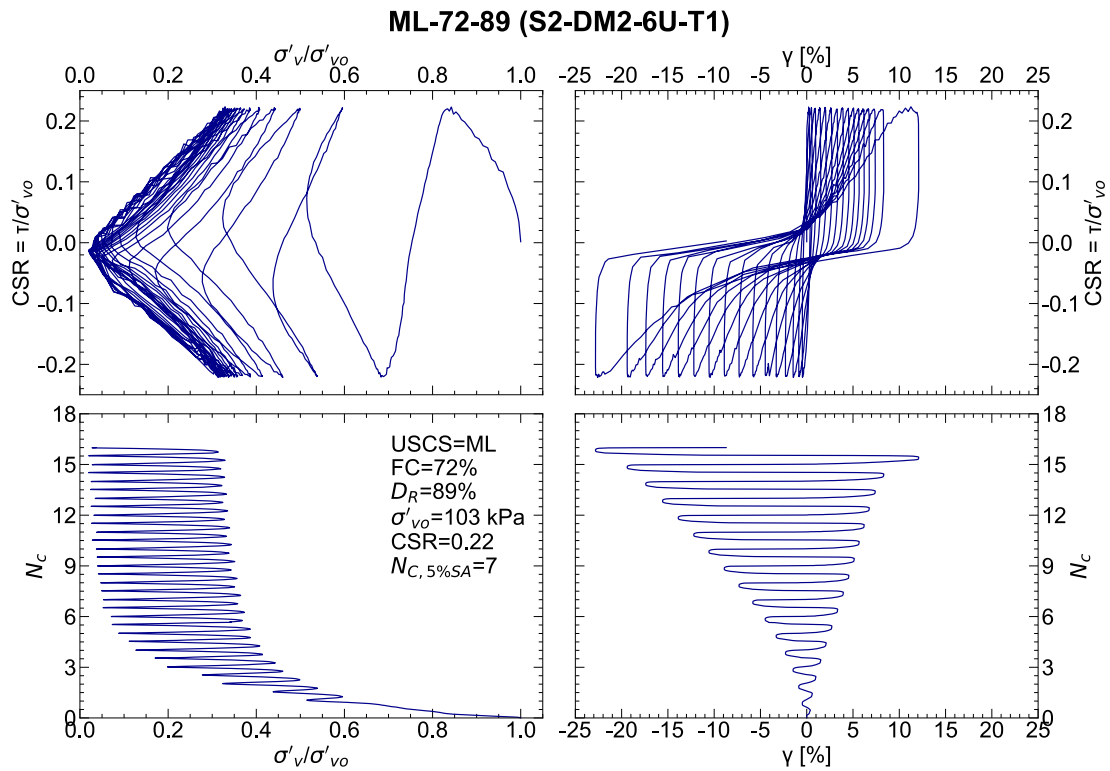


Figure D.2.2.19. CSS test results for ML-72-89 (S2-DM2-6U-T1).

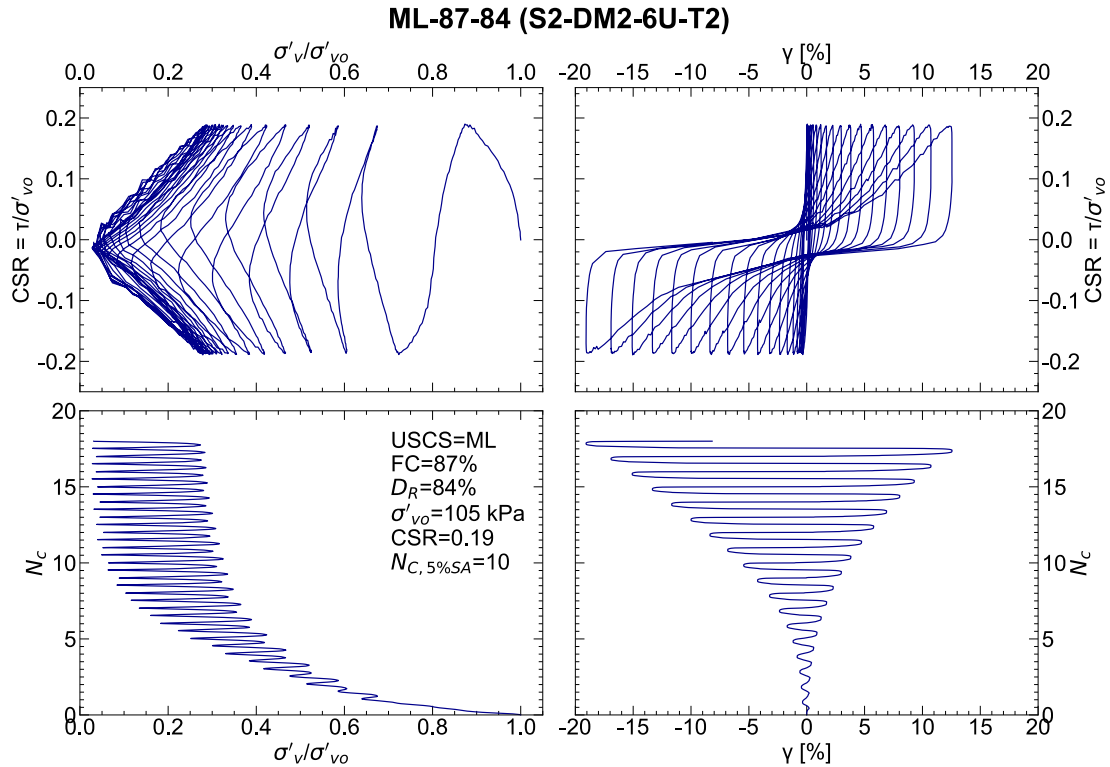


Figure D.2.2.20. CSS test results for ML-87-84 (S2-DM2-6U-T2).

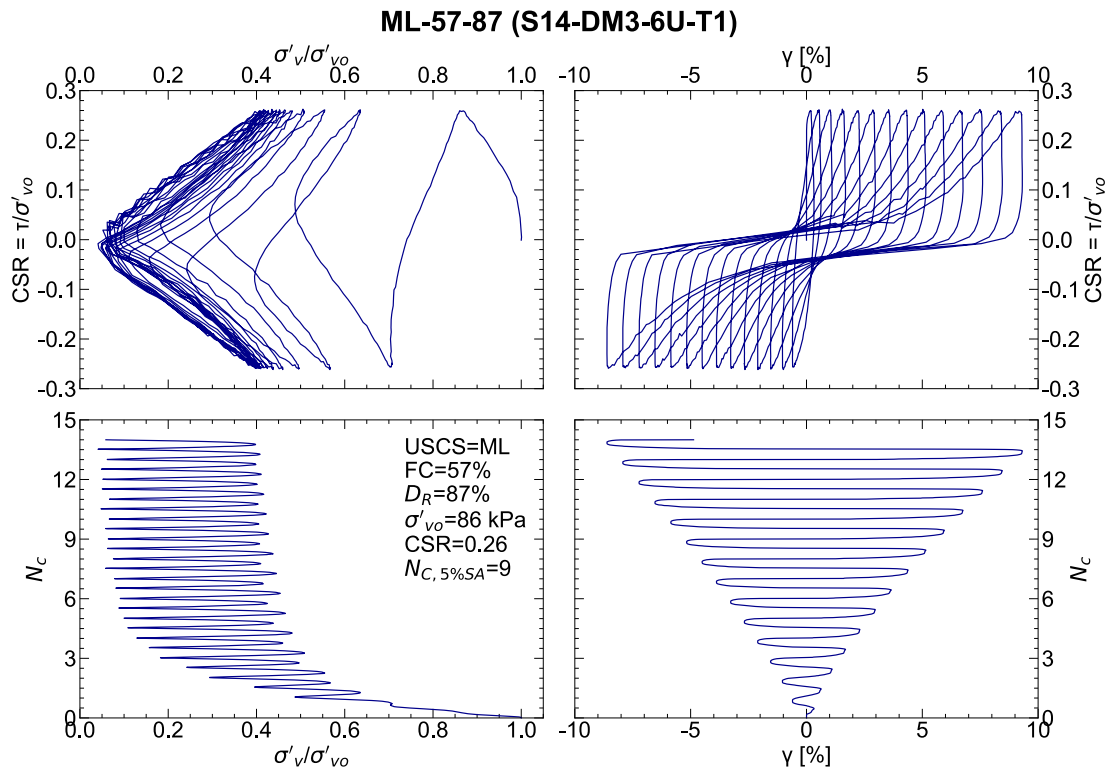


Figure D.2.2.21. CSS test results for ML-57-87 (S14-DM3-6U-T1).

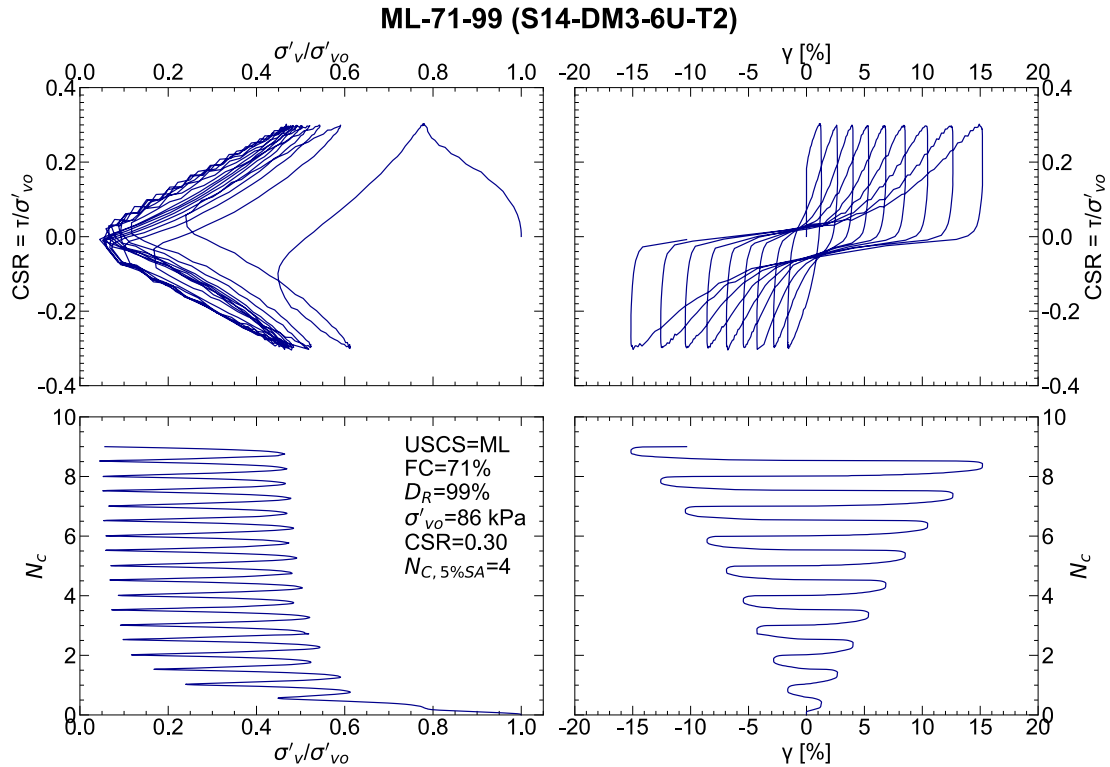


Figure D.2.2.22. CSS test results for ML-71-99 (S14-DM3-6U-T2).

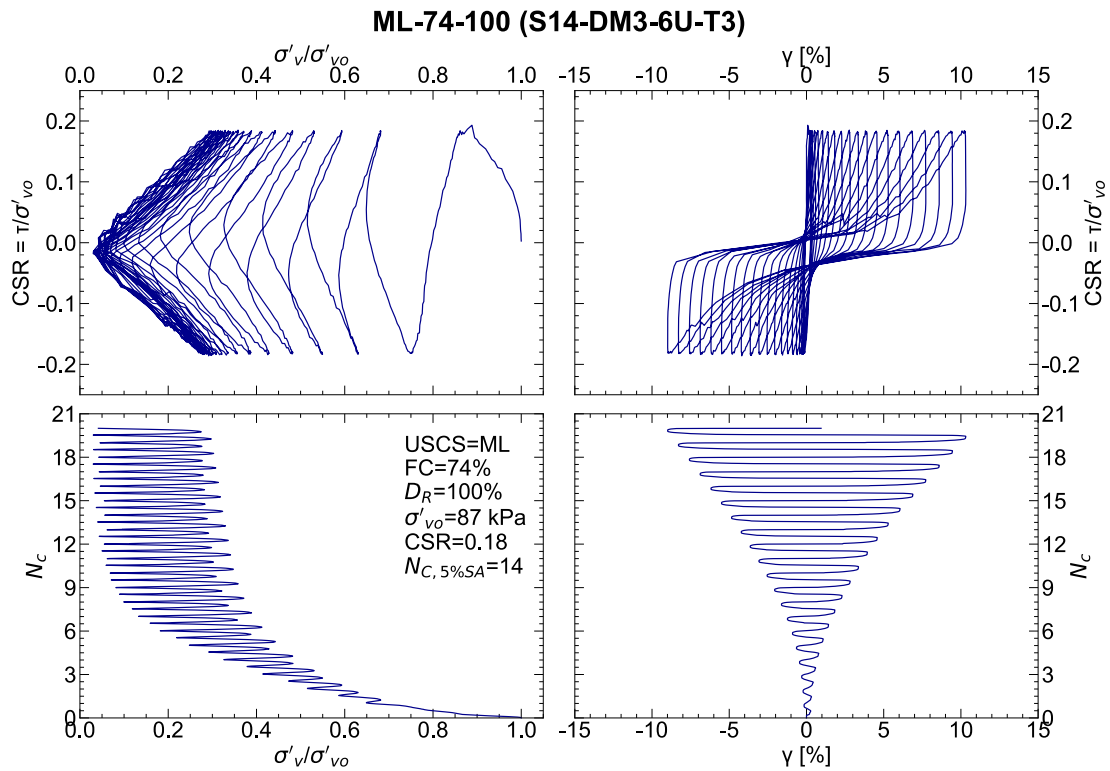


Figure D.2.2.23. CSS test results for ML-74-100 (S14-DM3-6U-T3).

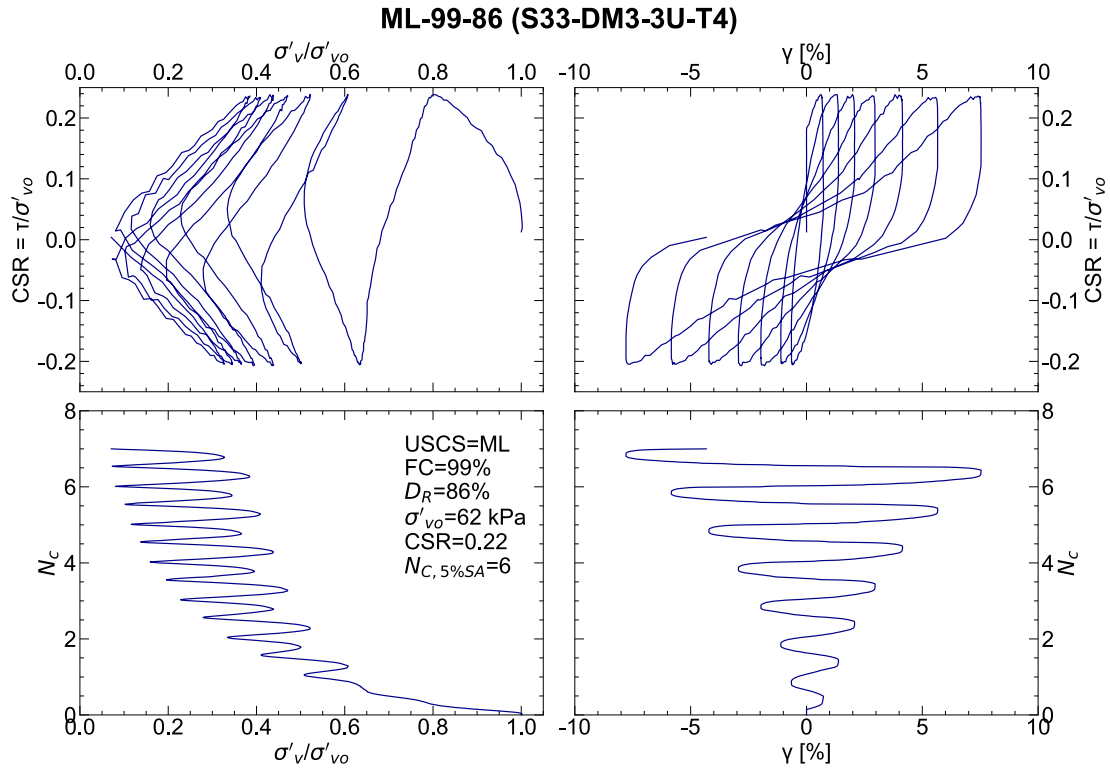


Figure D.2.2.24. CSS test results for ML-99-86 (S33-DM3-3U-T4).

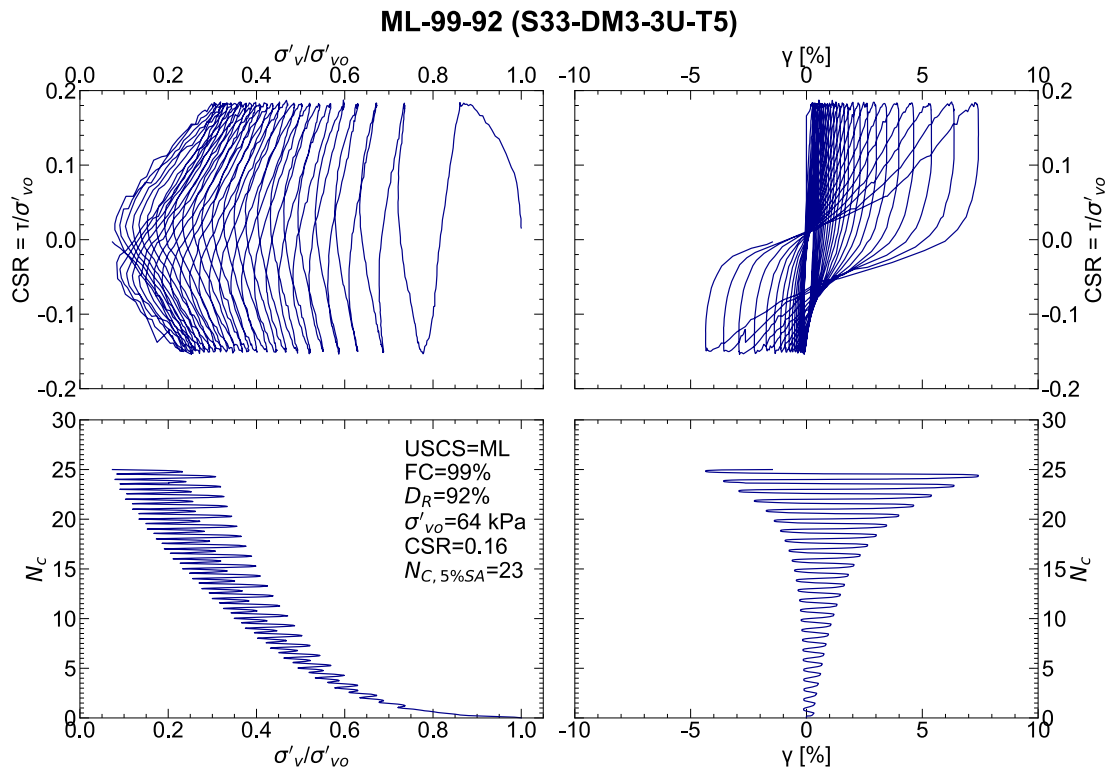


Figure D.2.2.25. CSS test results for ML-99-92 (S33-DM3-3U-T5).

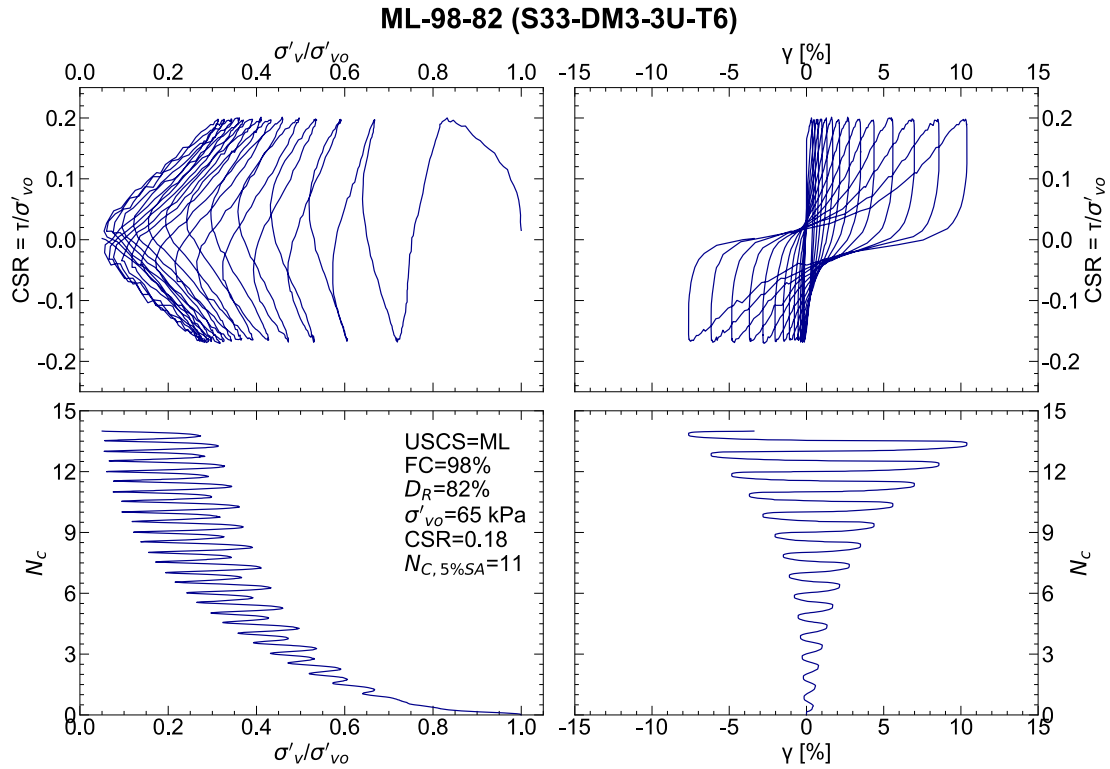


Figure D.2.2.26. CSS test results for ML-98-82 (S33-DM3-3U-T6).

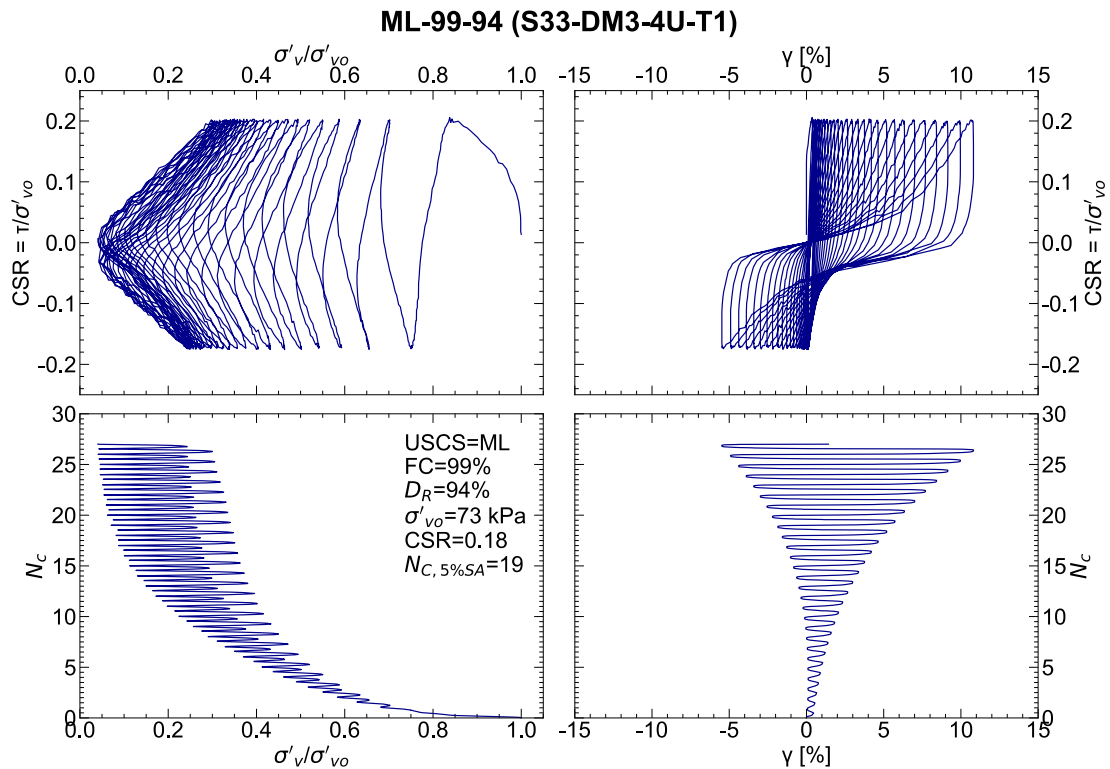


Figure D.2.2.27. CSS test results for ML-99-94 (S33-DM3-4U-T1).

ML-97-85 (S33-DM3-4U-T2)

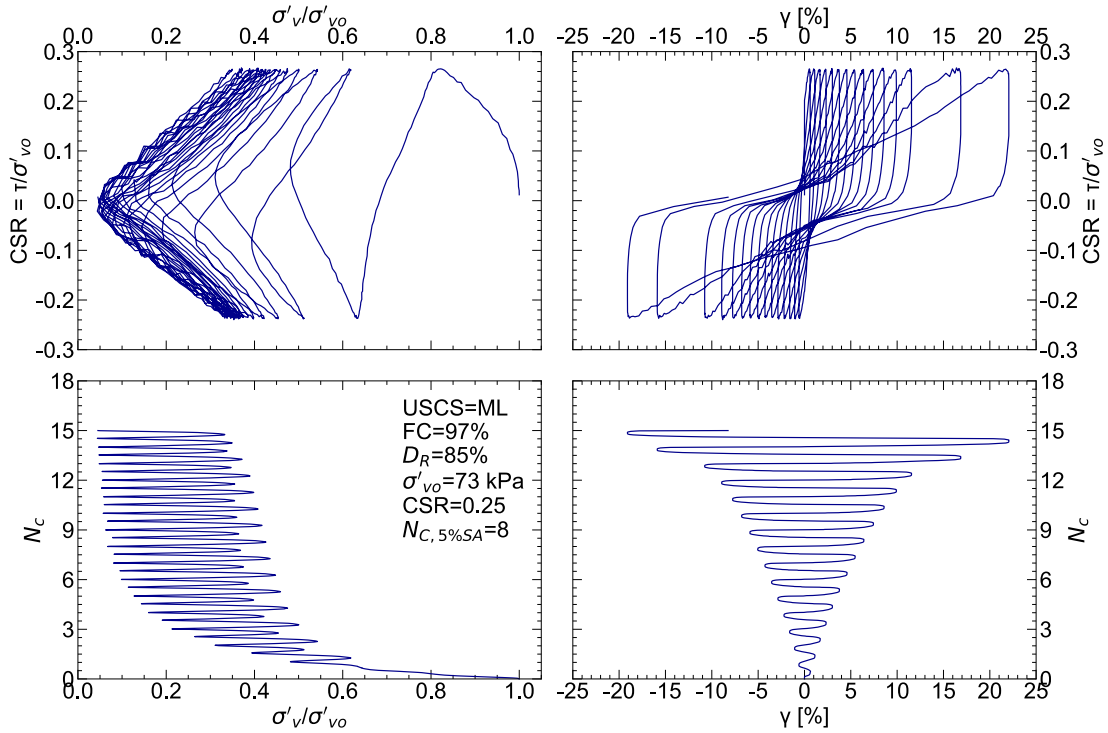


Figure D.2.2.28. CSS test results for ML-97-85 (S33-DM3-4U-T2).

ML-98-89 (S33-DM3-4U-T3)

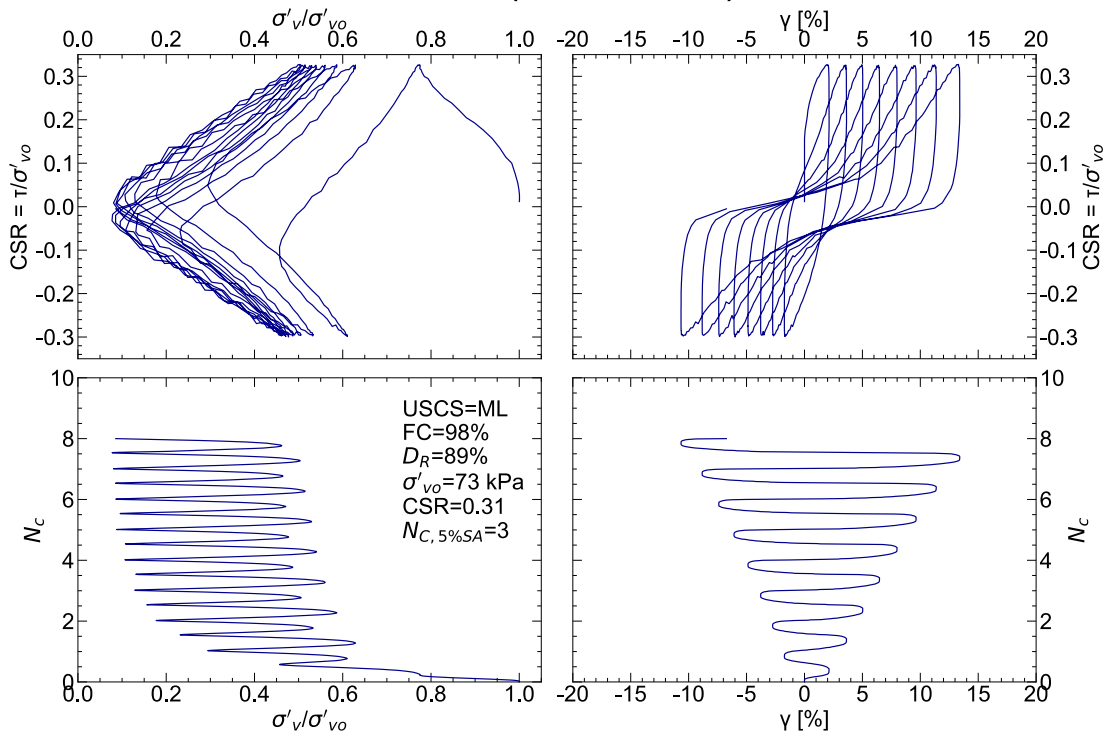


Figure D.2.2.29. CSS test results for ML-98-89 (S33-DM3-4U-T3).

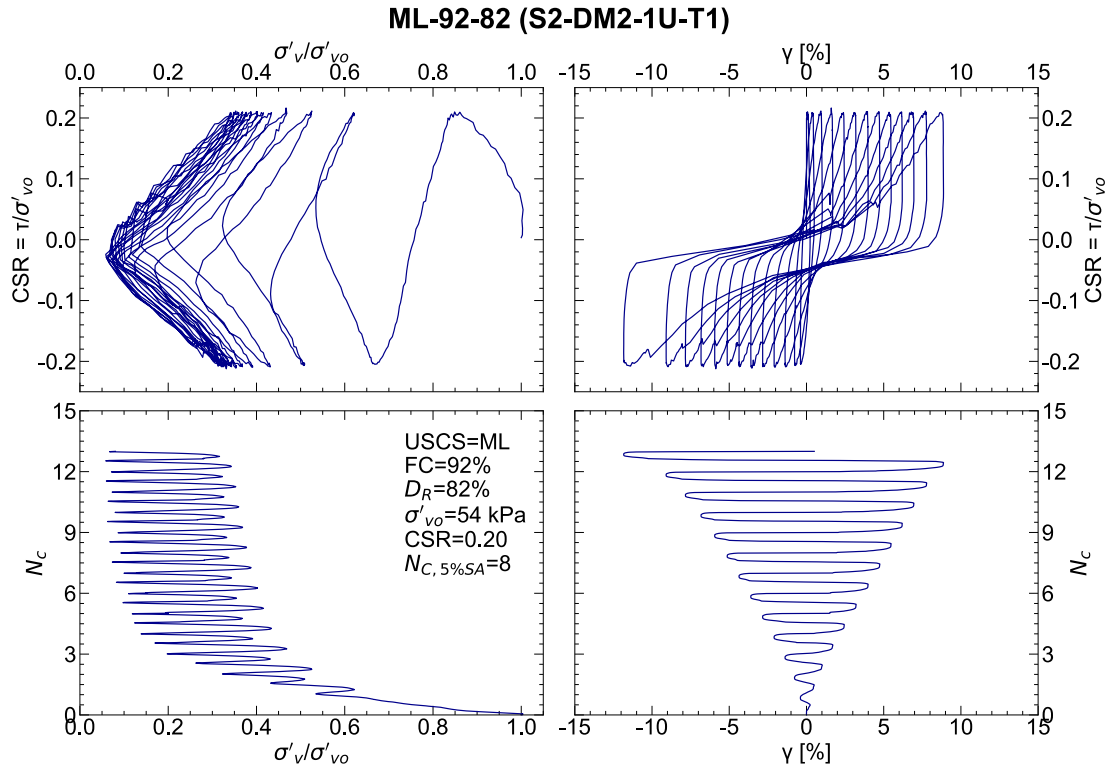


Figure D.2.2.30. CSS test results for ML-92-82 (S2-DM2-1U-T1).

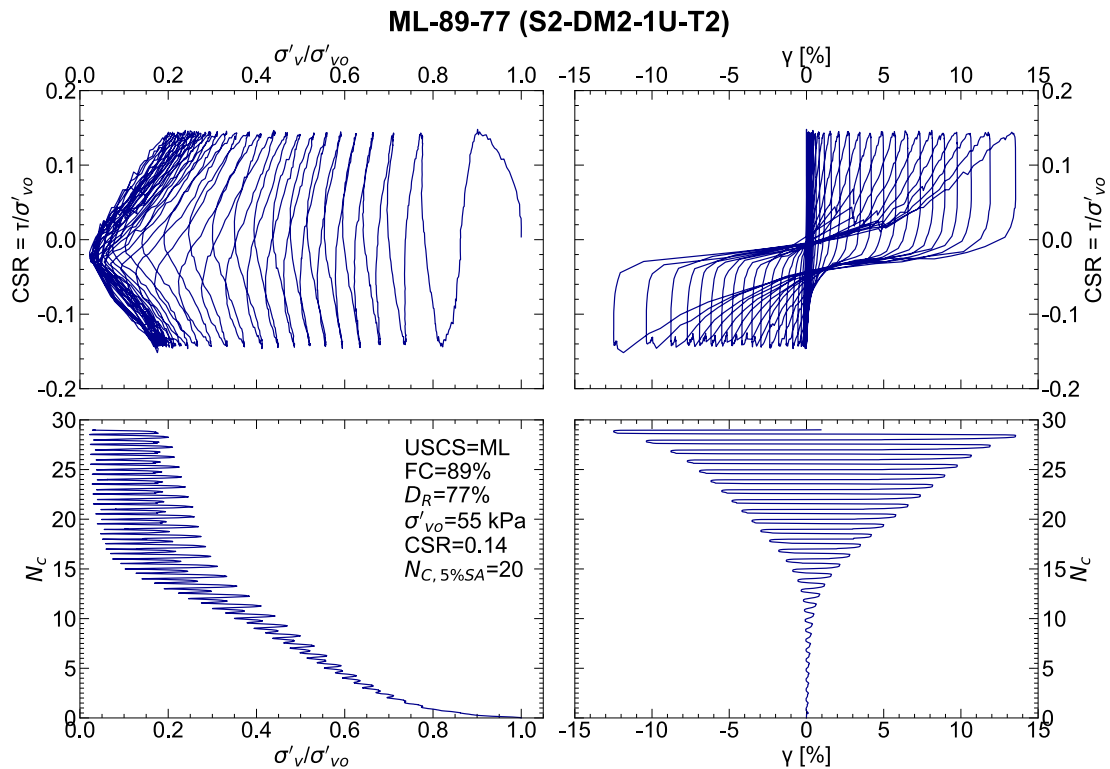


Figure D.2.2.31. CSS test results for ML-89-77 (S2-DM2-1U-T2).

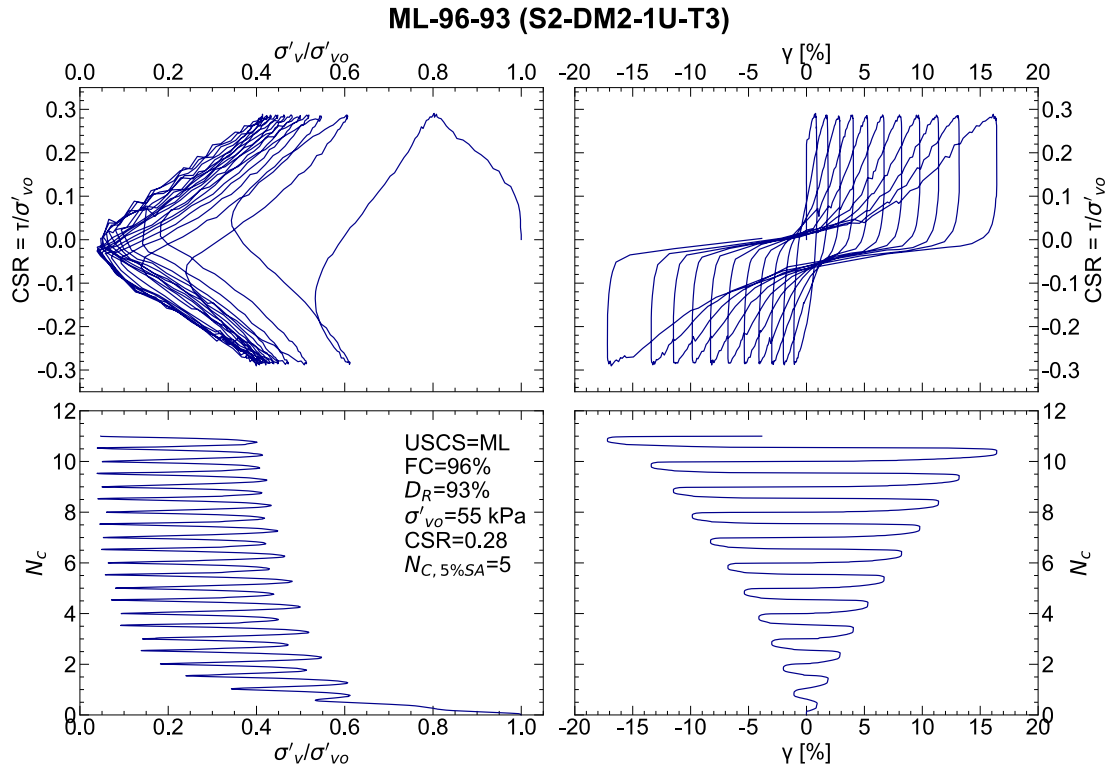


Figure D.2.2.32. CSS test results for ML-96-93 (S2-DM2-1U-T3).

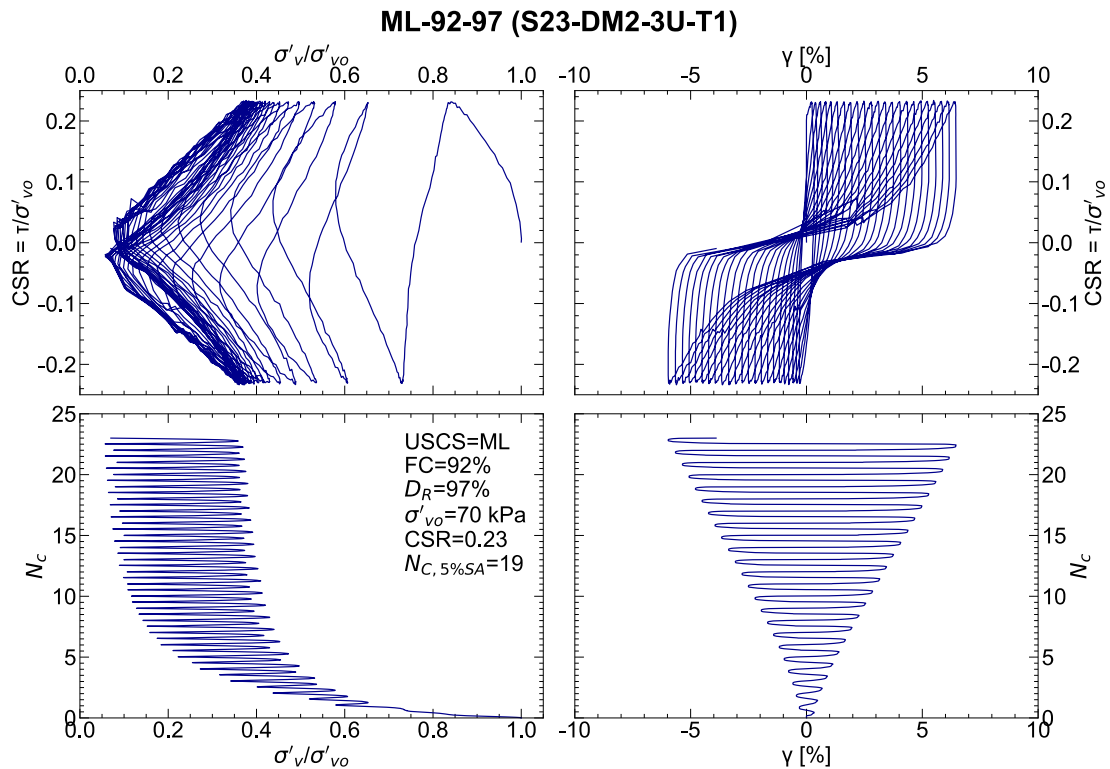


Figure D.2.2.33. CSS test results for ML-92-97 (S23-DM2-3U-T1).

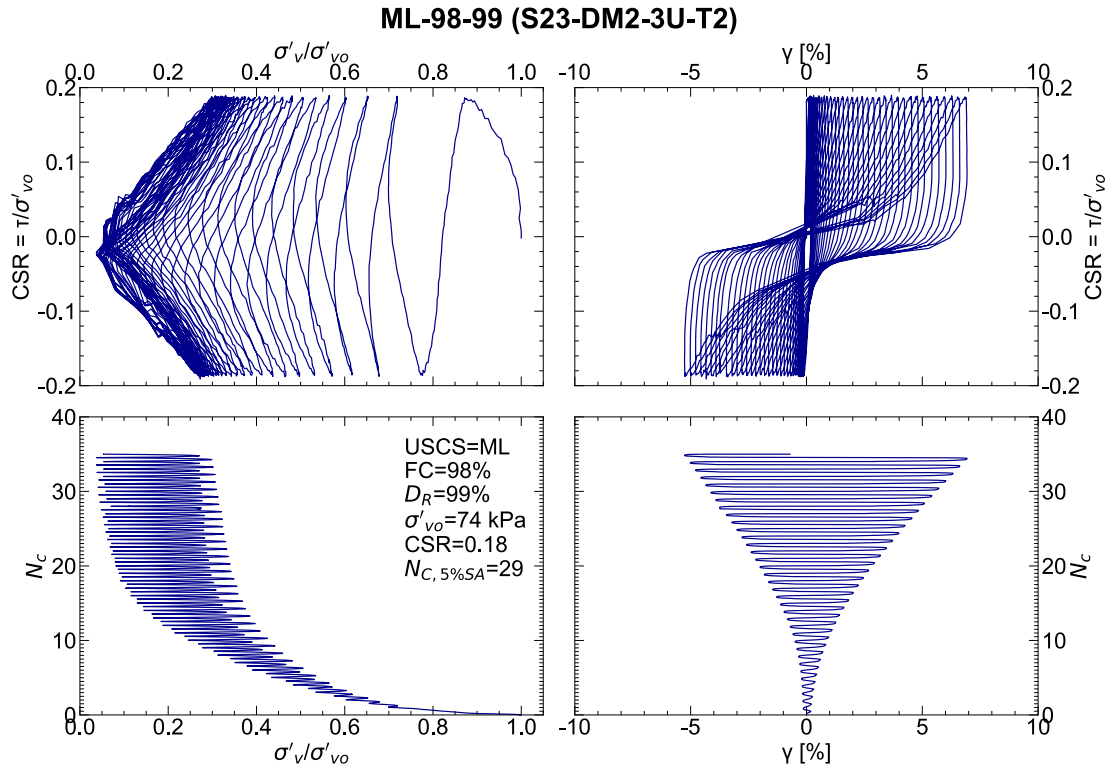


Figure D.2.2.34. CSS test results for ML-98-99 (S23-DM2-3U-T2).

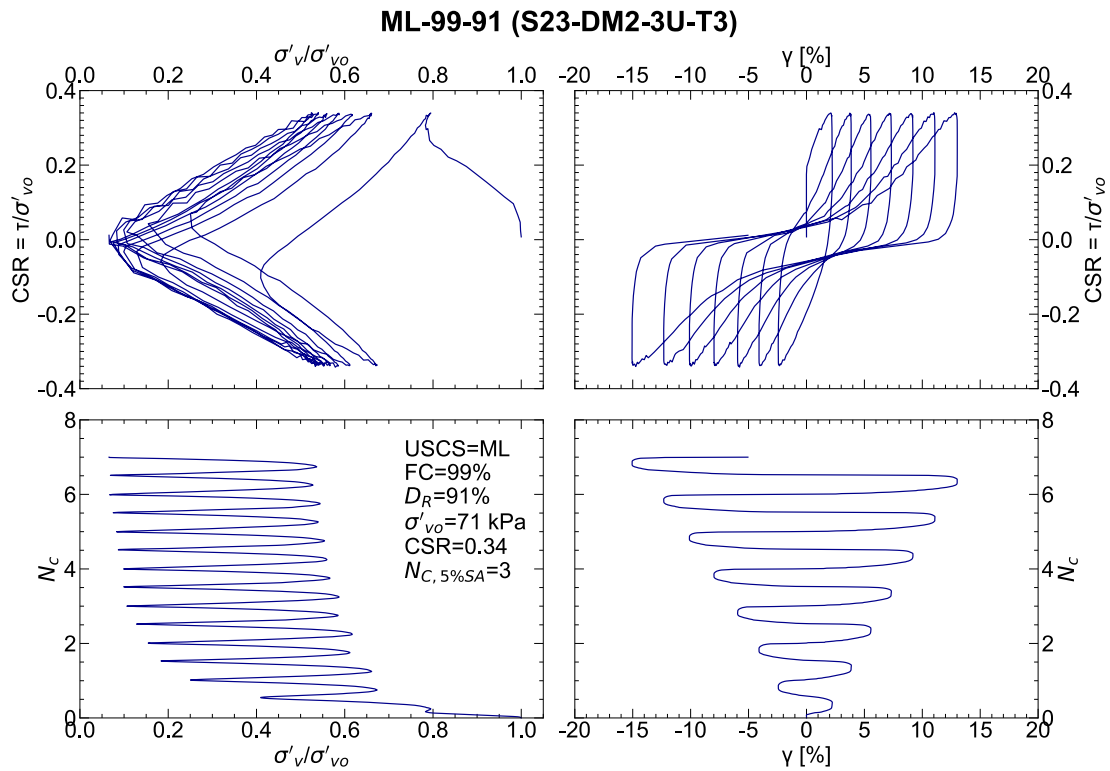


Figure D.2.2.35. CSS test results for ML-99-91 (S23-DM2-3U-T3).

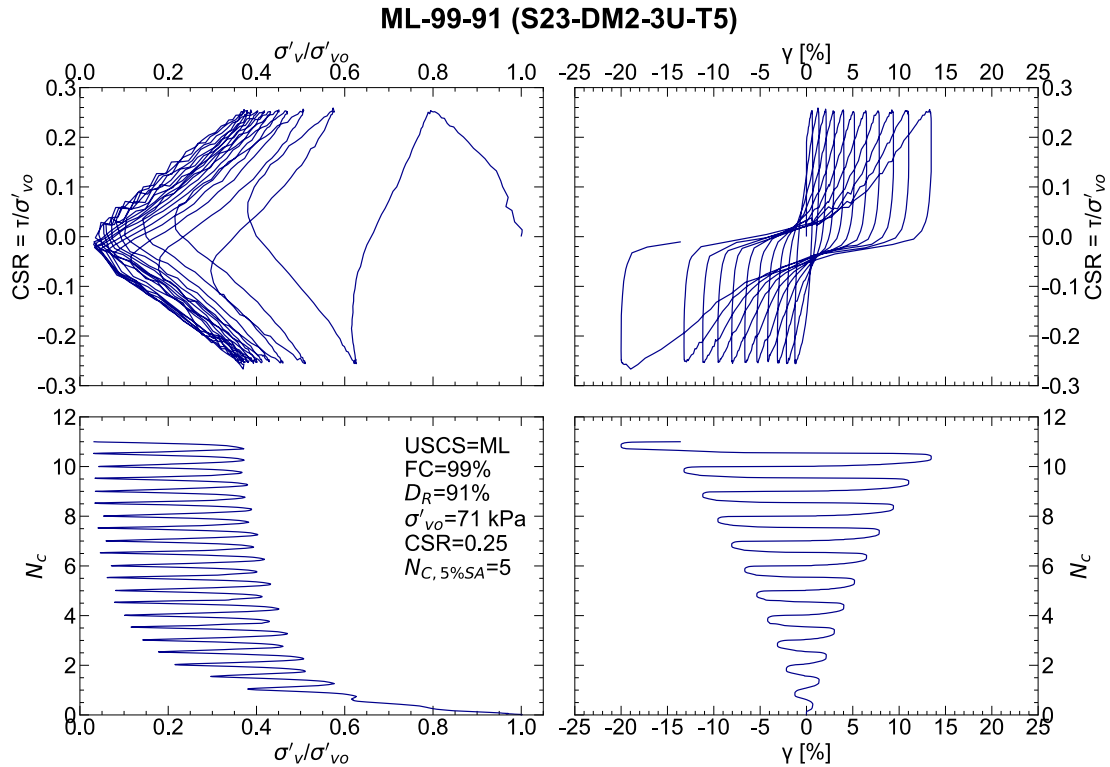


Figure D.2.2.36. CSS test results for ML-99-91 (S23-DM2-3U-T5).

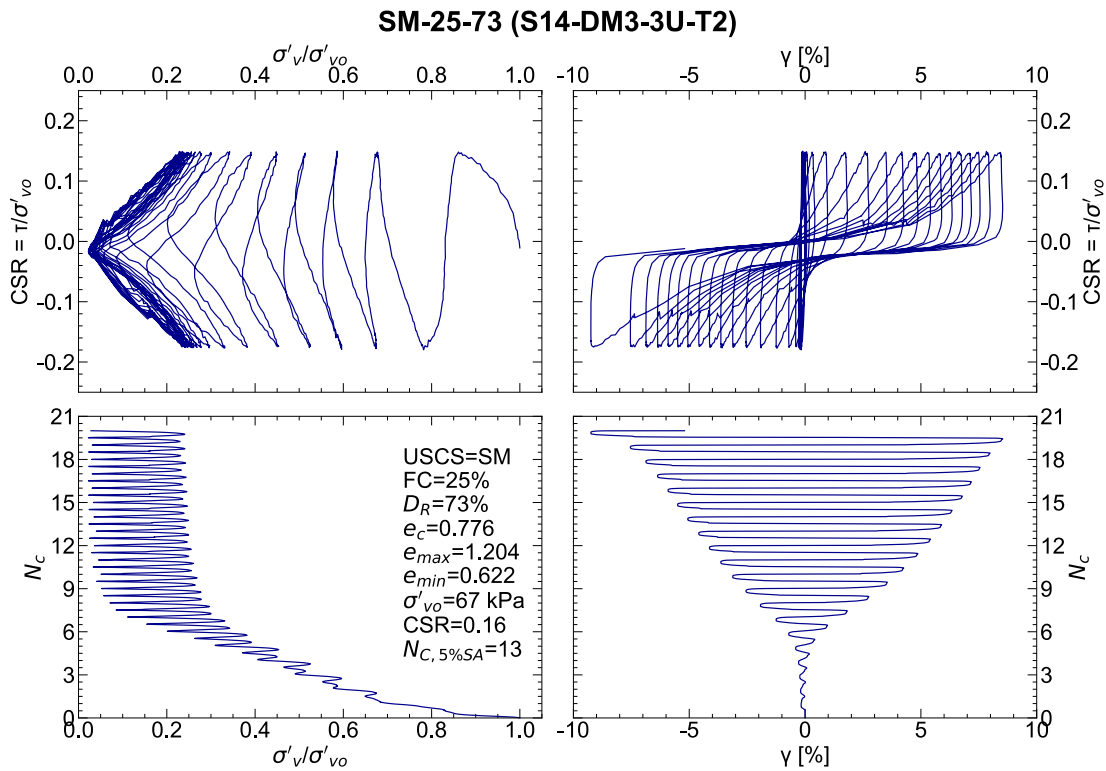


Figure D.2.2.37. CSS test results for SM-25-73 (S14-DM3-3U-T2), not in Chapter 5.

D.2.3 Post-cyclic Monotonic Simple Shear Test Results

SP-3-84 (S33-DM3-1U-T2)

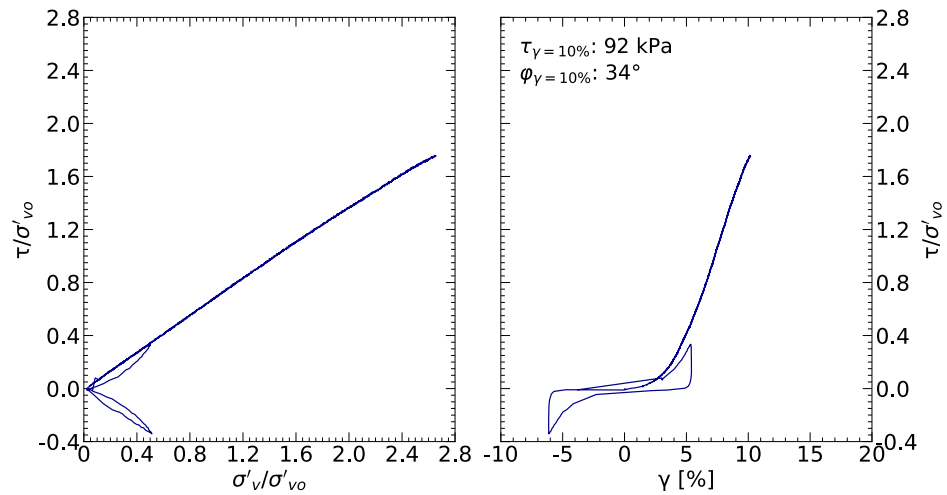


Figure D.2.3.1. Post-cyclic MSS test results for SP-3-84 (S33-DM3-1U-T2).

SP-2-88 (S33-DM3-1U-T3)

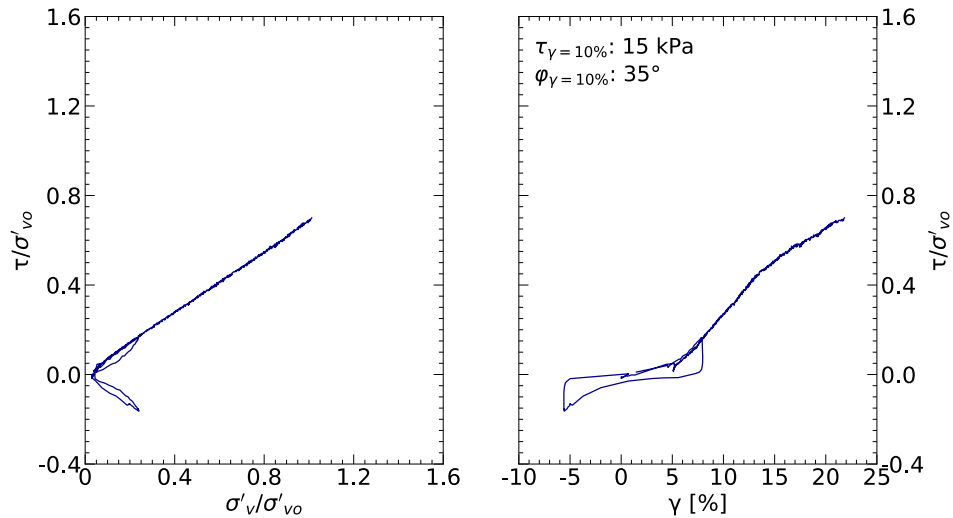


Figure D.2.3.2. Post-cyclic MSS test results for SP-2-88 (S33-DM3-1U-T3).

SP-3-78 (S33-DM3-1U-T4)

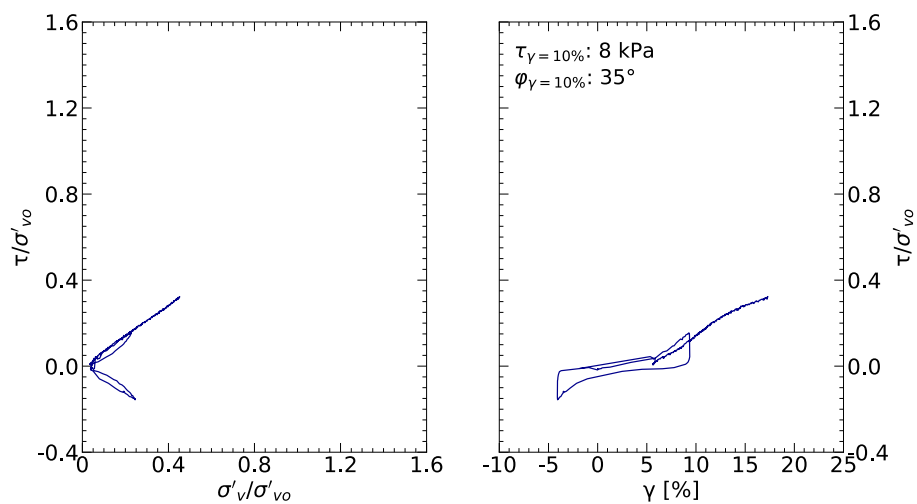


Figure D.2.3.3. Post-cyclic MSS test results for SP-3-78 (S33-DM3-1U-T4).

SM-28-85 (S33-DM3-1U-T1)

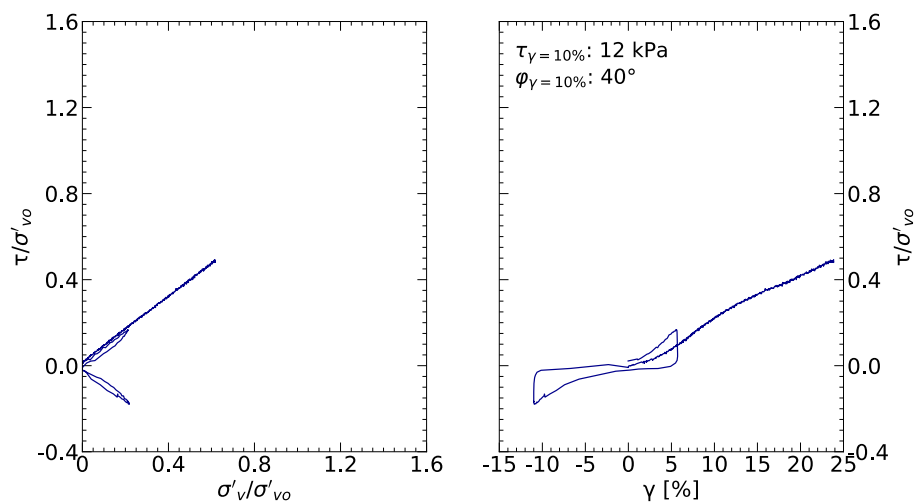


Figure D.2.3.4. Post-cyclic MSS test results for SM-28-85 (S33-DM3-1U-T1).

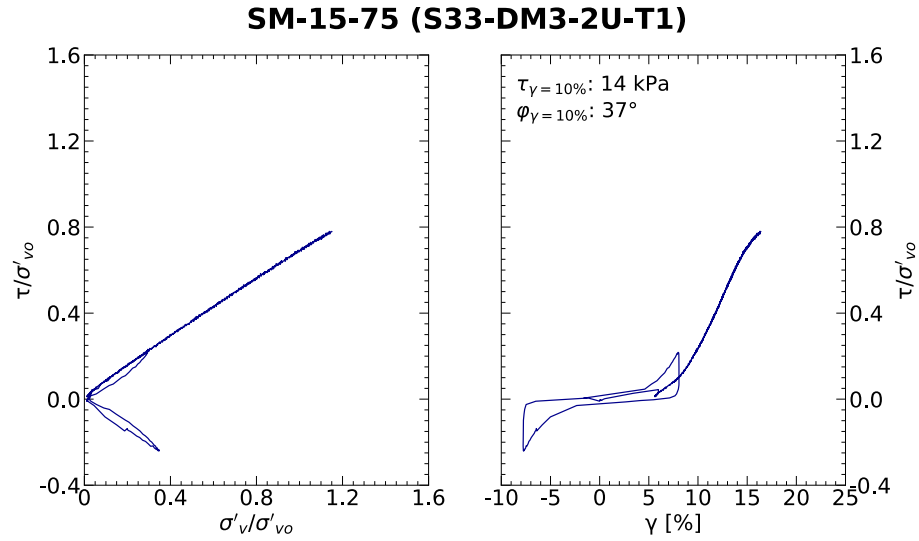


Figure D.2.3.5. Post-cyclic MSS test results for SM-15-75 (S33-DM3-2U-T1).

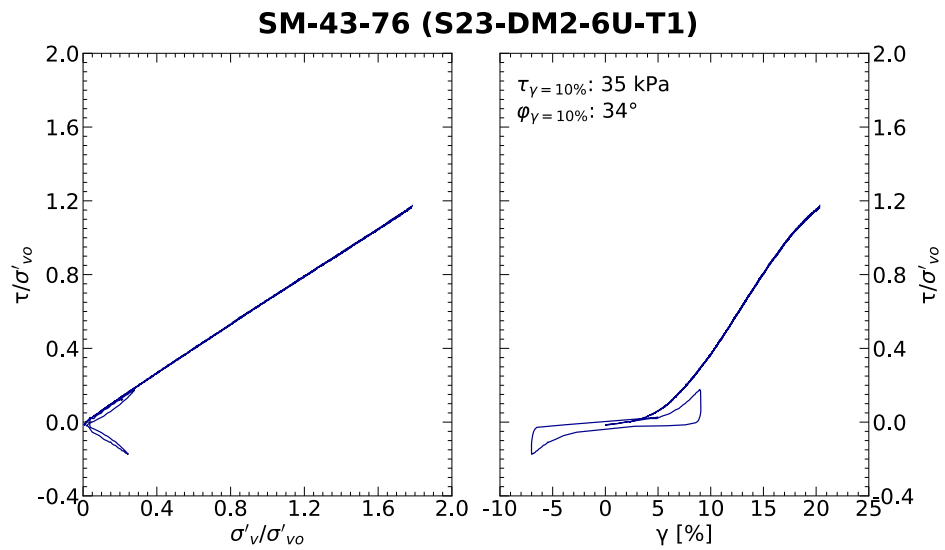


Figure D.2.3.6. Post-cyclic MSS test results for SM-43-76 (S23-DM2-6U-T1).

SM-39-79 (S23-DM2-6U-T2)

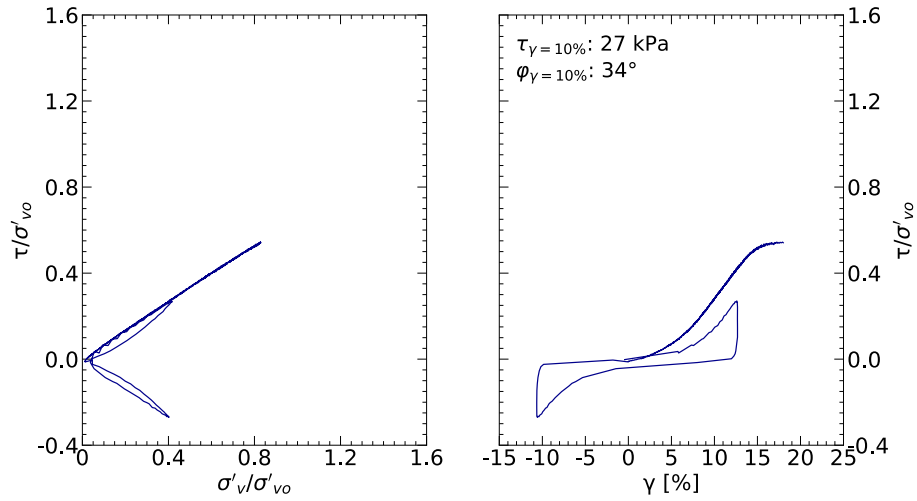


Figure D.2.3.7. Post-cyclic MSS test results for SM-39-79 (S23-DM2-6U-T2).

SM-29-71 (S23-DM2-6U-T3)

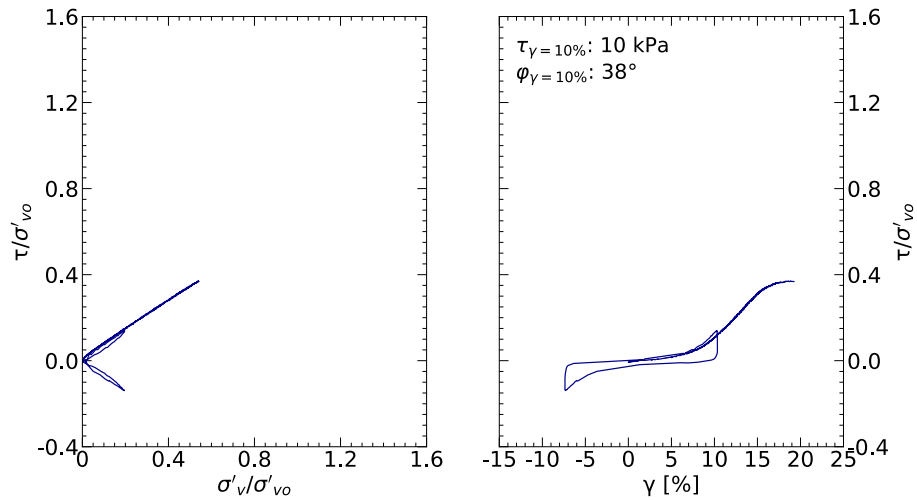


Figure D.2.3.8. Post-cyclic MSS test results for SM-29-71 (S23-DM2-6U-T3).

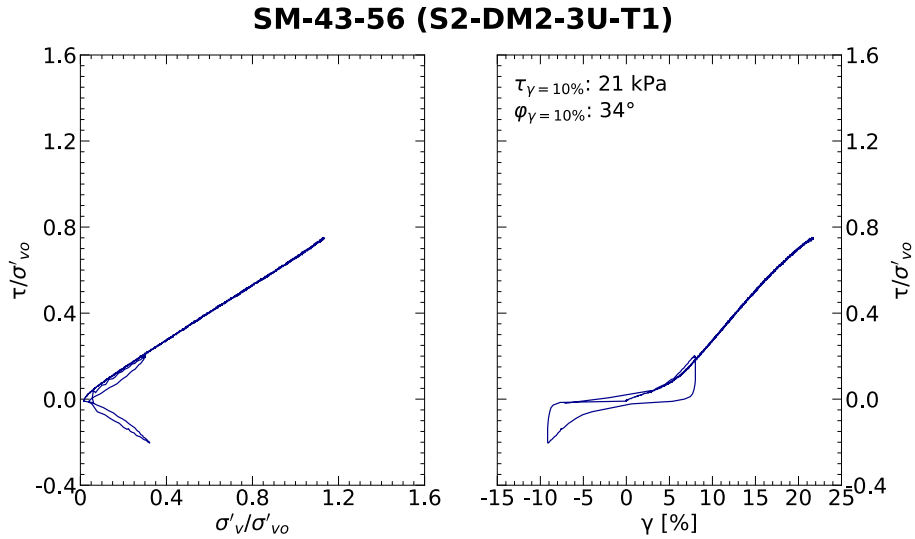


Figure D.2.3.9. Post-cyclic MSS test results for SM-43-56 (S2-DM2-3U-T1).

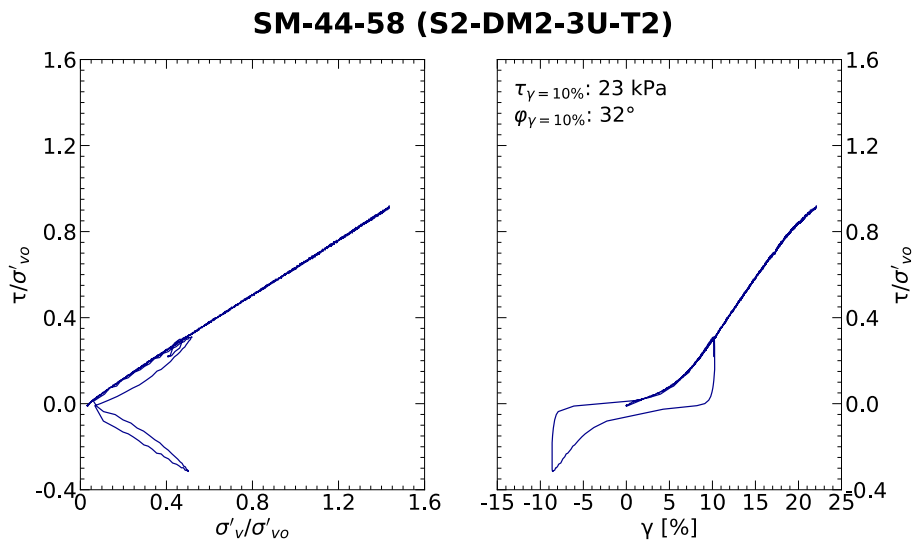


Figure D.2.3.10. Post-cyclic MSS test results for SM-44-58 (S2-DM2-3U-T2).

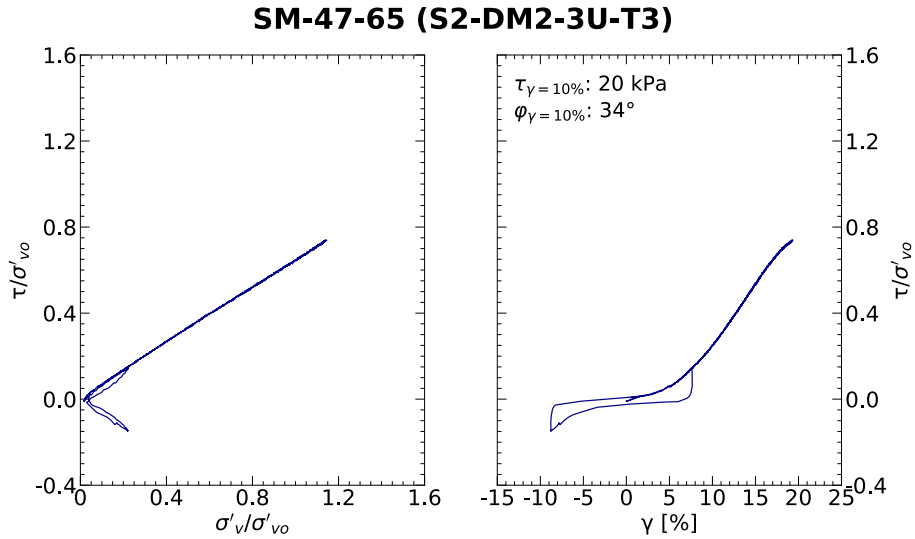


Figure D.2.3.11. Post-cyclic MSS test results for SM-47-65 (S2-DM2-3U-T3).

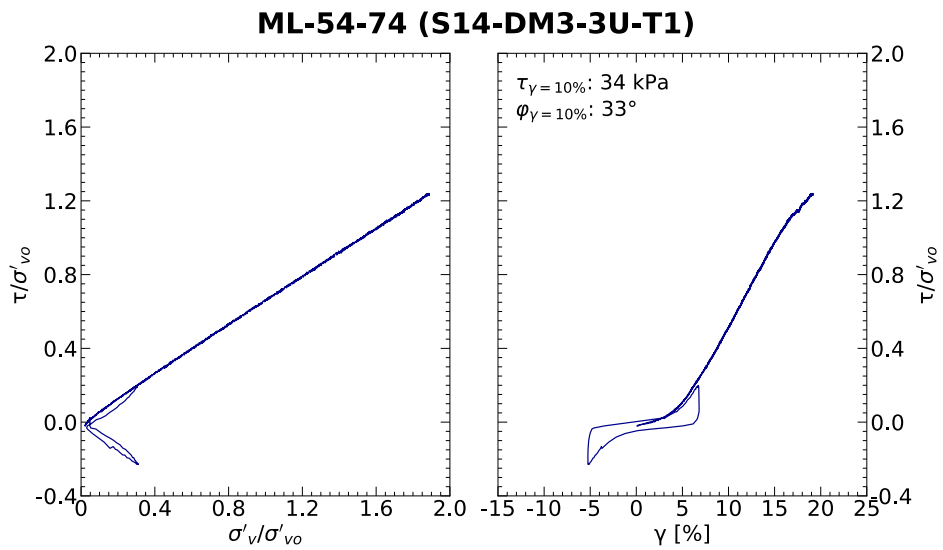


Figure D.2.3.12. Post-cyclic MSS test results for ML-54-74 (S14-DM3-3U-T1).

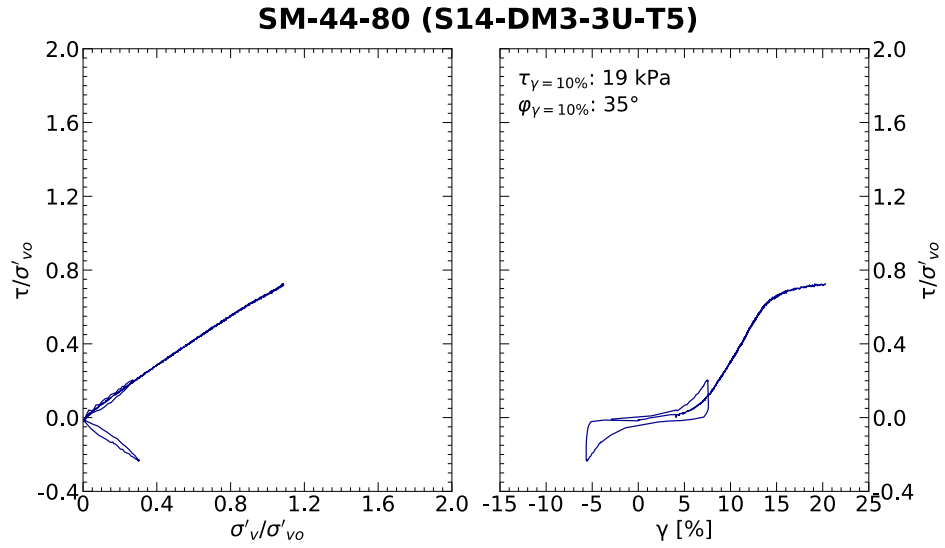


Figure D.2.3.13. Post-cyclic MSS test results for SM-44-80 (S14-DM3-3U-T5).

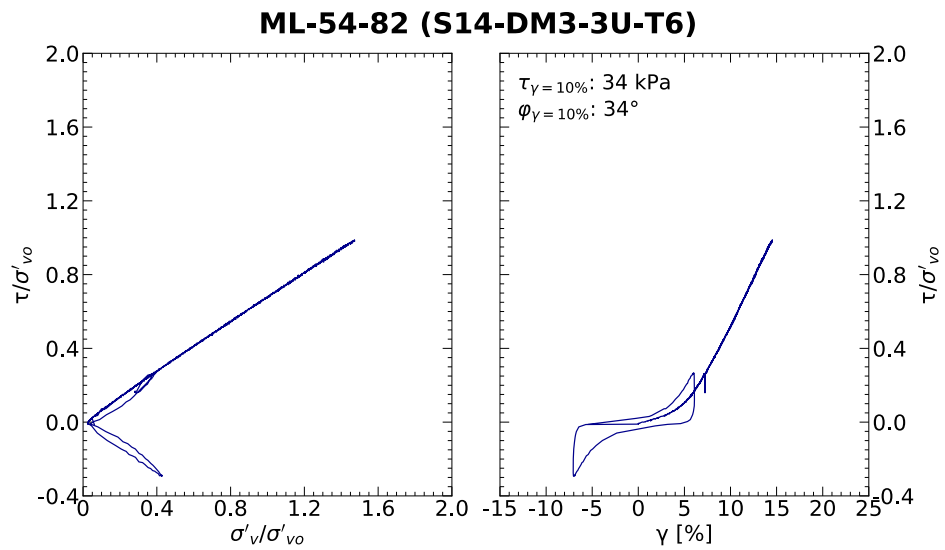


Figure D.2.3.14. Post-cyclic MSS test results for ML-54-82 (S14-DM3-3U-T6).

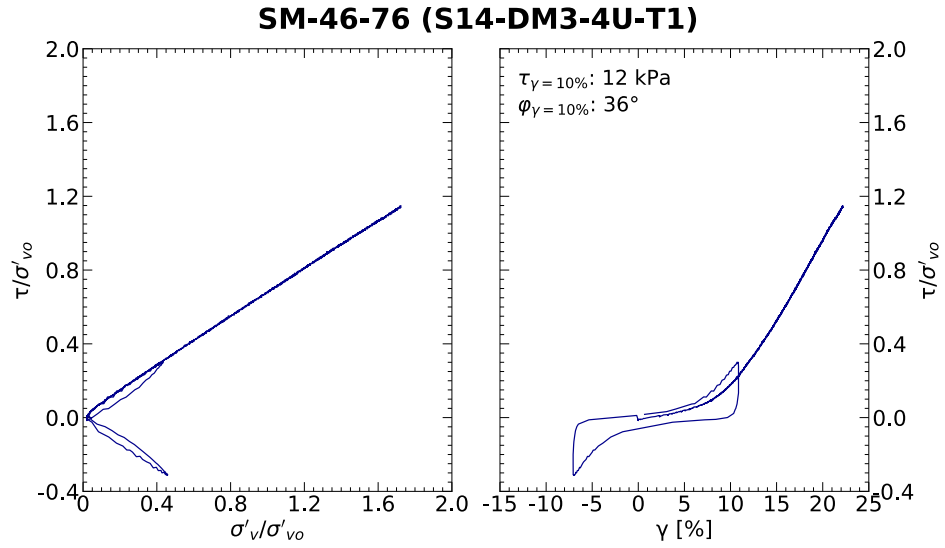


Figure D.2.3.15. Post-cyclic MSS test results for SM-46-76 (S14-DM3-4U-T1).

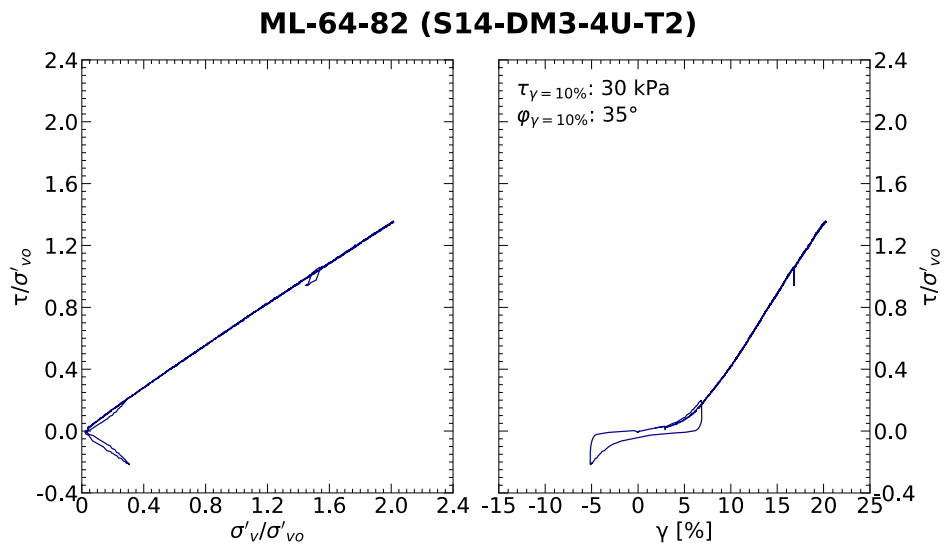


Figure D.2.3.16. Post-cyclic MSS test results for ML-64-82 (S14-DM3-4U-T2).

ML-59-81 (S14-DM3-4U-T3)

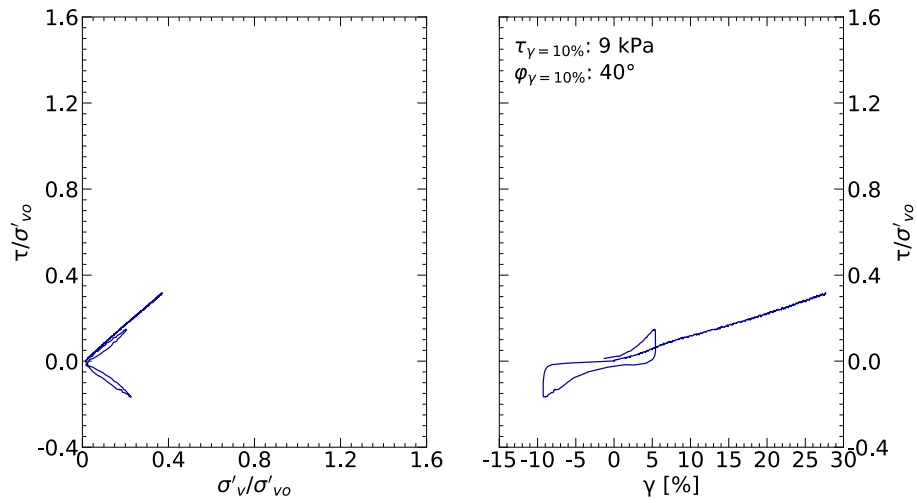


Figure D.2.3.17. Post-cyclic MSS test results for ML-59-81 (S14-DM3-4U-T3).

ML-72-89 (S2-DM2-6U-T1)

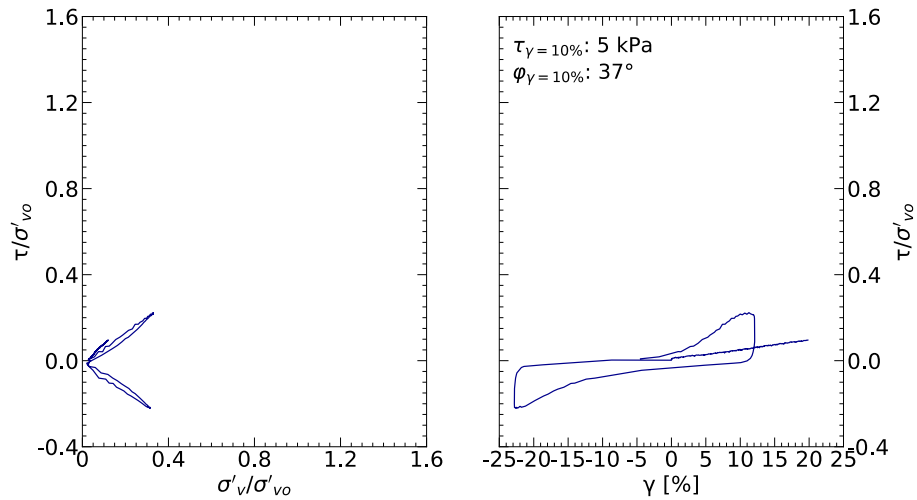


Figure D.2.3.18. Post-cyclic MSS test results for ML-72-89 (S2-DM2-6U-T1).

ML-87-84 (S2-DM2-6U-T2)

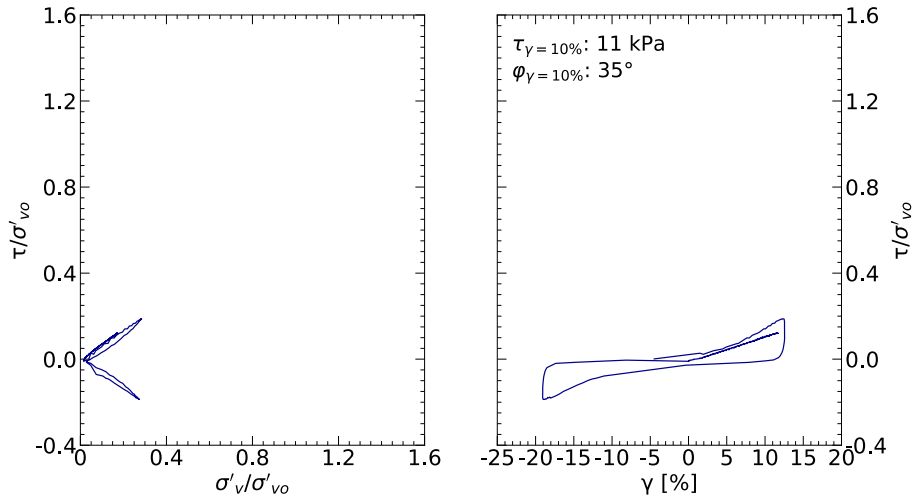


Figure D.2.3.19. Post-cyclic MSS test results for ML-87-84 (S2-DM2-6U-T2).

ML-57-87 (S14-DM3-6U-T1)

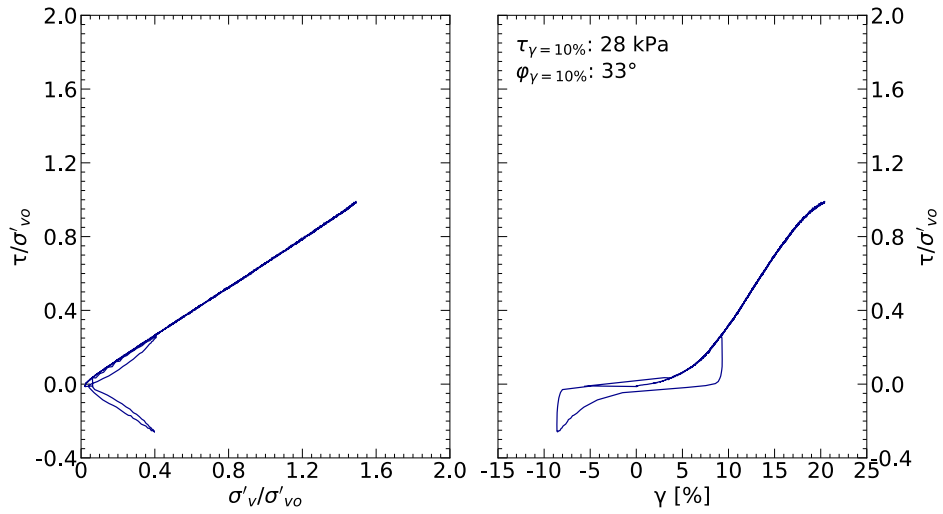


Figure D.2.3.20. Post-cyclic MSS test results for ML-57-87 (S14-DM3-6U-T1).

ML-71-99 (S14-DM3-6U-T2)

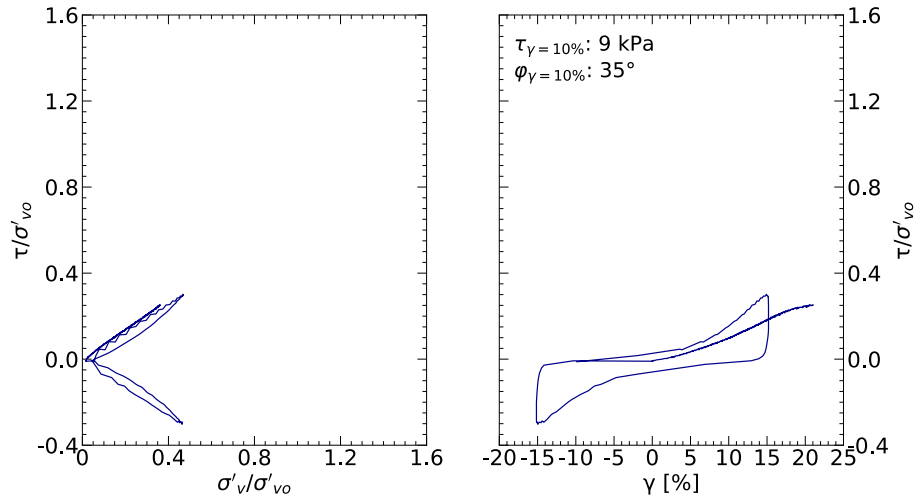


Figure D.2.3.21. Post-cyclic MSS test results for ML-71-99 (S14-DM3-6U-T2).

ML-74-100 (S14-DM3-6U-T3)

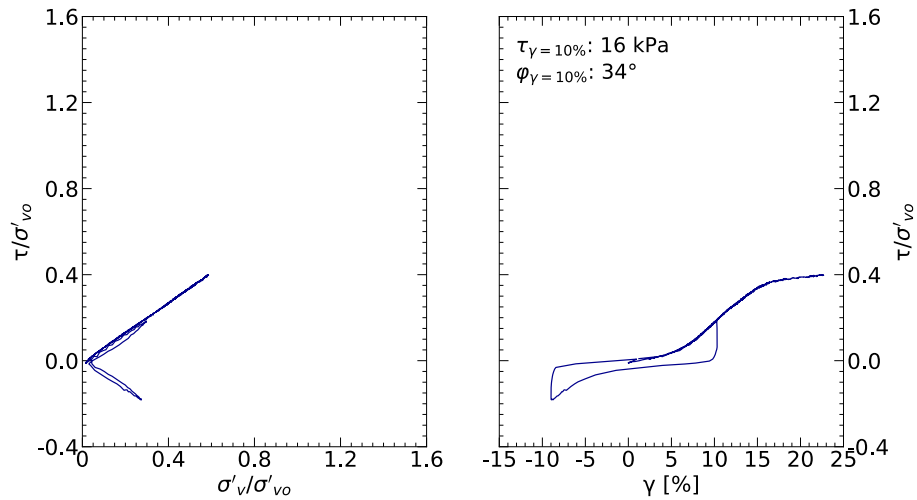


Figure D.2.3.22. Post-cyclic MSS test results for ML-74-100 (S14-DM3-6U-T3).

ML-99-86 (S33-DM3-3U-T4)

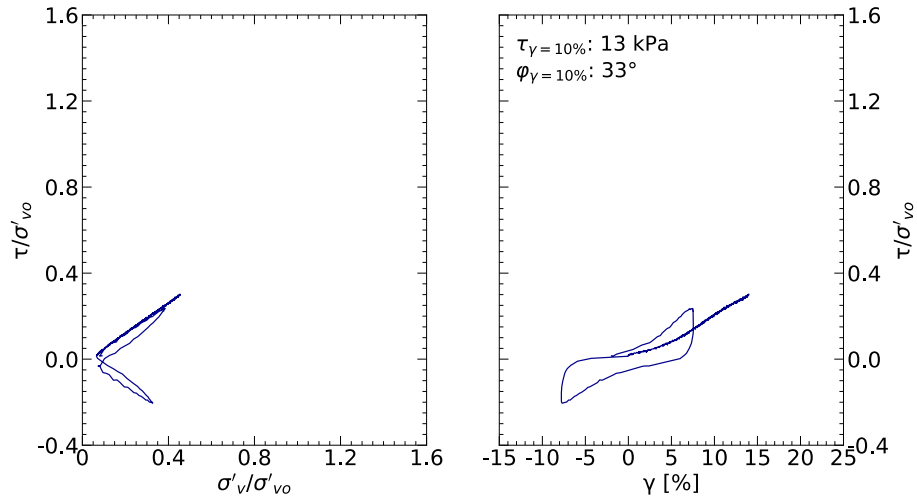


Figure D.2.3.23. Post-cyclic MSS test results for ML-99-86 (S33-DM3-3U-T4).

ML-99-92 (S33-DM3-3U-T5)

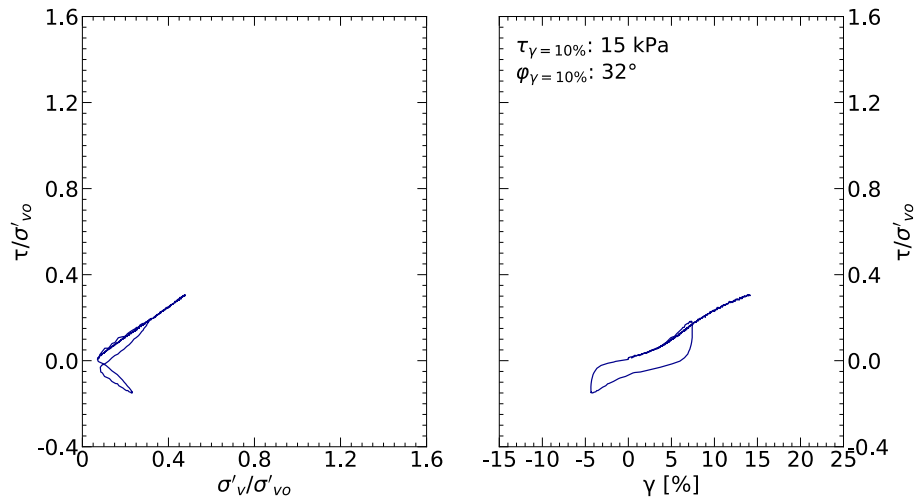


Figure D.2.3.24. Post-cyclic MSS test results for ML-99-92 (S33-DM3-3U-T5).

ML-98-82 (S33-DM3-3U-T6)

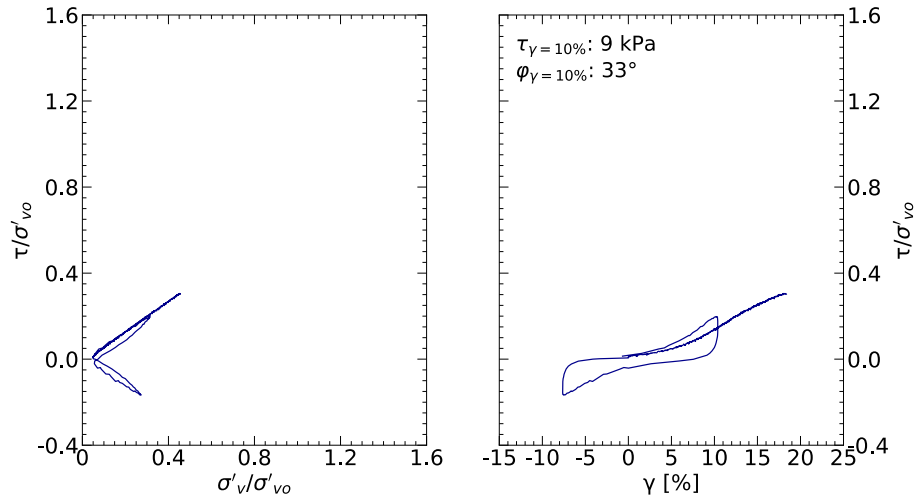


Figure D.2.3.25. Post-cyclic MSS test results for ML-98-82 (S33-DM3-3U-T6).

ML-99-94 (S33-DM3-4U-T1)

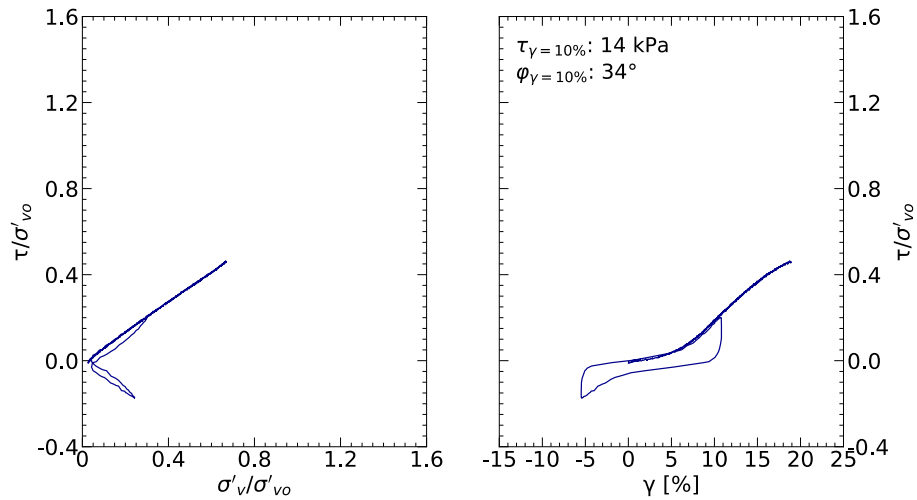


Figure D.2.3.26. Post-cyclic MSS test results for ML-99-94 (S33-DM3-4U-T1).

ML-97-85 (S33-DM3-4U-T2)

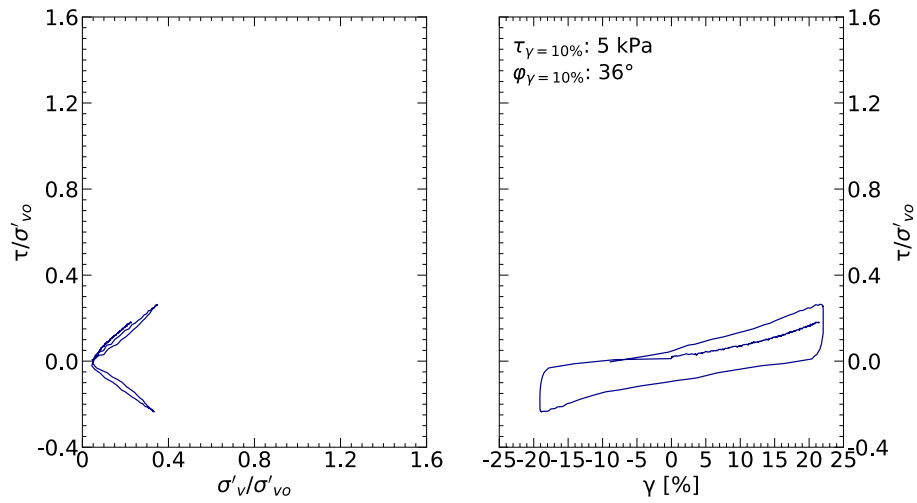


Figure D.2.3.27. Post-cyclic MSS test results for ML-97-85 (S33-DM3-4U-T2).

ML-98-89 (S33-DM3-4U-T3)

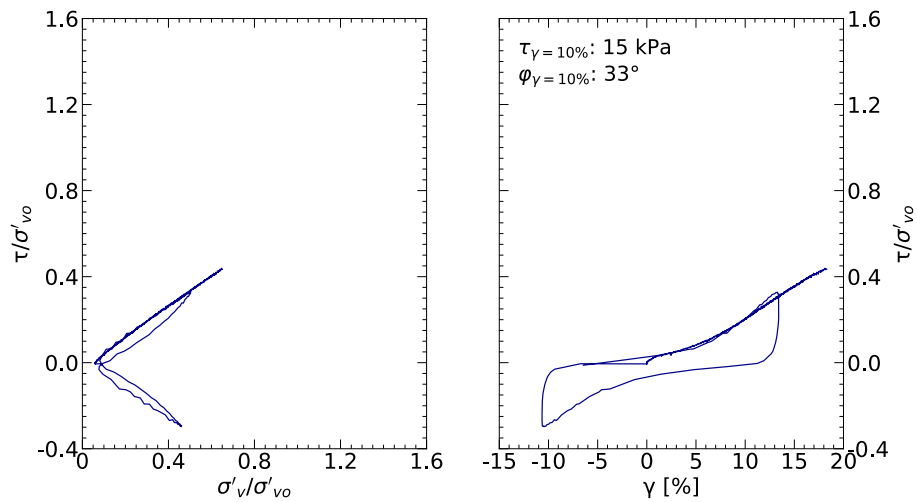


Figure D.2.3.28. Post-cyclic MSS test results for ML-98-89 (S33-DM3-4U-T3).

ML-92-82 (S2-DM2-1U-T1)

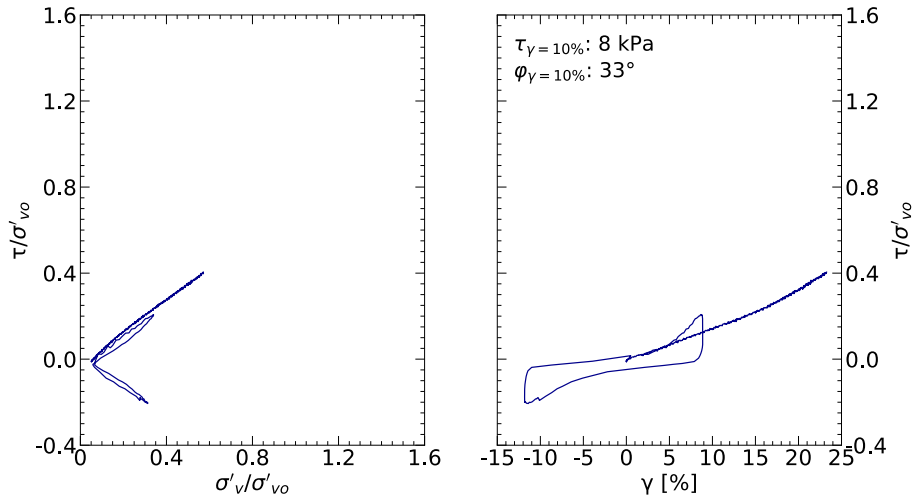


Figure D.2.3.29. Post-cyclic MSS test results for ML-92-82 (S2-DM2-1U-T1).

ML-89-77 (S2-DM2-1U-T2)

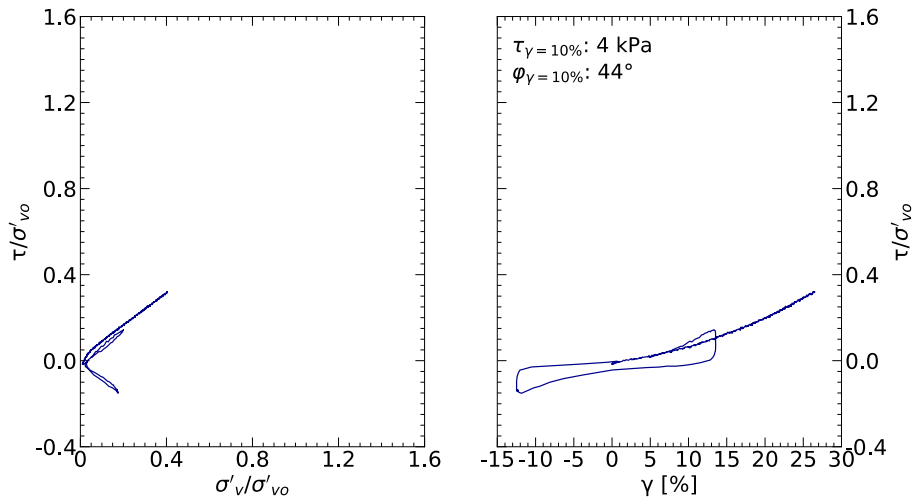


Figure D.2.3.30. Post-cyclic MSS test results for ML-89-77 (S2-DM2-1U-T2).

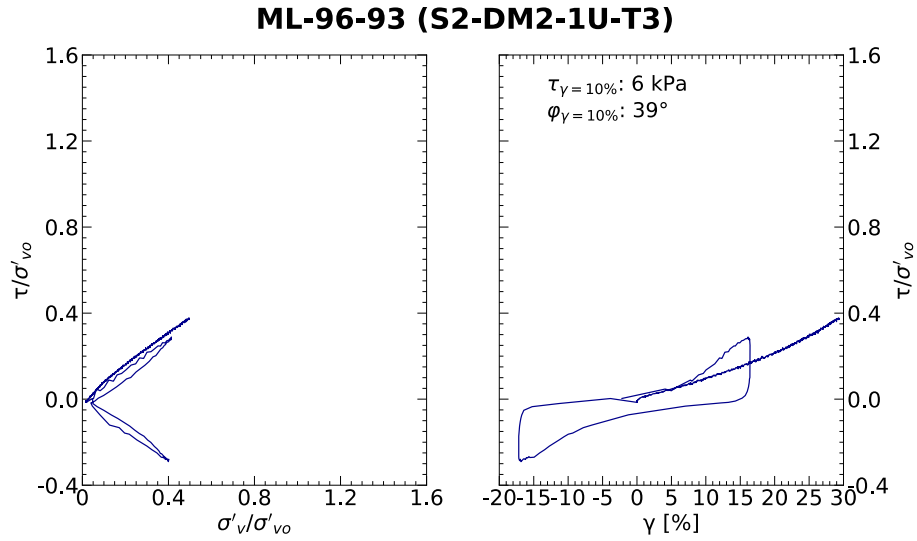


Figure D.2.3.31. Post-cyclic MSS test results for ML-96-93 (S2-DM2-1U-T3).

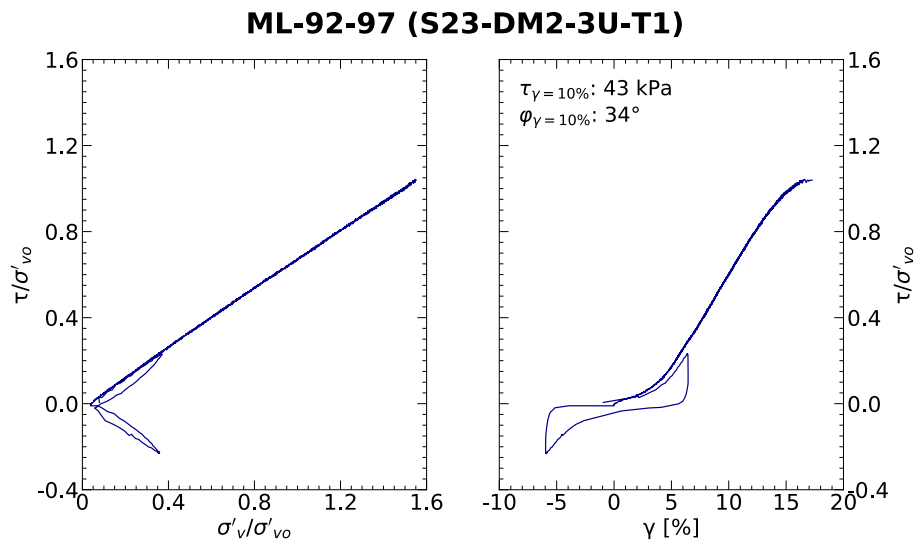


Figure D.2.3.32. Post-cyclic MSS test results for ML-92-97 (S23-DM2-3U-T1).

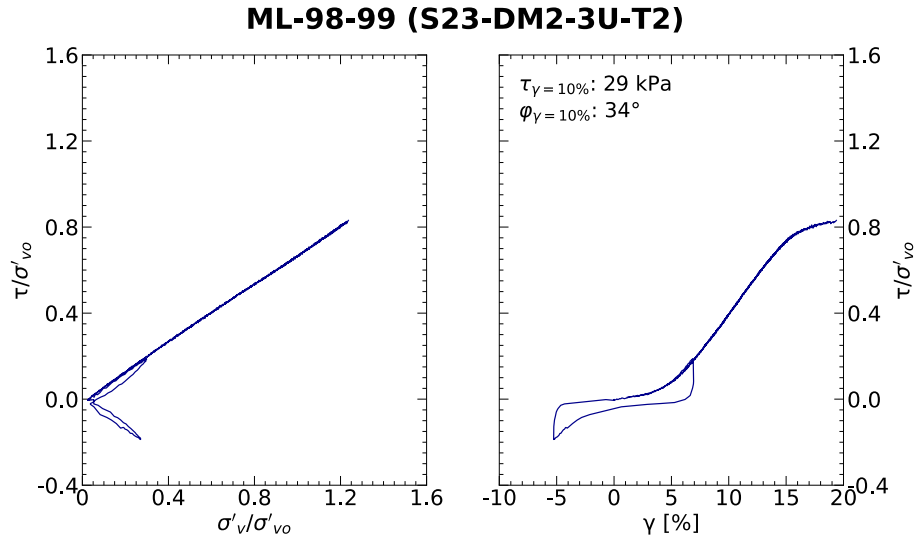


Figure D.2.3.33. Post-cyclic MSS test results for ML-98-99 (S23-DM2-3U-T2).

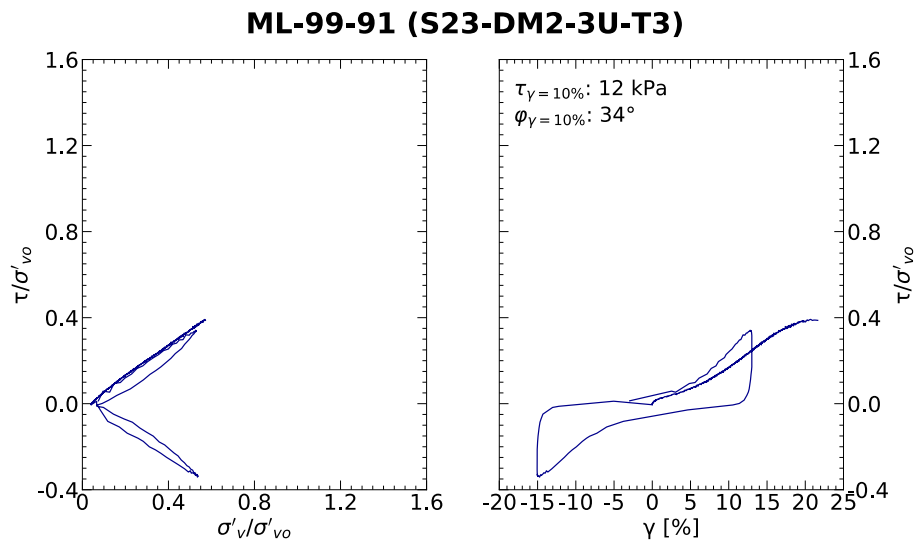


Figure D.2.3.34. Post-cyclic MSS test results for ML-99-91 (S23-DM2-3U-T3).

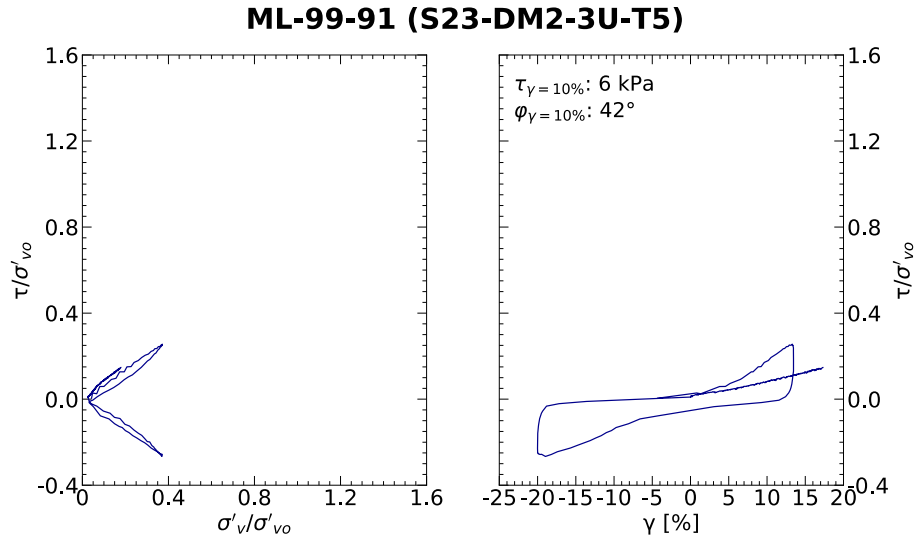


Figure D.2.3.35. Post-cyclic MSS test results for ML-99-91 (S23-DM2-3U-T5).

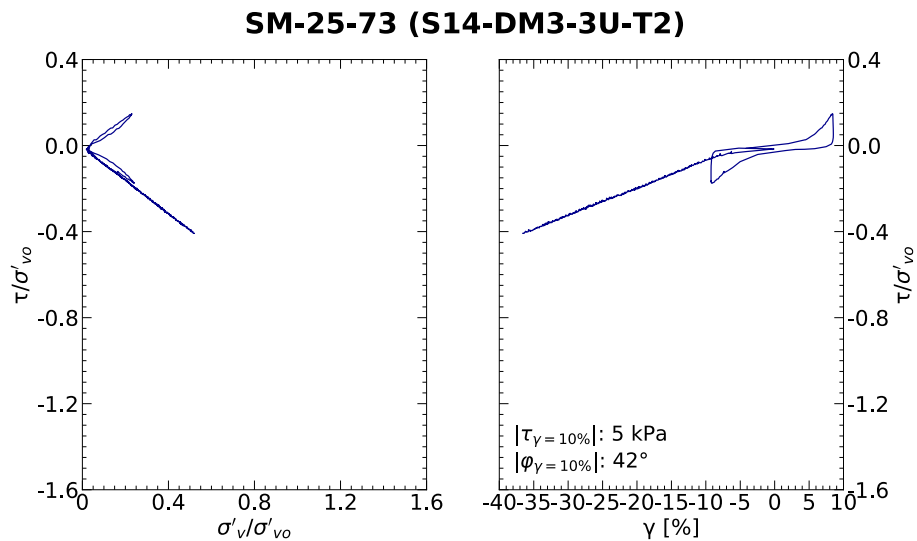


Figure D.2.3.36. Post-cyclic MSS test results for SM-25-73 (S14-DM3-3U-T2) retrieved from a 4.740-m depth. This test specimen is not presented in Chapter 5.

Appendix E

Steady State Testing of Reconstituted Specimens

Introduction

Steady state testing was conducted on reconstituted specimens prepared using soil composites C, G, and K described in Chapter 4. These soil composites are an equivalent of respective cyclic simple shear test specimen mixtures: S23-DM2-6U-T1, -T2, and -T3; S14-DM3-4U-T1, -T2, and -T3; and S33-DM3-4U-T1, -T2, and -T3. Their index properties are listed in Table E.1.

Specimen Preparation

Reconstituted specimens were prepared using the moist tamping method. The initial moisture content of soil was 8%. Specimens were prepared in five layers using 2% undercompaction. The target height and diameter of specimens were 90 mm and 41.5 mm, respectively. Filter paper was placed over porous stones to prevent the loss of fines, especially during the differential vacuum saturation. Two 0.051-mm thick membranes ($E = 1,370$ kPa) were used for each test specimen.

Saturation

All test specimens were subjected to differential vacuum saturation and subsequently to backpressure saturation. A differential vacuum of 15-25 kPa was used to stimulate the bottom-up flow of water thorough specimens. However, specimens comprised of soil with 98% fines (S33-DM3-4U) could not be flushed and had a B-value ranging from 0.69 to 0.78. To explore this issue, one specimen was prepared using the slurry deposition method. However, a B-value of 0.57 was achieved; thus, the method of specimen preparation did not improve the B-value. Considering the low B-values, the S33-DM3-4U reconstituted specimens were sheared in drained rather than undrained conditions, which was the case for other specimens.

Data Processing

Test data were corrected for area and membrane effects. The area correction was applied under the assumption of the specimen deforming as a right cylinder during shearing. Membrane corrections were applied to correct axial and radial stress for membrane strength following the Duncan and Seed (1967) procedure.

Results

The following figures illustrate the preliminary results of the steady state testing on S23-DM2-6U, S14-DM3-4U, and S33-DM3-4U in semi-log e - p' space. The fitting parameters e_{10-SS} (steady state void ratio at $p'_{SS} = 10$ kPa) and λ (slope of the fitted line in semi-log space) where $e_{SS} = e_{10-SS} + \lambda(1 - \log_{10} p'_{SS})$ were defined using the Cubrinovski and Ishihara (2000) form of the steady state line.

Table E.1. Index properties of soil composites and individual soil samples used to build them.

Soil composite (FC, USCS, G _s)	Individual soil sample ID	Individual soil sample FC [%]	Alternative Method (Chapter 4)				Japanese Standard Method	
			e _{min} , individual	e _{max} , individual	e _{min} , composite ± std. error	e _{max} , composite ± std. error	e _{min} , composite ± std. error	e _{max} , composite ± std. error
S23-DM2-6U (37%, SM, 2.69)	T1	43	0.565	1.314	0.572 ± NA	1.279 ± NA	0.551 ± NA	1.220 ± NA
	T2	39	0.575	1.293				
	T3	29	0.577	1.205				
S14-DM3-4U (56%, ML, 2.69)	T1	46	0.607	1.400	0.619	1.444	0.605	1.379
	T2	64	0.647	1.512	±	±	±	±
	T3	59	0.618	1.467	0.004	0.005	0.001	0.006
S33-DM3-4U (98%, ML, 2.70)	T1	99	0.912	2.202	0.896	2.224	0.898	2.039
	T2	97	0.845	2.096	±	±	±	±
	T3	98	0.890	2.188	0.015	0.014	0.004	0.012

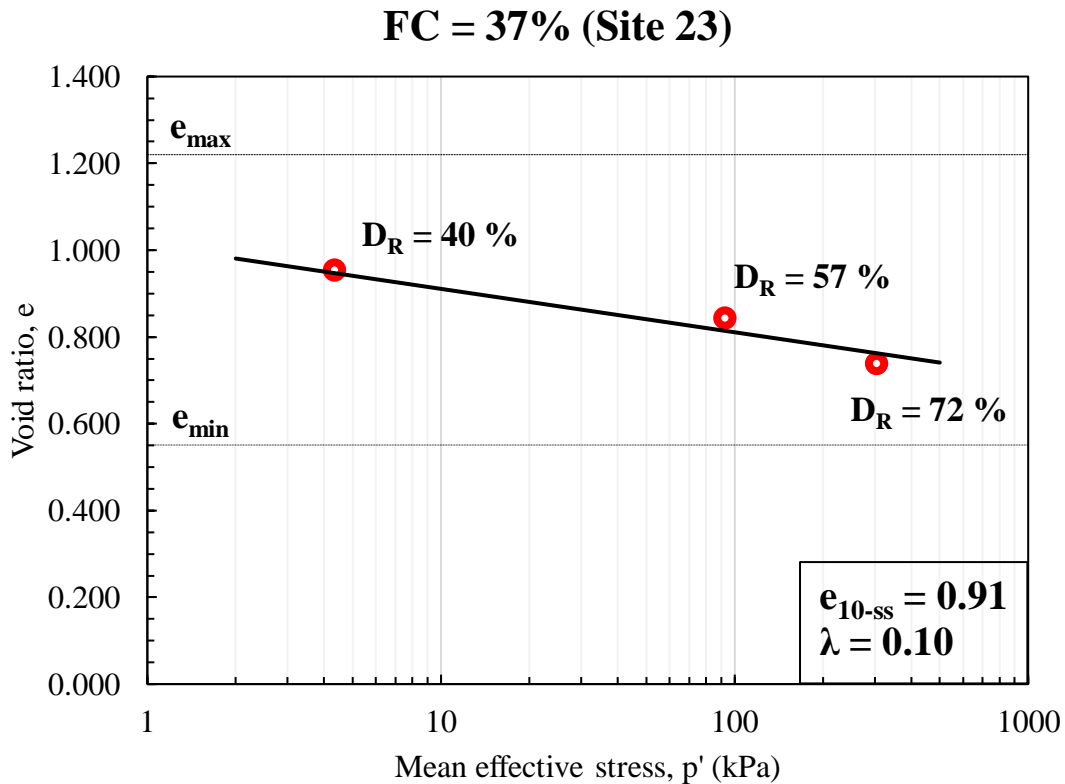


Figure E.1. Steady-state test data for S23-DM2-6U. (D_R = relative density at the end of consolidation, prior to shearing.)

FC = 56% (Site 14)

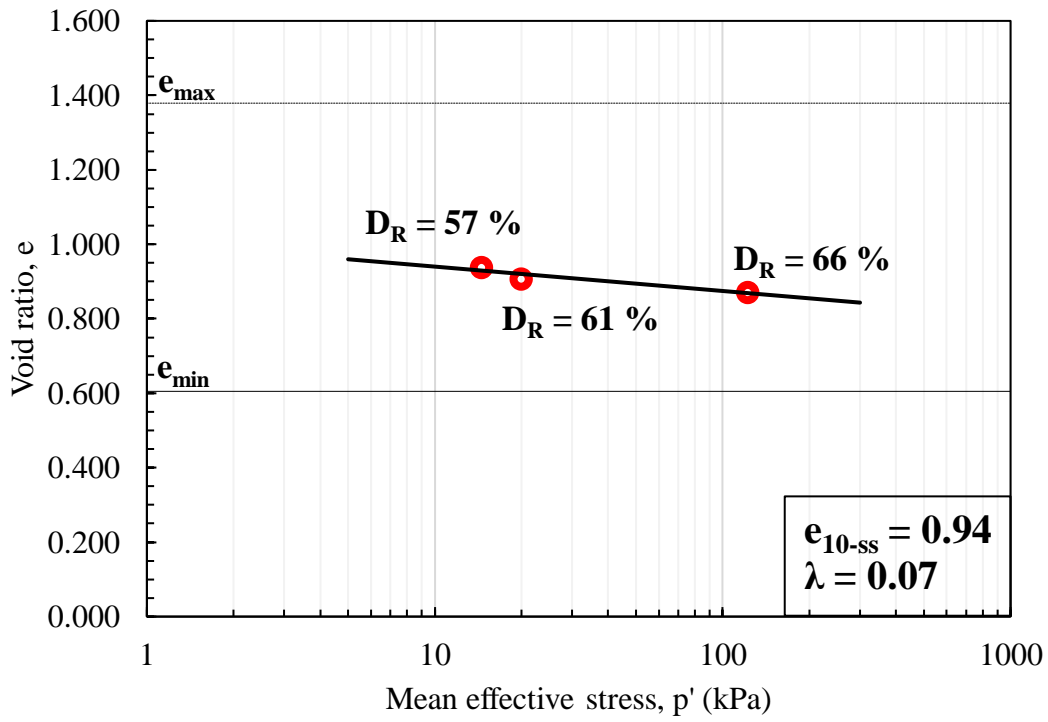


Figure E.2. Steady-state test data for S14-DM3-4U. (D_R = relative density at the end of consolidation, prior to shearing.)

FC = 98% (Site 33)

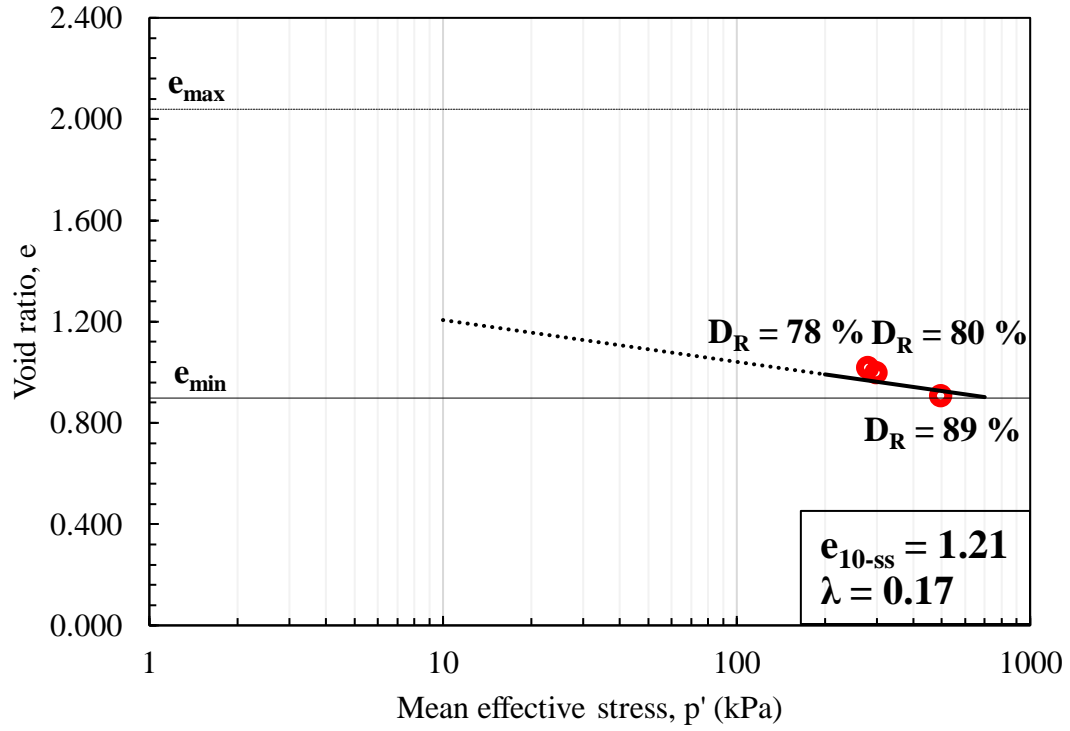


Figure E.3. Steady-state test data for S33-DM3-4U. (D_R = relative density at the end of consolidation, prior to shearing.)

References

- Cubrinovski, M., and Ishihara, K. (2000). Flow potential of sandy soils with different grain compositions. *Soils and Foundations*, 40(4), 103-119.
- Duncan and Seed (1967). Corrections for Strength Test Data. *J. of the Soil Mechanics and Foundations Division, ASCE*, 93(SM5), 121-137.